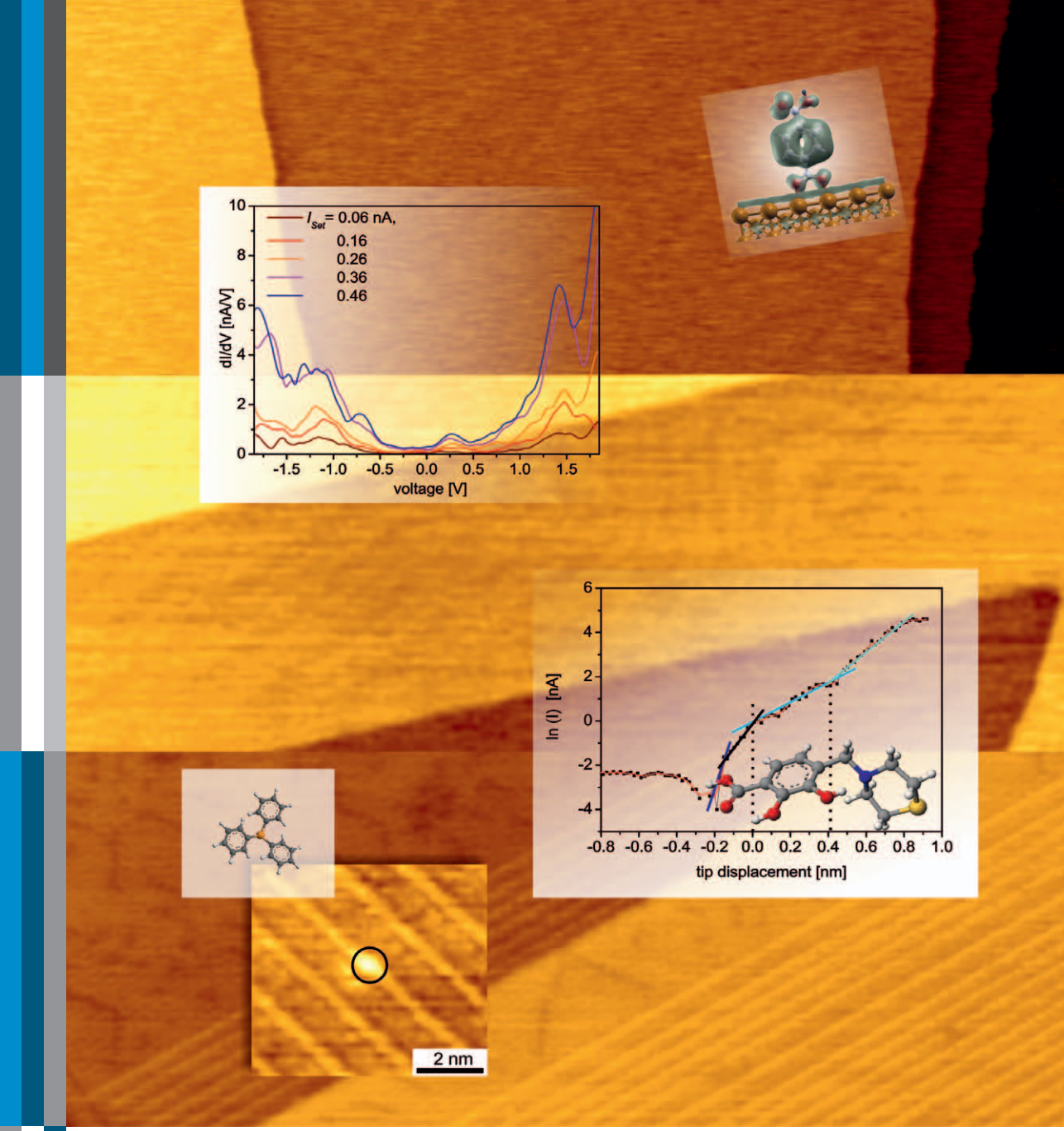

Alternative Systems for Molecular Electronics: Functionalized Carboxylic Acids on Structured Surfaces

Maria Christina Lennartz

Mitglied der Helmholtz-Gemeinschaft

JÜLICH
FORSCHUNGSZENTRUM

Schriften des Forschungszentrums Jülich
Reihe Information / Information Band / Volume 13

Forschungszentrum Jülich GmbH
Institute of Solid State Research (IFF)

Alternative Systems for Molecular Electronics: Functionalized Carboxylic Acids on Structured Surfaces

Maria Christina Lennartz

Schriften des Forschungszentrums Jülich
Reihe Information / Information Band / Volume 13

ISSN 1866-1777 ISBN 978-3-89336-667-5

Bibliographic information published by the Deutsche Nationalbibliothek.
The Deutsche Nationalbibliothek lists this publication in the Deutsche Nationalbibliografie; detailed bibliographic data are available in the Internet at http://dnb.d-nb.de.

Publisher and Distributor:	Forschungszentrum Jülich GmbH Zentralbibliothek 52425 Jülich Phone +49 (0) 24 61 61-53 68 · Fax +49 (0) 24 61 61-61 03 e-mail: zb-publikation@fz-juelich.de Internet: http://www.fz-juelich.de/zb
Cover Design:	Grafische Medien, Forschungszentrum Jülich GmbH
Printer:	Grafische Medien, Forschungszentrum Jülich GmbH
Copyright:	Forschungszentrum Jülich 2010

Schriften des Forschungszentrums Jülich
Reihe Information / Information Band / Volume 13

D 82 (Diss., RWTH Aachen, Univ., 2010)

ISSN 1866-1777
ISBN 978-3-89336-667-5

The complete volume ist freely available on the Internet on the Jülicher Open Access Server (JUWEL) at http://www.fz-juelich.de/zb/juwel

Alternative Systeme für die Molekularelektronik: Funktionalisierte Carbonsäuren auf strukturierten Oberflächen

Eine Möglichkeit die Miniaturisierung elektronischer Bauelemente voranzutreiben bilden sich selbst organisierende Bauteile einer „molekularen Elektronik“. Ein wichtiger Schritt hin zur Anwendung ist die Verknüpfung der konventionellen HL-Elektronik (CMOS) mit molekularen Bauteilen zu einem neuen kombinierten System (CMOL). Hierbei übernehmen Moleküle die Funktion des aktiven Bauelements während herkömmliche HL-Bauelemente als Ansteuerungseinheit genutzt werden.
Im Rahmen der vorliegenden Arbeit wurden Carbonsäuren untersucht, die durch ihre chemische Struktur geeignet sind mit dem in der CMOS Technologie verbreiteten Material Kupfer kombiniert zu werden. Sie organisieren sich selbstständig zu geordneten Monolagenstrukturen auf Cu(110)-Oberflächen, indem sie eine chemische Bindung mit Kupfer eingehen. Im Fokus der Arbeit stehen die elektronische Charakterisierung des Molekül/Substratsystems sowie die systematische Untersuchung von Einflüssen verschiedener Molekülteile. Es wurden die Methoden der Rastertunnelmikroskopie genutzt, sowie ergänzend XPS/AES, UV-VIS und LEED. Die Transporteigenschaften wurden sowohl durch I-V als auch durch I-z Messungen untersucht. Durch Variation des Abstands zwischen dem Molekül und der Messspitze konnten die Zustandsdichten einzelner Molekülorbitale angesprochen werden, deren Energien in Form von Peaks in den dI/dV Kurven erscheinen. Auf der Dichtefunktionaltheorie basierende Simulationen (der Forschungsgruppe IFF-1 des FZ Jülich) wurden herangezogen, um die gemessenen Peaks den spezifischen Molekülorbitalen zuzuordnen. So war es möglich ein Bild der Molekülorbitale im Bezug auf ihre Energie und ihre räumliche Ausdehnung zu erstellen. Es wurde gezeigt, dass z.B. ein N-Heteroatom zu einer Verschiebung der Molekülorbitale und damit zu einer Verringerung der Bandlücke führt. Durch die Untersuchung verschiedener Substituenten entstanden somit erste Teile eines „molekularen Baukastensystems“. Dieses ermöglicht es, Molekülteile gezielt nach ihren elektronischen Eigenschaften im kombinierten Molekül/Substratsystem zusammenzusetzen, anstatt jedes einzelne Molekül aufwändig zu untersuchen.
In einem weiteren Schritt wurde eine Carbonsäure mit einer zweiten funktionalen Endgruppe gewählt, welche die Bindung zu einer zweiten Elektrode aus einem unterschiedlichen Material ermöglicht und somit eine Diodenfunktionalität des Moleküls entstehen lässt. Die bindungsspezifische Anordnung dieser Thioethercarbonsäure sowie deren elektronische Eigenschaften wurden auf Au(111)-Oberflächen untersucht. STM Untersuchungen zeigten geordnete Strukturen und XPS Messungen bestätigen eine zerstörungsfreie Chemisorption der Moleküle. Die elektronischen Eigenschaften des Systems konnten erstmals durch die Abbildung der lokalen Zustandsdichten aus I-V Messungen sowie durch Messung der molekülgruppenspezifischen Abklinglängen beschrieben werden.
Schließlich wurde durch die Untersuchung von Halbleiter/Metall/Molekülsystemen eine weitere Möglichkeit aufgezeigt molekulare Systeme mit CMOS Materialien zu verknüpfen. Hierbei bildet die Ge(001)-Oberfläche zusammen mit sich selbst organisierenden Pt Nanodrähten ein strukturiertes Template für die selektive Anordnung von Triphenylphosphanmolekülen.

Alternative Systems for Molecular Electronics: Functionalized Carboxylic Acids on Structured Surfaces

Molecular electronics is recognized as a key candidate to succeed the silicon based technology as soon as the end of the semiconductor roadmap is reached. An important step towards the realization of molecular electronics is the combination of common CMOS devices and molecular elements to new systems.
Today, an advantageously used metal for wires and interconnects in electronic industry is copper due to its low resistance. Thus, it is essential to get a fundamental understanding of organic/copper interfaces and to combine functional molecular systems with linkers which are copper sensitive. Within the scope of this work, carboxylate molecules were investigated which chemically bind to copper. They self-assemble in highly ordered monolayer structures on, e.g., Cu(110) surfaces. Main task of this work is the electronic characterization of the combined molecule/metal system as well as the systematic investigation of the influence of specific molecular parts on the electronic transport. Scanning tunneling microscopy (STM) was used as main technique to investigate the topographic and electronic structures throughout the study, but complementary techniques like XPS/AES, LEED and UV-VIS spectroscopy were employed as well to get additional information. The transport properties were investigated by current-voltage (I-V) and current-distance (I-z) spectroscopy. Distance-dependent I-V measurements enable the detection of the density of states of the system with the orbital energies appearing as peaks in the dI/dV curves. Density functional theory based calculations (IFF-1, FZ Jülich) were used to assign the measured peaks to specific molecular orbitals. Thus, it is possible to display the molecular orbitals with respect to their energies and their spatial distribution. A detailed analysis of all experimentally probed molecular orbitals has shown that the calculated LDOS represents a characteristic fingerprint corresponding to the substitution pattern of the carboxylates bonded to Cu(110). It was shown that, e.g., nitrogen heteroatoms cause a shift in the molecular orbital energies and lead to a system with smaller HOMO-LUMO gap. With a detailed knowledge of the system parameters it is now possible to make precise theoretical predictions on the transport properties of other carboxylate species. Thus, a first toolbox is composed which allows to combine molecular moieties to build up a molecule linked to a metallic electrode with a designed functionality.
In a second step carboxylates with a second functional group were investigated. These molecules chemically bind to two different electrode materials, e.g., with one side of the molecule to copper and with the other side to gold. This causes a diode functionality of the molecule within the junction. The molecular self-assembly of these molecules (here TMBA) was investigated on Au(111) surfaces. STM investigations show ordered monolayer structures and XPS measurements confirm a nondestructive chemisorption of the molecules. The electron transport properties of the system could be revealed from I-V measurements by monitoring the local density of states as well as from I-z measurements by calculating the molecule specific tunneling decay constant β.
Finally, a short excursion presents an alternative approach to combine molecules with CMOS materials. This approach does not use the metal layer as linking point but the semiconductor areas. Semiconductor surfaces, like Ge(001), with self-assembled metallic Pt nanowires build a highly ordered 1D nanotemplate for the selective assembly of triphenylphosphane molecules.

Contents

Acknowledgement

This thesis would not have been possible without the support of many others. Thanks to all of you for scientific and technical support during my stay in Jülich.

First of all, I would like to thank Prof. Rainer Waser for initiating research in the field of Molecular Electronics at his institute and for providing the infrastructure. As my supervisor, Dr. Silvia Karthäuser holds a great share of responsibility for the successful completion of this work. Her ideas initiated this work and hours of discussion helped me to understand my results. Thank you!
Further, I would like to thank Dr. Nicolae Atodiresei and Dr. Vasile Caciuc for their support and the successful cooperation. Many results were only possible due to their ideas and calculations.
Thanks are also due to Prof. Harold Zandvliet from the University of Twente for the help and cooperation in the work for chapter 9. During the shared hours in front of the STM I learned a lot about the physics behind STM.
For the synthesis of the TMBA molecules I am grateful to Prof. Markus Albrecht and Dr. Miriam Baumert.
For the XPS measurements I am grateful to Dr. Astrid Besmehn.
Further afield, numerous colleagues have provided me with data, equipment, ideas and encouragement for which I am extremely grateful: Peter Kowalzik, Manfred Gebauer, Holger John, Hans Haselier, Tobias Menke, Lars Steffens, Marcel Manheller, and Frank Matthes.
Last by no means least, a big thank you is due to my friend, Roland for his never ending support and infinite patience.

1 Introduction

Molecular electronics is recognized as a key candidate to succeed the silicon based technology as soon as the end of the semiconductor roadmap is reached. The use of organic molecules in nanoscale nonlinear circuits offers many opportunities for new types of devices which will differ in fabrication, functionality, and architecture. Molecular wires, two-terminal switches and diodes, three-terminal transistor-like devices, and hybrid devices that use various different signals such as light, magnetic fields, electric fields, chemical or mechanical signals to control electron transport are only a few approaches [1, 2]. But even the fundamental question how electrical current flows across a single molecule is not satisfactorily understood. A prosperous method is to strengthen the fundamental research activity in this field by combining experimental techniques and different theoretical approaches to develop a full physical picture of molecular-scale charge transport. But not only molecular transport properties are essential, also a detailed understanding of coupling schemes of molecules, e.g., the interplay between the intermolecular and the molecular-substrate interactions is needed. The best molecular properties are useless when there is no way to address these molecules or when the molecule changes its properties due to the forming of a chemical contact [3]. Molecular electronics is incorporated in the field of nanotechnology which combines traditional science including physics, chemistry, electrical and electronic engineering, material science, biology, and medicine. Its principal efforts are directed towards the investigation of new materials and the development of new tools able to analyze and precisely characterize matter at the nanoscale. The fabrication of surface-supported nanostructures can be performed by two different strategies, by the so called "top-down" or by the "bottom-up" approach. Whereas the top-down approach follows the principle of scaling down and shrinking known structures to improve performance and yield, the bottom-up approach is a stepwise arranging of components to totally new and different structures. Thereby structures are created on a surface template through self-organization, intrinsically using the specific interactions of individual building blocks such as atoms or molecules with

each other and the surface [4, 5]. Self-organization is an efficient parallel technique because it takes place at the same time on countless equivalent positions of a given substrate. The resulting structure depends on the interactions of the individual building blocks, and a careful design of those building blocks opens a rich field of achievable structures. Especially, when using molecules as elementary units, bonding preferences as well as the interactions with the substrate can be tuned using the full variety of techniques available from state of the art synthetic chemistry. The organization can be directed by covalent bonds, metal-ligand interactions, hydrogen bonds, van der Waals forces, polar intermolecular interactions, hydrophobic or hydrophilic effects, etc., and combining different bonding mechanism allows to create hierarchical structuring.

In the past decades the molecular level design of new materials has expanded extensively in the interdisciplinary field of nanotechnology and various molecular systems fabricated with bottom-up techniques are reported in literature. Large 2D and 3D metal-organic coordination networks have been built which constitute grids of metallic centers regularly spaced by organic linker molecules using coordination bonds. When metallic atoms are used as molecular centers such structures have a potential for data storage as so called magnetic printboards [5–7]. Nanotubes and C_{60} molecular systems are investigated, e.g., with view to a possible application as active transistor [3], and a whole research field deals with DNA-templated electronics [8–10], sometimes also in combination with carbon nanotubes [11]. On the other side, a large research field deals with possible applications of single organic molecules as various components in electrical circuits. Countless molecules are investigated for a possible use as wires, diodes [12, 13], transistors [14], memory cells [15], or logic gates [16]. Kondo and Coulomb blockade effects have been observed, which could be the basis for the use of molecules as single electron transistors [17]. Similarly, observed negative differential resistance could enable resonant tunneling transistors [18].

Bringing back to mind that every active molecule needs an isolating environment and metallic contacts, literature often leads to thiol coupled molecules (like alkanethiols) as isolating matrix system and gold surfaces as electrodes. However, establishing molecular electronic devices will be achieved only by integrating them in a first step into existing CMOS technology [19] and thus the molecular system has to be compatible to common CMOS materials. Today, an advantageously used metal for wires and interconnects in electronic industry is copper due to its low resistance. Furthermore, the electromigration of copper is less than that of mate-

rials like aluminum or even gold. Therefore, it is essential to get a fundamental understanding of organic/copper interfaces and to combine functional molecular systems with linkers which are copper sensitive.
The selection of a specific molecule and its linkers to the metallic electrodes as well as the selection of the molecular environment allows to co-determine the resulting system structure by adjusting the relative strength and type of interactions. Nevertheless, the obtained patterns are often difficult to predict and the patterns are usually described after experimental tests and are not designed. This is mainly due to the degrees of freedom for every single molecule as perfectly visible in the system of alkanethiols on Au(111) surfaces [20] where the molecule has multiple degrees of freedom although it its chemically bonded to the surface. Even if the intermolecular interactions are ideally adjusted, the stochastic nature of the growth process can induce randomness or local disorder to the final structure. Thus, it would be advantageous to structurally organize the molecules by other means than only by tuning intermolecular interactions. One possibility to direct the self-organized growth at surfaces is the use of nanotemplates. These are substrates which exhibit a periodical variation of the adhesion energy for an adsorbing species. Nanotemplates for molecular self-assembly are either metallic substrates with an internal pattern, like structured or stepped crystal surfaces (e.g., (110)-oriented surfaces of face centered cubic crystals) or special adsorbates which structure the molecular surface by self-organization (e.g., oxygen on copper surfaces).
In this work several of the above mentioned concepts and aspects are combined to a new approach. Based on a nanotemplated metallic surface and starting with the smallest molecule which can be linked precisely to the metal surface and additionally has an intermolecular acting unit, structural and electron transport properties of a molecule/metal system are investigated. A stepwise extension and functionalization of the molecular system up to hierarchical structures is performed and possible transitions to three terminal devices are depicted.
Copper is used as metallic surface for molecular self-assembly in view of future applications. It has a face centered cubic crystal structure and thus the (110)-oriented surface builds a naturally striped nanotemplate. The carboxylic group (COOH) is chosen as linker to the Cu(110) surface and initial investigations have shown that both oxygen atoms chemically bind to the copper surface forming an equidistant and rigid adsorption geometry with a deprotonated carboxylic group and a delocalized electron pair [21]. Investigations are started with benzenecar-

boxylic acid (C_6H_5COOH) which consists of one carboxylic group and a benzene ring, allowing the molecule to interact with surrounding molecules via π-π interactions. Structural and electronic transport properties are investigated before systematically substituting atoms or adding additional functional groups. The HOMO (highest occupied molecular orbital)-LUMO (lowest unoccupied molecular orbital) gap is here a main physical quantity which displays changes in the intermolecular and in the molecule-substrate coupling. Attention is paid to the fact that only one part of the molecule is substituted per investigation step and that the adsorption configuration on the Cu(110) surface stays the same.
Further investigation steps combine different carboxylic acids and point out that the carboxylate/copper system is also suitable for more complex structures like mixed systems of electronically active and inactive molecules (matrix isolation approach) or hierarchical structures where different electron transport paths exist inside the molecular layer. Testing carboxylic acids for applications in devices a carboxylate based molecule is also investigated on a second metal substrate (here gold) which could act as top electrode contact. The chosen molecule can be chemically connected via a carboxylic end group to a copper electrode and with a thioether end group to a gold electrode. This leads to a directed bonding and to a diode functionality of the molecule if connected to two different metallic electrodes.
Finally, a short excursion presents a further approach to combine molecular electronic with common CMOS technology. This approach uses not the metal layer as linking point for the molecules but the semiconductor areas. Combining semiconductor surfaces, like Ge(001), with self-assembled metallic nanowires builds a highly ordered 1D nanotemplate for molecular assembly.
Scanning tunneling microscopy (STM) and spectroscopy (STS) in ultra high vacuum are used as main techniques throughout the study, but complementary techniques like X-ray photoelectron spectroscopy (XPS), low electron energy diffraction (LEED), or ultraviolet-visible (UV-VIS) spectroscopy are employed as well to achieve a more comprehensive picture. Additionally, theoretical calculations based on *ab initio* density functional theory (DFT) methods are consulted to describe structural and transport properties in more detail.
The thesis is organized as follows:

- First, an introduction is given on the physics of electron transport in a nanoscale junction, with and without molecules (chapter 2).

- In chapter 3, a description is given of the employed experimental techniques and their underlying theory. The focus is set on the techniques of STM and STS. Briefly mentioned are the surface analytical techniques (Auger, XPS) and UV-VIS spectroscopy. Furthermore, a detailed description is given on the UHV-STM setup and on the specific STM and STS data acquisition.

- Chapter 4 gives a short introduction on DFT based calculations. Main task of this chapter is to list the formalism and assumptions made for structure, energy, and electron transport calculations reported in this thesis.

- Chapter 5 introduces into the topic of molecular self-assembly and describes the self-assembly mechanisms and processes. The process flows for the preparation of self-assembled monolayers from solution and from gas phase are described because both methods are used within this work. Additionally, this chapter includes information on the structure of organothiols on gold and of small carboxylates on copper as a kind of state of the art review and basis for future comparisons.

- In this thesis Au(111) thin films, Cu(110) single crystals, and copper thin films are studied. Also, Ge(001) covered with Pt nanowires is used as substrate for molecular self-assembly. Thus, the preparation, characterization, and specifics of these different bottom electrode materials are described in chapter 6.

- In chapter 7 the structure of and the electronic transport through the carboxylate/Cu(110) interface are described in great detail. A stepped substitution process allows a detailed analysis of the change in electron transport. Four different carboxylates, namely bezenecarboxylic acid (C_6H_5COOH), benzene-1,4-dicarboxylic acid ($C_6H_4(COOH)_2$), pyridinecarboxylic acid (C_5H_4NCOOH), and pyridine-2,5-dicarboxylic acid ($C_5H_3N(COOH)_2$), are studied on this way in terms of their self-assembly behavior in close-packed structures and their electronic properties. Distance dependent current-voltage (I-V) spectroscopy is performed to display the molecular orbital structure of the combined carboxylate/copper system as local density of states (LDOS) distribution. Experimental results will be compared to *ab initio* calculations based on DFT methods to understand the influence of the different molecular orbitals on the electronic structure. A physical value describing the electron properties of a molecule/metal system is the HOMO-LUMO gap which can

be calculated for all molecules under investigation. Further analysis of the spectroscopic data gives information on the gap symmetry within the STM based Cu/Carboxylate/W junction and transition voltage spectroscopy will give insides into the present tunneling mechanisms. Current-distance (I-z) spectroscopy will be presented for one selected molecule (pyridinecarboxylic acid) to identify the tunneling decay constant of a pyridine unit. Additionally, this chapter includes a small paragraph about the possibility to fabricate mixed monolayers, where a small amount of carboxylic acid is embedded into a matrix of a self-assembled monolayer of suitable host-molecules. A proof of concept will be given by inserting pyridinecarboxylic acid into a complete monolayer of benzenecarboxylic acid.

- Chapter 8 reports on the investigations performed on 2,3-dihydroxy-4(thiomorpholinomethyl)benzoic acid (TMBA). A further step towards an application of functional molecules is the investigation of molecules which can be connected to different metal electrodes and this molecule combines the carboxylic end group with the well studied sulfur end group. The TMBA molecule can be connected with the carboxylate group to a copper surface and with the thioether group, e.g., to a gold surface. Additionally, these molecules act as ligands for the building of organometallic complexes. Thus, TMBA molecules can either work as molecular diodes, chemically connected between two metal electrodes, or as a host-matrix for single organometallic complexes. The self-assembly behavior is studied on Au(111) surfaces in pure films as well as in mixed molecular systems and electronic transport properties are studied by I-V and I-z spectroscopy. First theoretical calculations and XPS measurements will help to give a more comprehensive picture of the system.

- Finally, chapter 9 deals with the first approaches to self-assemble functional molecules on Pt nanowires grown on Ge(001) surfaces. A first success can be reported for the self-assembly of triphenylphosphane ($C_{18}H_{15}P$) molecules.

2 Physics in a Nanoscale Junction

The ability to measure and control electrical current through a molecule is a requirement for building electronic devices using individual molecules. It offers an unique opportunity to understand charge transport, an important phenomenon that occurs in many chemical and biological processes, on a single-molecule basis. Furthermore, it allows to read the chemical information of a single molecule electronically, which opens the door to chemical and biosensor applications based on the electrical detection of individual molecular binding events [22]. The most fundamental quantity describing the electrical properties of a bulk material is conductivity, based on which materials are often divided into conductors, insulators, and semiconductors. Conductivity is defined as $\sigma = \frac{I}{V} \cdot \frac{L}{A}$, where I is the current, V the applied bias voltage, L the length, and A the cross sectional area of the material. For a small molecule, A and L are difficult to define precisely, and better quantity is the conductance, G, given by $G = \frac{I}{V}$. So a basic aim in molecular electronics is to measure and calculate the conductance of a single molecule. To determine the conductance of a molecule, one must wire the molecule reliably to at least two electrodes. The conductance of the molecule thus depends not only on the intrinsic properties of the molecule but also on the electrode materials. The electrodes Fermi levels will influence the molecular energy levels and thereby alter the transport properties strongly. Furthermore, not only the electronic structure of the molecule is of interest, but the electrical transport as well. Transport through a molecule under bias is essentially a non-equilibrium, quantum kinetic problem. Contacting a molecule by two electrodes effectively "opens up" the system, replacing the discrete molecular energy levels with a continuous density of states and establishing a common electrochemical potential and a band lineup between the contacts and the molecule. Under bias, the two contact electrochemical potentials split, and the molecule, in its urge to establish equilibrium with both contacts, is driven strongly out of equilibrium.

2.1 A metal/molecule/metal junction

As mentioned above a nanoscale junction investigated in molecular electronic consists, in the basis setup, of three parts: one molecule and two electrodes which connect this molecule. The metal electrodes have a high, in general uniform density of states (DOS). These states (φ_1 and φ_2) are occupied by electrons up to the Fermi level following the Fermi-Dirac distribution function $f(\epsilon, \mu)$ with

$$f(\epsilon, \mu) = \frac{1}{exp(\frac{\epsilon-\mu}{k_B T}) + 1}, \tag{2.1}$$

where μ is the electrochemical potential of the first or second electrode, k_B the Boltzmann constant, ϵ the energy, and T the temperature. The molecule has a discrete set of energy levels with a highest occupied molecular orbital (HOMO) and a lowest unoccupied molecular orbital (LUMO). Under equilibrium ($V = 0$) the electrochemical potential is uniform across the junction ($\mu_1 = \mu_2$) and will usually lie somewhere inside the HOMO-LUMO gap of the molecule (Fig. 2.1(a)).

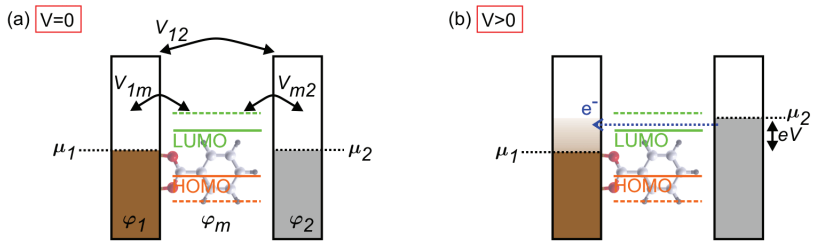

Figure 2.1: Schematic of a metal/molecule/metal junction. (a) Sketch of the energy level diagram without an external bias voltage ($V = 0$). The molecule is attached to two electrodes with the Fermi levels μ_1, μ_2 and the eigenstates φ_1, φ_2. Whereas the electrodes have a uniform density of states the energy levels of the molecules are represented by discrete lines. The coupling is described by the operators V_{1m}, V_{m2} and V_{12}. (b) Applying a voltage $V > 0$ shifts the Fermi levels of the electrodes by a value $\frac{1}{2}\, eV$. In the sketched case, the LUMO lies within the energy window which is spanned by the applied voltage, and resonant transport via this level occurs.

If a voltage V is applied across the junction, the electrochemical potentials of the electrodes are shifted against each other by an amount of $\mu_1 - \mu_2 = eV$. This is shown in Fig. 2.1(b) for the case of $V > 0$. The Fermi level of the left electrode

μ_1 decreases whereas that of the right electrode μ_2 increases by the same value. Within this a bias voltage window is opened and electrons can flow from the right to the left electrode.
At this point the transport in a nanoscale metal/molecule/metal junction has to be split into two principle mechanisms. If no molecular energy levels lie within the energy window which is spanned by the applied voltage, the molecule acts as an insulating barrier. In this case, electron transfer between the two electrodes is a non-resonant tunneling process. If molecular energy levels lie within the energy window, electrons will use these available states to cross the junction. Thus, the charge is transferred resonantly via the molecular states leading to a resonant tunneling process. Fig. 2.1(b) sketches the case where the LUMO is situated in the energy window and resonant tunneling occurs through this state. If a negative voltage ($V < 0$) is applied, the electrode level shifts are inverse and transport through the HOMO gets possible.

Which transport mechanism finally takes place is strongly dependent on the type of the molecule and its connection to the electrodes. Particularly, the location of the molecular states relative to the electrochemical potential of the electrodes and the shape of the molecular orbitals are crucial as well as the kind and the strength of the electronic coupling of the molecule to the electrodes.

2.2 Resonant transport

To understand the flow of current through molecules a detailed model of the metal/molecule interface is needed. The metal/molecule system can be described with an energy level diagram showing the molecular energy levels relative to the Fermi energy (E_F) in the metallic contacts. This energy level diagram has to be combined with an estimation of the broadening of the molecular levels due to the coupling to the contacts and with a description of the spatial profile of the molecular potential under bias.
Considering first a molecule with only weak electronic coupling to the metallic electrodes the energy levels can be lined up using the metallic work function (Φ) and the electronic affinity (EA) and ionization potential (IP) of the molecule. These values are associated with electron emission and injection to and from vacuum and may need some modification to account for the metallic contacts.

For example the actual EA, IP will possibly be modified from EA_0, IP_0 due to the image potential ϕ_{image} associated with the metallic contacts [23]:

$$EA = EA_0 + \phi_{image}, \tag{2.2}$$

$$IP = IP_0 - \phi_{image}. \tag{2.3}$$

The probability of the molecule losing an electron to form a positive ion is equal to $e^{(\Phi - IP)/k_BT}$ while the probability of the molecule gaining an electron to form a negative ion is equal to $e^{(EA-\Phi)/k_BT}$. Thus, it is expected that the molecule remains neutral as long as both $(\Phi - IP)$ and $(EA - \Phi)$ are much larger than k_BT, a condition that is usually satisfied for most metal-molecule combinations. Since it costs too much energy to transfer one electron into or out of the molecule, it prefers to remain neutral in equilibrium. The picture changes qualitatively if the molecule is chemisorbed directly on the metallic contact, i.e., a strong coupling regime exists. Then the molecular energy levels are broadened significantly by the strong hybridization with the delocalized metallic wave functions, making it possible to transfer fractional amounts of charge to or from the molecule. Indeed there is a change in the electrostatic potential inside the molecule due to the charge transfer and the energy levels of the molecule are shifted by a contact potential (CP). It is now more appropriate to describe transport in terms of the HOMO/LUMO levels associated with incremental charge transfer [24, 25] rather than the affinity and ionization levels associated with integer charge transfer. Whether the molecule-metal coupling is strong enough for this to occur depends on the relative magnitudes of the single electron charging energy (U) and the energy level broadening (Γ). Due to the fact that all molecules which are investigated within this work are chemically bonded to the metal on one side of the junction the systems will always end up in the strong coupling regime.

Additionally, the location of the Fermi energy relative to the HOMO and LUMO levels is a crucial factor for electron transport. Usually it lies somewhere inside the HOMO-LUMO gap but the exact position is dependent on the charging of the molecules due to the contact with the electrodes. Thus, E_F is treated as a fitting parameter within reasonable limits when trying to explain experimental I-V curves [26].

The broadening (Γ) of the molecular levels due to the coupling to the contacts can be described as combination of the states of the electrodes (φ_1, φ_2) with that

of the molecule (φ_m) following:

$$\Gamma_1 = 2\pi \sum_{i \in \varphi_1} |V_{i,m}| \delta(\epsilon_i - \epsilon_m), \tag{2.4}$$

$$\Gamma_2 = 2\pi \sum_{j \in \varphi_2} |V_{m,j}| \delta(\epsilon_j - \epsilon_m), \tag{2.5}$$

with the related energies ϵ and $\Gamma = \Gamma_1 + \Gamma_2$. Alternatively, the broadening can be related to the time τ it takes for an electron placed in one molecular level to escape into the contact: $\Gamma = \hbar/\tau$, i.e., $\Gamma/\hbar$ is the rate at which electrons are injected into the level from the contact or vice versa.
Finally, the spatial profile of the molecular potential under bias has to be described. As displayed in Fig. 2.1(b), the electrochemical potentials (μ_1, μ_2) of the two electrodes split when an external voltage V is applied to the junction and they are shifted in respect to the molecular levels. Taking the left electrode as reference leads then to

$$\mu_1 = E_F \quad \text{and} \quad \mu_2 = E_F + eV. \tag{2.6}$$

But not only the electrode potentials shift under bias also the molecular levels change their position. Here, S. Datta et al. [27] developed a very useful system to describe the resulting spatial profile. With the approximation that all molecular levels shift equally the average potential can be described with:

$$\langle \delta v_m(r) \rangle = \eta eV, \tag{2.7}$$

where the voltage division factor η is a number between 0 and 1. The chemical potentials of the electrodes can thus be calculated to:

$$\mu_1 = E_F - \eta eV \quad \text{and} \quad \mu_2 = E_F + (1-\eta)eV. \tag{2.8}$$

The value of η is directly related to the molecule and its coupling to the electrode, and some cases are depicted in Fig. 2.2.
For example, for low voltages ($eV < min(E_F - E_{HOMO}, E_{LUMO} - E_F)$) the change in the charge density will be very small because the molecule has a low density of states within the gap. This yields in a linear potential profile, as shown in the upper part of Fig. 2.2(a), and $\eta = 0.5$, if the molecule is roughly halfway between the contacts and the contact area on the electrode is large compared

to the length of the molecule. Within the same conditions but with a highly polarizable molecule, η will also be 0.5 but the potential profile will be flat inside the molecule (see lower part of Fig. 2.2(a)). On the other side, if there is a significant density of states in the molecule within the voltage gap window, it will lose or gain charge depending on the relative coupling to the contacts and the resulting potential profile will change to that displayed in Fig. 2.2(b) or (c), depending on the relative coupling to the electrodes 1 and 2. Furthermore, the

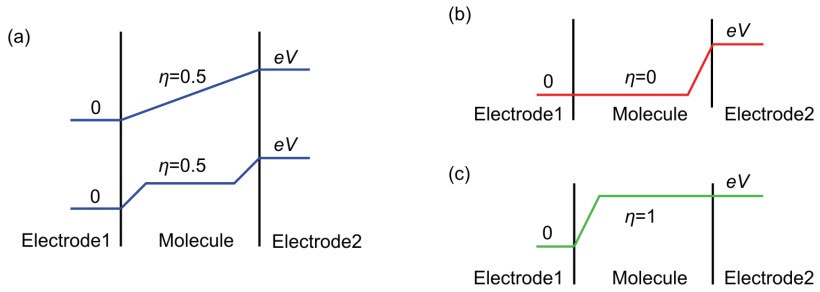

Figure 2.2: Four examples of potential profiles, illustrating the meaning of the voltage division factor η. Adapted from [26].

value for η is related to the kind of transport through the molecule. In the case of $\eta = 0$ and positive bias applied to electrode 1, the current starts to flow when μ_1 crosses the LUMO, while for negative bias, the current starts to flow when μ_2 crosses the HOMO. This explains why the positive branch of measured I-V characteristics sometimes looks different compared to the negative branch, since they involve different molecular orbitals. In the case of $\eta = 0.5$, conduction can take place through HOMO or LUMO for either bias polarity. If the equilibrium Fermi energy E_F is much closer to the HOMO to start with, conduction takes place through the HOMO and the LUMO plays no role. If E_F is much closer to the LUMO, conduction will take place through the LUMO and the HOMO will play no role. In either case the I-V characteristics will look much more symmetric, since the same orbitals are involved for either bias direction.

The current I across the junction is a function of the transmission coefficients between the three junction parts which includes all three above discussed aspects. In a first approximation it can be considered that only one discrete molecular energy level with energy ϵ is situated between the electrochemical potentials of the two metal electrodes. This level could represent either the HOMO or the LUMO

depending on which is closer to the equilibrium Fermi energy E_F. As described above, the flow of electrons between the electrodes and the molecular level can be described by the rate $\Gamma/\hbar$ and the actual number of electrons occupying this level is N. The net current across the left junction can than be written as

$$I_L = \frac{e\Gamma_1}{\hbar}\left[2f(\epsilon,\mu_1) - N\right] \tag{2.9}$$

and that across the right junction as

$$I_R = \frac{e\Gamma_2}{\hbar}\left[N - 2f(\epsilon,\mu_2)\right]. \tag{2.10}$$

Under steady state, the current across the two junctions will be equal ($I_L = I_R$) and the current across the whole junction can be calculated to

$$I = \frac{2e}{\hbar}\frac{\Gamma_1\Gamma_2}{\Gamma_1+\Gamma_2}\left[f(\epsilon,\mu_1) - f(\epsilon,\mu_2)\right]. \tag{2.11}$$

Given the level (ϵ), the broadening (Γ_1, Γ_2) and the electrochemical potentials μ_1 and μ_2 of the two contacts, equation (2.11) can be solved for a current I.
Up to now, the level ϵ was treated as discrete, ignoring the broadening that accompanies the coupling to the electrodes. To take this into account the discrete level has to be replaced with a Lorentzian density of states $D(E)$:

$$D(E) = \frac{1}{2\pi}\frac{\Gamma}{(E-\epsilon)^2 + (\Gamma/2)^2} \tag{2.12}$$

and equation (2.11) changes to

$$I = \frac{2e}{\hbar}\int_{-\infty}^{+\infty} D(E)\frac{\Gamma_1\Gamma_2}{\Gamma_1+\Gamma_2}\left[f(E,\mu_1) - f(E,\mu_2)\right]dE. \tag{2.13}$$

To include charge transfer effects the potential $U_{SC} = \langle \delta v_m(r) \rangle$ has to be added due to the change in the number of electrons. Taking the equilibrium value $2f(\epsilon_0, E_F)$ as starting point it follows

$$U_{SC} = U(N - 2f(\epsilon_0, E_F)). \tag{2.14}$$

The molecular level center ϵ will then float up or down by this potential

$$\epsilon = \epsilon_0 + U_{SC} \tag{2.15}$$

and since the potential depends on the number of electrons, the potential has to be calculated using a self consistent procedure as described in Ref. [26].
The one-level model described in the last section includes the three basic factors that influence molecular conduction, namely $E_F - \epsilon_0$, $\Gamma_{1,2}$, and U. However, molecules typically have multiple levels that often broaden and overlap. In general a formalism is needed that can do justice to multiple levels with arbitrary broadening and overlap. At this point semi-empirical approaches, like that of Datta et al. which is described here, fail and the transport properties have to be calculated *ab initio* with quantum mechanical methods such as the non-equilibrium Green's function (NEGF). Nevertheless, using the semi-empirical approach described here to fit the experimental I-V data by introducing one or more parameters leads to good results, as shown for example in [27].
However, also in the NEGF formalism [26] the current through the junction follows the equation:

$$I = \frac{2e}{h} \int_{-\infty}^{+\infty} T(E) \left[f(E, \mu_1) - f(E, \mu_2) \right] dE, \tag{2.16}$$

with a transmission coefficient $T(E)$ and the conductance of the junction gets a function of this coefficient

$$G = G_0 T(E), \tag{2.17}$$

with $G_0 = 2e^2/h = 77\,\mu\text{S}$ the quantum of conductance. The maximum conductance is reached when the transmission probability gets one, which is the case when an atomic metal wire is inserted between the electrodes but for single organic molecules the value of G is usually much lower [22].

2.3 Non-resonant transport

If no molecular energy levels lie within the energy window which is spanned by the applied voltage, the molecule acts as an insulating barrier. Thus, the current can be described by a simple tunneling model and the conduction mechanisms of solid state insulators can be applied (compare table 2.1).
The HOMO corresponds in this case to a valance band and the LUMO to a conduction band. When the Fermi level of the metal is aligned close enough to one energy level (either HOMO or LUMO), the effect of the other distant energy level on the tunneling transport is negligible, the problem reduces to a one-band model, and the widely used Simmons model is an excellent approximation [29].

Conduction mechanism	**Current behavior**	**Temperature dependence**	**Voltage dependence**
Direct tunneling	$J \sim \frac{V}{z} e^{-\frac{2z}{\hbar}\sqrt{2m\Phi}}$	none	$J \sim V$
Fowler-Nordheim tunneling	$J \sim V^2 e^{-\frac{4z\sqrt{2m}\Phi^{3/2}}{3q\hbar V}}$	none	$ln\left(\frac{J}{V^2}\right) \sim \frac{1}{V}$
Thermionic emission	$J \sim T^2 e^{-\frac{\Phi - q\sqrt{\frac{qV}{4\pi\epsilon z}}}{k_B T}}$	$ln\left(\frac{J}{T^2}\right) \sim \frac{1}{T}$	$ln(J) \sim V^{1/2}$
Hopping conduction	$J \sim V e^{-\frac{\Phi}{k_B T}}$	$ln\left(\frac{J}{V}\right) \sim \frac{1}{T}$	$J \sim V$

Table 2.1: Possible conductance mechanisms in solid state insulators. Adapted from Ref. [28].

The Simmons model expresses the tunneling current density through a thin barrier with the mean barrier height Φ_B as

$$J = \left(\frac{e}{4\pi^2\hbar z^2}\right)\left\{\left(\Phi_B - \frac{eV}{2}\right) exp\left[-\frac{2\sqrt{2m}}{\hbar}\alpha\sqrt{\left(\Phi_B - \frac{eV}{2}\right)}z\right] - \left(\Phi_B + \frac{eV}{2}\right) exp\left[-\frac{2\sqrt{2m}}{\hbar}\alpha\sqrt{\left(\Phi_B + \frac{eV}{2}\right)}z\right]\right\}, \tag{2.18}$$

where m is the electron mass, z is the barrier width, V is the applied bias, and α is a unitless adjustable parameter that is introduced to modify the simple rectangular barrier model or to account for an effective mass [30]. Equation (2.18) can be approximated in two limits: low bias and high bias as compared with the barrier height Φ_B. For the low bias range ($eV << \Phi_B$), Eq. (2.18) can be approximated as

$$J \approx \left(\frac{\sqrt{2m\Phi_B}e^2\alpha}{h^2 z}\right) V\ exp\left[-\frac{2\sqrt{2m}}{\hbar}\alpha\sqrt{\Phi_B}z\right], \tag{2.19}$$

whereas for the high bias regime ($eV > \Phi_B$), Eq. (2.18) can be approximated as

$$J \approx \left(\frac{e^3 V^2}{\hbar z^2 \Phi_B}\right) exp\left[-\frac{4\sqrt{2m}}{3\hbar eV}\alpha\Phi_B^{3/2}z\right]. \tag{2.20}$$

Equation (2.19) and (2.20) show that the current density is exponentially dependent on the barrier width z for low bias as well as for high bias. According to the Simmons model, the tunneling current can be written with a decay coefficient

β whereas this factor is either bias dependent or independent. For the low bias regime the current is

$$J \propto \frac{1}{z} exp(-\beta_0 z), \tag{2.21}$$

and β_0 is a bias independent decay coefficient with

$$\beta_0 = \frac{2\sqrt{2m}}{\hbar} \alpha \sqrt{\Phi_B}. \tag{2.22}$$

On the other hand, for the high bias regime, the current is

$$J \propto \frac{V^2}{z^2} exp(-\beta_V z), \tag{2.23}$$

and β_V is a bias dependent decay coefficient with

$$\beta_V = \frac{4\sqrt{2m}}{3\hbar e V} \alpha \Phi_B^{3/2}. \tag{2.24}$$

In a first approximation, the pre-exponential factor in the current equations (2.21) and (2.23) can be neglected compared to the exponential factor, leading to a current vs. distance dependence of

$$I = G(V) exp\left[-\beta(\Phi_B, V) z\right] V. \tag{2.25}$$

3 Experimental Techniques

Most results within this work have been obtained using scanning tunneling microscopy (STM). Hence this chapter will give a short introduction to the theory of STM. Complementary techniques that have been used in this thesis will also be briefly described here. Finally, an overview of the employed UHV-STM setup will be given.

3.1 STM

The working principle of STM [31] is to bring a sharp metallic tip into close vicinity of a flat conducting sample surface and keep it in front of the surface at a very small distance of typically below one nanometer. The tunneling tip is a wire that has been sharpened by chemical etching or mechanical grinding. Materials like W, Pt/Ir, or pure Ir are often used as tip materials. A schematic view of a STM is shown in Fig. 3.1. The sample and the tip are connected by an external voltage source V_T. If the distance between the tip and the sample is in the order of a nanometer, a tunneling current I_T flows between the tip and the sample. This current is used as the feedback signal in a z-feedback loop.
Two different operation modes are commonly used. In the constant-current mode, images are created by scanning with the tip in the xy plane and adjusting the z position in order to keep I_T constant. A three-dimensional map $z(x, y, I_T{=}\text{const.})$ is recorded. In the constant-height mode, the probe scans the surface while the signal of the z-scanner is kept constant, and a three-dimensional image $I_T(x, y, z{=}\text{const.})$ is created.
In a rather simplistic model the tunneling current is given by

$$I_T = I_0\, e^{-2\kappa z}, \text{ with } \kappa = \sqrt{2m\Phi}/\hbar, \tag{3.1}$$

with Φ the work function, m the electron mass, and z the distance between tip and sample. I_0 is a function of the applied voltage and the density of states in both, tip and sample. A typical value for the work function Φ is $5\,e$V, yielding a decay length κ of about 0.1 nm. Therefore, if the distance z is increased by 0.1 nm, the current drops by an order of magnitude. As a consequence, the tunneling current is focused only on the nearest atoms of the tip and the sample leading to the atomic-scale resolution of STM.

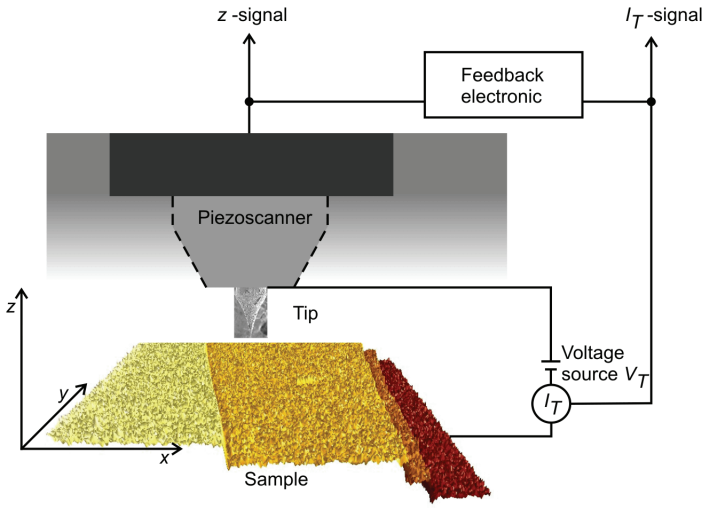

Figure 3.1: Schematic diagram illustrating the principle of a scanning tunneling microscope. A metallic tip is scanned across a conducting substrate in x- and y-direction. The strong dependence of the tunneling current on the distance (z) between the tip and the substrate surface is used to probe the topography of the sample.

3.1.1 The theory of STM

An accurate description of the tunneling process can be given with the transfer Hamiltonian approximation introduced by Bardeen [32], where the tunneling current is given by:

$$\begin{aligned} I_T = & \frac{2\pi e}{\hbar} \sum_{t,s} |M_{ts}|^2 \delta(E_t - (E_s + eV)) \\ & \times \left[f(E_t, \mu_t) \left[1 - f(E_s, \mu_s) \right] - f(E_s, \mu_s) \left[1 - f(E_t, \mu_t) \right] \right], \end{aligned} \tag{3.2}$$

with V the applied sample bias voltage, and $f(E,\mu)$ the Fermi-Dirac distribution function (see Eq. (2.1)). The δ-function attributes to the restriction of elastic tunneling processes. M_{ts} is the tunneling matrix element between the states φ_t of the tip and φ_s of the sample, having the energies $E_{t,s}$ with respect to the electrochemical potentials $\mu_{t,s}$. This expression can be simplified by assuming a step-like behavior for the Fermi-Dirac function, which in principle is only true for zero temperature and a rough approximation at 300 K, but provides reasonable results in the most cases. The current can thus be written as

$$I_T = \frac{2\pi e^2}{\hbar} V_T \sum_{t,s} |M_{ts}|^2 \delta(E_t - E_F)\delta(E_s - E_F). \tag{3.3}$$

The tunneling matrix element M_{st} quantifies the overlap of the wave functions φ_t and φ_s of tip and sample states in the tunneling gap and can be written for both cases as a surface integral over the whole surface $\mathbf{S}$:

$$M_{ts} = -\frac{\hbar^2}{2m} \int d\mathbf{S}(\varphi_t^* \nabla\varphi_s - \varphi_s \nabla\varphi_t^*). \tag{3.4}$$

To go behind the qualitative properties of the tunneling current a detailed description for the matrix element M_{ts} is needed. A common approximation in STM theory is the s-type wave function approximation (only s-type wave functions of the tip contribute to the tunneling process), introduced by Tersoff and Hamann [33, 34]. Additionally, the summation over the absolute squares of the wave functions together with the energy δ-functions in Eq. (3.3) can be evaluated to yield the local density of states (LDOS) of the sample ρ_s at the position (x, y) below the tip and the LDOS ρ_t of the tip. This leads to a modified expression of the tunneling current (Eq. (3.3)) of [35]:

$$I_T(V) \propto \int_0^{eV} \rho_t(E - eV)\rho_s(E, x, y)T(E, V, z)dE. \tag{3.5}$$

The electrochemical potential of the substrate is taken as a reference energy here ($\mu_s = 0$) and $T(E, V, z)$ is the transition matrix describing the tunneling probability. Equation (3.5) shows that the tunneling current depends on the density of states of the tip at an applied bias voltage V, on the density of states of the surface at the Fermi level, and on the transition matrix T. According to Eq. (3.1), i.e., using the simplified model of a rectangular shape for the barrier, $T(E, V, z)$

is given as

$$T(E,V,z) = exp\left[-2z\sqrt{\frac{2m}{\hbar^2}(\bar{\Phi} + \frac{eV}{2} - E)}\right], \tag{3.6}$$

with $\bar{\Phi} = (\Phi_t + \Phi_s)/2$ the average of the work functions of tip and samples and $z = L + R$ the distance between tip and sample measured as depicted in Fig. 3.2.

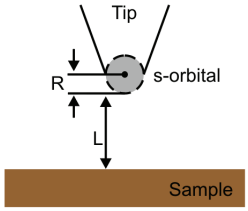

Figure 3.2: Schematic of the tip geometry in the s-type wave function approximation with respect to the sample surface.

Finally, for low bias voltages $eV << \Phi_t + \Phi_s$ the bias and energy dependence of the transmission factor T in Eq. (3.6) can be disregarded, leading to the following simplified expression for the current:

$$I_T(V) \propto e^{-2\kappa z} \int_0^{eV} \rho_t(E - eV)\rho_s(E,x,y)dE \tag{3.7}$$

where $\kappa = \sqrt{\frac{m}{\hbar^2}(\Phi_t + \Phi_s)}$ depends now only on the work functions of the tip and the surface. The first factor in Eq. (3.7) described the exponential z-dependence of the tunneling current, which is the "topography" information, while the integral factor depends on the density of states of tip and sample.

Thus, STM does not show a real geometric surface contour but a mixture of local electronic properties and topography. Therefore, STM measurements always need a careful interpretation and a stepwise investigation starting from a clean metal surface is useful, especially with regard to more complex structures (like molecules) adsorbed on these metal surfaces. Further, it is important to note that STM does neither map contours of constant electron density. As elastic tunneling only occurs for electrons at energies between E_F and $E_F + eV$, only the LDOS in this energy window contributes to the current signal. Thus, STM monitors images of constant LDOS windows at the Fermi level. This explains why the appearance of features in STM images is highly voltage dependent. Since the energy

states around the applied bias voltage contribute most to the tunneling current the displayed features vary with the applied bias voltage. Depending on the investigated surface material, surface features may emerge or vanish upon variation of the bias voltage, depending on the position of the energy states associated with them. Nowadays, the LDOS as well as the LDOS windows can be calculated by density functional theory which is introduced in chapter 4.
The aspect of monitoring LDOS windows becomes crucial in interpreting STM data obtained on molecular adsorbates. STM topography images of molecules often show internal structures and details but the interpretation is not straight forward due to the fact that protrusions on the STM image do not necessarily represent actual positions of atoms. It is rather expected that such features correspond to molecular orbitals, in particular the HOMO and LUMO molecular orbitals. This is easy understandable for molecules with HOMO and (or) LUMO states within the measurable voltage window of STM but molecules without states within this window are also "visible" in STM. This is due to the fact that non-resonant tunneling (as described in section 2.3) occurs and the contributions of the adsorbates to the current originates from tails of molecular orbital resonances crossing the Fermi level. These tails are usually rather small at the Fermi level and contributions from the substrate surface are also displayed.
The combined information of topography and electronic properties makes STM techniques complex but also to one essential measurement tool for molecular electronics. It is possible to get an image of the surface topography, identify different molecular species and to measure the electronic properties of exactly these molecules with high resolution.

3.1.2 Theory behind Scanning Tunneling Spectroscopy

Scanning tunneling spectroscopy (STS) is used to directly evaluate the electronic information which is included in the integral of Eq. (3.7) and of particular interest within this work. STS includes the approaches of current-voltage (I-V) and current-distance (I-z) spectroscopy. Current-voltage spectroscopy is performed by positioning the STM tip above a feature and opening the feedback loop, which results in a constant height z of the tip above the surface. While ramping the bias voltage V, the current I is recorded and either the differential conductance dI/dV is recorded simultaneously or numerically calculated afterwards. The differential

conductance can be calculated by taking the derivative of (3.7):

$$\frac{dI}{dV} \propto -\left(\int_0^{eV} \rho_s(E)\frac{d\rho_t}{dE}(E-eV)dE\right) + \rho_s(eV)\rho_t(0). \tag{3.8}$$

It is typically assumed that the tip-DOS does not depend on the voltage and accordingly that the integral term of Eq. (3.8) can be neglected. The differential conductance becomes

$$\frac{dI}{dV} \propto \rho_s(eV)\rho_t(0), \tag{3.9}$$

describing the ideal case for STS, probing the surface LDOS by rapidly ramping V without other influences. However, it has to be proven in each case that the dI/dV signal really does not depend on the electronic configuration of the tip. This can be done by measuring dI/dV curves on one sample with different STM tips.

Current-distance spectroscopy is performed by positioning the STM tip above a feature and opening the feedback loop. Then the applied bias is kept constant whereas the tip sample distance is varied and the current is simultaneously recorded. This kind of spectroscopy makes use of the fact that the surface state wave functions of the sample material decay into the vacuum with an exponential dependence on the distance z. The quantity of this exponential decay is a function of the material and can be described with the decay constant β. When plotting the current as a function of distance on a semi logarithmic scale the resulting curve slope is equal to β since the linear conductance G of the electrode/molecule/electrode junction (compare Eq. (2.17) of chapter 2) is defined in the Landauer formula as

$$G = G_0 T \quad \text{with} \quad G_0 = \frac{2e^2}{h}. \tag{3.10}$$

T gives the efficiency of the charge transport across the junction and can be split into one contribution for each of the two contact and one for the molecule $T = T_L \cdot T_R \cdot T_{mol}$. Combining T_L, T_R and G_0 to a pre-factor, denoted as the contact conductance $G_c = G_0 T_L T_R$, and assuming $T_{mol} = e^{-\beta z}$, as defined within the approximation of non-resonant tunneling (Simmons equations, compare section 2.3), leads to

$$G = G_c e^{-\beta z}. \tag{3.11}$$

For the special case of a STM based junction with a metallic tip, a vacuum level between tip and molecule, and a molecule which is bonded to a metallic substrate the value of β differs in dependence of the tip position within the junction due to the different materials. The conductance can be separated into contribution of the vacuum gap and of the molecular units [36–38], and can be written as

$$G = G_c exp\left[-\left(\beta_{vac} z_{vac} + \sum_{i=1}^{n} \beta_i z_i\right)\right], \tag{3.12}$$

with i the number of the molecular unit (and n units). The length of the molecular unit is denoted as z_i.
In the approximation of non-resonant tunneling through molecules as tunneling through a rectangular barrier the decay parameter β is given by equation (2.22) respectively by (2.24), for triangular barriers, and the potential barrier height Φ_B can additionally be extracted from the I-z data. For resonant tunneling the conductance G is strongly dependent on the transition matrix element T and a simple product with an exponential dependence due to coupling and superposition effects of the states (compare 2.2) is only a rough estimation. Thus, no generalizing term for the relation between the decay constant and the barrier height can be given and the accurate tunneling transmission efficiencies, based on the junction symmetry and the density of electronic state, have to be calculated based on methods like NEGF theory [37] in every single case.

3.2 Complementary techniques

STM is a local technique with high lateral resolution but with limited chemical sensitivity. Complementary information has thus to be gained from chemically more sensitive techniques. Within this work low energy electron diffraction (LEED) and Auger electron spectroscopy (AES) are performed on the copper sample surfaces to check their flatness and cleanliness. X-ray photoelectron spectroscopy (XPS) is performed to determine the binding chemistry, and composition of the molecular species adsorbed on the metal surface. Due to the important information given by XPS for investigation the principle of XPS will be described here. Additionally, ultraviolet-visible (UV-VIS) spectroscopy is used for all molecular species to measure the optical HOMO-LUMO gap which can be derived from the

onset of the energetically lowest absorption band and which can be compared to the HOMO-LUMO gap measured by STM.

3.2.1 XPS

XPS is a quantitative spectroscopic technique that allows to determine the elemental composition, empirical formula, chemical state, and electronic state of the elements that exist within a material. The principle of XPS is based on the photoelectric effect and spectra are obtained by irradiating a material with a beam of X-rays while simultaneously measuring the kinetic energy and number of electrons that escape from the material being analyzed. In detail, monochromatic photons with energy $h\nu$ are absorbed by atoms in a molecule or solid, leading to ionization and the emission of core (inner shell) electrons. The kinetic energy distribution of the emitted photoelectrons can be measured using a electron energy analyzer and can be recorded as a function of the energy of the irradiated photons. The principle of energy conservation requires that:

$$E_{kin} = h\nu - E_B - \Phi_s, \tag{3.13}$$

with E_B the binding energy of the electron and Φ_s the work function of the sample. The photoelectrons enter the analyzer with the kinetic energy E'_{kin}, lose the energy E_{pass}, and are detected with an energy E''_{kin}. Energy conservation has to apply also for the side of the analyzer and for the whole system, so that the relation between detected energy and binding energy E_B is $E''_{kin} = h\nu - E_B - \Phi_a - E_{pass}$. A schematic XPS energy diagram is depicted in Fig. 3.3.
Accordingly, the determination of the binding energy E_B requires the values of the work functions of the analyzer Φ_a and the sample Φ_s. However, it is sufficient to know the work function of the analyzer because the Fermi levels of the two systems can be equalized by an electrical contact. The spectrometer is then calibrated by measuring the binding energy of a well-known reference sample.
XPS is a surface sensitive technique due to the relatively small escape depth of the generated photoelectrons. The mean free path of the electrons is dependent on their kinetic energy and for typical energies between 10 and 1100 eV the mean escape depth is typically in the range of several nanometers [39]. The limited escape depth of the electrons can be exploit by angle-resolved XPS in order to obtain a depth profile of the chemical composition of the sample. A typical X-ray

photoelectron spectrum shows characteristic lines for the core shells of the atoms at low kinetic photoelectron energies, for the outer shells of the atoms at high kinetic energies and satellite peaks generated by plasmon excitations or shake-up processes. Furthermore, Auger peaks appear as well as peaks related to secondary electrons and inelastic scattered electrons which build the characteristic step-like shaped background of the spectrum. The background correction is usually done by the method established by Shirley [40].

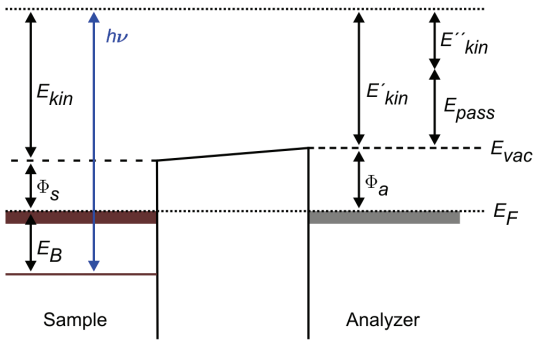

Figure 3.3: Schematic XPS energy diagramm. Irradiated are monochromatic photons with an energy of $h\nu$. These photons interact with the sample and electrons leave the sample with a kinetic energy E_{kin}. They enter the analyzer with an energy of E'_{kin}, and are detected with the energy E''_{kin}. The Fermi levels of the two systems have been equalized by an electrical contact between sample and analyzer.

The advantage of XPS is its chemical sensitivity , i.e., its sensitivity to the local charge distribution at the atomic positions. Different effects contribute to the actual binding energy E_B^{eff}:

$$E_B^{eff} = E_B + \Delta E_{chem} + \Delta E_{Mad} + \Delta E_r^{int} + \Delta E_r^{ext}, \tag{3.14}$$

where the chemical shift ΔE_{chem} and the Madelung term ΔE_{Mad} take into account the statistic effects influencing the ground state energy, whereas the ΔE_r terms describe relaxation effects due to dynamical processes related to the core electrons (ΔE_r^{int}) and the outer shell electrons (ΔE_r^{ext}). One essential term of this equation is the chemical shift which describes the change of the photoemission lines due to different chemical environments. One model to describe the physical principle of the chemical shift is the so called “charge potential model” with the main

equation:

$$\Delta E_B = E_i^0 + kq_i + \sum_j \frac{q_i}{r_{ij}}. \tag{3.15}$$

Here E_i is the binding energy of a particular core level on atom i, E_i^0 is an energy reference, q_i is the charge on atom i and the final term of the equation (3.15) sums the potential at atom i due to point charges on neighbored atoms j. The atom is considered as a hollow sphere with radius r_v and its valence electrons with charge q_i occupy the surface. Thus, the classical potential inside the sphere is the same at all points and equal to q_i/r_v. A change in the valence electron charge (density) of Δq_i changes the potential inside the sphere by $\Delta q/r_v$. Thus, the binding energy of all core levels will change by this amount. Moreover, as r_v increases the binding energy shift for a given Δq_i will decrease. Such a change takes place for example when one atom binds covalently to another one.

3.3 Experimental setup

Scanning tunneling microscopy systems are used to investigate molecular, submolecular and atomic properties. Surface topographies with their imperfections, impurities or contaminations are investigated as well as the molecular self-assembly behavior on metal surfaces. Moreover, energetic properties are accessible by STM in terms of mapping the local density of states (LDOS). Commonly STM is performed in ultra high vacuum (UHV) or in ultra pure solutions because an atmospheric environment would cause the instantaneous formation of adsorbate layers on any surface and thereby alter the surface properties. Especially, the local density of states or surface reconstructions can be altered by undesired adsorbates or even chemical reactions can take place on the surface, changing the material properties. In addition, a thin layer of water molecules, which is always present on any surface, constricts the imaging resolution. In the case of oxidizable surfaces, like copper, the amount of oxygen has to be reduced to ensure a clean surface for investigations. A UHV environment protects surfaces from oxidation, adsorption, or chemical reactions. It enables a reasonable storage time for metals such as gold or platinum and opens a process window for handling clean copper surfaces. Monolayer surfaces can be prepared, stored, and measured without environmental influences. Furthermore, for the preparation of molecular monolayers on reactive substrates, like copper, the possibility of in-situ deposition by sublimation is es-

sential. So, a UHV environment gets the standard for molecular self-assembly investigations by STM and a home-built setup, which is adapted to our unique requirements, is used for the experiments described in this thesis.

3.3.1 The UHV-STM system

The setup consists of four chambers, two main chambers, for measurements and for storage, and two small chambers, for substrate preparation and for molecule deposition. A small load lock is added to the setup for rapid sample and STM tip transfer into the vacuum system. The whole system is schematically drawn in Fig. 3.4, supplemented with photographs of the main parts.

The substrate preparation chamber is equipped with a turbo molecular pump (TMP), reaching a base pressure of $< 5.0 \cdot 10^{-8}$ mbar. An argon ion source (Vacuum Generators, Type AG21) is installed for sputter cleaning of sample substrates. For Cu(110) single crystal surfaces typically high voltages of 1-3 kV are applied with a sputter current of 20 μA for a sample size of 21 mm^2. The argon pressure during sputtering is about $1.0 \cdot 10^{-5}$ mbar.

The molecule deposition chamber is localized on the left side of the substrate preparation chamber and separated by a gate valve. It is equipped with a detached TMP system, reaching a base pressure of $< 1.0 \cdot 10^{-8}$ mbar, and can be separated in two parts by a gate valve [B]. The rotational stage for a sample holder is located in the upper part of the chamber and provides electrical connections for sample heating before, during, or after molecule deposition. The lower part consists of a small volume with two dosing valves to dose molecules or gases. The molecules are kept in small glass containers connected to these dosing valves, enabling an easy mounting of different molecules without breaking the vacuum of the chamber. Additionally, an easy access for cooling and heating the molecules from the outside is given in this way. The lower part of the chamber can be pumped independently over a bypass [A,C], which allows to clean the molecules before deposition by freezing/thawing cycles under vacuum conditions. If the vapor pressure of specific molecules is to low or to high for normal pressure and temperature conditions, the deposition pressure can be additionally changed by differential pumping through this bypass.

The storage chamber consists mainly of a rotational storage carousel with a variety of sample and tip mounting stages. Besides the normal storage stages, two

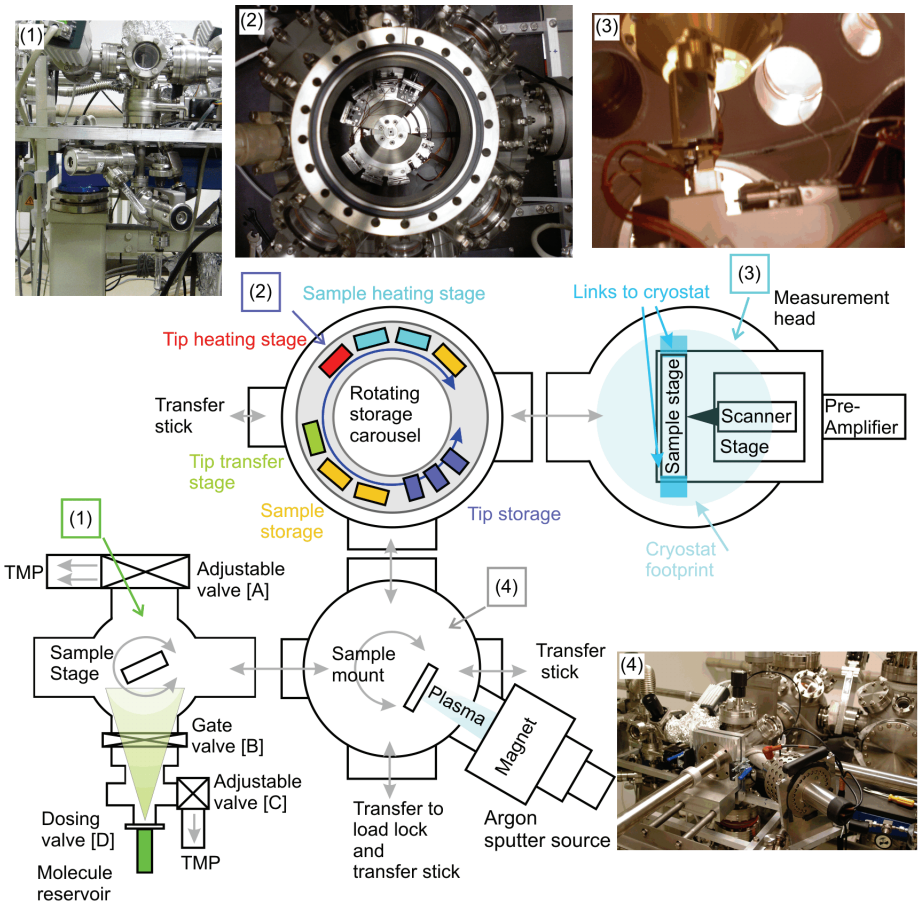

Figure 3.4: Schematic overview of the UHV-STM System, showing the layout of the four chambers. The photographs show: the molecule deposition chamber with the molecular containers below (1), the storage carousel inside the chamber from top view (2), the STM stage inside the measurement chamber (3), and the substrate preparation chamber with the argon ion source on the right side (4).

stages provide electrical contacts for heating the samples with a special filament embedded in the sample holder or by simple dc annealing. With these stages temperatures up to 1200 K can be achieved on the sample, controlled by an external pyrometer. One tip holder stage is equipped with a tungsten filament to remove adsorbates from the tip by heating. This chamber has a base pressure of $< 3.0 \cdot 10^{-9}$ mbar, reached by pumping with an ion getter pump.

The measurement chamber is pumped by an ion getter pump and a titanium sublimation pump. A base pressure of $< 9.0 \cdot 10^{-11}$ mbar allows to measure even reactive metal surfaces such as copper over periods of several days without significant surface contamination. The STM itself is a commercially available variable temperature STM (JEOL STM-4500S) with associated cryostat which is designed to work in the nominal temperature range of 20 K to 1400 K. Low temperatures can be achieved only with specific low temperature sample holders.

3.3.2 STM and STS data acquisition

STM and STS measurements have been performed on gold thin films, copper and germanium single crystals, see chapter 6. Homemade electrochemically etched tungsten tips were used for all measurements. The STM topography images shown in this thesis were obtained at room temperature in constant-current mode. The applied voltage and the reference current used during scanning are denoted as V_{Set} and I_{Set}. Positive bias voltage values are related to a tunneling of electrons from the STM tip into the unoccupied states of the sample.
While STM measurements are routinely performed at room temperature, STS measurements are often done at low temperatures, for example, to lower the molecular motion. As it turned out that low temperature STS measurements are not possible with the present setup, STS measurements were done at room temperature. Some special procedures and settings were used to improve the signal to noise ratio and to take reproducible spectra.
Before starting spectroscopic measurements, and after a series of measurements, topographic imaging of the sample was performed. Only areas with a clear molecular structure and without any vacancy islands or defects were chosen for spectroscopic measurements. The STM tip was positioned above a molecule and then the STM was put into spectroscopy mode. The STM-software allows to choose within three modes. Beside the normal current-voltage (I-V) spectroscopy and current-distance (I-z) spectroscopy a current imaging tunneling spectroscopy (CITS) mode is available. The CITS scan is a series of tunneling current images obtained with a fixed tip/sample distance and an optionally designated bias voltage. It is possible to obtain an I-V curve (max. 124 points) at each point of a chosen scan area and take an average image of the designated range. This mode allows to assign spatially varying electronic properties to local topographical features with high

precision. Unfortunately the resolution of the image and of the spectra is low, since the tunneling set point can not be optimized for spectroscopy and imaging simultaneously and the frequent voltage modulations can cause disturbances. Furthermore, CITS is very shock-sensitive and smallest height variations between the molecules can cause tip crashes. Hence, most I-V data shown in this thesis were taken in the normal I-V mode following a procedure described below. The scanning was turned of, hence the STM tip was kept fixed at one point. Still, there will be some lateral drift but this should not give rise to a problem, since the acquisition time for one spectrum is chosen in the range of 1-2 seconds. A series of I-V measurements was started with the tip position far away from the molecule. The distance is determined by the values of the voltage V_{Set} and the set point current I_{Set}. A typical tunneling current to start with was $I_{Set} = 0.1\,\mathrm{nA}$ at a sample bias of $V_{Set} = -2.0\,\mathrm{V}$. After the feedback loop had been turned off, the bias voltage was increased from -3.0 V to +3.0 V, while recording the resulting current at steps of 0.01 V. After each voltage sweep the feedback loop was turned on again and the tip height was readjusted before starting a new measurement. After ten sweeps I_{Set} was increased by 0.1 nA while the sample bias voltage was kept constant and a new series of sweeps was started. This procedure was repeated until $I_{Set} = 0.6\,\mathrm{nA}$ was reached. For even higher currents a significant change in the topographical image was visible, allegeable with the destruction of the molecular layer. The same procedure was repeated several times and with different tips. In this way an unambiguous assignment of the I-V curves to the electronic structure of the molecule/substrate system is possible. All spectroscopy data shown here were averaged over ten curves and compared with the data obtained for various molecules spread over the samples.

Current-distance spectroscopy measurements were taken by manually defining a spatial position of the STM tip on the sample. The vertical tip position is thereby defined by the set point voltage and current and denoted as distance zero. The tip is retracted by a defined value in the range of nanometer and then moved towards the sample. During movement the current is recorded in dependence on the distance related to zero.

The STM/STS data shown in this thesis were evaluated using WinSPM DPS (Version 2.00) from Jeol Ltd. and SPIP (Version 5.0.1.0) from Image Metrology.

4 The Theory of Molecular Electronics: DFT

Density functional theory (DFT) [41] is a parameter-free theoretical method which is built without any fitting to a particular experiment and thus is "*ab initio*". Using DFT, it is possible to calculate the electronic structure of a set of atoms with high precision.

DFT is based on the Born-Oppenheimer approximation which exploits the fact that electrons move much faster than atomic cores. A full calculation can thus be split into two nested calculation loops. In the inner one, DFT determines the electronic distributions for a given set of atomic nuclei positions, while in the outer loop this electronic distribution is used to calculate the forces between the atoms [42, 43]. The relaxation of the atomic positions is then a step-wise movement of the nuclei according to these forces until the forces become smaller than a predefined value. Due to the loop nesting, each relaxation step includes a full inner loop of self-consistent calculations. The final configuration is then the energetically optimal configuration for both (nuclei and electrons).

DFT is a single particle theory which solves the Schrödinger equation for one electron in the electric field of all nuclei and all other electrons. The Kohn-Sham equation [44] states that all these interactions can be described by an effective potential v_{eff} that is formed by the Coulomb potential of the nuclei v_{ext} (which is fixed in the inner loop), by the Coulomb potential of all electrons (Hartree-Potential) $v_H[n](\mathbf{r})$, and by an electronic exchange correlation term $v_{xc}[n](\mathbf{r})$. Both $v_H[n](\mathbf{r})$ and $v_{xc}[n](\mathbf{r})$ depend at each position $\mathbf{r}$ only on the electron density n:

$$v_{eff}(\mathbf{r}) = v_{ext}(\mathbf{r}) + v_H[n](\mathbf{r}) + v_{xc}[n](\mathbf{r}). \tag{4.1}$$

v_{eff} is used in the Schrödinger equation for the electron wave function ψ_i and energy ϵ_i:

$$\left(-\frac{\hbar^2}{2m} + v_{eff}(\mathbf{r})\right)\psi_i(\mathbf{r}) = \epsilon_i\psi_i(\mathbf{r}). \tag{4.2}$$

The electron density n is the probability distribution to find an electron at a position $\mathbf{r}$ and thus the sum of the absolute squares of all one-electron wave functions ψ at this position

$$n(\mathbf{r}) = \sum_{i=1}^{n_e} |\psi(\mathbf{r})|^2 . \tag{4.3}$$

Oversimplified the SCF (self-consistent field) loop is the following: Starting point is a initial test distribution n. This is inserted in Eq. (4.1) which produces v_{eff}. With this v_{eff} the Schrödinger equation (4.2) is solved. This provides the energy and the wave function, which in (4.3) creates a new n. This process is repeated until convergence, i.e., until the energy values obtained at the iteration $i+1$ differ from those of iteration i by less than a pre-defined small value. The theorems of Hohenberg and Kohn [41] state that this finally reached n is the real ground state electron density n_{GS}. Using n_{GS} all relevant physical quantities can be calculated, in particular the Hellmann-Feyman forces which are necessary to relax the nuclei positions in the outer calculation loop [42, 43].

Within this thesis LDOS calculations as well as total-energy calculations for the carboxylate/Cu(110) system are reported which base on DFT methods as roughly described above and detailed described in Ref. [25]. They were performed by using the generalized gradient approximation (GGA) for the exchange-correlation energy functional in the form proposed by Perdew-Burke-Ernzerhof (PBE) [45]. The Kohn-Sham equations [44] were solved self-consistently using the pseudopotential method [46] as implemented in the VASP program [47,48]. The electron-ion interactions were replaced by pseudopotentials described by the projector augmented-wave method (PAW) [49]. Each molecule/Cu(110) system was modeled by a periodic slab geometry using the theoretical lattice parameter of the bulk Cu ($\approx 0.364\,\mathrm{nm}$). In each supercell the slab consists of five atomic layers separated by a vacuum region of 0.23 nm. The size of the in-plane surface unit cell was set to 4×5. For this geometrical setup, the Kohn-Sham orbitals were expanded over a plane-wave basis set which includes all plane waves up to a cut-off energy E_{cut} of $500\,e\mathrm{V}$. The Brillouin zone integrations were carried out using only the Γ-point. The geometry of the molecule/Cu(110) system was optimized by relaxing the atomic positions of all molecule atoms and those in two surface layers. The equilibrium geometry of the molecule/Cu(110) surface was obtained when the calculated Hellmann-Feynman forces were smaller than $\approx 0.05\,e\mathrm{V/nm}$.

5 The Self-Assembly of Molecules

"Self-assembly" describes the tendency of organic molecules to organize themselves spontaneously into ordered structures in the presence of a metal, metal oxide or semiconductor surface. On well-defined, atomically flat surfaces the self-assembly process results in ordered structures with the molecular constituents having their minimum total energies. The adsorption process is mainly driven by interactions between the molecules and between molecules and surfaces. If only non-covalent interactions are used to direct the molecular constituents into the resulting surface pattern, the process is termed "supramolecular assembly" [6]. On the other hand, the term "self-assembled monolayer"(SAM) is reserved, according to Whitesides [50], for a two dimensional (2D) film with the thickness of one molecule that is attached to a solid surface through covalent bonds.

The surface properties of metals, metal oxides or semiconductors are changed by the adsorption of molecules. Therefrom, a number of useful applications have been investigated in the last decades. SAMs can provide customized functional surfaces, used as catalysts [51], chemical sensors [52], or as substrates for the deposition of various materials, e.g., with modified adhesion and wetting control [53], or an increased corrosion resistance [54]. They present a possible way of integrating molecular properties into larger-scale electronics and to fabricate electronic devices [2, 55] with well-defined structural and electrical properties. Additionally, SAMs themselves are nanostructures with nanoscale dimensions useful in nanolithography [56]. Supramolecular assemblies on the other hand can be used to create nanocavities, to provide well-defined reaction spaces, and they may also control host-guest chemistry or steer heterogeneous catalysis [5].

The following sections deliver a deeper insight into the kinds of interactions between the constituents, the preparation processes of SAMs, and the various structures of self-assembled monolayers.

5.1 The self-assembly process

The inherent capability of an adequate molecule/substrate system to spontaneously generate highly ordered structures on large scales is a fascinating facet of nature and a complex process. During the self-assembly of organic molecules on planar substrates, complex hierarchical structures are formed involving multiple energy scales and multiple degrees of freedom. The geometry arrangement of organic molecules on a surface is determined in a first level of organization by the footprint of the molecule. The next nearest neighbor distance of the substrate atoms in combination with the number of surface atoms which bond to one molecule (see paragraph 5.2) define the geometrical basis. In order to minimize the free energy of the organic layer, the molecules perform intramolecular conformation changes such as bond stretches, angle bends, or torsions, which in turn maximize the lateral interactions (e.g., van der Waals interactions, hydrogen bonds, or electrostatic interactions) in a second level of organization. The surface rearrangement of the substrate corresponds to a third level of organization. The balance of these forces determines the specific molecular arrangement, while the driving force is the minimization of the total energy. A further level of organization is defined by the terminal functional group of the molecules. Terminal functional groups can cause the building of molecular networks by interactions with the other terminal groups in the molecular monolayer and are responsible for the decision if only a monolayer or multilayers are formed. Figure 5.1 shows a schematic diagram of a SAM, highlighting the parts which are responsible for an increase of organization.

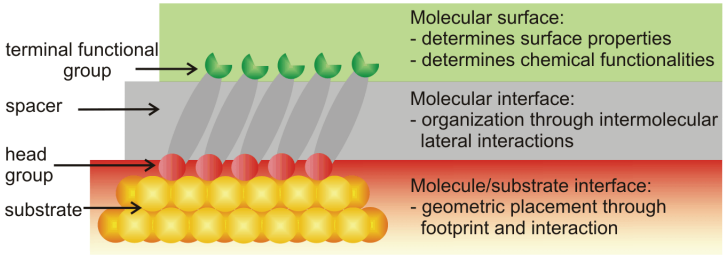

Figure 5.1: Schematic diagram of a self-assembled monolayer. Highlighted are the parts which are responsible for organization.

Every step of organization is set by the chosen molecule/substrate combination but the organization process can be influenced by external process parameters.

The number of available molecules influences the packing density and thus the orientation of the molecules on the surface. Few molecules on the surface are oriented predominantly flat-lying on the surface whereas many molecules are oriented upright on the surface to minimize there molecular footprint. Higher temperatures increase the mobility of the molecules on the surface and the mobility of substrate adatoms and enhance the rearrangement process.

5.2 Attaching molecules to the surface

Bare surfaces of metals and metal oxides tend to adsorb organic materials because the adsorbates lower the free energy of the interface between the respective material and the ambient environment. The character of the bond between the adsorbed molecules and the surface determines the interfacial electronic contact and the strength of the geometric fixation. Two main groups of links between molecules and solid surfaces can be distinguished: (i) covalent bonds, which result from the overlap of partially occupied orbitals of interacting atoms; and (ii) non-covalent bonds, which are based on the electrical properties of the interacting atoms or molecules.

Planar molecules with extended π-systems, such as benzene, have been found to physisorb onto surfaces, such as on highly oriented pyrolytic graphite (HOPG), Au(111), or Cu(110) in a flat-lying geometry. Functional end groups of neighboring molecules can interact with each other easily via hydrogen bonds, van der Waals forces, metal-ligand interactions or other intermolecular forces. If the molecules are sufficiently mobile to diffuse on the surface, the intermolecular interactions will guide the adsorbed molecules into two dimensional supramolecular systems. Then, by adjusting the molecular backbone size and the position or number of the functional recognition groups, complex supramolecular nanostructures can be designed [57].

Molecules with a chemical functionality, a so called “head group”, and a specific affinity for the selected substrate can interact with the substrate via covalent bonds. Covalent bonds are established if there is a significant overlap of the electron densities of the molecules and the substrate. This will result in a strong electronic and structural coupling. A large number of head groups exists, which bind to specific substrates forming directed covalent links. The most investigated covalent link is the bond between a thiol head group on the molecular side and

a gold substrate [58, 59]. Here, gold is favorable due to its proper non-oxidizing surface, but other metals are investigated like Ag [60], Pd [61], Hg [62], Cu [63] as well as semiconductor surfaces like Ge [64]. Besides the prominent thiolates, other functional molecules, such as alcohols (R-OH) or acids (R-COOH), have been demonstrated to form organized monolayers on metals or metal oxide surfaces, such as Al_2O_3, TiO_2 or CuO. The quantity of possible molecule/metal combinations is enormous due to the ongoing improvements in chemical synthesis. Thus, the selection of a special molecule/metal system for (electronic) investigation should be coupled to application ideas.
The head group defines the bonding side of the molecule but non-covalent interactions between the molecules can additionally influence the self-assembly process. $\pi - \pi$ interactions between phenyl rings for example can promote the building of molecular rows whereas interactions between molecules with electron donating groups anticipate the building of close-packed structures.

5.3 Preparation of self-assembled monolayers

The process of molecular self-assembly requires planar, clean substrate surfaces because step edges, defect sites or foreign atoms inhibit adsorption and organization. Thus, the preparation of self-assembled monolayers starts with the choice of the substrate form. If SAMs should be used as etch resists, protection layers or chemical sensors, the use of polycrystalline thin films as substrates is preferred because the quality is sufficient and the production costs are relatively low. Polycrystalline thin films can be grown on different templates such as silicon wafers, glass, or mica by chemical vapor deposition (CVD), physical vapor deposition (PVD), or electrodeposition. Dependent on the template/substrate material combination surfaces with a grain size up to several micrometers and a surface roughness of a few nanometers are possible [65]. Other applications of SAMs, for example special electronic components, need monocrystalline, structured surfaces so an epitaxial growth of the atomic layers is necessary. Monocrystalline thin films can be grown epitaxially if the template and the film material have a similar crystal unit cell. Gold films for example grow epitaxially on freshly cleaved mica with a strongly oriented (111) texture on the (100) surface of mica. These films are usually prepared by thermal evaporation and a RMS roughness in the range of sub-nanometer over an area of several micrometers can be achieved [66]. If the characteristics of the

SAMs themselves should be studied in detail, such as the organization process, the resulting structure, or electronic properties, oriented single crystal surfaces are required as substrates. Single crystal substrates provide the highest quality with respect to surface roughness, orientation, and cleanliness.
SAMs can be prepared in two different ways. The first possibility is the deposition out of solution. For this purpose the molecules are dissolved in an adequate solvent. Typical concentrations are in the range between micro- and millimol/l. The clean substrate is dipped into this solution for times between seconds and days, depending on the required surface coverage. A dense molecular layer is built when the molecular film and the solution reach equilibrium conditions. Annealing of the solution causes also a change in the layer by increasing the mobility of the molecules. Furthermore, heating can cause a diffusion of defects and vacancy islands towards step edges where they annihilate. Self-assembled monolayers of thiols on gold are prepared for example in this way [67]. The preparation out of solution is easy and cheap but not realizable for all substrate/molecule combinations. The substrates have to be clean and the substrate surface should stay adsorbate free at atmosphere. The solution has to be chemically pure and should not participate in the reaction process. Furthermore, the system has to be chemically resistant against the atmospheric environment (e.g., oxygen or water).
The second way to deposit molecules onto a substrate is gas-phase deposition. For this procedure, UHV systems with base pressures in the range of 10^{-5} to 10^{-10} mbar are used. In the case of organic molecules the deposition is done by sublimating them out of a crucible. In order to obtain a reproducible molecular flux and a collimated beam, a closed volume with only a small hole, as provided by a Knudsen cell, is typically used. Heating is necessary for many molecules because usually their vapor pressure is to low at room temperature. Heating, on the other hand, can also destroy the molecules. Evaporation has thus to be carried out at low deposition rates in order to keep the evaporation temperature low. The surface coverage and structure can be influenced by the exposure time, the pressure, and the temperature of molecules and substrate. Because of the vacuum environment gas-phase deposition allows to prepare SAMs on substrates like copper, which would oxidize on atmosphere [68]. Besides this, SAMs prepared in gas-phase have in general a higher uniformity and thus gas-phase deposition is often preferred although deposition from solution is easier and the equipment is more simple.
Furthermore, it is possible to prepare SAMs with more than one chemical com-

ponent. This so called "Mixed SAMs" can be created in several ways, one way is coadsorption containing mixtures of the molecules, and results in mixtures of molecular structures. This process allows the formation of SAMs with widely varying compositions and physical properties [69]. The other way to process mixed SAMs is a two-step process which begins with a full coverage monolayer of one chemical component which acts as a host matrix. In a second step the other chemical component is deposited. Insertion of these "guest-molecules" takes place preferentially at defect sites of the host-matrix. Depending on the chosen molecule combination and the deposition conditions single inserted molecules, bundles, or inserted domains are possible. The big advantage of this second method is that a detailed topographical and electronic analysis of a new molecular species in reference to a known molecular system is possible [38].

5.4 Structure of self-assembled monolayers

Many different thin film characterization techniques have been applied to investigate self-assembled monolayers. Mainly spectroscopic methods like optical ellipsometry, reflectance absorption infrared spectroscopy (RAIRS), X-ray photoelectron spectroscopy (XPS), low-energy electron diffraction (LEED), high-resolution electron energy loss spectroscopy (HREELS) and near edge X-ray absorption fine structure spectroscopy (NEXAFS) are used. In addition, an increased understanding of the SAM structures has been achieved by high-resolution topography methods such as scanning probe microscopy (SPM). Generally, due to the sensitivity to different features of the structure and the different averaging behavior, in order to obtain a complete picture of the molecule/metal system under investigation the use of several complementary methods is desirable. To get an overview of the large number of existing molecule/substrate systems which have been used to form SAMs, they are classified by the pair of chemisorbed head group of the molecule and the substrate (while the rest of the molecule can be almost freely chosen). The following paragraphs give an overview on two molecule/substrate systems, namely the thiol/gold system and the carboxylate/copper system. Alkanethiols (R-SH) on Au(111) are probably the most studied and best understood SAM system and, therefore, it is used as reference for many other systems. Carboxylic acids (R-COOH) on Cu(110) surfaces are a relatively seldom studied system up to now but it shows a high potential regarding future applications.

5.4.1 Organothiols on gold

For low coverages, the alkanethiols move freely on the surface and are described as a liquid phase (Fig. 5.2(a,b)). With increasing number, the molecules exist as "lying-down" species on the substrate surface (Fig. 5.2(c)) and form ordered domains with a characteristic striped structure. Upon further deposition, island of standing molecules are formed until at saturation a full-coverage monolayer is achieved (Fig. 5.2(d,e)). Due to the chemically passive alkane tail-group the monolayer growth is self-terminating and additionally adsorbed molecules can be easily removed by rinsing with a solvent or thermal desorption. Thus, the formation of bi-layers or adsorbates on the monolayers can be excluded. The monolayer formation is driven by van der Waals interactions between adjacent molecules and the strength of the interactions is proportional to the alkyl chain length, being responsible for the degree of order in the SAM. Alkanethiols adsorb under deprotonation as thiolates ($R\text{-}S^-$) with the sulfur as binding partner of the gold. The formed Au-S bond is covalent and has a strength of approximately 200 kJ/mol.

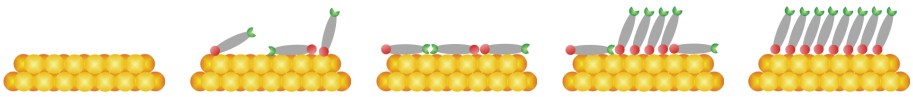

Figure 5.2: Evolution of a thin film, from the clean substrate (a) via intermediate phases (b-d) to a full-coverage self-assembled monolayer (e).

Throughout their growth process, alkanethiols on Au(111) exhibit a rich variety of structures before converging to the densely packed high-coverage structure of the complete monolayer. It is well established that the lowest-energy configuration consists of molecules ordered in a close-packed $(\sqrt{3} \times \sqrt{3})\mathrm{R}30^\circ$ lattice commensurate with the underlying surface. Optimal packing of the n-alkane component of the SAM is achieved by tilting the molecular axis with respect to the surface normal by $\approx 30°$. The hydrogens are in all-trans configuration. This phase yields the highest molecular density with a molecular footprint of exactly $0.216\,\mathrm{nm}^2/\,\mathrm{molecule}$ [59, 70–72] and may appear modulated by a $c(4 \times 2)$ superstructure [73–75]. It is characterized by a systematic arrangement of molecules showing distinct height differences [75]. Six slightly different $c(4 \times 2)$ superstruc-

tures with the same unit cell but different height distributions were observed frequently with STM and AFM, see Fig. 5.3. The height differences in the STM images are believed to be due to different conformations of the alkanes. Liu et al. [76] proposed a new mechanism for the height modulations being caused by different local density of states within the unit cell originating from changing hybridization of the sulfur bonding orbitals. Furthermore, they show that they can switch reversibly between the different structures by bias modulation. SAMs with these close-packed superstructures show a surface texture with rotational and translational domain boundaries, etch pits emerging during the assembly process, and surface features of the underlying gold substrate, like atomic terrace steps. Etch-pits represent one atom deep depressions in the underlying gold surface caused by lifting the herringbone surface reconstruction of the gold surface upon chemisorption of the thiols [77, 78]. Immediately after deposition the vacancy islands exist in a large number and have small dimensions, whereas upon annealing or with time they coalesce into larger depressions or fuse with terrace steps [74].

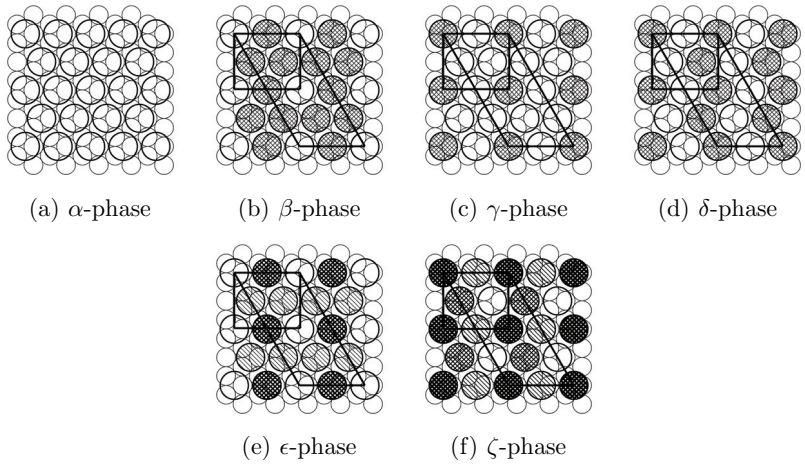

(a) α-phase (b) β-phase (c) γ-phase (d) δ-phase

(e) ϵ-phase (f) ζ-phase

Figure 5.3: Schematics of the different c(4×2) supercells of alkanethiols on Au(111) by [75]. Gray shaped molecules appear lower in STM.

The striped patterns obtained at low coverage are generally denoted as $(p \times \sqrt{3})$ structures, where p is the stripe separation and $\sqrt{3}$ the spacing within the stripes in units of the Au(111) lattice parameter or nearest neighbor distance (NN). The configuration with the lowest reported molecular surface density consists of fully

stretched molecules arranged in rows parallel to the next nearest neighbor (NNN) or $[11\bar{2}]$ direction of the substrate. The distance between rows consisting of two alkane chains with head groups "faced" to each other is approximately twice the length of the molecule [79–81]. Increasing the coverage leads to the formation of denser striped phases with lower inter row distances. For these striped phases where the periodicity is lower than twice the chain length conflicting models have been proposed. These models can be classified into two categories: those where the molecules lie in a prone position, and those where the alkanethiols are in a standing-up configuration. Today, the accuracy of height measurements, by e.g., UHV-STM, allows to differentiate between lying and standing molecules. Munuera et al. [81] describe the differences in height distributions for various denser packed striped structures in great detail.

Beside the intensively reported investigations on the alkanethiol system, slightly different systems like dialkyl disulfides and dialkyl sulfides are also reported in literature. Dialkyl disulfides were investigated on Au(111) surfaces and it is generally believed that adsorption of dialkyl disulfide on gold occurs via S-S bond cleavage. Therefore, dialkyl disulfides form identical SAMs on gold as alkanethiols, consisting of gold-bound thiolates [82, 83]. On the other hand, most studies concerning the SAMs formed from dialkyl sulfides show significantly different monolayer properties such as less dense packing, order, and lower film thickness than those prepared from alkanethiols and dialkyl disulfides. While first investigations pointed out that the adsorption of dialkyl sulfides on gold undergoes a C-S bond cleavage [84] newer investigations show evidence for the intact adsorption of the molecules without a C-S bond cleavage. Beside STM investigations, XPS and SIMS (Secondary ion mass spectrometry) investigations were considered to prove the intact adsorption of dialkyl sulfides on gold [83, 85, 86]. J. Noh and coworkers give in [85] a detailed description of surface structures consisting of lying-down and standing-up dialkyl sulfide molecules.

5.4.2 Carboxylates on copper

Compared to the extensive studies of organothiols on gold surfaces, very few investigations have been undertaken to study the self-assembly process of carboxylic acids on metal surfaces. The carboxylate group is capable of forming strong bonds to different metals like copper, nickel, palladium or platinum. The topographical

structures of simple carboxylic acids (functional group COOH) such as formic and acetic acid have been the subject of earlier work and have been reviewed by Netzer [87]. The topographical structure of small tartaric acid molecule is reported as well as that of benzoic acid and thiophene carboxylic acid by Barlow [51]. During the adsorption process of carboxylic acids onto copper surfaces the acid group is deprotonated. Both oxygen atoms of the carboxylate group bind chemically to the copper surface, forming an equidistant and rigid adsorption geometry. Neither RAIRS nor HREELS investigations show signals related to C=O or COOH but signals related to the carboxylate ion COO^-, so a deprotonated carboxylic group with a delocalized electron pair is assumed. In contrast to the thiol-sulfur bond, the chemisorbed carboxylate moiety is then attached to the surface with two points and a free tilting and turning of the molecule to form an energetically optimal monolayer is restricted. Only one degree of freedom for tilting or rotation around the σ-bond between phenyl ring and COOH group exists, for example for benzoic acid. The adsorption sites of the Cu(110) surface closely match the distance between the two oxygen atoms of the carboxyl moiety and the special striped structure of Cu(110) builds a template for the self-assembly process. Thus, the Cu(110) surface represent an ideal surface for self-assembly. The phenyl ring as central moiety for carboxylic acids has a delocalized π-system and can in principle interact with the neighboring molecules via π-π interactions. Benzoic acid is the simplest carboxylate with a ring unit and the self-assembly process, investigated by Frederick et all. [68], is used as a proof of concept for the in-vacuo processing of monolayers before investigating other carboxylic acids. For increasing coverages, ordered domains of different structures including lying-down and standing-up molecules evolve from disordered regions [51, 68].

The formation of ordered monolayers is strongly dependent on the deposition temperature, since the deprotonation of the carboxylate moiety occurs only above 119 K [88]. Below 200 K, multilayer formation occurs for higher coverages, since additional benzoic acid molecules will not be desorbed. Above 580 K, the chemisorbed monolayer of benzoates becomes unstable. For temperatures between 200 K and 580 K the SAM of the benzoates undergoes structural changes in dependence of surface coverage. For low coverages the benzoates lie flat on the surface and with increasing coverage ordered domains of lying benzoates are formed, denoted as α-phase. The α-phase consists of four lying-down molecules per unit cell with an optional standing benzoate in the center. This structure is stabilized by the formation of benzoate-dimers by including two surface adatoms per two

benzoates [68, 89]. Upon further deposition, a β-phase is formed, consisting of dimer rows and including more standing-up benzoates [68]. For the phase with highest coverage a c(8×2) surface order is observed as the dominant phase by STM and LEED [68, 90]. For those layers both oxygen atoms of the carboxylate group are chemisorbed on short bridge sites of the outermost copper layer, forming rows in [001]-direction of the surface with a packing density of one benzoate molecule per four outermost copper surface atoms. The phenyl rings of the molecules are arranged in the same plane as the carboxylate moiety, perpendicular to the surface.

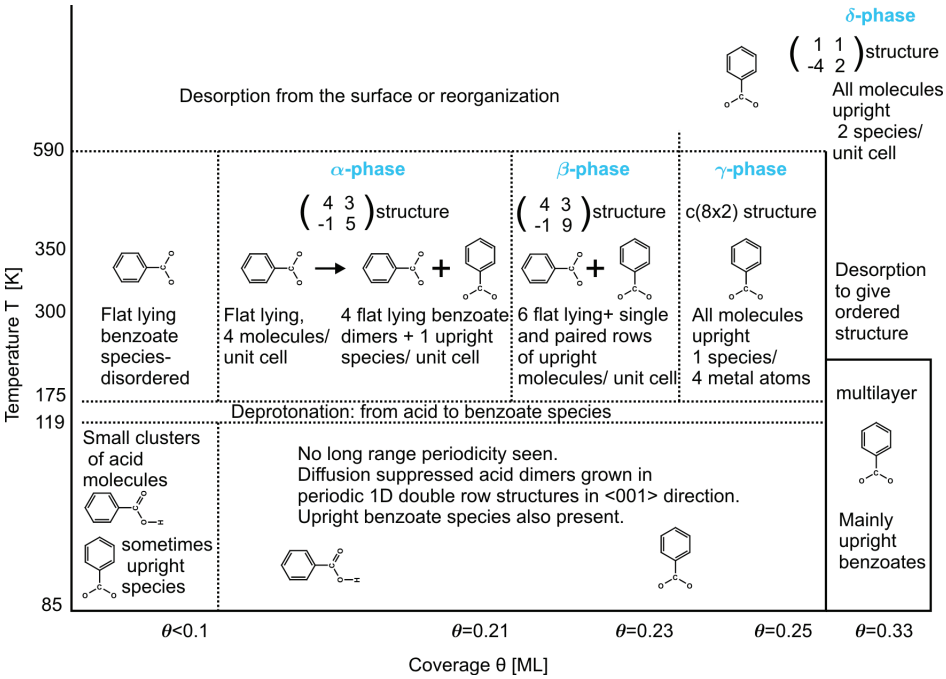

Figure 5.4: Phase diagram of benzoic acid on Cu(110).

Recently we found a closer packed structure appearing after heating samples, with high molecular coverage, close to the desorption point of the benzoate species. At temperatures around 590 K parts of clean copper arise due to desorption of molecules from the surface and, furthermore, the high temperature elevates the mobility of the molecules on the surface enabling the remaining molecules to form this new structure. The structure can be described by a (1 1;-4 2) unit cell with two molecules in the unit cell. It is stabilized by copper adatoms which are present

on the Cu(110) surface even at room temperature [21, 68]. The various forms of benzoic acid seen on Cu(110) are compiled in the phase diagram shown in Fig. 5.4, constructed from the results presented in the above mentioned references, collected by Barlow and Ravel [51]. This is a modified version including the close-packed molecular phase appearing at high temperatures.

6 Bottom Electrode Materials

Various metallic, semi-conducting and insulating thin films, and single crystals were investigated in the last years as substrates for molecular electronic [51,58,91, 92]. High demands are made on these substrates. The substrate has to work as template for molecular assembly and additionally it has to work as continuously conducting bottom electrode. To generate highly ordered molecular structures on a large scale the surface lattice and the superstructure of the substrate material need to be comparable to ensure commensurable monolayer. A high binding energy between molecule and substrate material and a low energy barrier between adjacent binding sites promotes the regular film growth, by increasing the surface mobility of the molecules during the adsorption process. Furthermore, for low energy barrier surfaces the number of adatoms on the surface is higher and this promotes the ordered self-assembly of molecules [93, 94]. The substrate surfaces have to be adsorbate free, defect free, and atomically flat showing only large scale terraces. For STM investigations the aspect of substrate cleanliness and flatness gets even more important. STM needs a continuously conducting bottom electrode material with a RMS surface roughness in the range of the height of a single atomic step. Nonconducting areas as well as height differences can cause tip crashes during scanning.

Gold thin film surfaces, especially (111)-oriented gold surface, became the most investigated substrates and in this way a standard for molecular investigations because they have a high surface quality, are cheap and available in large quantities. Taking an applications of molecular electronics in combination with common standard materials in semiconductor industry into account other materials than gold become favorable. Copper for example is already integrated into the silicon based technology. Another approach is to make use of the semiconductor materials used in industry, for example germanium, and take them as substrates for molecular self-assembly.

Beside the question of the right material the surface orientation is also an impor-

tant point. Depending on the molecular system or desired applications different surface morphologies can be favorable. It was the ambition of initial experiments with self-assembled monolayers to fabricate surfaces with a homogeneous molecule coverage and the aim was to create absolutely homogeneous and flat monolayers. Therefore, flat surface morphologies were needed, for example the Au(111) surface. During the last years various concepts to built up a molecular device were developed and structuring of the surfaces becomes interesting. Structured surfaces, like the Cu(110) surface, can act as template for an aligned self-assembly of molecules. Carboxylates on Cu(110) surfaces are one example for such an aligned SAM growth on a template. Nanowires on a flat surface can also be used as template besides the fact that they can act as interconnects between nanoscale devices. Nanowires can be produced also by self-assembly on semi-conducting materials, for example one-dimensional atomic chains of Pt or Au on Ge(001) substrates [95].
In this thesis gold (111)-oriented thin films, copper (110)-oriented single crystals, and copper thin films are studied. Furthermore, germanium in (001)-orientation covered with platinum nanowires is used as substrate for molecular self-assembly.

6.1 The standard substrate: Au(111) thin films deposited on mica

The crystal structure of gold is face centered cubic (fcc) with a lattice constant of $a_{crystal} = 0.408\,\text{nm}$. The (111)-oriented surface of the hexagonal close packed (hcp) lattice has an in-plane vector of $a = 0.286\,\text{nm}$ and an out-of-plane lattice vector of $b = 0.24\,\text{nm}$. Single gold crystals would be the best available template for molecular growth but the cleaning process is cost and time consuming so they are commonly not used. In contrast, crystalline gold thin films can be prepared by evaporation on various templates with a reasonable effort in large quantities and are much easier to handle than single crystals. Crystalline gold thin films can be fabricated by evaporation of gold on mica [96], on silicon [97], or on glass [98]. Mica, a natural mineral (Muscovite: $KAl_2[(OH)_2|AlSi_3O_{10}]$), was used as template for gold growth for all samples shown in this thesis. Mica crystals consist of thin sheets and can by cleaved easily along the (001)-plane. The cleaved surface is clean, defect free and atomically flat. The surface is dominated by oxygen atoms

of the silicate. The distance between the oxygen atoms in the crystal lattice is around 0.26 nm, which promotes (111)-oriented epitaxial growth of gold [99].

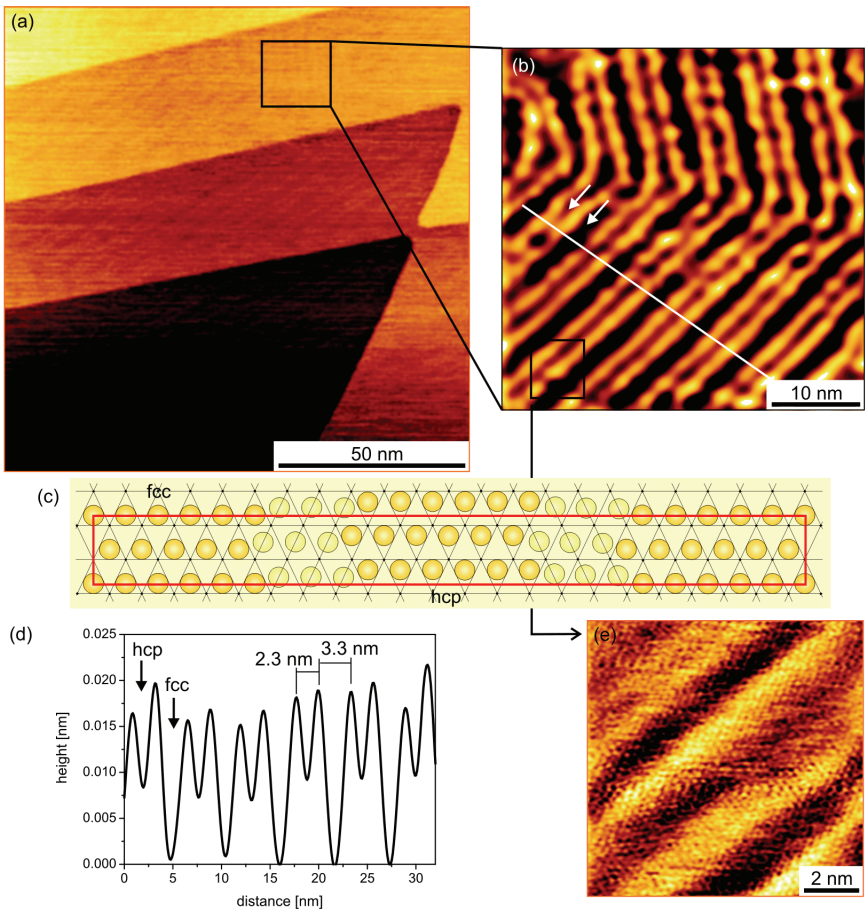

Figure 6.1: STM topography scan of an Au(111) thin film on mica. (a) General survey of $125 \times 125\,\mathrm{nm}^2$ size, showing gold terraces with a height difference of one atom. (b) High resolution scan of the Au(111) $(23 \times \sqrt{3})$ herringbone reconstruction, schematically shown in (c). A line profile (d) identifies the different parts of the unit cell in great detail and fcc and hcp regions are marked in the STM scan. (e) High resolution scan of the reconstruction with single gold atoms on the surface.

Ultra-clean muscovite mica was bought from Plano GmbH and the gold films were prepared in a three step evaporation process as described in great detail in [66, 100, 101]. After evaporation and annealing the substrates were trans-

ferred directly into the UHV-STM system or stored in N,N-dimethylformamide (C_3H_7NO, DMF). This solvent is suitable for gold sample storage because it does not react with mica or gold.
The crystallinity and the cleanliness of the samples was verified by STM measurements. Figure 6.1(a) shows a constant-current STM image of a typical patch of the clean, crystalline, (111)-oriented gold surface. The surface is dominated by atomically flat terraces with monoatomic steps of 0.24 nm height, along the $[0\bar{1}1]$-, $[\bar{1}10]$- or $[01\bar{1}]$-directions of the surface. Zooming in and scanning one terrace in more detail shows series of parallel double lines, forming a zigzag pattern with 120 ° angles (Fig. 6.1(b)). This pattern is the characteristic reconstruction of the Au(111) surfaces and can be described with a unit cell of $(23 \times \sqrt{3})$. It is caused by a stress-induced surface contraction along the $[1\bar{1}0]$-direction, see Fig. 6.1(c), and leads to an extra surface atom per 22 regular surface atoms. In one part of the reconstruction unit cell, the surface atoms occupy hexagonal close packed (hcp) sites, while in the adjacent part, they occupy face centered cubic (fcc) sites. The hcp region has a width of 0.25 nm and is noticeably narrower than the 0.38 nm wide fcc region. The consistently alternating of hcp and fcc regions can be displayed by the line profile of Fig. 6.1(d). Also visible here are the 0.02 nm high domain walls formed by surface atoms occupying bridge sites between the fcc and hcp regions. This so called herringbone structure is described in literature [77,102] and characterized by topographical STM investigations here to get a defined starting point for molecular investigations. Figure 6.1(e) shows a high resolution STM image were single gold atoms on the surface can be distinguished.
Characteristic for the density of the electronic states on the clean Au (111) surface is a Shockley-type surface state having a band onset at ≈ -0.4 eV. Furthermore, an increase in the density of states is visible below -1 eV corresponding to the L_2 band edge of gold [103, 104]. The dI/dV spectrum with its characteristic features appearing between ± 1 eV is plotted in Fig. 6.2. W. Chen and coworkers had shown here that a negligible difference exists between spectra taken at hcp and fcc regions [104].

6.2 An alternative metal substrate: Cu(110)

Copper metal substrates are considered to be an interesting alternative to the commonly used gold substrates. Copper surfaces work as templates for the self-

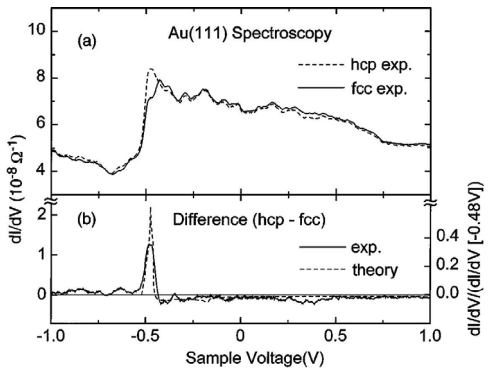

Figure 6.2: (a) Average dI/dV spectra taken with the STM tip held over a hcp region and a fcc region of the Au(111) reconstruction. (b) The difference plot shows no significant variation between the hcp and fcc spectra. Figure taken from [104].

assembly of molecules but it has to be taken into account that copper oxidizes upon contact with atmosphere and that oxygen can inhibit the self-assembly process of molecules. Hence copper surfaces have to be cleaned under vacuum conditions before molecule deposition. So a sputter cleaning and annealing process has to be developed based on literature data [68]. The process details are described in the next section. Within the framework of this thesis especially (110)-oriented copper surface were investigated. The Cu(110) surface is a textured surface which allows to assemble molecules with a preferred alignment. Single crystals were used here for investigations because the clean substrates must be stored under vacuum conditions. The handling of single crystals and thin films is in this case the same. Besides this textured surface, copper thin films were investigated within the framework of a project which deals with the combination of current CMOS technology and molecular electronics.

6.2.1 Single crystals

The crystal structure of copper is fcc with a lattice constant of $a_{crystal} = 0.3615\,\text{nm}$. The (110)-oriented surface is one diagonal plane of the crystal unit cell and shows a striped pattern. The pattern originates from the packing density of the fcc lattice. The higher surface atoms form rows in $[1\bar{1}0]$-direction with an interatomic distance of $a = a_{crystal}/\sqrt{2} = 0.2556\,\text{nm}$. The distance in [001]-direction between the rows is $b = a_{crystal} = 0.3615\,\text{nm}$. A schematic of the (110)-oriented surface is

shown in Fig. 6.3(a). The step height of the surface terraces is $h = 0.1278\,\mathrm{nm}$.

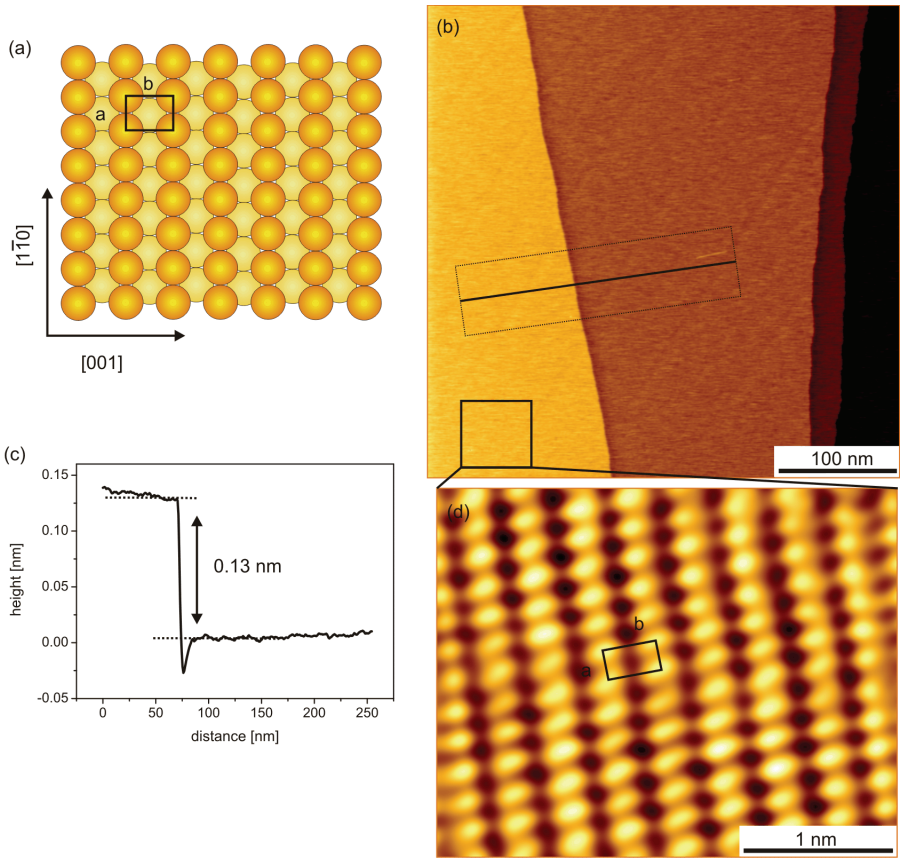

Figure 6.3: (a) Schematic drawing of the Cu(110) surface structure. The unit cell vectors are $a = 0.2556\,\mathrm{nm}$ in $[1\bar{1}0]$-direction (along the atom rows) and $b = 0.3615\,\mathrm{nm}$ in [001]-direction. (b) General survey STM scan of $400 \times 400\,\mathrm{nm}^2$ size, showing copper terraces with a height difference of one atomic layer. A line profile (c) out of scan (b) can identify the terrace height of exact one atomic copper layer. (d) STM scan of the Cu(110) unit cell in atomic resolution.

Copper single crystals were bought from MaTecK GmbH with a roughness depth of $< 0.03\,\mu\mathrm{m}$ and an orientation accuracy of $< 0.1\,^\circ$. Further cleaning and planarization was done in a UHV system. The single crystal samples were cleaned by repeated cycles of Ar^+-ion bombardment and annealing. The parameters for copper crystal preparation can be found in literature, for example in [68], but they have to be readjusted for every facility. Several parameters were tested regarding

sputter pressure, energy and time as well as regarding heating temperature and time. The cleaned samples were investigated with XPS/AES, LEED, and STM methods.

The adsorption behavior of the clean copper surface in vacuum was studied by XPS [105, 106]. For XPS measurements the crystal was Ar^+-sputtered and annealed and the type and amount of adsorbates depending on the vacuum pressure and storage time were monitored. The results of these measurements can be found in [101, 107]. The measurements indicate that great care must be taken while handling the copper substrates. Handling at 10^{-9} mbar during an experiment is considered safe in terms of oxygen adsorption, whereas for higher pressures the surface is quickly covered by oxygen.

Auger electron spectroscopy (AES) [105, 108] was used after every cycle of Ar^+-sputtering to find out how many cycles of sputtering are sufficient to get an adsorbate free surface. The measurements were performed with an Omicron AES-spectrometer. Figure 6.4 shows one AES spectrum before (a) and one spectrum after (b) several cleaning cycles. The first spectrum shows the Auger peaks of copper but also peaks of the adsorbates argon, nitrogen, and oxygen whereas the second spectrum shows only the copper peaks. This shows that our cleaning cycles remove the adsorbates from the surface.

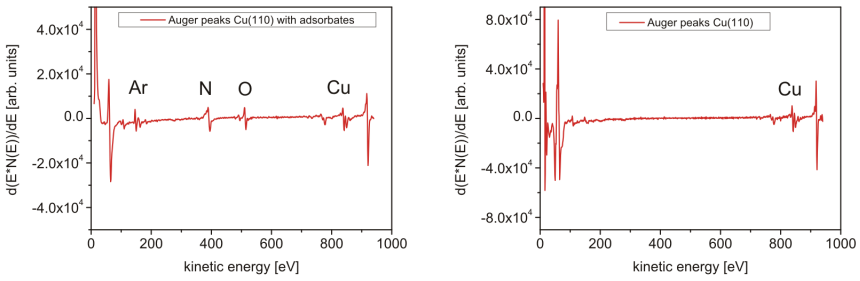

(a) (b)

Figure 6.4: (a) AES spectrum of a copper single crystal surface before sputter cleaning. The spectrum shows beside the Auger peaks of copper also peaks which can be related to argon (Ar), nitrogen (N) and oxygen (O). (b) AES spectrum of the same crystal after several cleaning cycles. Now only the Auger peaks of Cu are detected.

To prove the crystallinity and orientation of the copper surface after the cleaning process (sputtering and heating) the samples were verified by low energy electron diffraction (LEED) [108]. The measurements were performed with an Omicron

LEED-spectrometer. After the first cleaning cycle the LEED spectrum shows blurry features related to the copper pattern and additional spots which can be related to oxygen on the surface. With proceeding cleaning cycles the features of the copper pattern get sharper and the additional spots disappear. This means that adsorbates are efficiently removed by sputtering and that the surface is reorganized after sputtering through adequate heating. The LEED pattern of a clean, crystalline Cu(110) surface is shown in Fig. 6.5(a). For comparison Fig. 6.5(b) shows LEED pattern of the clean Cu(110) surface and with 1L oxygen coverage on Cu(110), observed by [109].

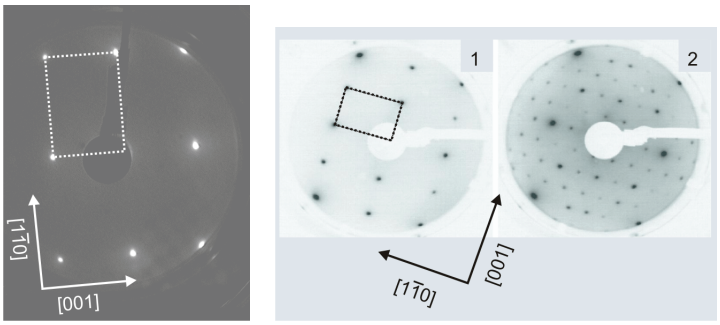

(a) (b)

Figure 6.5: (a) LEED pattern of the clean Cu(110) observed at 64.8 keV after several cleaning cycles. For comparison (b) shows a LEED pattern of the clean Cu(110) surface (1) and one with 1L oxygen coverage (2), observed by L.D. Sun [109].

Additionally, the Cu(110) surfaces were characterized by STM to optimize the cleaning cycles with respect to the surface morphology. A general survey STM scan of $400 \times 400\,\mathrm{nm}^2$ size monitoring the clean, crystalline, (110)-oriented copper surface is shown in Fig. 6.3(b). The surface is dominated by atomically flat terraces with a monoatomic step height of 0.13 nm (Fig. 6.3(c)). Scanning the surface with high resolution (Fig. 6.3(d)) shows the above mentioned rows and the expected unit cell size of $a = 0.25\,\mathrm{nm}$ and $b = 0.36\,\mathrm{nm}$.
The procedure for cleaning the samples consists finally of four cycles with the parameters described in table 6.1. Longer or stronger sputtering results in larger terraces, but induces more defects [110], which can be difficult to remove by heating. During annealing similar considerations have to be taken into account. Moderate heating heals defects and adsorbates, but stronger heating causes diffusion of buried impurities and defects to the surface. If the temperature exceeds the thermal roughening temperature ($T_R \sim 1030\,\mathrm{K}$), a complete reorganization of the

surface occurs and a stepped morphology evolves [111].

(a) Argon-ion sputtering:

Energy	Focus	Pressure	Time
3.0 keV	2.4 keV	$1.0 \cdot 10^{-5}$ mbar	30 min

(b) Heating:

Temperature	Pressure	Time
860 K	$2.0 \cdot 10^{-9}$ mbar	60 min

Table 6.1: Parameters for copper single crystal cleaning.

This cleaning process is further used for samples which were placed for a longer time at atmosphere, to remove oxygen adsorbates (compare Fig. 6.6) after a longer time of storage in vacuum or to remove molecules after investigation.

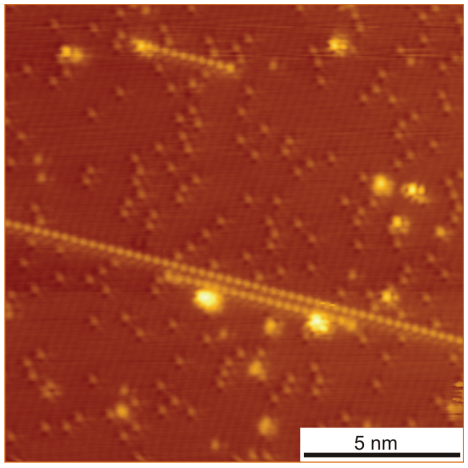

Figure 6.6: High resolution STM topography scan of a Cu(110) surface with a sub-monolayer oxygen coverage. The copper rows are visible in the background and single oxygen dimers (O_2) adsorbed on top. The dimers adsorb in between the copper rows and with further exposure they form rows perpendicular to the copper rows.

6.2.2 Thin films

Copper thin films offer in principle an alternative to the copper single crystals. Especially for applications they are important because they are cheaper than single crystals. Copper thin films can be grown on various substrates and in different orientations [65, 112, 113]. Copper thin films on silicon oxide (SiO_2) and silicon nitride (Si_3N_4) are relatively easy to fabricate by deposition and show a preferential growth with {111}-texture. Up to now, not many investigations were done on the fabrication of thin films with {110}-texture. Reported in literature are investigations to grow Cu(110), e.g., on molybdenum with (110)-orientation [114] but this procedure is also very cost intensive. Platzman and coworkers recently presented that it is possible to create polycrystalline copper thin films with a morphology good enough to deposit molecules (terephthalic acid) on top [65]. These investigations on tantalum nitride (TaN) are comparable with our investigations on SiO_2 and Si_3N_4 taking into account that we were not able to heat the samples after deposition.

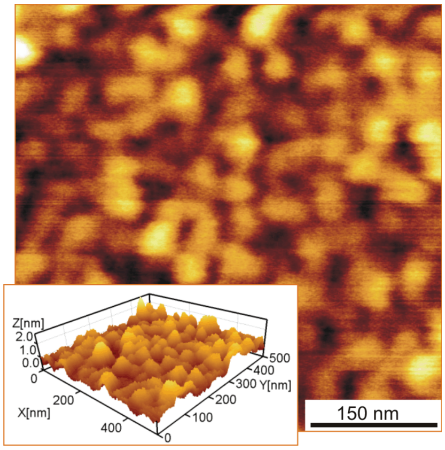

Figure 6.7: AFM scan of 0.5 μm × 0.5 μm size showing the surface of a 20 nm thick Cu thin film surface. The film is deposited on SiO_2. Many grains with different sizes are visible with an average grain size of 60 nm × 60 nm. The inset shows the 3D image of the same surface and the depth of the crevices gets visible.

The dependence of the properties of the thin Cu films on the deposition method (thermal evaporation, electron beam evaporation, and sputter deposition), on the film thickness (20-200 nm), the substrate type, and the cleaning conditions was

investigated. Without an additional annealing step after deposition we could fabricate thin films by sputter deposition (deposition rate: 1.7 nm/s) with a grain size of around 60 nm × 60 nm separated by crevices of less than one nanometer and a RMS roughness of 0.3 nm for 0.5 μm × 0.5 μm areas. This is comparable to the results of Ref. [65] which present these values after annealing. Figure 6.7 shows an AFM (Atomic Force Microscopy) image of a 20 nm thick copper thin film surface deposited with sputter deposition on a SiO_2 template. Many grains with different sizes are visible but the average grain size is 60 nm × 60 nm and the RMS roughness is only 0.3 nm. The inset shows the 3D image of the same surface and the depth of the crevices gets visible (less than 2 nm).

6.3 From conducting to semi-conducting substrates: Pt NW´s on Ge(001)

An alternative approach to assemble molecules with a preferred alignment besides the use of structured crystal surfaces, like the Cu(110) surface, is to use nanowires as template. Pt nanowires grow on Ge(001) surfaces with a cross section of one atom, with a straight alignment, and without defects.
Atomically clean Ge(001) surfaces exhibit a well ordered (2×1)/c(4×2) domain structure [115]. Figure 6.8(a) shows a STM image of a clean dimer reconstructed Ge(001) surface observed by A. Houselt [95]. The dimer rows in the c(4×2) domains have a zigzag appearance, the other dimer rows have a symmetric appearance and consist of dimers that rapidly flip-flop between their buckled configurations [116, 117]. Pt was deposited at room temperature (0.2-0.3 monolayers) and initially intermixes with the bulk, but upon a high temperature annealing treatment (1050(±25) K) the Pt comes up to the surface and builds Pt dimers. Upon reaching a critical coverage of Pt dimers they spontaneously form an atomic Pt chain in between the substrate dimer rows. After deposition of Pt onto the surface and subsequent annealing, two different types of terraces are formed on the Ge(001) surface, so called α- and β-terraces [92]. The α-terraces have symmetric and asymmetric Ge dimers and are similar to the normal dimer reconstructed Ge(001) terraces [118]. A STM image of such a terrace is shown in Fig. 6.8(b). The β-terraces are also dimer terminated but the termination consists of an ordered array of dimers. The atomic structure of the β-terrace is discussed in great

detail in [95] and shown in Fig. 6.8(c). Important for further studies is that the β-terraces have dimer vacancy lines which do not exist on bare Ge(001) surfaces and on the α-terraces. Pt nanowires can only be observed on these β-terraces.

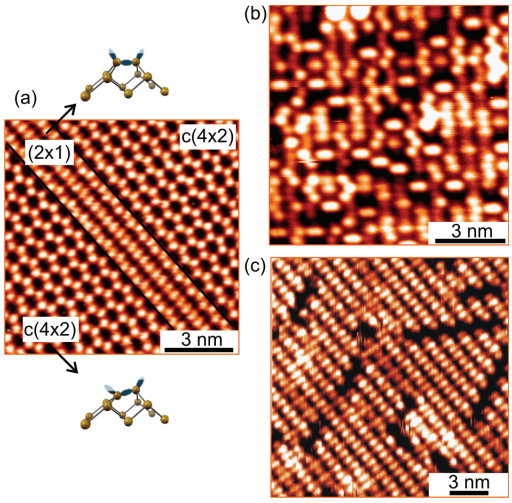

Figure 6.8: (a) STM image of the clean Ge(001) surface prior the Pt deposition. The dimer rows that have a zigzag appearance show the c(4×2) reconstruction. At the center of the image the dimer rows have a (2×1) reconstruction. (b) STM image of an α-terrace and (c) of a β-terrace after Pt deposition on Ge(001) and annealing. The images are taken fom [95, 117] and accordingly from [119].

The cleaning of the Ge(001) substrates, the deposition of the Pt and a first STM observation of every sample was done in the group of Prof. H.J.W. Zandvliet at the University Twente, the Netherlands. Than, the samples were covered with some monolayers of oxygen as capping layer for transport. With this the samples could be transported without vacuum environment. For molecular assembly investigations the samples were mounted and transferred into our UHV-STM system. The capping layer of oxygen was removed with a high temperature annealing treatment (around 900 K) and with this Pt atoms from the bulk pop-up as Pt dimers again and form Pt nanowires. Interestingly, in all investigations only β-terraces were found after oxygen removal. A STM image of the typical topography with Ge(001) terraces covered with Pt nanowires after oxygen removal is shown in Fig. 6.9(a).

The surfaces were investigated in great detail before molecular self-assembly. Figure 6.9 shows, therefore, not only a STM overview image of 68×48 nm^2 size with

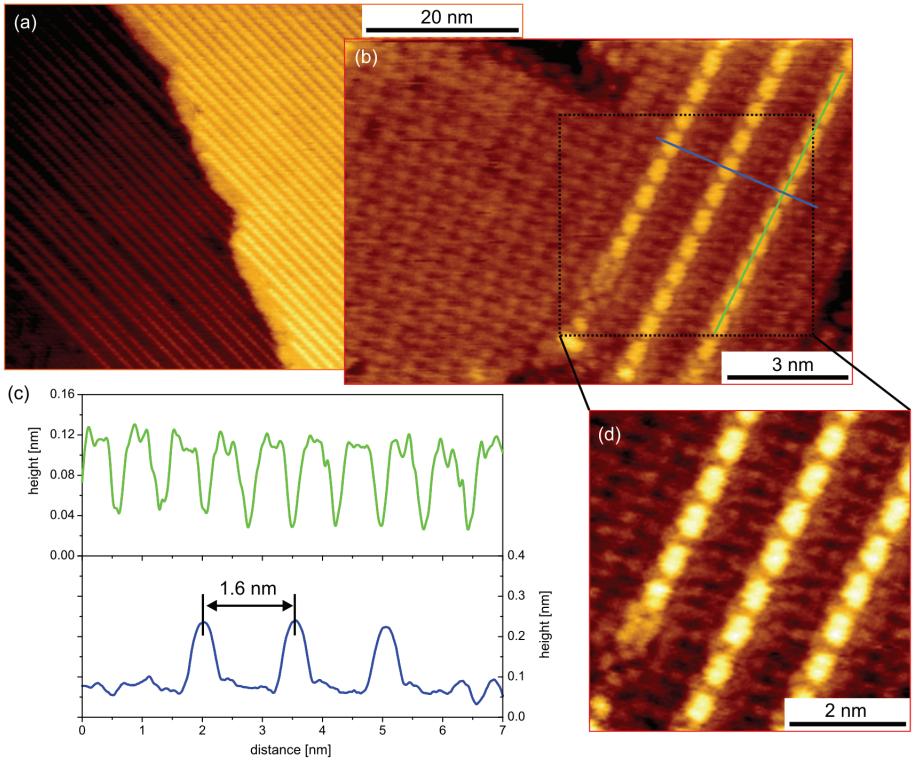

Figure 6.9: (a) STM image ($68 \times 48\,\mathrm{nm}^2$, $V_{Set} = 1.2\,\mathrm{V}$ and $I_{Set} = 1.07\,\mathrm{nA}$, T=293 K) of a Ge(001) surface covered with Pt chains. Only β-terraces with chain coverage are detectable. The chains are close packed and only in the lower left part of the image large inter-chain distances are visible. The STM scan (b) shows a Ge terrace partly filled with chains. These detailed images are used for distance measurements. Line profiles (c) show the distance and the heights in the chains (green) and between them (blue). Image (d) is a part scan of figure part (b) in high atomic resolution. Here the Pt dimer position on the underlying substrate is identified as an intermediate position between the Ge dimer rows.

β-terraces covered with Pt nanowires (a) but also line scans over the Pt wires (c) and a high resolution scan of a patch of atomic Pt chains (d). Observations show that the Pt chain length is only limited by the terrace size of the Ge surface and the chains are closely packed (a). The chains have a cross section of one atom and are kinkless and defect free. Furthermore, the chains are located between the substrate dimer rows, visible on the left side of figure part (b). High resolution scans like (b) are the basis for line profiles (c) which give information about the distances between the scanned features. The inter-chain distance is found to be

mostly 1.6 nm, also spaces of 2.4 nm (lower left side of Fig. 6.9(a)) and sometimes 3.2 nm etc. are found. The Pt dimers in neighboring (1.6 nm) rows are in-registry with each other while they are out of registry for 2.4 nm row distances. The Pt dimers have a distance of about 0.8 nm between each other. In STM scans with high atomic resolution, like in Fig. 6.9(d), for example the structure of the germanium dimers underneath the Pt dimers gets visible after removing on Pt dimer with the STM tip. Further descriptions and explanations of the system can be found in the PhD thesis of Houselt [95].

7 Carboxylates on Cu(110)

Carboxylates on copper surfaces and especially on Cu(110) surfaces constitute a promising metal electrode/molecule system for future applications, irrespective of the final circuit design. This is based on the fact that copper is a material already integrated in semiconductor industry processes or in catalytic processes and also on the idea that a metal substrate and the corresponding molecules themselves should be able to design the structure wanted for application. Here, the focus is set on close-packed structures, i.e., many addressable molecules per area and less degrees of freedom for every single molecule. If a structured metal is chosen as surface for the self-assembly, the motion of molecules on the surface is restricted and the adsorption energies are site specific. The Cu(110) surface has a row pattern, as shown in section 6.2, and therewith molecules will preferentially adsorb in between the rows or on top of the rows. Previous investigations have shown that carboxylic acids chemically bind with both oxygen atoms to two copper atoms on top of one row [51,68,90]. In the case of carboxylic acids with a π-conjugated ring system, like benzenecarboxylic acid, a further orientation of the system is given through the intermolecular interactions during self-assembly such that all molecules are oriented in the same direction. In the ideal case, the surface is covered with close-packed molecular rows without domain boundaries. Depending on the substituents of the carboxylic acid this homogeneous layer can act as part of an electronic device due to the different transport paths through the molecules perpendicular to the aromatic ring plane or through the backbone of the molecule. Choosing simple carboxylic acids for the layer it can act as matrix for the insertion of functional molecules, e.g., redox-active molecules, which can be precisely addressed.

Till now, only few structure investigations are done on close-packed carboxylate molecules on the Cu(110) surfaces and this chapter will give insights into the electronic transport properties for the first time. A series of carboxylic acids was investigated by distance dependent current-voltage spectroscopy and current-distance

spectroscopy. The results will be interpreted in view of electronic transport properties and will be compared to data from literature on comparable systems, e.g., π-conjugated thiols on Au(111) [27]. Additionally, the experimental results will be compared to *ab initio* calculations based on DFT, as roughly described in chapter 4. This theoretical work was done by N. Atodiresei and V. Caciuc at the Institute for Advanced Simulation (Quantum Theory of Materials) at the Forschungszentrum Jülich GmbH. Previous work on the structure of benzenecarboxylic acids on Cu(110) [21] has shown that these precise theoretic calculations help to explain experimental data and allow a further understanding of the system. Note that all investigated molecules chemically bind with the carboxylate group to the copper surface and that for clarity the molecules are named with their short names even when they are adsorbed.

7.1 Investigation path

In order to study the structure of and the electronic transport through the carboxylate/Cu(110) interface investigations are focused on a stepped substitution process. Starting point is benzenecarboxylic acid C_6H_5COOH (BCA, trivial name: benzoic acid), the simplest carboxylic acid (R-COOH) with an aromatic ring system. It serves as reference system for the investigation of the self-assembly behavior and the electronic transport properties (experimentally and theoretically). In a first step, the influence of an additional side group substituted in para position of the BCA molecule is studied. Exchanging the hydrogen atom with a second functional group increases the possibilities of the molecule to interact with other molecules. Especially groups which are suitable to create chemically functionalized surfaces or which exhibit extreme dipole moments are of interest. The influence of such an additional functional group is investigated here by the substitution of the hydrogen atom through a carboxylic group (COOH), resulting in benzene-1,4-dicarboxylic acid $C_6H_4(COOH)_2$ (BDCA, trivial name: terephthalic acid). On one hand, these molecules should adsorb on the Cu(110) surface in comparable geometries to BCA due to their common anchoring group and common aromatic ring structure. On the other hand, the electron density of the aromatic ring will be influenced systematically by the electron pushing or electron withdrawing properties of the substituents. In this way, the influence of the electron density of the aromatic ring system, resulting in an altered π-π interaction of neighboring molecules

and altered molecule substrate interactions, can be studied and the differences in the electron transport properties of the molecular layer can be characterized with only minor influence of the molecular geometry. In a further step, carboxylic acids with an aromatic ring structure are investigated where successively heteroatoms will be included. These structures provide the possibility to influence the electron density directly without any obvious geometrical influence. In this thesis nitrogen will be presented as possible heteroatom candidate. Exchanging one CH group of the aromatic ring with one nitrogen atom results in pyridinecarboxylic acid (PCA, C_5H_4NCOOH). Here a differentiation between insertion in ortho, meta or para position is necessary because a change of the electron density with distance dependence is expected. In a final step, both substitutions can be combined with the investigation of molecules like pyridine-2,5-dicarboxylic acid (PDCAH, $C_5H_3N(COOH)_2$), including a nitrogen heteroatom inserted in the aromatic ring and an additional carboxylic head group.

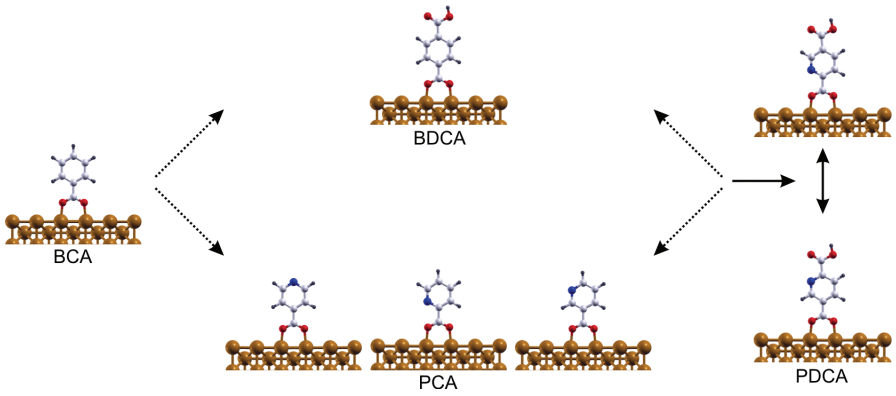

Figure 7.1: Progression of molecular investigations illustrated by a ball-and-stick model. Starting point is benzenecarboxylic acid (BCA) chemisorbed on the Cu(110) surface. This molecule is further functionalized by substituting a H atom through a COOH group, results in benzene-1,4-dicarboxylic acid (BDCA) whereas a substituting of a CH group through a N atom leads to meta-, ortho- or para-pyridinecarboxylic acid (PCA). Finally both substitutions can be combined, ending with pyridinedicarboxylic acid (PDCA), which can be adsorbed in two conformations onto the Cu surface.

Within this chapter a detailed description will be given for all molecules under investigation. This includes information about the preparation conditions, about topographical investigations, spectroscopic investigations and a comparison with theoretical data. Figure 7.1 shows the substitution steps under investigation:

starting with benzenecarboxylic acid (BCA), coming to benzene-1,4-dicarboxylic acid (BDCA) and pyridinecarboxylic acid, and ending with pyridinedicarboxylic acid. Additionally, this chapter includes a small paragraph about the possibility to fabricate mixed monolayers, where a small amount of carboxylic acid is embedded into a matrix of a self-assembled monolayer of suitable host-molecules. A proof of concept will be given by inserting pyridinecarboxylic acid into a complete monolayer of benzenecarboxylic acid. Finally, the obtained data will be summarized and compared in a discussion part.

7.2 Experimental details

The Cu(110) single crystal samples were prepared by cycles of repeated Ar^+-sputtering and annealing, following the process described in table 6.1 of section 6.2. Due to the reactive surface of copper, the deposition of molecules was processed immediately after the last annealing step. BCA, BDCA, PCA and PDCA were used as delivered by the commercial supplier, with the purities as listed in table 7.1. All carboxylates were deposited from vapor phase, in-situ, using a demountable and separately pumped home-built, knudsen-type thermal evaporator, as described in paragraph 3.3.1. All molecular species used here are in solid phase at room temperature and pressure. They were used for deposition after several freezing/thawing cycles in vacuum. The deposition parameters depend primarily on the sublimation temperature of the molecules given at a special vapor pressure. In dependence of the molecular species, lowering the pressure (10^{-5} to 10^{-6} mbar) causes normally a sublimation of the molecules in a sufficiently high dose. Otherwise the molecules were heated or cooled to in- or decrease the deposition rate. The deposition times were fitted to the sublimation rates, with the aim to create close-packed monolayer structures on the substrates, and are spread between 15 seconds and 30 minutes. The powder temperatures during sublimation were varied from room temperature (BCA, PCA and PDCA) to approximately 356-363 K for BDCA. Furthermore, the substrate was kept at 423 K during deposition. This allows to exclude any multilayer formation which occur in the case of molecules with an additional functional top group, like BDCA. To increase the molecular order on the substrate the samples were temporarily heated after deposition in an environmental pressure of 10^{-9} mbar to temperatures of around 373 K. The resulting monolayer films were investigated by imaging in constant-current mode and

electronic characterization in spectroscopy mode with UHV-STM. Special care has been taken for the selection of the set point, since benzoate monolayers are easy to disorder by scanning with high voltages or currents. For example, Frederick et al. [120] report a structural change in the c(8×2) structure of BCA molecules above a threshold voltage of 2.9 ± 0.1 V (at 1.0 nA), or above a threshold current of > 0.5 nA (at 3.0 V).

Molecule	**Supplier**	**Purity**
BCA	Sigma-Aldrich	99 %
BDCA	Sigma-Aldrich	99 %
PCA	Merck	98 %
PDCA	Sigma-Aldrich	98 %

Table 7.1: Carboxylic acids in use: supplier and purity.

The mixed monolayers were prepared by insertion of pyridine-2-carboxylic acid into a dense monolayer of benzenecarboxylic acid. In a first step, benzenecarboxylic acid was deposited from vapor phase on freshly cleaned Cu(110) substrates. The powder temperature during sublimation was RT, the substrate temperature around 423 K at a pressure of $2 \cdot 10^{-5}$ mbar. In this manner the Cu(110) surface was saturated with a monolayer of molecules in 15 minutes. The samples were immediately transferred through the vacuum system and characterized by STM. In a second step, the samples were transferred back into the deposition chamber and pyridine-2-carboxylic acid was deposited. An exposure time of 20 min was chosen for these experiments with the powder at room temperature, the substrate at 423 K and a background pressure of $3 \cdot 10^{-5}$ mbar. Finally, the resulting samples were characterized by STM again.
Additionally, UV-VIS adsorption measurements were done on the carboxylates dissolved in DMF (respectively ethanol, or H_2O) as millimolar solutions.

7.3 Benzenecarboxylic acid

Benzenecarboxylic acid (BCA) as simplest carboxylate with an aromatic ring unit is starting point for the experimental investigations. The structure of BCA was investigated in great detail and compared to structure data available from literature (see paragraph 5.4.2). Thus, BCA can be used as reference system for

all further investigations on carboxylic acid molecules on Cu(110) surfaces. The structural investigations will be briefly presented here. Furthermore, electronic investigations on BCA on Cu(110) have been performed for the first time and electronic characterizations in terms of the tunneling mechanism, the LDOS, and the HOMO-LUMO gap will be presented here.

7.3.1 The structure of benzenecarboxylic acid SAMs

The dominant phase for Cu(110) surfaces saturated with BCA molecules is the c(8 × 2) structure. Figure 7.2(a) shows a STM topography scan of a typical surface coverage after BCA deposition.

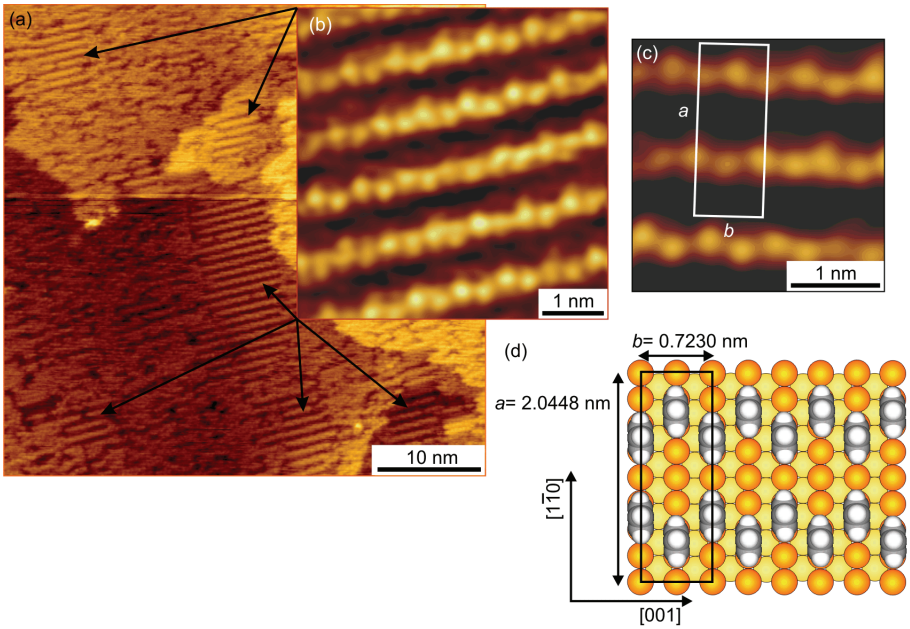

Figure 7.2: STM topography scans of BCA on Cu(110), showing the typical surface structure after deposition (a), the c(8 × 2) domain structure (b), and the unit cell in molecular resolution (c). The schematic, in part (d), illustrates the position of the BCA molecules in the c(8 × 2) structure with respect to the underlying copper substrate. The orange balls correspond to the first copper layer and the brighter yellow ones to the second layer.

The surface is homogeneously covered with molecules and domains with c(8 × 2) structure are visible (Fig. 7.2(b)). For this structure both oxygen atoms of the carboxylate group are chemisorbed on short bridge sites of the outermost copper layer, forming rows in [001]-direction of the substrate. The phenyl rings of the molecules are arranged in the same plane as the carboxylate moiety, perpendicular to the surface. High resolution scans ($2.8 \times 2.8\,\mathrm{nm}^2$, $I_{Set} = 0.46\,\mathrm{nA}, V_{Set} = 0.36\,\mathrm{V}$), like in Fig. 7.2(c), show the domain structure in molecular resolution. The bright stripes seen in the images are parallel to the [001]-direction, have a slight zigzag nature and neighboring stripes have an antiphase relationship with respect to the zigzag. The unit cell parameters are measured to $a = 2.04 \pm 0.20\,\mathrm{nm}$ and $b = 0.72 \pm 0.07\,\mathrm{nm}$, consistent with the data reported in literature [51, 68]. This unit cell represents a packing density of one benzoate molecule per four outermost copper surface atoms (θ=0.25 ML). The unit cell is marked in the high resolution scan of Fig. 7.2(c) as well as in the schematic model of the benzoates on the underlying copper lattice (d).

In the following, this close-packed c(8 × 2) structure of BCA is used to study the electron properties of the BCA/copper interface.

7.3.2 Current vs. voltage spectroscopy

The electronic properties of benzenecarboxylic acid monolayers on Cu(110) surfaces were studied by current-voltage (I-V) spectroscopy and extended by DFT based calculation results. This offers information concerning the electronic structure of the carboxylate/copper interface as well as information about the tunnel mechanism and the LDOS of the combined molecule/substrate system.

An I-V characteristic of a SAM of BCA molecules on Cu(110) is shown in Fig. 7.3. It was measured by positioning the STM tip (W) above a molecular feature and controlling the tip-sample distance by the set point parameters (I_{Set}, V_{Set}), as described in paragraph 3.3.2. Leaving one of these two parameters constant and changing the other one changes the vertical distance between tip and sample. This offers no absolute value for the distance but a tendency and as discussed later the curve shape displays the position of the tip above the sample. In principle, it is possible to convert these set points to absolute values with the help of current-distance (I-z) spectroscopy measurements, but this procedure is very complex, error-prone, and not realizable for all molecule/substrate systems.

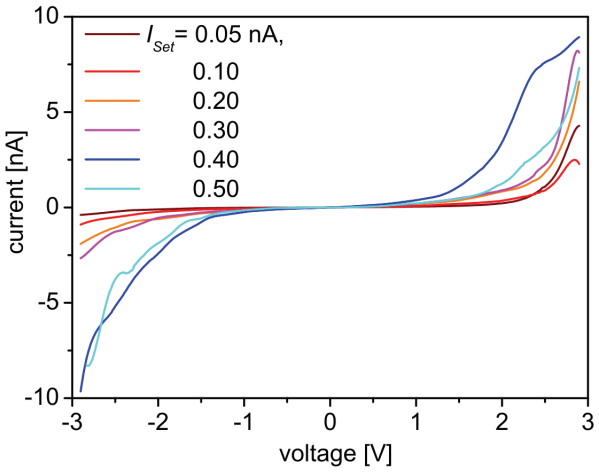

Figure 7.3: I-V characteristic of benzenecarboxylic acid (BCA) molecules chemically bonded to the Cu(110) surface, as topographically imaged in Fig. 7.2(c). The curves were measured at one set point voltage of $V_{Set} = 1.0\,\mathrm{V}$ but at different set point currents ($I_{Set} = 0.05$ to $0.5\,\mathrm{nA}$).

Displayed here are the average curves for six different current set points, $I_{Set} = 0.05\,\mathrm{nA}$ to $I_{Set} = 0.5\,\mathrm{nA}$, recorded with a voltage set point of $V_{Set} = 1.0\,\mathrm{V}$ (Fig. 7.3). All curves are highly reproducible, reflecting the strong binding of the benzoate molecules to the copper surface. At currents higher than 0.6 nA unstable current-voltage curves were observed, allegeable with the destruction of the molecular layer through a mechanical contact between tip and molecules. The voltage window for the I-V measurements of BCA on Cu(110) was found to be $V_{Sweep} = \pm 3\,\mathrm{V}$. Outside these margins a field-induced breakdown of the Cu/BCA/W junction takes place, changing the molecular layer irreversibly.

7.3.2.1 Combining experiment and theory: LDOS investigations

One main point which describes the carboxylate/copper system, in terms of electron transport through a junction, is the electronic structure of the molecule/surface interface near the Fermi level. Whereas the surface of a metal is characterized by reactive electron energy levels that are corresponding to the surface states, the molecule is characterized by discrete energy levels in which the most reactive orbitals are the highest occupied molecular orbitals (HOMOs) and the lowest un-

occupied molecular orbitals (LUMOs). The bonding between the molecule and the surface involves the interaction of these reactive molecular orbitals with the surface states of the metal and results in new bonding and antibonding molecular orbitals of the combined molecule/surface system. Figure 7.4 shows a schematic of the hybridization of the molecular orbitals with the Cu *d*-bands. The hybridization leads to a splitting of the molecular orbitals into sub-bands with bonding and antibonding character [21].

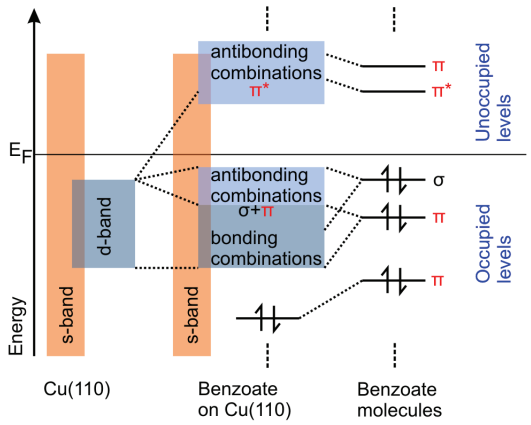

Figure 7.4: Schematic of the hybridization of the molecular orbitals with the Cu *d*-bands. The hybridization leads to a splitting of the molecular orbitals into two sub-bands with bonding and antibonding character.

The precise energetic alignment of these new molecular orbitals with respect to the Fermi level of the substrate, i.e., the local density of states (LDOS), is experimentally accessible through the derivative of the current measured in I-V spectroscopy, as described in paragraph 3.1.2. Peaks appearing in the dI/dV vs. V plot, in the so called "spectroscopy plot", monitor the energetic positions of the molecular orbitals. The dI/dV data are calculated numerically from the measured I-V curves. Sometimes a normalization of the differential conductivity $(dI/dV)/(I/V)$ is advisable for an appropriate evaluation of the tunneling spectra, especially when large voltage ranges are covered. In this case small features in the differential conductivity dI/dV can become invisible due to the large increase in the dI/dV itself. On the other hand, not only the peak visibility but also the peak position can be strongly influenced by the normalization procedure [121]. Thus, all spec-

troscopy plots were calculated as dI/dV vs. the applied bias voltage V and as $(dI/dV)/(I/V)$ vs. V, respectively. Hence there are no additional peaks visible in the spectra but a strong overestimation and shift of peaks around $V = 0$ and there is no physical meaning behind the normalization only dI/dV vs. V plots are shown here.

Figure 7.5 shows the spectroscopy plot for BCA molecules chemically adsorbed on a Cu(110) surface calculated from the measured I-V data, displayed and described in the previous paragraph (compare Fig. 7.3). With decreasing tip-sample distance the electric field strength is increased, the voltage drop over the vacuum gap gets smaller and the molecular orbitals were indeed probed. The distinguished peaks of the dI/dV spectrum can be assigned to an orbital mediated tunneling (OMT) through the HOMO and LUMO states of the molecule. Starting from a set point current of $I_{Set} = 0.3\,\mathrm{nA}$ and going to $I_{Set} = 0.5\,\mathrm{nA}$, an accretion of defined peaks in the dI/dV spectra can be monitored.

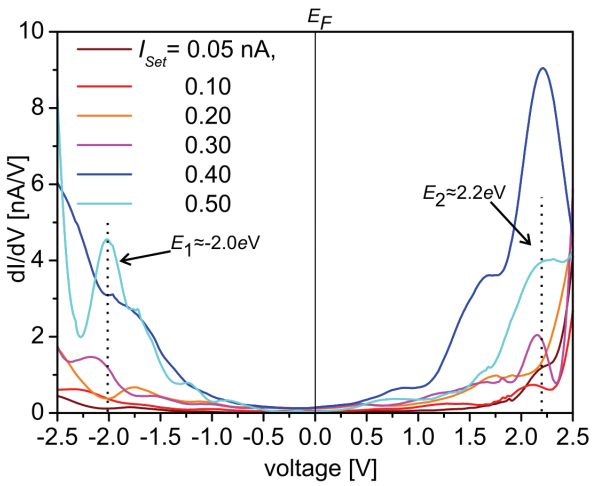

Figure 7.5: dI/dV characteristic of benzenecarboxylic acid (BCA) molecules chemically bonded to the Cu(110) surface calculated from the measured I-V data, imaged in Fig. 7.3. The curves were measured at one set point voltage of $V_{Set} = 1.0\,\mathrm{V}$ but different set point currents ($I_{Set} = 0.05$ to $0.5\,\mathrm{nA}$). Highlighted are the two detectable peaks corresponding to an occupied (E_1) and an unoccupied (E_2) molecular orbital energy.

Two pronounced peaks appear in the dI/dV curves, one at a negative sample bias voltage of around $V_1 = -2.0\,\mathrm{V}$ and one at a positive sample bias voltage of around $V_2 = 2.2\,\mathrm{V}$. Assigning the appearing peak at negative voltage to the first occu-

pied molecular orbital (energy E_1) below the Fermi energy (E_F) and the peak at positive voltage to the first unoccupied molecular orbital (energy E_2) above E_F, these two orbitals define the HOMO-LUMO gap of the BCA/Cu(110) system. The energy gap can be calculated to $\Delta E_{STM} = 4.2\,e\mathrm{V}$.
Theoretically angular-momentum resolved local density of states calculations offer a picture consistent with the experimental dI/dV obtained for adsorbed benzoate molecules on Cu(110). Note that the calculated local density of states (LDOSs) at the molecular side will be used to define the molecular orbitals (MOs) of the combined system consisting of the molecule adsorbed on the Cu(110) surface. The theoretical LDOS can then be decomposed into σ- and π-like contributions, where a σ molecular orbital represents the contributions p_x and p_y in the molecular plane while a π MO originates from the p_z-like orbitals perpendicular to the molecular plane. Furthermore, calculations have shown that apart from a slight broadening of the energetic levels no changes appear in the LDOS characteristics when going from single molecules to a BCA molecular layer. Thus, the LDOS of the single molecules adsorbed on the Cu(110) are taken for interpretation.
The LDOS calculated for the adsorbed BCA on Cu(110) by DFT can be directly compared to the experimental dI/dV curves, as shown in Fig. 7.6(a). A remarkable conformity exists between the measured dI/dV and the calculated LDOS data. Both measured peaks appear in the calculated LDOS data at nearly the same energy. Furthermore, the calculations identify both orbitals as π-type MOs, denoted as occupied MO π_1 and unoccupied MO π_1^*. Beside these two main features, a third σ-type peak with low intensity is visible in the calculated spectrum between -1.0 and $-1.25\,e\mathrm{V}$. Plotting the spatial distribution of the charge density in a specific energy range associated with the molecular DOS (Fig. 7.6(b)) points out that this σ-type orbital is located at the molecule/substrate interface and thus represents the bonding part of the mixed molecule-surface states. The location of this orbital near the surface plane and not wide in space above the surface, as for instance π_1 and π_1^*, explains why it is not clearly detected in experiment (it can be suspected in the curve for $I_{Set} = 0.5\,\mathrm{nA}$). A very small tip-sample distance is needed to detect this localized orbital equivalent with an immersion of the tip into the molecular layer and a destruction of the layer. However, probing this molecular orbital would monitor only the character of the chemical bonding between molecule and substrate and this bond is equal for all investigated molecule. Since investigations are focused on the change of electronic properties caused be a substitution of atoms and functional groups this σ-type orbital is excluded from

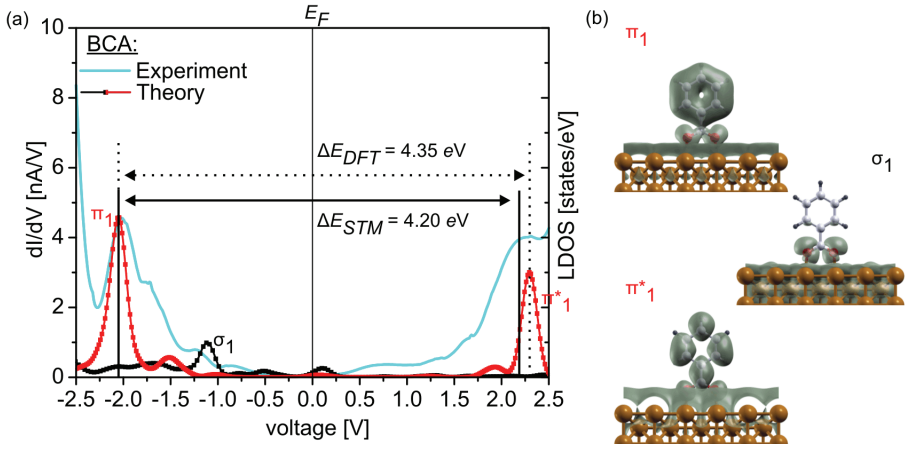

Figure 7.6: (a) Calculated LDOS of a BCA molecule chemically bonded to the Cu(110) surface. The red line represents the contributions of the states with a π-type character, while the black line represents the states with a σ-type character. Additionally shown is the experimental dI/dV spectrum (cyan) acquired over a BCA molecule on Cu(110) at a set point of $V_{Set} = 1.0\,\mathrm{V}$ and $I_{Set} = 0.5\,\mathrm{nA}$. Theoretical and experimental data show a high conformity and the energy gaps between HOMO and LUMO orbitals are nearly identical. (b) Charge density plots of the electronic states of BCA in a specific energy range corresponding to the LDOS depicted in (a). Remarkable here are the different extensions of the molecular orbitals.

the definition of the HOMO-LUMO gap in the following. With this definition, the experimentally detected orbitals are indeed related to HOMO and LUMO. The HOMO-LUMO gap can be calculated to $\Delta E_{DFT} = 4.35\,e\mathrm{V}$ which is in close agreement with the experimental data.

7.3.2.2 I-V curves: a mirror image of the gap symmetry

Another key quantity to evaluate the magnitude of the charge transfer between an adsorbate and a substrate is the junction geometry. The ratios inside the STM junction, consisting of the substrate/molecule interface, the molecule, and the molecule/tip interface (often including a vacuum gap), influence the charge transfer in several ways. For example, the geometrical length of the vacuum gap can cause a change from molecule mediated tunneling to vacuum barrier tunneling. Not only the geometrical ratios but also interaction strengths or dipole fields influence the charge transfer. Some of these influences will be probed by changing

the distance between molecule and tip in distance dependent current-voltage spectroscopy. Concerning this, a closer look onto the experimental I-V data provides information.

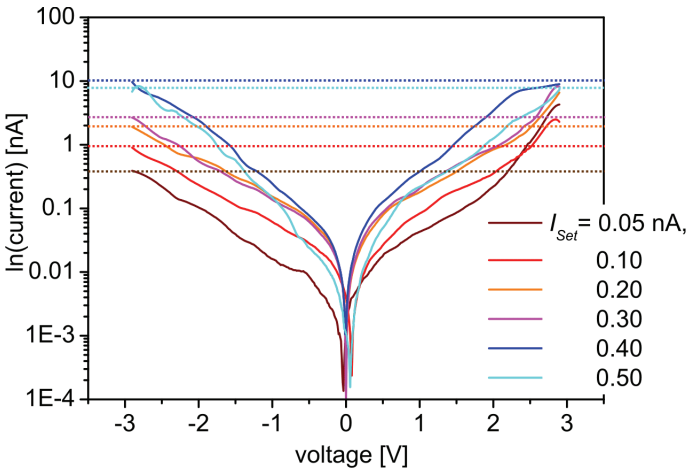

Figure 7.7: I-V characteristic of benzenecarboxylic acid (BCA) molecules chemically bonded to the Cu(110) surface, as shown in Fig. 7.3, but plotted on a semi logarithmic scale. Horizontal dashed lines highlight here that curves taken at small set point currents show a steeper slope at positive bias voltages whereas curves with higher set point current are symmetric.

A comparison of the different I-V curves (Fig. 7.3) shows that the current and therewith the conductance increases with increasing set point current. This increase in current with increasing I_{Set} can generally be explained by the constriction of the vacuum gap between tip and molecule. With increasing current, i.e., decreasing of the distance, the vacuum gap gets smaller and the system gets more conducting.

Furthermore, the I-V curves for low current set points show an asymmetric shape comparing positive and negative voltage whereas the curves for higher current set points show a symmetric shape. This behavior gets much clearer when the current-voltage characteristic of Fig. 7.3 is plotted on a semi logarithmic scale (see Fig. 7.7). Curves taken at small set point currents (large tip-sample distance) show a steeper slope at positive bias voltages than at negative ones. This asymmetry is often explained only by the asymmetry of the metal/molecule/metal junction in STM setups. Therefore, depending on the polarity of the voltage, the

electrons have to tunnel through potential barriers of different heights. In the case of STM junctions the molecule is coupled to the metallic substrate by strong interactions whereas the top of the molecule is only weakly coupled to the tip. Thus, the current should be much smaller for positive substrate voltage (conduction through LUMO) than for negative substrate voltages (conductance through the HOMO) [27].
However, all I-V curves taken with the tip far from the sample show an inverse behavior, the current is higher in the positive bias regime. In addition, I-V curves with smaller tip-sample distances show symmetric I-V characteristics for the Cu(110)/BCA system. This behavior is related to the special potential differences inside the gap. The above mentioned explanation is based on the assumption that the electrochemical potential μ_1 of the sample is fixed with respect to the molecule. If this is the case, the hole potential drops at the molecule vacuum interface. The factor η which describes how the electrostatic potential difference is divided between the two contacts (metal/molecule and molecule/tip) is thereby zero [27]. In detail η is defined as

$$\eta = \frac{d + \frac{1}{2}l}{z} \quad with\ z = d + l + s. \tag{7.1}$$

with d the bond length, l the molecule length and s the vacuum gap size. In the case of a Cu/BCA/W junction the potential barrier profile will depend on both metal/molecule interfaces and the potential is expected to drop not only at the vacuum interface. Figure 7.8 shows the change in the electronic structure of a metal and a molecule when a junction is formed between them. The energy levels of a molecule and a metal are aligned at the vacuum level with energy $E_{vac}(\infty)$, when the separation between them is large (a). When metal and molecule come into contact without rearrangement of the electric charge, the molecule is in the potential of the surface dipole of the metal, and its energy levels are raised to have a common vacuum level in an extremely narrow interfacial gap (b). The vacuum energy level in this region is denoted as E_{vac}.

Matching these general plots with the two interfaces in the junction shows that the difference between them is located at the point where the potential wells of metal and molecule merge (marked with a red circle in Fig. 7.8(b)). In the case of the BCA/W interface the barrier profile is characterized by the vacuum gap between metal and surface and only weak interactions. The space between molecule

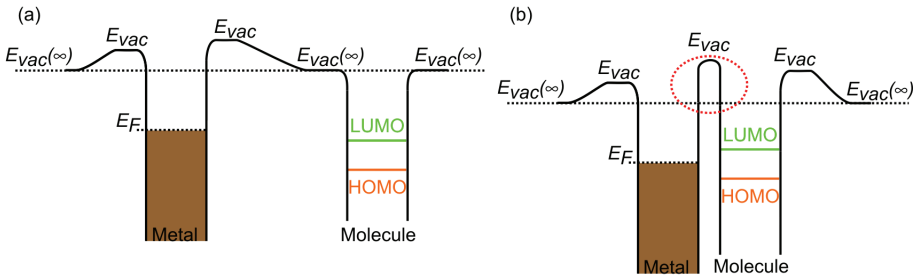

Figure 7.8: (a) Electronic structure of a metal and organic molecule at infinite distance. (b) Contact of a metal thin film and an organic molecule. The molecule is within the electric field of the surface dipole layer of the metal, and the interfacial vacuum level is common. When metal and molecule come into real contact, the actual potential well (area highlighted by the red circle) can be lowered, heightened, or can get asymmetric. Images according to [122].

and metal allows an alignment of the potential wells of metal and molecule over the gap region and the potential wells become a flat plateau. At the Cu/BCA interface the profile will depend strongly on the charge of the adsorbed molecule, which in turn depends on the interaction between the molecule and the substrate. If at least part of the electronic charge of the molecules is retained on deprotonation, the adsorbed molecule will be negatively charged, creating an intrinsic dipole. There is a net electronic charge transfer to the molecule which up-shifts the vacuum level by introducing a dipole-induced potential step at the interface. Given that the chemisorption implies a close proximity between the metal and the organic molecules, the "push-back" effect also plays a role and will down-shift the vacuum level by decreasing the metal-surface dipole potential energy [123]. The overall change in metal work function at the interface that is the shift in vacuum level Δ, is thus the sum of these two contributions. For the Cu/BCA interface an increase in the tunneling barrier with respect to the bare Cu(110) surface will be expected. Calculations of Δ using DFT indeed show an increase of the local work function of $\Delta = 0.47\,eV$ [21] for the Cu/BCA interface. An increase of the work function at the bond is reported in literature [124] for the comparable bonding system of a single carboxylate (4-[*trans*-2(pyrid-4-yl-viny)] carboxylic acid) chemically bonded to a Cu(111) surface. Combining these two interfaces leads to a junction as sketched in Fig. 7.9.

On the BCA/W interface the potential barrier profile is characterized by the vacuum gap size s. If the gap size is large, i.e., the set point current is low, the

main part of the potential drops over this vacuum barrier and this interface will dominate the potential barrier profile of the whole junction. This would be equal to the above mentioned case of $\eta = 0$. On the other junction side, the potential barrier of the permanent dipole moment, sketched in the lower part of Fig. 7.9(a), characterizes the potential profile. It leads to a smaller charge transfer from the surface to the organic/metallic interface [122, 123], which is located mostly at the carboxylate moiety. This additional barrier leads to a shift of the threshold for the orbital mediated tunneling through the HOMO to a more negative voltage, the value η is now unequal zero.

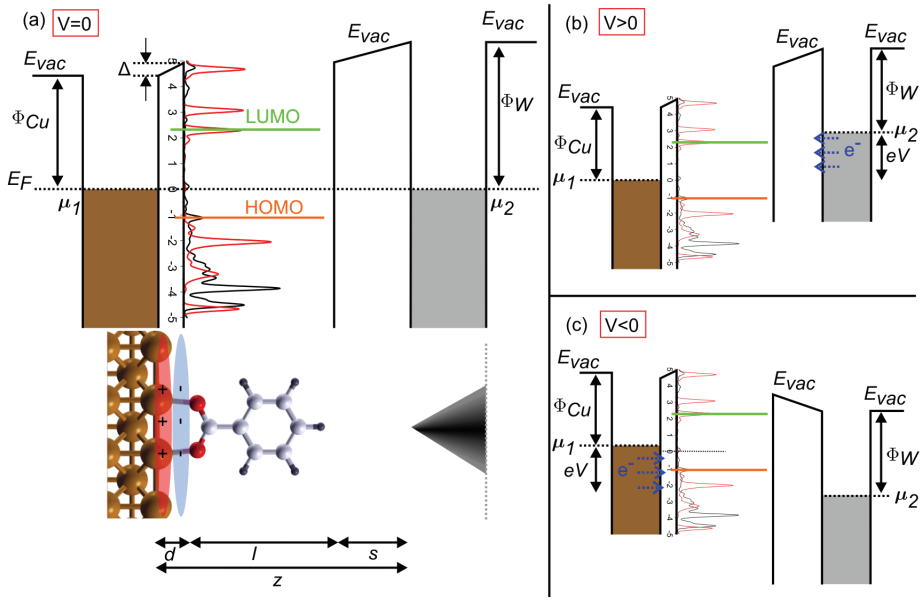

Figure 7.9: (a) Interfacial energy diagram of the Cu/BCA/W junction with a shift E_{Vac} at the sample/molecule interface due to the dipole layer formation. In this junction, the organic side is charged negative, making the side less comfortable for an electron, and making the sign of Δ positive. The molecule/tip interface has no energy shift because of the vacuum gap contact. Φ_{Cu} and Φ_W are the work functions, μ_1 and μ_2 the chemical potentials of the electrodes. Additionally labeled are the different length (d, l, s and z) in the junction. (b) Energy diagram for the same junction with an additional applied positive bias voltage ($V > 0$). Electrons tunnel from the tip into empty states of the sample in the energy range between μ_2 and $\mu_1 = \mu_2 + eV$. (c) At negative bias voltages ($V < 0$) the electrons tunnel from the occupied states of the sample towards the tip.

If a voltage is applied at the junction, the conductance through HOMO is inhibited by the dipole moment whereas the conduction through LUMO is not affected (compare Fig. 7.9(b,c)). With decreasing vacuum gap sizes the voltage drop over the vacuum gap gets smaller and the dipole barrier gains influence, η gets larger. The vacuum barrier between tip and molecule is the current limiting barrier, and thus the current rises more steeply and finally reaches a higher value in the case of a smaller vacuum gap size s. When the potential drop at both interfaces gets the same the potential barrier profile becomes symmetric ($\eta = 0.5$). This effect is visible in the I-V characteristics of Fig. 7.7 at around $I_{Set} = 0.4\,\mathrm{nA}$.

The situation inside the gap can be roughly estimated by a model where neither μ_1 (sample) nor μ_2 (tip) remain fixed with respect to the sample and η is unequal to zero. The molecule then conducts strongly when either μ_1 or μ_2 coincides with a molecular orbital energy so that the threshold for conduction is given by

$$eV > \min\left(\frac{E_F - E_{HOMO}}{\eta}, \frac{E_{LUMO} - E_F}{1-\eta}\right) \tag{7.2}$$

(positve substrate voltage)

or

$$eV > \min\left(\frac{E_F - E_{HOMO}}{1-\eta}, \frac{E_{LUMO} - E_F}{\eta}\right), \tag{7.3}$$

(negative substrate voltage)

where min(x,y) denotes the smaller quantities of x and y. An estimation of the value η can be made with the known Cu/BCA/W junction geometries. The bond length between copper and the BCA molecule is $d = 0.194\,\mathrm{nm}$ as detected by [21, 125], the molecular length is around $l = 0.599\,\mathrm{nm}$ (similar to [126]) plus a typical vacuum gap length above the molecule of s and a tip-sample distance z allows to calculate η to

$$\eta = \frac{d + \frac{1}{2}l}{z} = \frac{0.494\,\mathrm{nm}}{0.793\,\mathrm{nm} + s}. \tag{7.4}$$

Thus, η is directly related to the vacuum gap size s. The molecule orbital energies for BCA adsorbed on Cu(110) were found in paragraph 7.3.2.1 to

$$E_F - E_{HOMO} = 2.0e\mathrm{V} \text{ and } \quad E_{LUMO} - E_F = 2.2e\mathrm{V} \tag{7.5}$$

for high current set points. Calculating this conduction threshold for various vacuum gap sizes s shows that with $\eta \approx 0.49$, i.e., $s = 0.20\,\mathrm{nm}$, the molecules could conduct through HOMO for both bias polarities, leading to the observed symmetric I-V curves. This is in accordance with the data for α,α'-xylyl dithiol on Au(111) which has a comparable molecule geometry with its π-conjugated ring system [27].
Furthermore, this calculation allows to make an estimation of the absolute value for the gap sizes measured in STS. A symmetric I-V profile is expected at a vacuum gap size of $s = 0.20\,\mathrm{nm}$ and seen in the I-V curves at $I_{Set} = 0.4\,\mathrm{nA}$, resulting in

$$z = d + l + s \approx 0.99\,\mathrm{nm} \sim I_{Set} = 0.4\,\mathrm{nA}. \tag{7.6}$$

Every I-V curve shows a region of linear increase around the Fermi level and a sharp rise in current above certain threshold voltages within the negative and the positive bias regime. The onset of this exponential decay is dependent on the current set point and starts at lower voltages for higher current set points. This first linear and above a certain threshold voltage exponential behavior of the current monitors different tunneling regimes. As described in chapter 2, the linear behavior around the Fermi level is related to direct tunneling below the lowest energy level of the molecule and can be described by the Simmons equation (compare section 2.3). If the applied voltage is large enough to shift the Fermi levels of the metal electrodes (tip and substrate) such that a molecular level enters the energy window spanned by the two Fermi levels of the electrodes, the current rises sharply. The tunneling mechanism is now molecule mediated, resonant tunneling and can be explained by a coherent electron transport model as described by Datta et al. [27] (compare section 2.2). With a measured HOMO-LUMO gap energy of $\Delta E_{STM} = 4.2\,e\mathrm{V}$ the likelihood of accessing different transport mechanisms, such as resonant tunneling prior the field-induced device breakdown is given here.

7.3.2.3 Transition voltage spectroscopy

A relatively new, simple and elegant approach to get more detailed information about the tunneling regimes in a metal/molecule/metal junction is the so called "transition voltage spectroscopy" (TVS). The idea behind TVS was found by Beebe et al. [127] and is based on a simple replot of the I-V data in a form that is based on

the physics of field emission. They state that the position of the nearest molecular level in a two-terminal device can be derived from the I-V measurements even if the bias is moderate and resonance is not yet reached. The experimental feasibility of this concept was proven by different research groups in the last two years [128–131] and the physical interpretation was promoted by Huisman et al. [132]. According to the propositions of Beebe et al. [127, 128], plotting $ln(I/V^2)$ versus $1/V$ (the so called "Fowler-Nordheim plot") from the collected I-V data shows an inflection point, consistent with the voltage where a change in tunneling mechanism occurs. Since the magnitude of the voltage required to enact this transition is molecule specific, measurements of the transition voltage constitute a form of spectroscopy and the transition voltage is a variable characterizing the electronic transport properties of the specific molecule/metal system.

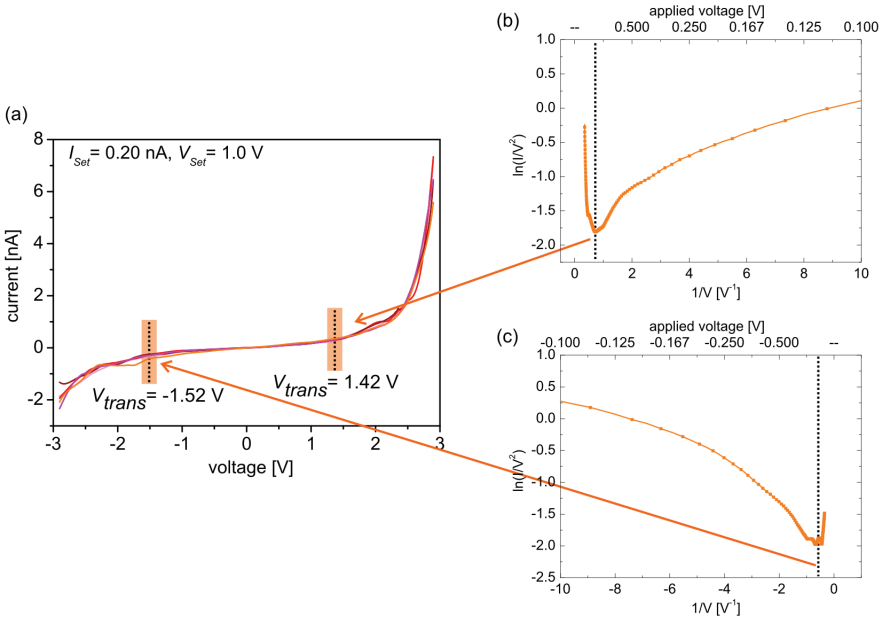

Figure 7.10: (a) Current-voltage data set for BCA on Cu(110), measured at V_{Set} = 1.0 V and I_{Set} = 0.2 nA, plotted on standard axes. The Fowler-Nordheim plot of the averaged I-V data is shown in (b) for the positive and in (c) for the negative bias regime. V_{trans} is determined from the minimum of the Fowler-Nordheim plots, marked with dashed lines.

Exemplary, Fig. 7.10(a) shows the I-V curve shape for a batch of five I-V curves measured on BCA molecules adsorbed on Cu(110), recorded at a set point current of $I_{Set} = 0.2\,\mathrm{nA}$ and voltage of $V_{Set} = 1.0\,\mathrm{V}$. The two curves on the right side of Fig. 7.10 represent the average of the five I-V curves plotted as Fowler-Nordheim plot for positive (b) and negative (c) bias voltage values. The voltage (V_{trans}) required to change the functional dependence of current on the applied voltage is marked with dashed lines in plot (b), (c) and also in (a). Different transition voltage values are commonly found for positive and negative bias voltages because the asymmetric voltage drops at the two metal/molecule interfaces cause the transition voltage to be dependent on bias polarity. For the Cu/BCA/W junction ($I_{Set} = 0.2\,\mathrm{nA}$, $V_{Set} = 1.0\,\mathrm{V}$) the transition in mechanism occurs at $V_{trans} = -1.52\,\mathrm{V}$ and at $V_{trans} = 1.42\,\mathrm{V}$. The transition voltages for the complete current-voltage data set measured are listed in table 7.2. Listed in every column is the averaged value of around five I-V curves collected at one set point current I_{Set}. Whereas there is no variation in the values for one set point current the values differ for different I_{Set}.

I_{Set}	0.10 nA	0.20 nA	0.30 nA	0.40 nA	0.50 nA
V_{trans}(neg) [V]	-1.46	-1.52	-1.47	-0.91	-0.66
V_{trans}(pos) [V]	1.36	1.42	1.25	1.19	1.34

Table 7.2: Compilation of the calculated V_{trans} values for all measured I-V curves. Listed in every column is the averaged value of around five I-V curves collected at one set point current I_{Set}.

But not only the values differ between the different current set points, also the transition occurs for $I_{Set} = 0.1$ to $0.3\,\mathrm{nA}$ first at positive bias voltage values and at $I_{Set} = 0.4$ and $0.5\,\mathrm{nA}$ first at negative bias polarities. This behavior is in accordance with the results of the last paragraphs, taking into account that the transition voltage V_{trans} is here proportional to the barrier height [127, 132]. For large distances the π_1-orbital is detected as HOMO. Thus, the absolute value for HOMO mediated tunneling is larger than the one for LUMO mediated tunneling. Between 0.3 and 0.4 nA the system gets symmetric and HOMO and LUMO mediated tunneling occurs at the same value. At a small tip-sample distance (0.5 nA) the transition energy is lower for occupied states, reflecting that the σ_1-orbital is now probed at lower energies than the π_1-orbital.

Taking the above mentioned small HOMO-LUMO gap size of $\Delta E_{STM} = 4.2\,eV$ and the barrier profile as sketched in Fig. 7.9 into account, the change in mechanism monitored here through the transition voltage for the Cu/BCA/W junction is a change from direct tunneling to resonant tunneling.

7.3.2.4 UV-VIS spectroscopy: cross-checking STS data

Finally, the STM measured energetic gap can be compared to gap sizes resulting from other spectroscopic techniques such as adsorption spectroscopy [133]. Figure 7.11 shows the UV-VIS adsorption spectrum of BCA in ethanol ($c = 1{\cdot}10^{-3}$ mol/l). The optical gap can be derived from the onset of the energetically lowest adsorption band with a value of $\Delta E_{opt} \sim 4.2\,eV$. This is the lowest neutral excitation, i.e., transition of an electron from the HOMO to the LUMO of the molecule. To compare both STM and UV-VIS gap sizes an exciton binding energy E_B has to be added to the optical gap, typical values for this are between $E_B = 0.1$ and $1.5\,eV$ [134], and the influence of the chemical adsorption of the molecule on the surface has to be taken into account. Comparing ΔE_{STM} and ΔE_{opt} here shows that there is only a very small exciton binding energy and that isolated an bonded BCA molecules have comparable energy gap sizes.

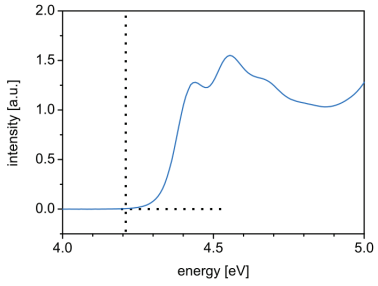

Figure 7.11: Optical absorption spectrum of BCA dissolved in ethanol. The horizontal and vertical dashed lines serve as guide to the eye to help determine the adsorption edge. The onset position of the energetically lowest adsorption band leads to an optical gap of $\Delta E_{opt} \sim 4.2\,eV$ in the liquid phase.

7.4 Benzene-1,4-dicarboxylic acid

Benzene-1,4-dicarboxylic acid (BDCA) is similar to benzenecarboxylic acid but with an additional carboxylic acid moiety in the para position of the phenyl ring. It should adsorb on the Cu(110) surface in comparable geometries as BCA due to their common anchoring group and common aromatic ring structure. On the other side, the electron density of the aromatic ring will be influenced by the electron withdrawing properties of the substituents. Compared to BCA, BDCA is a relative sparse investigated system. Thus, the topographic structure as well as the electronic properties were investigated and will be presented in the following.

7.4.1 The structure of benzene-1,4-dicarboxylic acid SAMs

The topographic structure of benzene-1,4-dicarboxylic acid was investigated by D.S. Martin et al. [135] with RAIRS, LEED, temperature programmed desorption (TPD) and reflection anisotropy spectroscopy (RAS). They found an adsorption behavior of BDCA which is comparable to that of BCA. In common with a number of previous studies on monocarboxylic acids, BDCA adsorbs on the Cu (110) surface as a monocarboxylate following deprotonation of one carboxylic group. At low coverages the molecules adsorb in a flat-lying geometry on the Cu(110) surface. Both carboxylic groups can interact via their oxygen atoms with the copper surface atoms and additionally the phenyl ring can interact with the Cu(110) surface through its extended π-system. At higher surface coverages structures of standing-up molecules were found. The BDCA molecules are bonded to the surface with one deprotonated carboxylic group whereas the other carboxylic group points towards the vacuum interface. The perpendicular orientation observed at higher coverage accompanies with the loss of the π-interaction between the ring and Cu surface but this is easily compensated by the adsorption energy of additional carboxylates, and by increasing intermolecular interactions between upright molecules with increasing coverage. The terephthalate molecules were found to be oriented with the carboxylate bonding along the $[1\bar{1}0]$-direction which implies that the plane of the aromatic ring has to be also aligned along this direction. By a coverage dependent LEED study the first structure of standing molecules was found to be a (10×2) structure. With further increasing coverage no clearly detectable structure was found until with maximum surface coverage a (2×1)

structure was detected. At this high coverage steric constraints require the rotation of the terephthalate ring out of the $[1\bar{1}0]$-direction. A centered structure could be excluded instead of the (10×2) structure but information on the exact number and location of the molecules within the unit cells cannot be given by LEED. With further molecular exposure the molecules build multilayers due to the functional top group of the BDCA molecules. Both the carbonyl (C=O) and the hydoxyl (O-H) part of the carboxylic top group can interact via hydrogen bonds with additional molecules resulting in flat-lying second layer BDCA molecules.

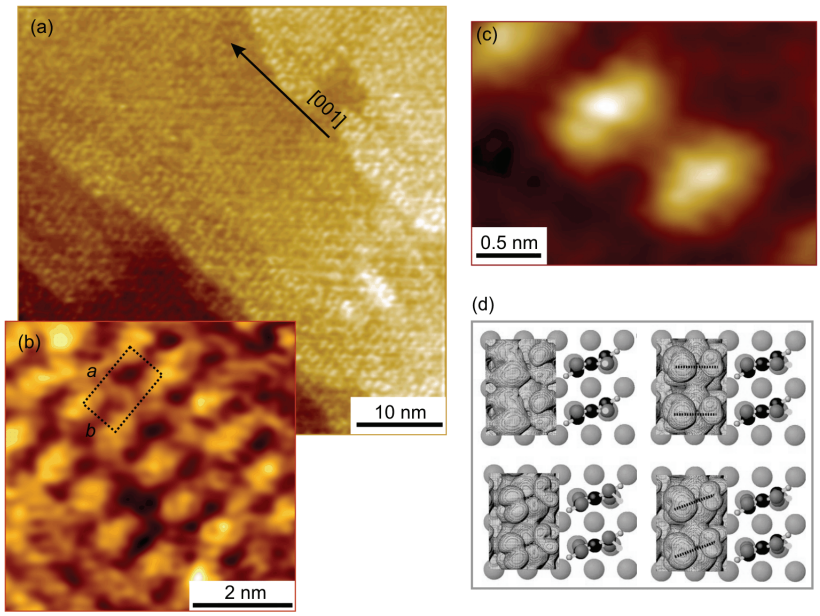

Figure 7.12: STM topography scans of BDCA on Cu(110) showing a direct, row like texture in [001]-direction (a), small bunches with a rectangular unit cell (b), and oval molecular features (c). The high resolution scan of (c) was taken with a set point current of $I_{Set} = 0.1\,\mathrm{nA}$ and an applied bias voltage of $V_{Set} = 1.0\,\mathrm{V}$, comparable with the simulated STM features of (d), which demonstrates that the spots visible in STM have different forms dependent on the submolecular geometric structure.

STM investigations on BDCA point out that it is difficult to prepare an ordered layer on Cu(110). All our investigation show disordered layers with a directed texture or layers with a strong alignment of the molecules in [001] but a defuse

alignment in $[1\bar{1}0]$- direction, as visible in the STM scan of Fig. 7.12(a). BDCA has two carboxylate groups which can in principle react with the copper surface and thus it has the tendency to lie flat on the surface. If with further coverage more molecules are available on the surface and the molecules change their position from flat-lying to standing-up, the additionally coming molecules can either arrange in this order or can adsorb on top of the existing layer due to intermolecular interactions. This causes a large disorder in the resulting film and it can be supposed that only a very slow exposure of molecules at low pressure results in large domain structures of close-packed molecules. Due to the high sublimation point of BDCA and the limited pressure range for sublimation in the experimental setup ($p > 1 \cdot 10^{-7}$ mbar) it was not possible to reach these large domains here and multilayer growth starts before a (2×1) could be formed. Nevertheless, it was possible to deposit the above mentioned layers where batches of close-packed standing-up molecules can be found and no multilayer formation was monitored. These batches have molecular distances ranging between the unit cell vectors of a (10×2) and a (2×1) structure which is in accordance with the diffuse LEED pattern reported by Martin et al. [135]. Figure 7.12(b) shows a STM scan of a batch of ordered molecules with a distance of $a = 1.79 \pm 0.18$ nm and $b = 0.73 \pm 0.07$ nm corresponding to a (6×2) unit cell. High resolution STM scans on these structures (Fig. 7.12(c)) show oval molecular features which indicates that the molecules adsorb with their terephthalate rings parallel to each other in $[1\bar{1}0]$-direction.

Finally, it should be noted here that there is one theoretical work on BDCA on Cu(110) surfaces. Before focusing on the electronic properties of the BDCA molecules, as described in the following, Atodiresei et al. performed *ab initio* pseudopotential calculations in order to elucidate the role of the intermolecular interactions on the two-dimensional order of BDCA on Cu(110) surfaces. Since the chemical functionalization of this surface can be hindered by a hydrogen bond between BDCA molecules, Atodiresei et al. investigated if indeed this scenario takes place. Their calculations show that an adsorbate-substrate geometry with a hydrogen bond between adjacent BDCA molecules is energetically not favorable. Instead, a geometry which exhibits a H-O bond in the carboxylic group plane oriented toward the benzene ring is calculated. The total energy of this adsorption configuration is in the (2×1) structure slightly higher ($\sim 0.08\,e$V) than that with a H-O bond pointing toward the vacuum interface. This small energy dif-

ference opens the possibility that the hydrogen atom can fluctuate between these configurations. Within the experiments (performed at RT) such a small barrier is negligible because the thermal energy is sufficient to overcome this barrier. By calculating the lateral variation of the energy integrated LDOS, they simulated STM images for all BDCA adsorption configurations under consideration and thus provide a connection to experiments. The simulated images exhibit specific features for each case considered, shown in Fig. 7.12(d) for the case of a (2×1) structure scanned at $V_{Set} = 1.0\,\mathrm{V}$. These investigations are a further hint that the additional top group is not fixed even in closer packed structures, leading to different oriented features visible in STM and LEED.

7.4.2 Current vs. voltage spectroscopy

The electronic properties of benzene-1,4-dicarboxylic acid monolayers on Cu(110) surfaces were studied by current-voltage (I-V) spectroscopy and extended by DFT based calculation results.

7.4.2.1 Experimental data

Distant dependent current-voltage spectroscopy was again carried out by positioning the STM tip (W) above a molecular feature and controlling the tip-sample distance by the set point parameters (I_{Set}, V_{Set}), as described in paragraph 3.3.2. All I-V curves were taken on molecules situated inside areas of ordered, close-packed molecules with a structure similar to that displayed in Fig. 7.12(b). Only curves measured on the same structure were averaged. This offers reliable information concerning the electronic structure of the carboxylate/copper interface as well as information about the tunneling mechanism and the LDOS of the combined molecule/substrate system. For the Cu(110)/BDCA system investigated here, the most reliable and reproducible STM data were recorded at positive bias voltages of less than 1.0 V and tunneling current set points of around $I_{Set} = 0.1\,\mathrm{nA}$.
Thus, for STS data acquisition the set point voltage was kept constant at a value of $V_{Set} = 0.77\,\mathrm{V}$ whereas the set point current was varied from $I_{Set} = 0.06$ to $0.46\,\mathrm{nA}$ in steps of $0.1\,\mathrm{nA}$. The voltage window for the I-V measurements of BDCA on Cu(110) was found to be $V_{Sweep} = \pm 2\,\mathrm{V}$ which is smaller than that of BCA. This is not unexpected because the molecular layer of BDCA can be easily

disordered by the electric field between tip and sample due to the additional functional groups of the BDCA molecules which point towards the tip. Within the electric field at low tip-sample distances the tip interacts with the top carboxylic group and can cause structural rearrangements of the monolayer or even lifts the molecule from the surface. However, all measured I-V curves within the voltage range are highly reproducible and the STM topographical scans, taken before and after spectroscopy data collection, remain unchanged, i.e., there is no tip influence on the molecular layer.

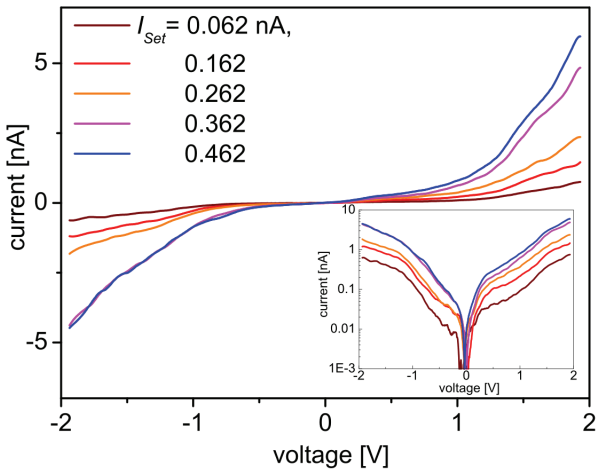

Figure 7.13: I-V characteristics of benzene-1,4-dicarboxylic acid (BDCA) molecules chemically bonded to the Cu(110) surface, as topographically imaged in Fig. 7.12(b). The curves were measured at one set point voltage of $V_{Set} = 0.77\,\mathrm{V}$ but at different set point currents ($I_{Set} = 0.06$ to $0.46\,\mathrm{nA}$). The inset shows the same data but plotted on a semi logarithmic scale, displaying the symmetry of the measured I-V curves comparing positive and negative bias voltage.

Fig. 7.13 shows the I-V characteristics of BDCA molecules on Cu(110). A comparison of the I-V curves collected with different set point currents, i.e., at different tip-sample separations, shows an increase in current with an increasing I_{Set}. This behavior was also monitored for BCA molecules on Cu(110) (compare paragraph 7.3.2.2) and can generally by explained by an increasing gap conductance due to the reduction of the vacuum gap between tip and molecule. Comparing in a second step the curve shapes separately in the negative and in the positive bias

regime shows various different features. The inset of Fig. 7.13 shows, therefore, the I-V data plotted on a semi logarithmic scale. Every single curve has an asymmetry whereas the total conductance at around 2 V is the same. Furthermore, each curve has a flat, linear shape around zero volt and an exponential slope for higher voltages but the onset of the exponential slope is different for negative and positive bias and seems also to be set point dependent. Kinks appear in all curves but it is not possible to find a general tendency in the appearance. All this points to a direct tunneling mechanism for small applied bias voltages and an orbital mediated tunneling mechanism for higher voltages with slightly different orbital contributions at different set points. Investigations of the LDOS, an estimation of the junction size and symmetry as well as TVS will give here further insights.

7.4.2.2 LDOS and the HOMO-LUMO gap

The LDOS of the Cu/BDCA system near the Fermi level, especially the energetic position of the HOMO and LUMO, primarily defines the electron transport through the Cu/BDCA/W junction at small vacuum gap sizes. Thus, the differential conductance dI/dV is numerically calculated from the measured I-V data. Figure 7.14 shows the dI/dV vs. V plot for the BDCA molecules calculated from the data imaged in Fig. 7.13. Starting with the tip far away from the surface, i.e., at the lowest detectable set point current ($I_{Set} = 0.06\,\mathrm{nA}$), the resulting dI/dV curve is flat and no peaks appear in the measured voltage range. The voltage drop over the vacuum gap in the junction is here too large to probe any molecular orbital. Moving the tip closer to the surface ($I_{Set} = 0.16\,\mathrm{nA}$ to $0.36\,\mathrm{nA}$) decreases the vacuum gap size, the voltage drop over the molecule gets larger, and molecular orbital mediated contributions to the electronic transport can be monitored. Two peaks appear in the dI/dV curves and increase in intensity. At $I_{Set} = 0.36\,\mathrm{nA}$ they have a defined shape with a maximum at around $V_1 = -1.2\,\mathrm{V}$ and at around $V_2 = 1.5\,\mathrm{V}$. Due to the direct relation between dI/dV and LDOS the peaks can be allot to an occupied molecular orbital at $E_1 = -1.2\,e\mathrm{V}$ and an unoccupied molecular orbital at $E_2 = 1.5\,e\mathrm{V}$.

Expecting a close similarity between the bonding mediated orbitals of benzenecarboxylic acid and benzene-1,4-dicarboxylic acid, due to the equal bonding group and the benzene ring structure, the peak at an energy of $E_1 = -1.2\,e\mathrm{V}$ could also be related to the bonding carboxylate group as the E_1 peak detected for BCA (compare paragraph 7.3.2.1). Accordingly, this peak should be excluded

in HOMO-LUMO gap calculations of the BDCA/Cu(110) system, and thus no HOMO peak is detected within the experimental voltage window. For unoccupied MOs no state related to this bonding carboxylate group was reported for the BCA molecule and the peak at E_2 is set as experimental LUMO. The HOMO-LUMO gap size can then only be estimated as $\Delta E_{STM} > 3.3\,eV$ from the experimental STS data. There is a remarkable conformity between the measured dI/dV data and the calculated LDOS in the case of the Cu/BCA system, as reported in paragraph 7.3.2.1. If this conformity exists also for the Cu/BDCA system, the HOMO-LUMO gap can be estimated from comparing experimental and theoretical data. Additionally, data from other spectroscopic methods like ultraviolet photoelectron spectroscopy (UPS) and inverse photoelectron spectroscopy (IPS) or UV-VIS spectroscopy can be used for calculating the HOMO-LUMO gap size.

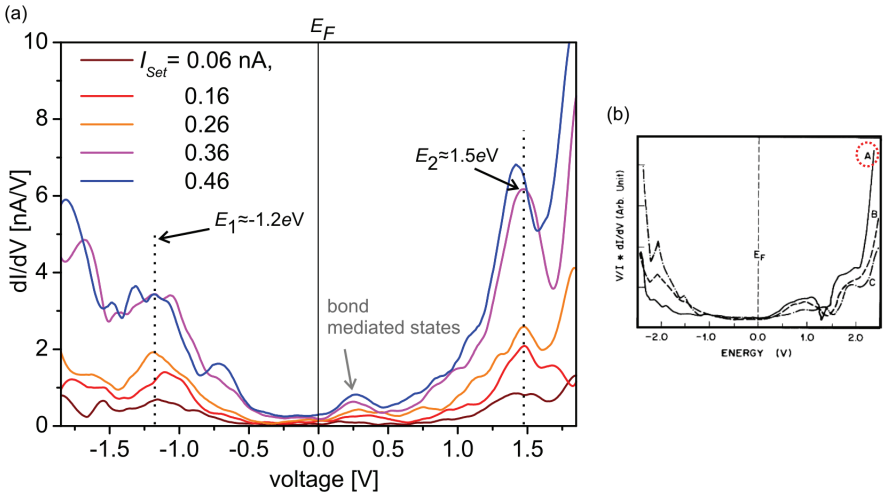

Figure 7.14: (a) dI/dV characteristic of benzene-1,4-dicarboxylic acid (BDCA) molecules chemically bonded to the Cu(110) surface calculated from the measured I-V data, imaged in Fig. 7.13. The curves were measured at one set point voltage of $V_{Set} = 0.77\,V$ but at different set point currents ($I_{Set} = 0.06$ to $0.46\,nA$). Highlighted are the two detected peaks corresponding to an occupied (E_1) and an unoccupied (E_2) molecular orbital energy. Additionally states related to the Cu-molecule bond are visible. (b) dI/dV spectrum (line A) of the clean Cu(110) surface, taken from [136].

At $I_{Set} = 0.46\,nA$ (blue line in Fig. 7.14) a slightly different peak position of the LUMO was monitored and some additional features appear in the LDOS. The shift of an unoccupied molecular orbital to a lower energy appears for small

tip-distances and is reported in literature, e.g., by Proehl [133]. The origin of this behavior is the largely increased interaction of the tip with the molecule. Interference effects become important, and the high electric field can influence the electronic states [137]. Two new features appear in the LDOS, one feature close below the Fermi energy and one close above. Due to the fact that these two peaks appear close to E_F and only at a small tip-sample distance they can be related to bond mediated states, i.e., to antibonding combinations of the σ-states of the terephthalate molecule with the d-electrons of the copper surface (compare Fig. 7.4). Furthermore, a monitoring of the pure Cu(110) surface states, through a destruction of the molecular layer by the tip, can be excluded because the dI/dV spectrum of the bare Cu(110) looks different, as depicted in Fig. 7.14(b) line A.
To get further information about the nature of the detected molecular orbitals and to estimate a HOMO-LUMO gap size the experimental data were compared with LDOS calculations for the chemically adsorbed BDCA molecule on Cu(110). The calculated LDOS is shown in Fig. 7.15(a), displayed together with the experimental dI/dV data at $I_{Set} = 0.46\,\mathrm{nA}$. Furthermore, charge density plots of the electronic states of BDCA in a specific energy range corresponding to the LDOS plotted in (a) were generated and are displayed in Fig. 7.15(b). They are a powerful tool for spectroscopy investigations because they image the correlation between molecular orbital energy and molecular geometry.
Comparing experiment and theory shows a good peak conformity and the measured main peaks (E_1, E_2) appear in the calculated LDOS data as well as the small features around E_F. The slightly different position of the unoccupied molecular orbital attracts attention but this shift may appear in experiment due to the electric field at very small tip-sample distances, as explained above and visible in Fig. 7.14(a). The character of this unoccupied MO is π-type, denoted as π_1^* in the plot, and it is related to the aromatic ring system, as displayed in the charge density plot of the electronic states of BDCA in the specific energy range around π_1^* (Fig. 7.15(b)). As typically for π-molecular ring systems the orbital is delocalized over the whole ring.
The experimentally accessible occupied MO can be identified as σ-type orbital, denoted as σ_1. Plotting the spatial distribution of the charge density for this σ-type MO (Fig. 7.15(b)) points out that it is indeed located at the molecule/substrate interface and thus represents the bonding part of the mixed molecular-surface states as mentioned above. Further occupied molecular orbitals appear at lower negative energies in the calculated LDOS. A second σ-type orbital has an energy

of $E_2 = -2.10\,eV$ and can be related with the charge density plot to a MO reflecting the carboxylic top group of the BDCA molecule. The first occupied MO with π character is located only slightly lower in energy ($E_3 = -2.21\,eV$), reflecting the occupied states of the molecular ring system.

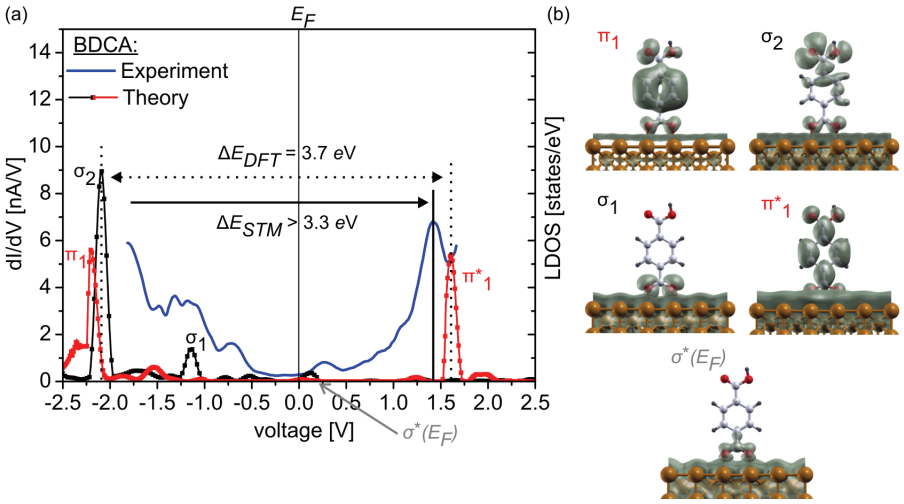

Figure 7.15: (a) Calculated LDOS of a BDCA molecule chemically bonded to the Cu(110) surface. The red line represents the contributions of the states with a π-type character, while the black line represents the states with a σ-type character. Additionally shown is the experimental dI/dV spectrum (blue) acquired over a BDCA molecule on Cu(110) at a set point of $V_{Set} = 0.77\,V$ and $I_{Set} = 0.46\,nA$. (b) Charge density plots of the electronic states of BDCA in a specific energy range corresponding to the LDOS displayed in (a).

Beside these main features, small state densities are displayed in the calculated LDOS around the Fermi Energy (e.g., denoted as $\sigma^*(E_F)$ in Fig. 7.15), comparable with the features visible in experiment at close tip-sample distances. Plotting the space extensions of these state densities with respect to the molecule geometry (e.g., last chart in Fig. 7.15(b)) displays a minor location on the carboxylate moiety of the BDCA molecule and a major one on the copper surface. Thus, these features represent bonding mediated states, i.e., the antibonding combinations of the σ-states of the terephthalate molecule with the d-electrons of the copper surface, as assumed.

The investigations point out that the calculated data of BDCA on Cu(110) are in close agreement with the measured dI/dV data and that a calculation of the Cu/BDCA HOMO-LUMO gap will result in a good approximation. The expected

HOMO position is then approximately 2.10 eV below the substrate Fermi level and thus outside the experimentally accessible voltage window of ± 2 V. The HOMO-LUMO gap can be calculated to $\Delta E_{DFT} = 3.7\,e$V.

In addition to the calculated HOMO-LUMO gap a rough estimation of the gap size can be made from UV-VIS spectroscopy data. Figure 7.16 shows the UV-VIS adsorption spectrum of BDCA dissolved in DMF ($c = 1 \cdot 10^{-3}$ mol/l). The optical gap can be derived from the onset of the energetically lowest adsorption band with a value of $\Delta E_{opt} \sim 4.0\,e$V. This is the lowest neutral excitation, i.e., transition of an electron from the HOMO to the LUMO, of the molecule. To compare both gap sizes an exciton binding energy has to be added to the optical gap, typical values are between $E_B = 0.1$ and $1.5\,e$V [134], and the influence of the chemical adsorption of the molecule on the surface has to be taken into account. Thus, the calculated value for the gap size is in accordance with the optical one.

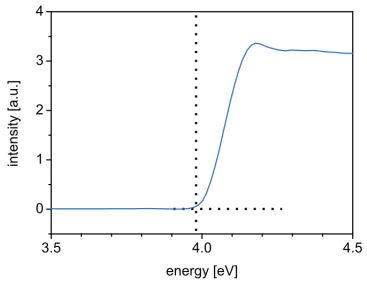

Figure 7.16: Optical absorption spectrum of BDCA dissolved in DMF. The horizontal and vertical dashed lines serve as guide to the eye to help determine the adsorption edge. The onset position of the energetically lowest adsorption band leads to an optical gap of $\Delta E_{opt} \sim 4.0\,e$V in the liquid phase.

7.4.2.3 Cu/BDCA/W junction symmetries

The charge transfer through a metal/molecule/metal junction is mainly defined by the ratios within the junction. Orbital mediated tunneling dominates the electron transport through the Cu/BDCA/W junction for small tip-sample distances as seen in the last paragraph but for larger distances, e.g., for $I_{Set} = 0.06$ nA, no molecular orbitals can be probed by STS and direct tunneling is the predominant mechanism. Thus, the junction size seems to influence the transport mechanism.

With a change in the junction size the vacuum gap size is changed at the BDCA/W interface, leading to a varying voltage drop at this interface. But not only the vacuum gap size changes, also the influence of dipole fields etc. on the potential barrier profile and thus on the charge transfer changes. The situation within the Cu/BDCA/W junction is similar to that in the Cu/BCA/W junction, detailed described in paragraph 7.3.2.2. At the BDCA/W interface the potential barrier profile is characterized by the vacuum gap size s as in the case of BCA. At the Cu/BDCA interface the potential barrier profile will depend strongly on the charge of the adsorbed molecule, which depends on the interaction between the molecule and the substrate. Similar to BCA the adsorbed BDCA molecule will be negatively charged, creating an intrinsic dipole. Due to the fact that the BDCA molecule itself has no dipole the dipole-induced potential step at the interface is expected to be smaller here. Thus, the overall change in the metal work function at the interface, i.e., the shift in vacuum level Δ, should be smaller but with a value above zero. This additional barrier leads to a threshold for the orbital mediated tunneling and an adequate description of the barrier profile can be given only by a model where neither the electrochemical potential μ_1 (sample) nor μ_2 (tip) remain fixed with respect to the sample. The value η which describes how the electrostatic potential difference is divided between the two contacts is thereby unequal zero. An estimation of the value η in dependence of the vacuum gap size s can be made with the known Cu/BDCA/W junction geometries. With a bond length of $d = 0.194\,\mathrm{nm}$ (equal to the value d for Cu/BCA), a molecular length of around $l = 0.796\,\mathrm{nm}$, a junction length of $z = d + l + s$, the weighting factor η can be calculated to

$$\eta = \frac{d + \frac{1}{2}l}{z} = \frac{0.592\,\mathrm{nm}}{0.99\,\mathrm{nm} + s}. \tag{7.7}$$

The threshold for conductance can be calculated for various vacuum gap sizes s following equation (7.2) and (7.3) with the molecular orbital energies. Note here that for all measured I-V curves the σ_1 orbital is detected as first occupied molecular orbital and thus defines the first point where either μ_1 or μ_2 can coincides with a molecular orbital energy. The relevant values for equation (7.2) and (7.3) are

$$E_F - E_{HOMO} = 1.2e\mathrm{V} \text{ and } \quad E_{LUMO} - E_F = 1.5e\mathrm{V}. \tag{7.8}$$

Calculating the conduction threshold for various vacuum gap sizes s shows that with $\eta \approx 0.46$, i.e., $s = 0.30\,\mathrm{nm}$, the molecules could conduct through HOMO for both bias polarities, leading to symmetric I-V curves and with $\eta < 0.543$, i.e.,

$s < 0.10\,\text{nm}$, the I-V curves should be asymmetric. All measured I-V curves show a symmetric profile in the measured bias voltage range so the junction sizes are assumed to be between $s = 0.30$ and $0.1\,\text{nm}$.

7.4.2.4 Transition voltage spectroscopy

The experimental I-V characteristics for BDCA show a region of linear increase around the Fermi level, and a sharp rise in current above certain threshold voltages. This first linear and above a certain threshold voltage exponential behavior of the current indicates different tunneling regimes. Thus, transition voltage spectroscopy was performed to get detailed information about the point where the tunneling mechanism changes and since the magnitude of the voltage required to enact this transition is molecule-specific, the transition voltage is used as a variable characterizing the electronic transport properties of the specific molecule/metal system.

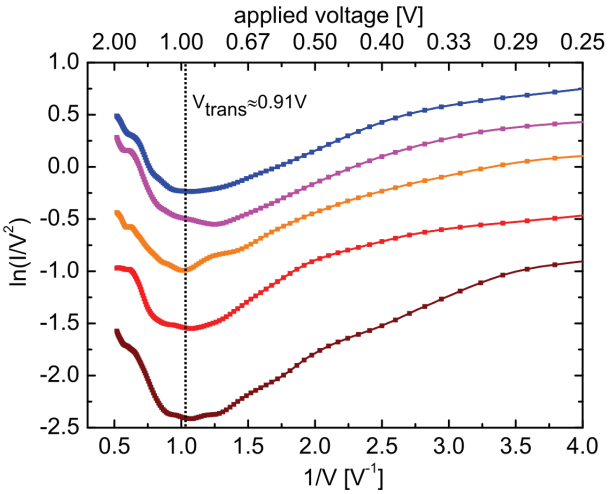

Figure 7.17: Folder-Nordheim plot for the positive bias voltage regime of the measured current-voltage data set of BDCA on Cu(110). The different curves correspond to different set point currents, starting at $I_{Set} = 0.06\,\text{nA}$ (brown) and going to $I_{Set} = 0.46\,\text{nA}$ (blue). V_{trans} is determined from the minimum of the Fowler-Nordheim plots, marked with a dashed line.

To find this transition point the I-V characteristic of Fig. 7.13 is replotted as $ln(I/V^2)$ vs. $1/V$, separately for the positive and negative bias voltage regime.

Exemplary, Fig. 7.17 shows the Folder-Nordheim plot in the positive bias voltage regime for all set point currents I_{Set}.
The voltage (V_{trans}) required to change the functional dependence of current on the applied voltage is determined from the minimum of every curve and the transition voltages for the complete current-voltage data set measured are listed in table 7.3.

I_{Set}	0.06 nA	0.16 nA	0.26 nA	0.36 nA	0.46 nA	$\overline{x}_{arithm}$
V_{trans}(neg) [V]	-0.57	-0.60	-0.52	-0.53	-0.52	-0.55
V_{trans}(pos) [V]	0.93	0.93	0.99	0.78	0.92	0.91

Table 7.3: Compilation of the calculated V_{trans} values for all measured I-V curves. Additionally, the arithmetic mean of V_{trans} is listed in the last column.

Comparing the transition voltage values for different set point currents but for the same bias polarity points out that there is no large variation between the values. Thus, the arithmetic mean is calculated to $V_{trans} = -0.55\,\mathrm{V}$ and to $V_{trans} = 0.91\,\mathrm{V}$. It is marked with a dashed line in Fig. 7.17. Whereas there is only a small variation in the values for one bias polarity different transition voltage values are found for positive and negative bias voltages. This is not unusual due to the asymmetric voltage drops at the two metal/molecule interfaces which cause the transition voltage to be dependent on bias polarity. Summarizing, the transition occurs in the measured Cu/BDCA/W junction first at negative bias polarities, pointing to a HOMO mediated tunneling. This is in accordance with the result of section 7.4.2.3 where a HOMO mediated tunneling is predicted from geometry estimations.
Taking the above mentioned small HOMO-LUMO gap size of $\Delta E_{DFT} = 3.7\,e\mathrm{V}$ and the tunneling gap geometry as estimated in paragraph 7.4.2.3 into account, the change in mechanism monitored here through the transition voltage for the Cu/BDCA/W junction is a change from direct tunneling to resonant tunneling.

7.5 Pyridinecarboxylic acid

Pyridinecarboxylic acid (PCA) is similar to benzenecarboxylic acid, wherein one CH group in the aromatic six-membered ring is substituted through a nitrogen atom. Due to the three possible exchanging positions a differentiation between an

insertion in ortho, meta, or para position is necessary. All isomers should adsorb on Cu(110) surfaces in the same way as benzenecarboxylic acid because of the equivalent anchoring group and the similar ring structure. Thus, these structures provide the possibility to influence the electron density of the aromatic ring directly without any obvious geometrical influence. Furthermore, slight variations in the electron density are expected for the different PCA isomers because of the position dependent interactions between the nitrogen atom and the carboxylic group. Pyridine-2-carboxylic acid (o-PCA) was chosen for the experimental investigations in this thesis and LDOS calculations are done on all three isomers. On one side pyridinecarboxylic acid molecules are well investigated molecules in human medicine because, e.g., pyridine-3-carboxylic acid is vitamin B_3 or pyridine-2-carboxylic acid acts as a chelating agent for elements such as chromium, zinc, manganese, copper, iron, and molybdenum in the human body. On the other side it is a sparsely investigated system for molecular electronics with, to my knowledge, only one study of the self-assembly process of pyridinecarboxylic acids on TiO_2 surfaces [138, 139].
Here distance dependent current-voltage spectroscopy was performed on pyridine-2-carboxylic acid on Cu(110) surfaces to get first information on the electronic properties in terms of the tunneling mechanism, the LDOS and the HOMO-LUMO gap. Additionally, current-distance spectroscopy was performed to examine the dependency of the current on the tunneling distance z and to measure the material dependent decay parameter β.

7.5.1 Current vs. voltage spectroscopy

The topographic investigation of pyridine-2-carboxylic acid on Cu(110) surfaces reveals close-packed molecular assemblies with the preparation conditions described in paragraph 7.2. Figure 7.18(a) displays a STM overview scan of o-PCA on Cu(110) showing a direct, row like texture in [001]-direction. The molecules exhibit the clear tendency to order on the Cu(110) pattern with a distinct adsorption on the copper rows and to form structures with similar molecular orientations, as visible at various places on the Cu terrace in figure 7.18(a). The prepared molecular monolayers still show a high defect density which could be certainly reduced by a slower sublimation process at lower background pressure (not reachable with the used experimental setup). Spectroscopic investigations were done

only on bunches of close-packed molecules with a periodicity in both surface directions ([001] and $[1\bar{1}0]$). A high resolution topography scan ($1.8 \times 0.9\,\mathrm{nm}^2$, $I_{Set} = 0.205\,\mathrm{nA}, V_{Set} = 1.075\,\mathrm{V}$) collected before a series of spectroscopy measurements is shown in Fig. 7.18(b). The interatomic distance of nearest neighbor molecules is here $a \approx 0.37 \pm 0.04\,\mathrm{nm}$.

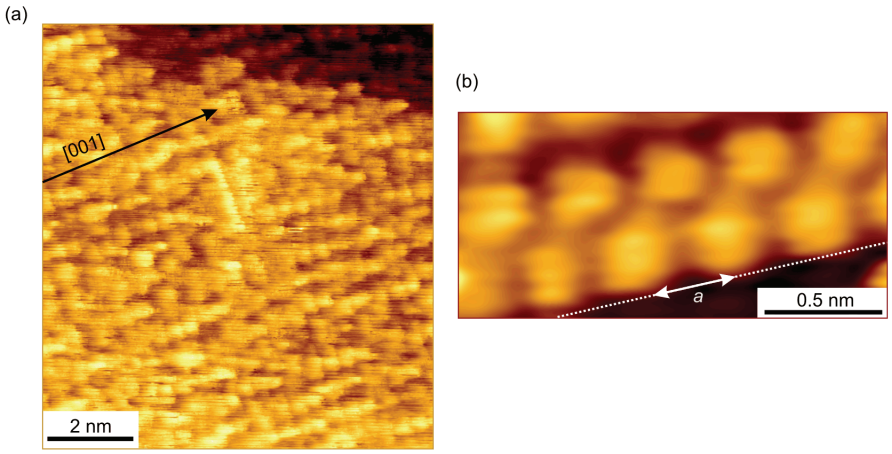

Figure 7.18: (a) STM topography scans of o-PCA on Cu(110) showing a direct, row like texture in [001]-direction. Areas with regular features appear everywhere on the sample. (b) High resolution scan of molecular features within an ordered array.

Distance dependent current-voltage spectroscopy was performed on these structures and the I-V data were analyzed in analogy to the I-V data collected on the BCA/Cu and the BDCA/Cu systems. At first, the derivative dI/dV of the current I with respect to the voltage V was calculated numerically from the I-V data. Figure 7.19 shows the measured I-V data (a) and the dI/dV characteristics (b). Displayed are the averaged curves for six different set point currents, $I_{Set} = 0.125$ to $0.625\,\mathrm{nA}$, recorded with a set point voltage of $V_{Set} = 1.0\,\mathrm{V}$. All curves are reproducible up to a current of $0.625\,\mathrm{nA}$ and the voltage window for the I-V measurements was found to be $V_{Sweep} = \pm 1.7\,\mathrm{V}$. Outside these margins a field-induced breakdown of the Cu/PCA/W junction takes place, changing the molecular layer irreversibly.
Comparing the different dI/dV curves of Fig. 7.19(b) shows an accretion of three peaks within the measurable voltage window. Two peaks appear at negative

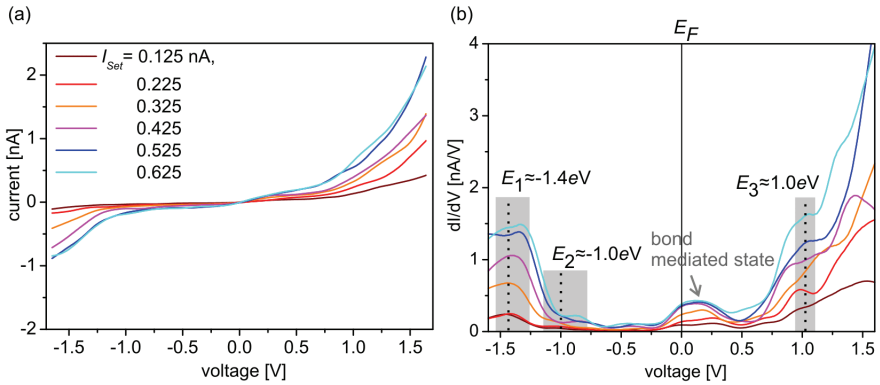

Figure 7.19: (a) I-V characteristics of pyridine-2-carboxylic acid (o-PCA) molecules chemically bonded to the Cu(110) surface, as topographically imaged in Fig. 7.18(b). The curves were measured at one set point voltage of $V_{Set} = 1.0\,\mathrm{V}$ but at different set point currents ($I_{Set} = 0.125$ to $0.625\,\mathrm{nA}$). (b) dI/dV plot calculated numerically from the I-V data showing two peaks related to occupied states (E_1 and E_2), a mixed molecule-surface mediated state close above the Fermi energy E_F, and a small peak feature at $E_3 \approx 1.0\,e\mathrm{V}$.

sample bias voltages, one at around $V_1 = -1.4\,\mathrm{V}$ and the other one at around $V_2 = -1.0\,\mathrm{V}$. A slight shift in the peak position is visible for both peaks at higher set point currents, pointing to a very close tip-sample distance and a shift in the orbital energies due to the applied electric field. The peak at around $-1\,\mathrm{V}$ can be recognized as the peak related to the bonding carboxylate group, it appears at nearly the same position in the spectra of BCA and BDCA. Thus, the experimental HOMO has an energy of $E_1 = -1.4\,e\mathrm{V}$. A further peak appears with decreasing tip-sample distance close above the Fermi energy. This peak can be related to the antibonding combinations of the σ-states of the PCA molecule with the d-electrons of the copper surface, as sketched in Fig. 7.4. The measured I-V curves show a diffuse image of the unoccupied molecular states above $0.5\,\mathrm{V}$ and I-V measurements on various molecules within an ordered array show the same behavior. A continuous increase is monitored, comparable to dI/dV curves where no molecular states can be detected because their energies are above the experimentally accessible range, as e.g., in the alkanethiol/Au(111) system, but for set point currents above $I_{Set} = 0.325\,\mathrm{nA}$ a peak feature appears at an energy of $E_3 = 1.0\,e\mathrm{V}$. To get more dI/dV data for this voltage range, CITS measurements were performed on a bunch of molecules at set point currents of $I_{Set} = 0.525$ and

0.625 nA. They show exactly the same peaks for negative as well as for positive voltages, including the peak at $E_3 = 1.0\,eV$ with the for CITS typical narrow peak width. Thus, the feature at +1.0 V is assumed to be the LUMO which shifts inside the detectable voltage window for small tip-sample distances due to the applied electric field. Figure 7.20 shows a dI/dV curve (cyan line) taken from the CITS image done at $I_{Set} = 0.625\,nA$.
To get further information about the nature of the detected orbitals and to get a survey of the unoccupied state energies the LDOS (calculated by DFT methods) is plotted in addition to the experimental data in Fig. 7.20.

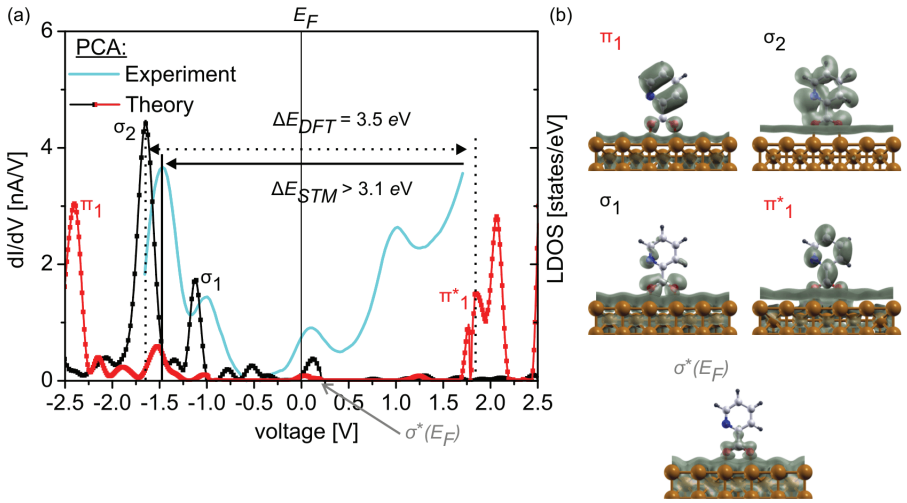

Figure 7.20: (a) Calculated LDOS of an o-PCA molecule chemically bonded to the Cu(110) surface. The red line represents the contributions of the states with a π-type character, while the black line represents the states with a σ-type character. Additionally shown is an experimental dI/dV spectrum (cyan) taken from a CITS measurement on o-PCA molecules on Cu(110) at a set point of $V_{Set} = 1.0\,V$ and $I_{Set} = 0.625\,nA$. (b) Charge density plots of the electronic states of o-PCA in a specific energy range corresponding to the LDOS displayed in (a).

Both experimentally detected occupied molecular orbitals appear in the calculated LDOS with comparable energies. They are σ-type orbitals and can be related with the help of the isosurface plots (Fig. 7.20(b)) to the carboxylate/Cu interface states (E_2) and to the nitrogen atom (E_1). The first occupied π-orbital appears at an energy of $-2.4\,eV$ in the calculated LDOS and is thus not accessible within the experiment. It is related to the pyridine ring and its electron density distribution is spreed over large parts of the molecule due to the delocalized π-system of

the ring. That applies also for the first unoccupied molecular orbital. The broad π_1^*-type molecular orbital peak is located around $E = 2.0\,eV$ with a first maximum at $1.8\,eV$. This is just outside the experimental measurement range. Comparing these calculated LDOS investigations with the experimentally observed curve progression suggests the following. The σ_1-orbital is localized on the benzoate group, close to the copper surface, and a very small tip-sample distance is needed to detect it experimentally. This can be confirmed through the distance dependent I-V measurements shown above. However, at these small tip-sample distances the large electric field causes shifts in the orbital energies, especially in unoccupied ones [137]. Thus, the small peak seen in experiment at $1.0\,eV$ can monitor the peak onset of the π_1^*-orbital despite the fact that this orbital is higher in energy (without an applied electric field). Finally, the calculated LDOS displays the experimentally observed state above the Fermi energy, denoted with $\sigma^*(E_F)$ in Fig. 7.20(a) and (b). From the theoretical data the HOMO-LUMO gap of the o-PCA/Cu system can be calculated to $\Delta E_{DFT} = 3.5\,eV$ whereas from the experimental data only an estimation of $\Delta E_{STM} > 3.1\,eV$ is possible.

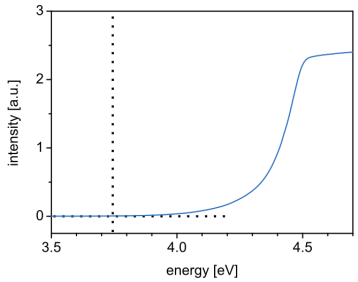

Figure 7.21: Optical absorption spectrum of o-PCA dissolved in water. The horizontal and vertical dashed lines serve as guide to the eye to help determine the adsorption edge. The onset position of the energetically lowest adsorption band leads to an optical gap of $\Delta E_{opt} \sim 3.7\,eV$ in the liquid phase.

The calculated data for the HOMO-LUMO gap are roughly cross-checked with the size of the optical gap measured by UV-VIS spectroscopy. For this purpose o-PCA was dissolved in H_2O ($c = 1 \cdot 10^{-3}$ mol/l). The optical gap of o-PCA is derived from the onset of the energetically lowest adsorption band with a value of $\Delta E_{opt} \sim 3.7\,eV$, as displayed in Fig. 7.21. This is in accordance with the calculated data because to compare both gap sizes an exciton binding energy E_B has to be added to the optical gap, typical values for this are between $E_B = 0.1$

and 1.5 eV [134], and the influence of the chemical adsorption of the molecule on the surface has to be taken into account, too.

Beside the LDOS investigations, transition voltage spectroscopy was performed to characterize the electronic transport properties of the o-PCA/Cu system. The first linear and above a certain threshold voltage exponential shape of the I-V curves (compare Fig. 7.19(a)) points to the existence of different tunneling mechanisms within the measured voltage window. Thus, the measured I-V data were replotted as $ln(I/V^2)$ vs. $1/V$, separately for the positive and negative bias voltage regime, and displayed in Fig. 7.22.

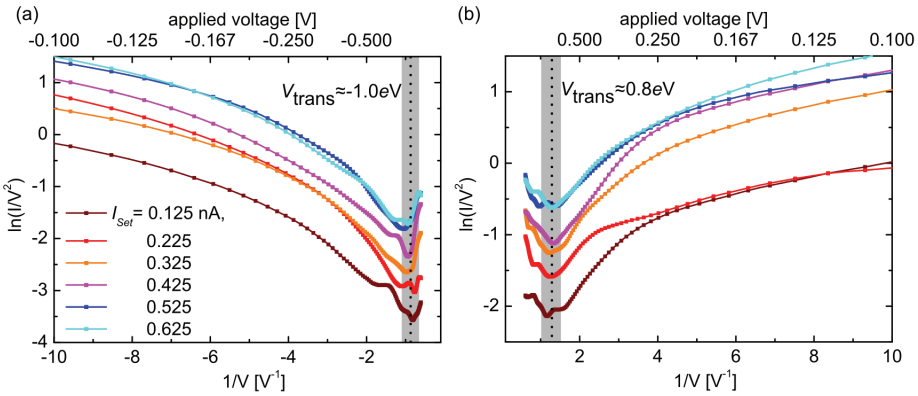

Figure 7.22: Folder-Nordheim plots of the measured current-voltage data set of o-PCA on Cu(110). The $1/V$ vs. $ln(I/V_2)$ diagram is divided in a plot for the negative (a) and the positive (b) bias voltage regime. Shown are different curves corresponding to different set point currents, starting at $I_{Set} = 0.125$ nA (brown) and going to $I_{Set} = 0.625$ nA (cyan). V_{trans} is determined from the minimum of the Fowler-Nordheim plots and marked with dashed lines.

The voltage required to change the functional dependence of current on the applied voltage (V_{trans}) is determined from the minimum of every curve and the transition voltages for the complete current-voltage data set measured are listed in table 7.4. Comparing the transition voltage values for different set point currents but for the same bias polarity points out that there is a decrease in the data for negative bias values. For set point currents of $I_{Set} = 0.125$ nA the transition point occurs at $V_{trans} = -1.25$ V whereas at smaller tip-sample distances, e.g., at $I_{Set} = 0.525$ nA, the transition point is found at smaller voltages. This behavior is in accordance with that visible in the LDOS, where a slight shift of the occupied molecular

orbital related peak E_1 is monitored. This area is marked in gray in Fig. 7.19 (b). Additionally, the peak at E_2 appears slowly in the LDOS spectrum with decreasing tip-sample distances due to its localized orbital structure and thus its accessibility for MO mediated transport increases as a function of tip position. For positive sample bias voltages the transition point values fluctuate around $V_{trans} = 0.81\,\mathrm{V}$. Keeping in mind that the transition point is the lowest limit for MO mediated transport [132] the positive transition point reflects the small peak appearing in the LDOS at positive bias voltages as MO mediated.

I_{Set} [nA]	0.125	0.225	0.325	0.425	0.525	0.625	$\overline{x}_{arithm}$
V_{trans}(neg) [V]	-1.25	-1.08	-1.02	-1.06	-0.97	-0.91	-1.05
V_{trans}(pos) [V]	0.85	0.80	0.82	0.76	0.85	0.76	0.81

Table 7.4: Compilation of the calculated V_{trans} values for all measured I-V curves. Additionally, the arithmetic mean of V_{trans} is listed in the last column.

As already seen in the plotted I-V data (Fig. 7.19(a)) of o-PCA on the Cu(110) surface the current rises with increasing set point current. This has been explained in general by a decreasing tip-sample distance and thus with a higher junction conductivity. In the case of BCA and BDCA a more detailed description of the dependence of the current on the tip-sample distance, i.e., of the potential barrier profile of the junctions, was given dependent on the junction geometries, the weighting factor η and the HOMO and LUMO energies related to the Fermi energy. Due to the ambiguous situation of the LUMO peak in experiments for o-PCA an alternative way was chosen to examine the dependency of the current and it is presented in the following paragraph.

7.5.2 Current vs. distance spectroscopy

Current-distance (I-z) spectroscopy is an established method to characterize the chemical characteristic of a molecule/metal system and the local electronic charge. Here I-z spectroscopy was performed, as described in section 3.3.2, on regular structures of pyridine-2-carboxylic acid on Cu(110), as imaged in Fig. 7.18. The curves reported here are taken by first retracting the tip and then approaching it towards the sample surface while simultaneously measuring the current. Thus, the x-axis is a relative axis where the origin denotes the position of the tip at

the tunneling set point parameters ($I_{Set} = 0.26\,\mathrm{nA}$ and $V_{Set} = 1.28\,\mathrm{V}$). Negative displacements represent an increase in tunneling distance (i.e., the tip is retracted), and positive displacements a decrease in tunneling distance (i.e., the tip is moved towards the sample). Figure 7.23 shows a characteristic graph of I-z measurements for o-PCA plotted on a semi logarithmic scale. At large tip-sample distances, below $-0.3\,\mathrm{nm}$, the detected tunneling current is lower than the noise level of the preamplifier.

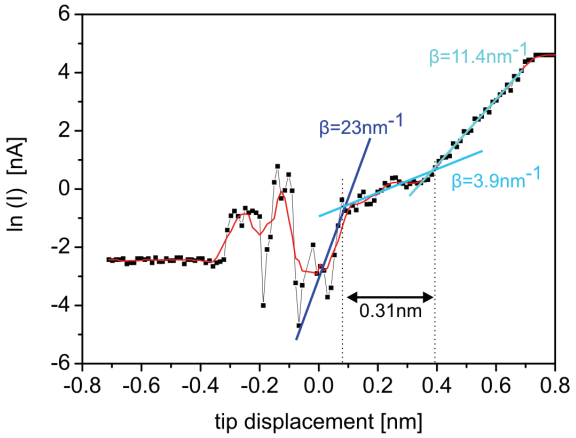

Figure 7.23: Current-distance spectroscopy of o-PCA molecules chemically bonded on a Cu(110) surface. The origin of the x-axis corresponds to the tunneling set point parameters ($I_{Set} = 0.26\,\mathrm{nA}$ and $V_{Set} = 1.28\,\mathrm{V}$). The slopes of the current in the semi logarithmic plot reflect the current-decay parameters (β) and are material dependent.

Between -0.3 and $-0.1\,\mathrm{nm}$ the current fluctuates due to an unstable tunneling contact at these large tip-sample distances. These features are setup related and often seen in I-z characteristics measured at room temperature. Above $-0.1\,\mathrm{nm}$ the tunneling contact is stable and three different domains can be identified within this I-z characteristic. All parts show a logarithmic dependency of the current I on the distance z and differ only in the slope of the function $\ln(I) = f(z)$. In the first domain, up to $0.08\,\mathrm{nm}$, a steep increase in current is visible. Due to the fact that at this position the tip moves through the vacuum gap the proportionality of $ln(I)$ and z can be explained by a simple 1D tunneling model as described by Simmons [29]. For large barrier heights and small barrier widths as well as for low and intermediate voltages the current-voltage dependence can be described by

the Wentzel-Kramers-Brillouin (WKB) approximation for an 1D square potential barrier:

$$I \propto V\, exp\left(-\frac{2\sqrt{2m^*}}{\hbar}\sqrt{\Phi_B}z\right) \tag{7.9}$$

and

$$\beta = \frac{2\sqrt{2m^*}}{\hbar}\sqrt{\Phi_B} \tag{7.10}$$

valid for $eV \ll \Phi_B$, where e is the electron charge, V the applied bias voltage, Φ_B the apparent barrier height, m^* the effective electron mass, z the tip-surface distance, $\hbar$ the reduced Planck constant, and β the tunneling decay constant. The slope of the semi logarithmic plot on the recorded tunneling current versus tip displacement is hence proportional to the tunneling decay constant of the respective material. Linear curve fitting on the experimentally obtained curve slope leads here to a tunneling decay constant of $\beta_{Vac} = 23\,\mathrm{nm}^{-1}$ for the first part of the I-z curve. Using equation (7.9), $\beta_{Vac} = 23\,\mathrm{nm}^{-1}$ and $m^* = m_e$ (for metals), a value for the apparent barrier height of $\Phi_B(Vac) = 5.04\,e\mathrm{V}$ results, which is in the typical range for metallic surfaces [140].

At a tip displacement of 0.08 nm a kink appears in the I-z curve, monitoring the contact point where the tip touches the molecular layer, and the slope is reduced. The slope stays almost constant up to a distance of 0.38 nm and increases again behind this point. The second domain has a length of around 0.31 nm and can be related to the pyridine moiety of the molecule. The tunneling decay constant can be calculated to $\beta_{Pyridine} = 3.9\,\mathrm{nm}^{-1}$. This decay constant value for the pyridine moiety ranges between the literature values of the ferrocene moiety ($\sim 2.8\,\mathrm{nm}^{-1}$) [38] and of the phenyl moiety ($\sim 4.2\,\mathrm{nm}^{-1}$) [141]. Deducing the apparent tunneling barrier height for the pyridine moiety Φ_B(Py) with the same approach as used above, results in values smaller than $0.3\,e\mathrm{V}$ depending on the exact value of m^*. However, this value of Φ_B(Py) implies that equation (7.9) is no longer applicable here, since $eV > \Phi_B$(Py) for the majority of the applied bias voltages. Remaining in the simple tunneling model, reported by Simmons, this new situation with an applied voltage higher than the potential barrier is equal to a triangular barrier whose properties are changed with increasing voltage. In this case the tunneling current can be described by

$$I \propto V^2\, exp\left(-\frac{4\sqrt{2m^*}}{3e\hbar V}{\Phi_B}^{3/2}z\right) \tag{7.11}$$

and

$$\beta = \frac{4\sqrt{2m^*}}{3e\hbar V}{\Phi_B}^{3/2}. \tag{7.12}$$

Assuming $m^* = m_e$, and inserting $\beta_{Pyridine} = 3.9\,\mathrm{nm}^{-1}$ in equation (7.12) leads to a value of $\Phi_B(\mathrm{Py}) = 0.82\,e\mathrm{V}$ for the apparent tunneling barrier height. This value is still low but in good agreement with the value V_{trans} obtained by transition voltage spectroscopy (compare paragraph 7.5.1) which describes the onset value for molecule mediated tunneling in the system. Within the Simmons model used here V_{trans} is proportional to Φ_B, as deduced by Beebe et al. [127].
A third domain is visible in the I-z characteristic of o-PCA molecules on Cu(110) (Fig. 7.23) between a tip displacement of 0.38 nm and 0.7 nm. Above this point the current amplifier limited the tunneling current. The slope in this third domain leads to a β value of $\sim 11.4\,\mathrm{nm}^{-1}$ and can be related to the bonding carboxylate moiety, and there are points that corroborate this. First, the length of a pyridine-2-carboxylate molecule chemically bonded to the Cu(110) surface is around 0.79 nm (including an O-Cu bond length of 0.194 nm) for an upright molecule configuration. Now excluding the top C-H bond and the ring structure (~ 0.31 nm) which the tip has already "crossed" leads in a rough estimation to a tip-Cu distance of 0.37 nm as the starting point of the third domain. The measured length of the third domain is shorter and thus can display the bonding carboxylate moiety. Second, the value of the tunneling decay constant in this area is large compared to that of the pyridine moiety, equivalent to a larger barrier height. Indeed, this barrier heightening reflects the PCA/Cu interface geometry. As described in detail for the BCA/Cu interface in paragraph 7.3.2.2, a dipole moment is induced at the carboxylate/Cu interface and causes an additional barrier added to the work function of the Cu(110) surface.

7.5.3 Theoretical predictions for the LDOS of the PCA isomers

As mentioned at the beginning of this section, pyridinecarboxylic acid has three isomers among which pyridine-2-carboxylic acid (ortho) was experimentally investigated here. However, the experimental differential conductance curves confirm the calculated LDOS with such a high accordance that it can be assumed that the calculated LDOS for the other two isomers are good predictions for the electronic structure of these systems. Figure 7.24 shows the calculated LDOS plots for all three isomers. The first molecule is the experimentally investigated pyridine-2-

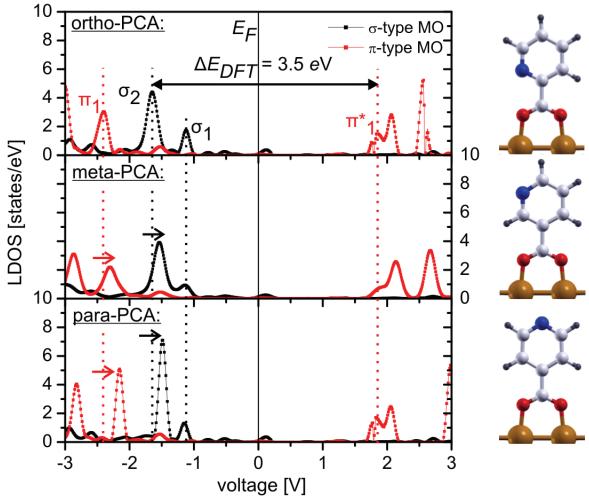

Figure 7.24: Calculated LDOS for the three different PCA molecule configurations chemically bonded to the Cu(110) surface. The red lines represent the contributions of the states with a π-type character, while the black lines represent the states with a σ-type character. The first molecule is the experimentally investigated pyridine-2-carboxylic acid followed by pyridine-3-carboxylic acid and by pyridine-4-carboxylic acid. Comparing the three isomers shows a slight reduction of ΔE_{DFT} caused by a shift of the occupied σ_2 level towards the Fermi energy.

carboxylic acid (ortho-PCA) followed by pyridine-3-carboxylic acid (meta-PCA) and by pyridine-4-carboxylic acid (para-PCA). Displayed are the relevant MO energies around the Fermi energy and the energy gap ΔE_{DFT} for the ortho-PCA. Comparing the three isomers a constant energy for the unoccupied molecular π_1^*-orbitals and for the occupied σ_1-orbital is found. Furthermore, a characteristic shift of the occupied σ_2- and π_1-orbitals towards the Fermi energy with increasing distance between the position of the inserted N atom and the Cu surface is observed. Thus, it can be summarized that the LDOS and consequently the energy gap ΔE_{DFT} is dependent on the position of the insertion of the nitrogen atom in the ring.

7.6 Pyridinedicarboxylic acid

Pyridinedicarboxylic acid (PDCA) is a combination of BDCA and PCA. Starting from the BCA molecule an additional carboxylic acid moiety is inserted in the

para position of the phenyl ring and additionally one CH group in the aromatic six-membered ring is substituted through a nitrogen atom. Here pyridine-2,5-dicarboxylic acid (PDCA, $C_5H_3N(COOH)_2$) was chosen for investigations. The molecule should adsorb on the Cu(110) surfaces in the same way as benzenedicarboxylic acid, with one carboxylic group deprotonated and bonded and the other one pointing towards the vacuum interface because of the equivalent anchoring groups. Due to the fact that PDCA can chemisorb in principle with both carboxylic groups on the Cu(110) surface two molecule configurations are possible in the PDCA/Cu system. Therefore, it is differentiated in the following between $C_7H_4N^{(2)}O_4$, describing a PDCA with the nitrogen on position two in the ring (counting the ring atoms from the carbon atom located at the bonded carboxylate unit), and $C_7H_4N^{(3)}O_4$, denoted as configuration {1} and {2}. Experimentally there is no possibility to influence the orientation of the molecule during the adsorption process, or to monitor topographically which configuration is preferentially adsorbed.

Distance dependent current-voltage spectroscopy was performed on pyridine-2,5-dicarboxylic acid on Cu(110) surfaces to get information on the electronic properties in terms of the tunneling mechanism, the LDOS and the HOMO-LUMO gap. The experimental differential conductance curves will be compared with the calculated LDOS in the following. These theoretical investigations give astonishing insights into the electronic structure of PDCA and the focus of this paragraph is set on the identification of submolecular structures by combining experiment and theory.

7.6.1 Current vs. voltage spectroscopy

Distance dependent current-voltage spectroscopy was performed on close-packed molecular structures of pyridine-2,5-dicarboxylic acid SAMs. A high resolution topography scan ($1.8 \times 1.09\,\mathrm{nm}^2$, $I_{Set} = 0.3\,\mathrm{nA}, V_{Set} = 1.5\,\mathrm{V}$) collected before a series of spectroscopy measurements is shown in Fig. 7.25(a). The interatomic distance of nearest neighbor molecules is here $a \approx 0.39 \pm 0.04\,\mathrm{nm}$. Figure 7.25(b) shows the results of a series of I-V measurements collected at various tip-sample distances. All curves were collected at a set point voltage of $V_{Set} = -2.0\,\mathrm{V}$ but the set point currents were chosen between $I_{Set} = 0.10$ and $0.60\,\mathrm{nA}$. Every plotted curve is the average of ten curves taken on the same molecule and is identical

with other curves obtained for molecules spread over samples. A relatively large voltage window of $V_{Sweep} = \pm 3.0\,\mathrm{V}$ was found for the detection of PDCA molecules compared to, e.g., PCA molecules as investigated in the last section.

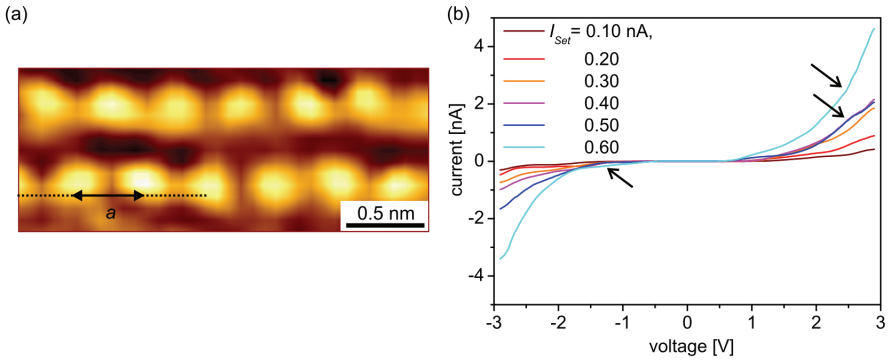

Figure 7.25: (a) High resolution STM topography scan of PDCA molecules ordered in a close-packed structure of standing-up molecules on the Cu(110) surface. The scan size is about $1.8 \times 1.09\,\mathrm{nm}^2$, scanned with tunneling set point parameters of $I_{Set} = 0.3\,\mathrm{nA}$ and $V_{Set} = 1.5\,\mathrm{V}$ and the interatomic distance of nearest neighbor molecules is here $a \approx 0.39 \pm 0.04\,\mathrm{nm}$. (b) I-V spectra taken on the PDCA molecules in dependence of the set point current. Some of the appearing kinds within the I-V curves are highlighted through black arrows.

Comparing the different curves shows that they are asymmetric, showing a steeper increase of the tunneling current at positive bias voltages. Furthermore, kinks are visible in the curve shape but the positions and forms are irregular and not the same for curves detected with different set point currents. The situation of the peak shape gets clearer when numerically calculating the differential conductance dI/dV for the measured I-V data. The kinks appear now as conductance peaks, related to the molecular orbital energies, but still no accordance is visible between all curves. Starting from a set point current of $I_{Set} = 0.1\,\mathrm{nA}$ and going to 0.3 nA, an accretion of defined peaks in the dI/dV spectra can be measured. The peaks do not change their shape or their energy. This means that at this large tip-sample distance the STM detects the same molecular orbitals. Further increasing I_{Set} causes changes in the number of monitored peaks as well as changes in their intensity and energetic position until at 0.7 nA the tip causes irreversible changes in the molecular layer. It is not possible to coherently explain the differences in the orbital energies only through a shift of MO energies in the applied electric

field and other effects are assumed to cause these shifts.

7.6.1.1 Electronic mapping of molecular orbitals

Parallel to these experimental investigations, theoretical *ab initio* total-energy calculations had been performed in the framework of the DFT on the PDCA/Cu(110) system by V. Caciuc and N. Atodiresei. These calculations show that, in the case of the PDCA molecule, four different adsorption geometries must be taken into account due to their different adsorption energies. Beside the above mentioned two adsorption configurations $\{1\}$ and $\{2\}$, different conformers may exist on the surface due to possible intramolecular interactions because of the presence of the nitrogen atom in the aromatic ring. If the PDCA molecule adsorbs in configuration $\{2\}$ on the surface, the orientation of the COOH top group becomes important and three conformations are conceivable. The conformers $\{2a\}$ and $\{2b\}$ differ through a rotation of the COOH group around the C-C bond between ring and carboxylic group. On the other hand the conformers $\{2b\}$ and $\{2c\}$ differ through a rotation of the hydroxyl (OH) group around the C-O bond within the carboxylic group. Comparing the different adsorption geometries, in terms of their adsorption energies, leads to a PDCA adsorbed in conformation $\{2c\}$ onto the surface as ground state. It exhibits a hydrogen bond between the carboxylic group and the nitrogen atom of the aromatic ring. However, the other metastable conformations without a hydrogen bond are with 120 meV ($\{2a\}$) and 190 meV ($\{2b\}$) slightly higher in energy, with respect to the ground state configuration $\{2c\}$. Furthermore, the calculated adsorption energies of the $C_7H_4N^{(2)}O_4$ ($\{1\}$) and $C_7H_4N^{(3)}O_4$ $\{2a\}$ configurations are practically identical and are similar to those reported for other molecules that adsorb via carboxylate groups on the Cu(110) surface [21, 142, 143].
Figure 7.26 shows the LDOS calculated for the four possible adsorption geometries related to the position of the nitrogen atom and the H atom of the carboxylic group. Also presented is the spatial distribution of the charge density in a specific energy range associated with the molecular LDOS for the conformation $\{2a\}$. Close to the Fermi level the LDOS shows three occupied σ-orbitals which can be related, with the help of the charge density plots, to the carboxylic top group (σ_3), the nitrogen atom in the ring (σ_2), and the binding carboxylate group (σ_1). For the bonding σ_1 and the antibonding σ_1^* states, the charge density is mainly localized on the carboxylate group (COO^-) leaving the top carboxylic group (COOH)

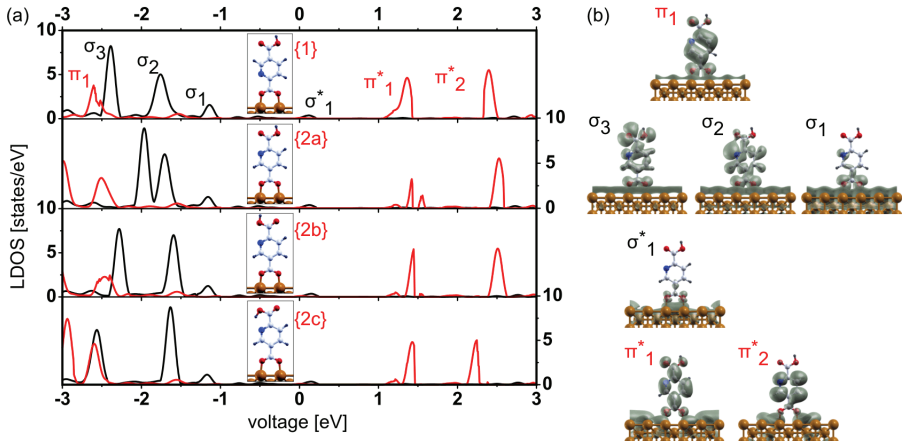

Figure 7.26: (a) Calculated LDOS of a PDCA molecule chemically bonded to the Cu(110) surface in four possible configurations: $C_7H_4N^{(2)}O_4$, $C_7H_4N^{(3)}O_4$ $\{2a\}$ with the H atom of the carboxylic group pointing up, $C_7H_4N^{(3)}O_4$ $\{2b\}$ with the H atom pointing up above the nitrogen atom, and $\{2c\}$ with the H atom pointing down towards the N atom. The red line represents the contributions of the states with a π-type character, while the black line represents the states with the σ-type character. (b) Charge density plots of the electronic states of $C_7H_4N^{(3)}O_4$ $\{2a\}$ in a specific energy range corresponding to the LDOS depicted in (a).

at the vacuum interface with no charge contribution. This charge density localized between the bonding carboxylate functionality and the copper surface illustrates the interaction of the orbitals of the molecule with the *d*-band electrons of the copper, as similarly described for BCA, BDCA, and PCA. Furthermore, the LDOS calculations show three π-orbitals which are all predominantly located at the pyridine ring. From the electronic point of view, the presence of nitrogen in conjugated heterocyclic molecules lowers their π-orbital energies while some of the σ-orbitals are pushed to higher binding energies. This feature can be seen for all adsorption geometries shown in Fig. 7.26(a). One can also observe that the hydrogen bond (configuration $\{2c\}$) shifts the σ_3-orbital to lower binding energies. As a general observation, the carboxylate group of PDCA is involved in all bonding molecular states like π_1 and σ_3 to σ_1.

For an interpretation of the experimental data of the PDCA molecules all dI/dV curves were plotted separately and compared with the calculated LDOS for the four different adsorption geometries. Due to the fact that all detected peaks are the same between $I_{Set} = 0.1$ and 0.3 nA the interpretation starts at 0.3 nA.

At first, a description of the unoccupied molecular orbitals, e.g., σ_1^*, π_1^*, and π_2^*, will be given here and an analysis of their behavior in dependence of the set point current. At 0.3 nA a first peak at +1.5 V and at 0.4 nA the appearance of a second peak at around +2.3 V are observed. With increasing current, both peaks then shift to lower energies whereas σ_1^* is not detectable. By combining the experimental peak energies with the LDOS calculations for the four possible adsorption geometries of the PDCA molecules (Fig. 7.26(a)), it can be concluded that the first appearing peak is related to the π_1^*-orbital and the second one to the π_2^*-orbital. Comparing the isosurface plots (Fig. 7.26(b)) of these two orbitals reveals that in all geometries the π_1^*-orbital has an extension at the carboxylic top group whereas the π_2^*-orbital is located mostly at the aromatic ring. Accordingly, if the tip is moved towards the sample, first the π_1^*-orbital and then the π_2^*-orbital should be detected, which is indeed the case. At closer distances the electric field of the tip causes the shift of these orbitals to lower energies as reported also for other π-conjugated systems [137]. Furthermore, the isosurface plots show a location of the σ_1^*-orbital direct at the copper surface, explaining that no detection is possible within the current window of experiment. From the analysis of the unoccupied MOs no differentiation between different adsorption geometries can be made. All LDOS fit more or less to the experimental dI/dV curves, visible on the right hand sides of the spectra in Fig. 7.27.

The occupied molecular orbitals , e.g., π_1, σ_3, σ_2, and σ_1, show a more complex behavior depending on the set point current. At I_{Set} = 0.3 nA two peaks are detectable in the experimental dI/dV spectrum beside the unoccupied π_1^*-orbital peak. The first peak appears as a sharp peak at around −2.6 V whereas the second one, at around −1.75 V, is broad and could be caused by monitoring two molecular orbitals. Comparing the isosurface plots leads to an expected appearance of the σ_3-orbital, of the σ_2-orbital in lower intensity, and eventually of the π_1-orbital at this tip-sample separation. Analysis of the top group related σ_3-peak shows that the experimental data do not fit to geometry $\{1\}$ and $\{2b\}$. These geometries can be excluded as the starting configuration of the PDCA molecules under investigation. With this we can conclude that the PDCA molecules are not adsorbed in configuration $\{1\}$. The two remaining conformations are both consistent with the experimental data (see Fig. 7.27(a)). In the case of conformation $\{2a\}$ both orbitals σ_3 and σ_2 can be assigned to the broad peak, whereas in conformation $\{2c\}$ the energies of σ_3 and π_1 are the same. At this set point, only the orbitals located in the upper part of the PDCA molecule are monitored. Decreasing the

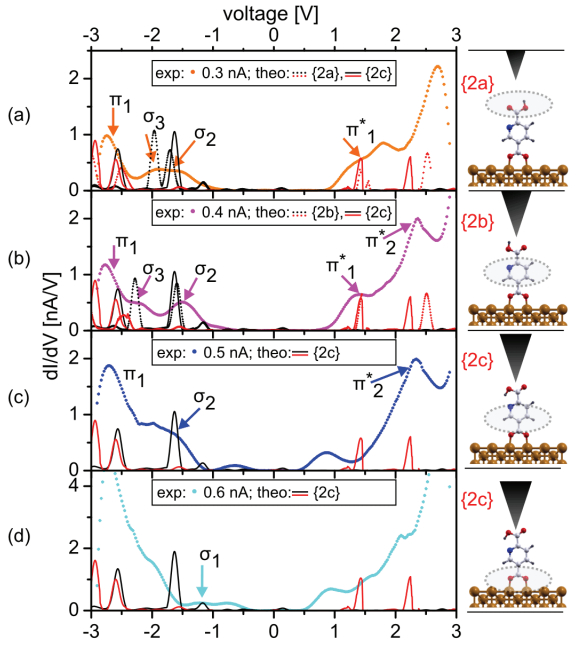

Figure 7.27: Experimental dI/dV spectra acquired on PDCA molecules on Cu(110) with varying current set points at $V_{Set} = -2.0\,\mathrm{V}$ and calculated LDOS with the σ- and π-orbitals marked in black and red. With increasing set point current (a-d) the PDCA molecules change their conformations. Outlined in the schematic plots on the right are the molecular parts detected as a function of tip height.

tip-sample distance, i.e., increasing I_{Set} to 0.4 nA, results in dI/dV spectra plotted in Fig. 7.27(b). Three occupied MOs are visible in the experimental spectrum. The peak at high negative energy, corresponding to the π_1-orbital, stays constant, whereas the σ_2-peak gets sharper at slightly lower negative energy. In between these peaks a new peak can be detected at around $-2.2\,\mathrm{V}$. Comparing again the LDOS calculations with the measured data and considering the shape of the MOs as revealed by the isosurface plots it can be concluded that conformation $\{2a\}$ is not compatible with the measured dI/dV curves whereas conformation $\{2b\}$ fits best. The middle peak is identified to be the σ_3-orbital. In the case of molecules like PDCA, a changing of conformations in dependence of the set point current is possible because the carboxylic top group can rotate around the C-C bond. Thus, experimental data point to a rotation in the presence of the applied electric field from conformation $\{2a\}$ to $\{2b\}$. The dI/dV spectrum at $I_{Set} = 0.5\,\mathrm{nA}$ shows a convergence of the π_1 and the σ_3 peak and they are recorded with high

intensity at −2.7 V. The conformation which fits best to the experimental data is here conformation {2*c*}, shown in Fig. 7.27(c). This again points to a rotation, in the way that the H atom of the top carboxylic group rotates around the C-O bond. Further lowering the tip position (0.6 nA) results in dI/dV curves reflecting also the molecular orbital located at the binding carboxylate group, i.e., σ_1 (Fig. 7.27(d)). This σ-type orbital is localized near the Cu(110) substrate and has an energy close to the Fermi energy.
Compiling the results of the detailed single set point analysis concerning the adsorption geometries shows that two interpretations are possible. A first possibility is that the investigated PDCA molecules are adsorbed in the stable conformation {2*c*}, with a hydrogen bond between the carboxylate top group and the nitrogen. In this case the dI/dV spectra at $I_{Set} = 0.4$ nA can not be fully explained by the present data. The second possibility is a combination of different conformations which are converted by rotations of the atoms of the carboxylic top group. Starting with conformation {2*a*}, the top carboxylic group rotates with increasing electric field, resulting in conformation {2*b*} at $I_{Set} = 0.4$ nA. The hydrogen atom is then located above the nitrogen atom and due to interactions, caused by the increasing electric field, the H atom of the carboxylic top group flips around the C-O bond. The molecule ends in conformation {2*c*} at $I_{Set} = 0.5$ nA. Recent publications have shown that a configurational change of a molecule on a metal surface can be imaged by STM [144, 145] and that a rotation of molecules in an increasing electric field can be monitored by a sequence of STM images [146]. Consequently, the change of electronic properties related to different adsorption geometries can be monitored by STS, as reported here.
In summary, this proves that distance dependent I-V spectroscopy can not only map the molecular orbital energies of the PDCA/Cu(110) system but also the spatial distribution of the different orbitals. While delocalized states like the unoccupied π-orbitals are monitored over a range of set points, the in plane localized σ-orbitals are observed at specific set points. Thus, combining DFT calculations and distance dependent STS enables an electronic mapping of molecules connected to a metal surface. Furthermore, the LDOS calculated for PDCA bonded to a metallic surface is used as a fingerprint for analyzing their adsorption geometries.

Additionally to the here intensively discussed I-V curves of PDCA on Cu(110) recorded with a negative tunneling voltage set point of $V_{Set} = -2.0$ V the same

data set was measured with a positive tunneling voltage set point of $V_{Set} = 2.0\,\mathrm{V}$ on the same molecules. An identical analysis, separately comparing occupied and unoccupied molecular states for different set point currents was done and shows a complementary molecular behavior. Plotting the experimental data together with the calculated LDOS for the different adsorption geometries above the Fermi energy shows the same peak appearance and no differentiation between different adsorption geometries can be made. All LDOS curves fit more or less to the experimental dI/dV curves. Comparing the experimentally observed peak positions for the occupied MOs shows that other adsorption geometries are monitored as in the case above described. Configuration $\{1\}$ ($C_7H_4N^{(2)}O_4$) can be excluded directly because the LDOS does not fit to the measured peak positions. Furthermore, conformation $\{2c\}$ (H-bond between the hydrogen atom of the top carboxylic group with the nitrogen atom of the ring) has to be excluded for all measured tip-sample distances because either the σ_2- or the σ_3-orbital peak are not in accordance with the theoretical data. Conformation $\{2b\}$ does not fit to the differential conductance curves at large tip-sample distances ($I_{Set} \leq 0.3\,\mathrm{nA}$) but at smaller ones and then it is the best fitting conformation. On the contrary, conformation $\{2a\}$ fits for large distances but for smaller ones the experimental data could only be described when including a large shift of all orbital energies. Compiling the results of the detailed single set point analysis concerning the adsorption geometries shows again a conformation change in presence of the electric field. Starting with conformation $\{2a\}$ the top carboxylic group rotates with increasing electric field, resulting in conformation $\{2b\}$ at $I_{Set} = 0.4\,\mathrm{nA}$. This conformation is then stable up to small tip-sample distance. This different behavior for positive and negative tunneling set point voltages is coherent because the set point voltage is applied directly before and after every voltage sweep. This means that in the case of positive set point voltages V_{Set} the tip is negatively charged before every I-V measurement and the measurement starts at positive bias voltages. Accordingly the hydrogen atom of the top carboxylic group will be attracted by the tip and points up.

7.6.1.2 The HOMO-LUMO gap

Since the LDOS near the Fermi level primarily defines the electronic transport through a metal/molecule/metal junction at small vacuum sizes the HOMO-LUMO gap is an important value to compare the electron transport properties

of different molecules within the same junction geometry. Due to the different adsorption geometry slightly different HOMO-LUMO gaps are found for pyridine-2,5-dicarboxylic acid on the Cu(110) surface. Due to the fact that the experimentally observed peaks match with the calculated ones table 7.5 summarizes these values and the mean value $\Delta E_{DFT} = 3.08\,e\mathrm{V}$ is used in the following in order to compare the electronic transport properties of different molecules by use of the energy gap size.

adsorption geometry	HOMO (σ_2) [eV]	LUMO (π_1^*) [eV]	ΔE_{DFT} [eV]
$\{2a\}$	-1.70	1.43	3.13
$\{2b\}$	-1.59	1.45	3.04
$\{2c\}$	-1.63	1.45	3.08
$\overline{x}_{arithm}$	-	-	3.08

Table 7.5: Compilation of the HOMO and LUMO energy values as well as of the energy gaps for all measured adsorption geometries. Additionally, the arithmetic mean of ΔE_{DFT} is listed in the last row.

7.7 Mixed Monolayers

Mixed monolayers play an important role for further applications of molecule/metal systems because, among others, single functional molecules can be inserted in an inert molecular layer and thus can be addressed very precisely. Furthermore, molecules which do not form monolayers by themselves can be integrated. Thus, functional monolayers can be achieved which are structurally better, more reproducible and which show less defects. Finally, diverse approaches have shown that the mixture of two molecules offers the chance for the formation of supramolecular units and hybrid structures with new and interesting properties [5,147]. As mentioned in the introduction of this chapter, carboxylic acid molecules could work either as active layer themselves or as matrix system for the insertion of functional molecules, e.g., redox- or light-active molecules. The possibility to fabricate mixed monolayers where a small amount of molecules is embedded into a SAM matrix of an other molecule type was tested for the carboxylate/Cu(110) system within the scope of this work. A proof of concept is given by inserting pyridine-2-carboxylic acid into a dense monolayer of benzenecarboxylic acid on the Cu(110) surface.

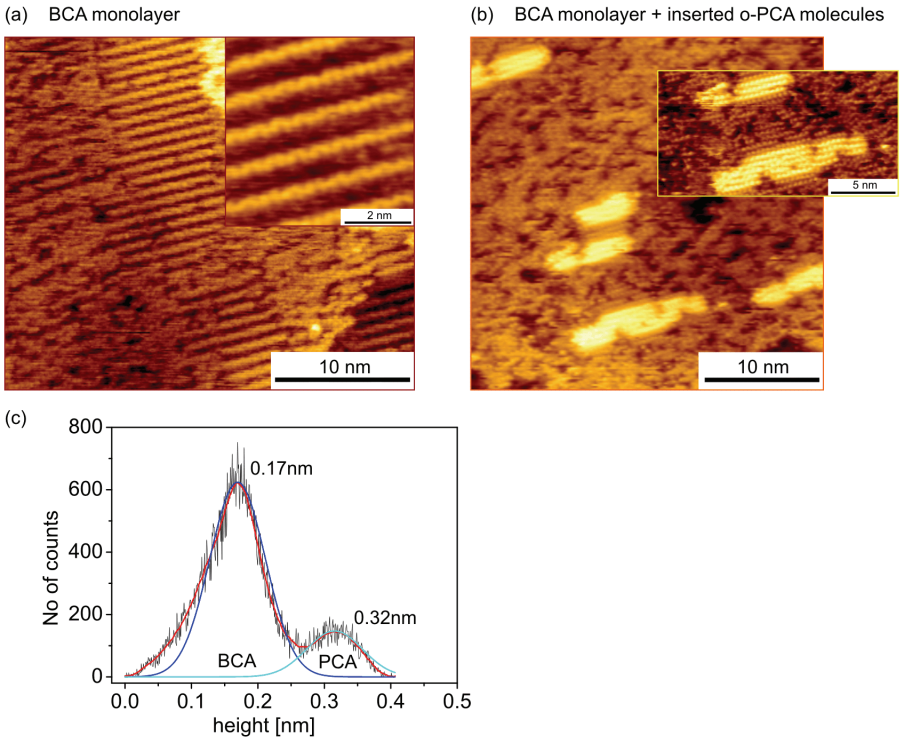

Figure 7.28: (a) Topography of the BCA monolayer before inserting host-molecules. Areas with c(8 × 2) structure are visible as well as close-packed defect rich areas but all molecules have the same height. (b) Topography scan of PCA inserted into BCA. Areas of ordered PCA molecules are visible, surrounded by BCA molecules. The PCA appear higher in STM although the geometrical height different is negligible small. Thus, the measured height monitors directly the difference in tunneling conductance between the two molecules. (c) These two heights are clearly visible in the height distribution histogram of the mixed SAM. Fitting two Gaussian peaks to the graph results in an average height difference of 0.15 nm.

First, benzenecarboxylic acid was deposited on the Cu(110) surface, as described in section 7.2, and topographic STM images show Cu(110) terraces with a monolayer coverage of uniform height. Close-packed areas as well as defect rich domains of upright molecules are visible but all molecular structures have the same height. Figure 7.28(a) shows a typical topography scan of the benzoate layer and the inset shows the c(8 × 2) domain structure in high resolution. In a second step pyridine-2-carboxylic acid was deposited on the sample and the result was investigated by STM. Figure 7.28(b) shows a STM scan of the SAM layer after PCA

exposure where new features are visible in the molecular coverage. Domains were imaged with molecular spots which appear brighter in the STM scan, attributed to pyridine-2-carboxylic acid molecules. These new domains are close-packed, highly ordered, and surrounded by small bunches of ordered benzenecarboxylic acid molecules, as visible in the high resolution inset of Fig. 7.28(b). This points to a combination of desorption of chemisorbed molecules and an insertion of new molecules during the adsorption process. Alternatively, an adsorption of PCA molecules at defect sites of the BCA layer and a reorganization of the surrounding molecules could take place but the low number of single PCA molecules contradicts this assumption. The height difference between the PCAs and the BCAs is determined by a topography histogram (Fig. 7.28(c)) and is $\sim 0.15\,\mathrm{nm}$ at a tunneling set point of $I_{Set} = 0.308\,\mathrm{nA}$ and $V_{Set} = 0.768\,\mathrm{V}$. Due to the fact that both molecules have nearly the same geometric length ($l_{BCA} = 0.599\,\mathrm{nm}$ and $l_{PCA} = 0.593\,\mathrm{nm}$) the STM detects here the differences in the tunneling conductance between the embedded PCA molecules and the surrounding BCA SAM. The better conductance of the PCA molecule compared to BCA results in a higher appearance of the PCA in STM. This shows that further investigations on this system can deduce the current transport properties of the embedded molecules from the STM height differences.
As described in detail in the last paragraphs (compare 7.3.2.3 and 7.5.1), the transport mechanism within the STM based junction changes for both molecules (BCA and PCA) from direct tunneling to molecule orbital mediated tunneling below 1.5 V. A quantitative evaluation of the conductance difference in terms of the decay constant β is, however, only possible if the topography image is taken at a voltage where both molecular systems have the same tunneling mechanism. Furthermore, an adequate approximation for the relation between the decay constants and the detected height difference is, up to now, only available for the direct tunneling regime (see Ref. [36, 37, 148] and section 3.1.2) and thus continuing studies on this system should be done with scan voltages of $V_{Set} < 0.5\,\mathrm{V}$ to get comparable decay constant values.

7.8 Conclusion

Electronic transport investigations on the carboxylate/Cu(110) system have been successfully performed for the first time. It was possible to fabricate close-packed

SAM of upright standing molecules for all investigated carboxylates. These structures were characterized electrically by STS and additional information could be grained from the theoretical calculations. Here, the focus was set on investigations which study how substitution of the various carboxylates chemisorbed on the Cu(110) surface influences the HOMO-LUMO gap.
In conclusion, it could be demonstrated that the molecular backbone and functional top groups influence the HOMO-LUMO gap. The experimental differential conductance curves confirm the theoretical LDOS results and one the other hand theoretical calculations can explain specifics in the experimentally observed curves. For instance the LDOS around the Fermi level is precisely predicted by DFT, as shown, e.g., in Fig. 7.6, or the absence of the σ_2 peak in the experimental conductance curve of BDCA due to a too small experimentally accessible voltage window can be explained by calculation (Fig. 7.15). It was found that carboxylic top groups as well as nitrogen substituents in the aromatic ring system lead to a reduction of the HOMO-LUMO gap. Combining both experimental ways of substitution, a reduction of the energy gap size in the order $\Delta E_{BCA} > \Delta E_{BDCA} > \Delta E_{PCA} > \Delta E_{PDCA}$ was observed. A detailed analysis of all molecular orbitals experimentally probed has shown that the calculated LDOS represents a characteristic fingerprint corresponding to the substitution pattern of the carboxylates bonded to Cu(110). With a detailed knowledge of the system parameters it should thus be possible to make precise theoretical predictions on the transport properties of other carboxylate species. But not only molecule specific molecular orbital distributions could be probed by STS, furthermore, it was impressively monitored that the detection of MOs is tip-sample distance dependent. The ring related π-orbitals were probed in a wide current set point range due to their delocalized character, whereas the σ-type orbitals are located directly at their related atom and thus were detected only in between a small distance window. A detailed distance dependent current-voltage study in combination with energy calculations for pyridine-2,5-dicarboxylic acid has shown that it is possible to identify different adsorption configurations and conformations within one molecule under continuously varied experimental conditions. A conformational change of the detected molecules caused by the applied electric field between tip and Cu substrate could be monitored. In addition, it was found that the chemical bond formed between the respective carboxylate and the copper surface is not influenced by the HOMO-LUMO gap of the molecule. The related occupied MO σ_1 stays at a constant energy for all molecules under investigation.

Furthermore, it has been shown that system parameters like the tunneling junction symmetry or the local tunneling barrier height can be extracted from I-V characteristics. Within the approximations of a coherent molecular transport model, an estimation of the absolute value of the vacuum gap size could be made for different set point currents. Typical values for the vacuum gap sizes were found to be between 0.4 and 0.1 nm.
The tunneling process had been further studied by transition voltage spectroscopy and for all investigated molecule species a transition between direct tunneling at large tip-sample distances and molecule orbital mediated tunneling for smaller distances was found. The onset of this molecule orbital mediated tunneling is molecule specific and follows the LDOS structure precisely.
Current-distance spectroscopy measurements were performed primarily on pyridine-2-carboxylic acid and the tunneling decay constant of the pyridine unit was measured to $\beta_{Pyridine} = 3.9\,\mathrm{nm}^{-1}$.
First investigations on the fabrication of a mixed carboxylate monolayer on the Cu(110) surface show a successful embedding of pyridine-2-carboxylic acid into a benzenecarboxylic acid layer. Both molecules have a nearly identical geometrical length but pyridine-2-carboxylic acid appears higher (brighter) in the STM topography images of the mixed layer, confirming the smaller decay constant of the pyridine unit compared to the already known decay constant of the phenyl unit ($\sim 4.2\,\mathrm{nm}^{-1}$).

8 2,3-dihydroxy-4(thiomorpholinomethyl) benzoic acids on Au (111)

A further step towards an application of functional molecules is the investigation of molecules which can be connected to different metal electrodes in a predefined way. Based on the investigations of carboxylic acids which reliably bind on Cu(110) surfaces, as reported in the last chapter, molecules with a carboxylic end group and a second, functional end group on the other molecular side become interesting. With the 2,3-dihydroxy-4(thiomorpholinomethyl) benzoic acids (TMBA) a promising molecule was found which combines the carboxylic end group with the well studied sulfur end group. The TMBA molecules can be connected with the carboxylate groups to a copper surface and with the thioether groups, e.g., to a gold surface. Additionally, these molecules act as ligands for the building of organometallic complexes, similar to the complexes presented in [149]. The molecules as well as various complexes were synthesized by M. Baumert [150] in the group of Prof. M. Albrecht at the Institute of Organic Chemistry at the RWTH Aachen University. Thus, TMBA molecules can either work as molecular diode, asymmetrically connected between two metal electrodes, or as host-matrix for single organometallic complexes. A schematic drawing of the ligand and a related titanium complex is given in Fig. 8.1.

Indispensable prerequisite for these applications is a self-assembly behavior of the ligand on one, at best on both, metal substrates and thus investigations on the self-assembly behavior of TMBA on Au(111) surfaces will be presented in this chapter. Additionally, the insertion behavior of TMBA molecules into an insulating molecular matrix system, here octanethiol (C8), will be reported. Beside the structural study, this chapter will give first insights on the electronic properties of the ligand system, pure as well as in the octanethiol environment. The

STM based investigations are supplemented with XPS and UV-VIS spectroscopy measurements.

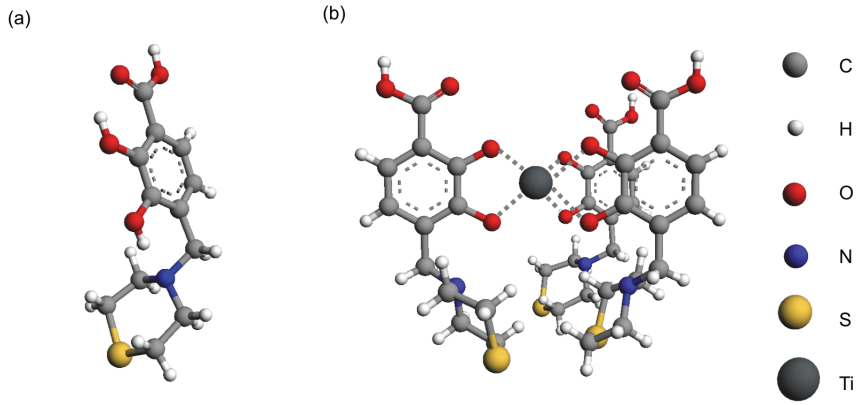

Figure 8.1: Schematic drawing of the 2,3-dihydroxy-4(thiomorpholinomethyl) benzoic acid (TMBA) molecule (a) and a related titanium complex (b).

8.1 Experimental details

Crystalline gold thin films with a (111)-orientation were used as templates for the self-assembly of TMBA molecules. The gold films were fabricated by evaporation on mica substrates as described in section 6.1. To avoid adsorbates on the gold surface the samples were used directly after fabrication or were stored in DMF. TMBA was synthesized and purified at the Institute of Organic Chemistry at the RWTH Aachen University in the group of Prof. M. Albrecht [150] and was used as received. For all studies the molecules were dissolved in DMF as millimolar solution. The monolayers were prepared by wetting the gold surface with one drop of solution. After several minutes the samples were rinsed with DMF and immediately transferred into vacuum. The average thickness of the resulting molecular layer is strongly dependent on the exposure time and multilayer growth occurs when wetting the samples for several hours due to the slow evaporation of DMF.

All UHV-STM investigated samples were prepared with a molecular exposure time of less than five minutes, resulting in submonolayer to monolayer cover-

ages. Additional samples for XPS analysis were prepared by wetting the sample for 24 h to achieve molecular multilayers. For insertion experiments octanethiol ($CH_3(CH_2)_7SH$) was used as matrix molecule and employed as purchased from Sigma-Aldrich. The gold samples were exposed to a millimolar solution of alkanethiol solved in ethanol for around 24 h, then immediately transferred to vacuum and characterized by UHV-STM. After analysis, the samples were taken out of the vacuum system and were wet with the TMBA solution for several hours. After deposition the samples were rinsed with DMF, transferred into vacuum, and characterized again. All films were investigated by imaging in constant-current mode and electronically characterized in spectroscopy mode with UHV-STM. Homemade electrochemically etched tungsten tips were used as STM-tips.

Photoelectron spectroscopy was performed to determine the binding chemistry, packing density, and purity of the prepared TMBA SAMs after STM investigation. Thus, XPS spectra were recorded with a XPS 5600 system (Physical Electronics, USA) using a monochromatic Al-K_α X-Ray source at 13 kV and 300 W. The photoelectrons were collected by the spectrometer in normal emission geometry. With a X-ray monochromator and a pass energy of 11.75 eV for the analyzer, an instrumental energy resolution of 0.1 eV was achieved. The energy scale was referenced to the Au $4f_{7/2}$ line at a binding energy of 83.7 eV. For monolayer and multilayer samples survey and high resolution spectra of the S 2p, C 1s, O 1s and Au 4f region were recorded.

Additionally, UV-VIS adsorption measurements were done on the TMBA molecules dissolved in DMF as millimolar solution.

8.2 Structure characterization of TMBA monolayers

First, pure monolayers of TMBA are investigated by STM and STS as well as by XPS. In Fig. 8.2 a characteristic STM scan of a TMBA self-assembled monolayer, prepared with a molecular exposure time of 2 min, is shown. The topographic survey scan shows the typical terrace character of the gold surface and a molecular coverage of slightly below one monolayer. Three types of domains can be distinguished on the surface: one with a disordered arrangement of TMBA molecules, denoted as “A” in the following, one with a striped pattern (“B”), and a third domain type with a solid like surface (“C”). Ordered areas are localized

between disordered areas and striped pattern can be found everywhere on the sample whereas the solid type areas are often connected to step edges. Topography scans with a smaller scan size show the different domains in more detail and allow a further characterization in case of domain structures, unit cells, or molecular superstructures.

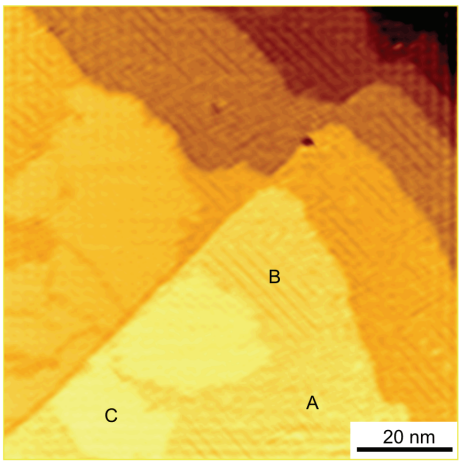

Figure 8.2: $90 \times 90\,\mathrm{nm}^2$ large STM topography scan of a TMBA self-assembled monolayer grown on a crystalline Au(111) surface (exposure time: 2 min). Monitored are several gold terraces and three different domain types, denoted as "A", "B" and "C". The TMBA molecules form disordered structures (A), structures with a striped pattern (B) and solid type domains structures (C).

Thus, Fig. 8.3(a) shows a STM topography scan with a size of $67 \times 67\,\mathrm{nm}^2$. Three different domain types are visible again but now a histogram and height profiles can monitor further differences in the molecular structures. The height profile in Fig. 8.3(b) displays a height difference between the two terraces of 0.24 nm, equal to an atomic gold step height. A second step is measured to be 0.14 nm between the striped pattern area and the solid type domain. This height difference is associated with a domain boundary between lying-down and standing-up molecules, as described in [79, 151] for the comparable alkanethiol/Au(111) system. Accordingly, domains of type "B" consist of lying-down molecules and type "C" domains of standing-up molecules. A height distribution histogram (Fig. 8.3(c)) of the scanned area shows three distinct peaks equivalent with the presence of three different heights within the scanned area. Fitting Gaussian peaks to the

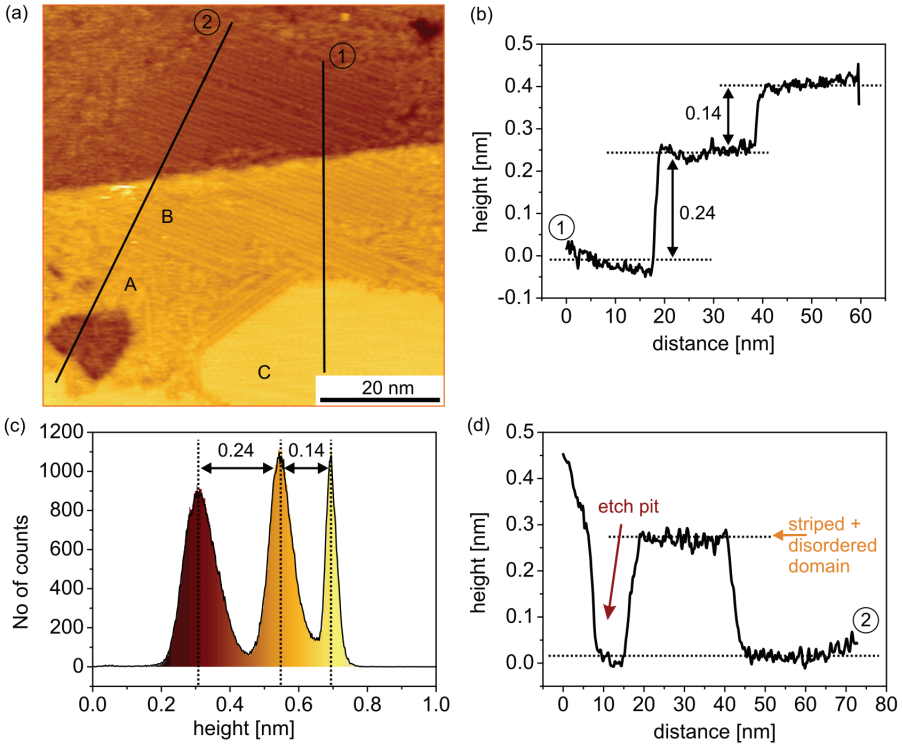

Figure 8.3: (a) STM scan of the TMBA monolayer surface on Au(111). The scan is taken over an area of $67 \times 67\,\mathrm{nm}^2$ with tunneling parameters of $I_{Set} = 0.46\,\mathrm{nA}$ and $V_{Set} = 0.36\,\mathrm{V}$. (b) Height profile along line 1, marked in (a), showing a terrace height of one gold layer and the height difference between lying-down and standing-up molecules. (c) Histogram showing again the surface heights but additionally the peak width distribution. (d) Second height profile which shows that the disordered and the striped structures have the same height and that the hole in the upper layer is one gold atom deep (0.24 nm).

graph results in an average height difference of 0.24 nm between the first and the second peak and 0.14 nm between the second and the third one which verifies the heights measured in the line scan. Thus, the first peak is related to the striped and disordered areas on the lower molecule terrace, the second peak to the striped and disordered areas of the higher terrace, and the third peak is related to the solid type domains. Additionally, the peaks have different width distributions which indicates larger height fluctuations in the lying-down than in the standing-up phase. A second height profile (Fig. 8.3(d)) across an area of lying-down

molecules forming the line pattern ("B") and a disordered area ("A") shows no height difference and accordingly the disordered domains consist also of lying-down molecules. Finally, the second line scan crosses a small hole in the upper terrace with a depth of 0.24 nm. This height corresponds exactly to one atomic gold step and due to the fact that the bottom of the hole is covered with molecules it can be identified as so called "etch pit". These etch pits, or vacancy islands, are a common feature seen for sulfur coupled molecules on (111)-oriented gold surfaces [20]. They are formed during the molecular assembly process when the herringbone reconstruction of the gold surface is lifted due to the formation of chemical or coordination bonds between the thioether head groups and the gold surface.
The presence of etch pits on the surface initiates further studies regarding the interaction between the TMBA molecules and the gold surface. The presence of etch pits indicates strong interactions between the molecules and the sample but their number and size is significantly smaller than for alkanethiol or dialkyl disulfide SAMs. Due to the sulfur end group on one side of the TMBA molecule the main interaction between molecule and gold surface will be on this side. In principle there are two possibilities for the TMBA molecule to adsorb on the surface. Either it can chemisorb on the surface by a dissociated adsorption process related to the cleavage of the S-C bond in one of the dialkyl sulfide sidearms, leading to a gold bound thiolate such as those formed from alkanethiols and dialkyl disulfides, or by an adsorption without dissociation such as for dialkyl sulfides. Furthermore, it can physisorb on the surface like dialkyl sulfides in low-coverage structures [83].

8.2.1 XPS analysis

To reveal the interactions between TMBA molecules and the gold surface XPS spectra were performed on TMBA mono- and multilayer samples. Figure 8.4 shows an overview of the substrate/molecule related XPS core level spectra. Explicitly, part (a) shows the XPS spectrum in the Au 4f region with the main peak at 83.7 eV which is used for calibrating the binding energy as a system standard.
XPS core level spectra in the S 2p region of the TMBA monolayer on Au(111) were taken to get detailed information on the bonding situation of the sulfur head group. A strong triplet peak was detected for the TMBA monolayer with components at

160.9 eV, 161.8 eV, and 162.9 eV. Each of these sulfur 2p components consists of a S $2p_{1/2}$/S $2p_{3/2}$ doublet separated by 1.18 eV with an intensity ratio of 1:2 [152].

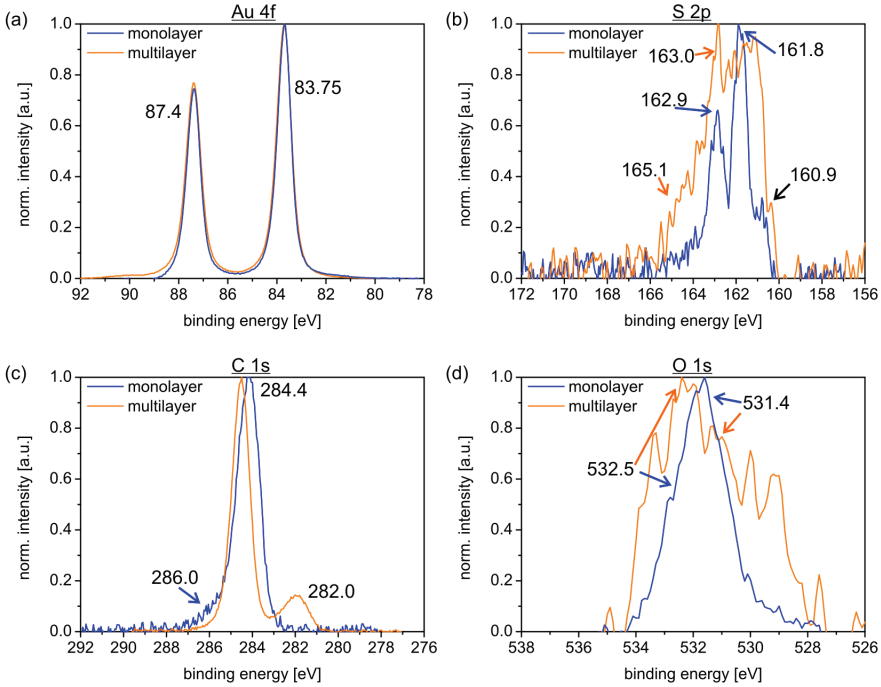

Figure 8.4: High resolution XPS spectra of a TMBA monolayer and a TMBA multilayer on Au(111). The Au 4f core levels (a) have their main peak detected at 83.75 eV and are used for calibration. The S 2p core level spectra (b) show a broad multi peak which is related to three components at energies of 160.9 eV, 161.8 eV and 162.9 eV. An additional peak is detected at 165.1 eV only for the multilayer and can be related to intermolecular interactions (C-O-H··S) inside the multilayer. The TMBA related C 1s core levels are shown in (c) with a main peak, related to the C-C and C=C bonds at 284.4 eV, and a second peak, related to the C-S-C bond inside the molecule at 286 eV. After peak fit analysis the O 1s core level spectra (d) are separated in two peaks related to responses from the C-OH group (531.4 eV) and the COOH group (532.5 eV) with a ratio of 2:1.

Figure 8.5 shows this triplet peak and as guide to the eyes the three single contributions are highlighted by Gaussian peaks which fit well to the main S $2p_{3/2}$ parts. The main peak was detected at 161.8 eV, a medium one at 162.9 eV and a smaller peak at 160.9 eV. The main peak at 161.8 eV is related to chemisorbed sulfur and is almost identical to the peak reported for alkanethiol or dialkyl disulfide SAMs [153]. It is also reported in literature for monosulfides and tetrahydroth-

iophene and it is assumed that the $\sim 162\,eV$ binding energy can be produced without C-S cleavage. That means that sulfur in the monosulfide can bind onto the Au surface in the same configuration as alkylthiolates without C-S cleavage and can exhibit this peak [153, 154]. For the TMBA SAM system investigated here this proves that the molecules bind chemically on the surface and it points to a non dissociated adsorption mechanism.

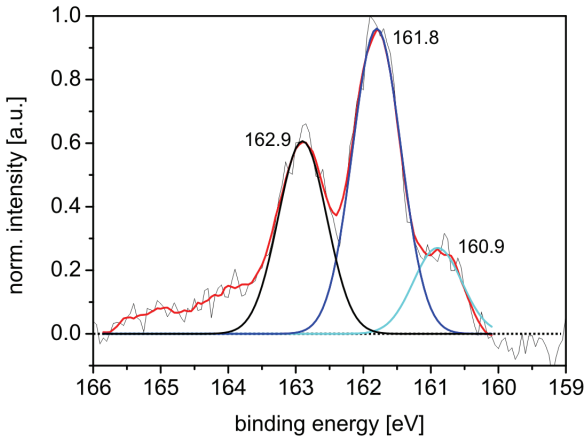

Figure 8.5: High resolution XPS spectrum of a TMBA monolayer on Au(111). The S 2p core levels are displayed with components at 160.9 eV, 161.8 eV, and 162.9 eV. The main peak as well as the smallest one is related to chemisorbed sulfur on gold. Here, all peaks are highlighted through their related Gaussian peak fit.

An additional chemisorbed sulfur related peak with a weak intensity was observed at 160.9 eV. The origin of this sulfur peak is not ascertained and various possibilities are discussed in literature. This peak can be explained by different assumptions: it may result from atomic sulfur [153, 155], differently bound sulfur resulting from a change in the adsorption configuration of the molecules [153, 156], or from a change in the adsorption site of the sulfur atoms on the Au(111) surface [153, 157]. The peak form, as detected for the TMBA monolayer here, was observed for other molecules with a similar molecular backbone, like tetrahydrothiophene, leading to the suggestion that there is a change in the adsorption sites or configurations. Different domain structures were found by STM investigations (as reported above) on the TMBA monolayers which indicates different adsorption geometries and thus gives an explanation for the peak detection.

The third peak, with a weak intensity, was observed at 162.9 eV and is assigned to unbound sulfur. It is usually found in SAMs of complex molecules or dialkyl monosulfides and for these systems the peak is the main peak. In the case of the here investigated TMBA molecule, or the similar tetrahydrothiophene molecule, the bond peak at 161.8 eV is much more pronounced. This result implies that the sulfur atoms embedded in the TMBA molecular ring system exhibit stronger adsorption activity than those in dialkyl monosulfides. However, the peak appearance can be related to the special surface structure of the investigated samples. The above shown STM topography scans (Fig. 8.2 and 8.3) show small areas of disordered lying down molecules which are typically only loosely bonded to the surface (over van der Waals interactions or similar) and thus can cause this peak appearance.

For multilayer films this third peak at 162.9 eV was detected with the same intensity as the second peak at 161.8 eV (compare Fig. 8.4) simply indicating that the presence of unbound sulfur increased during multilayer growth due to the molecule saturated gold surface. Additionally, a fourth peak appears in the XPS spectra of TMBA multilayers at 165.1 eV which can be related to intermolecular interactions between the carboxylic groups and the thioether groups of the unbounded molecules.
As mentioned at the beginning of this paragraph, XPS core level spectra were taken also of the C 1s and O 1s region. They prove the adsorption of TMBA as complete molecule onto the gold surface due to the detection of components of all parts of the molecule. The XPS spectrum of the C 1s region (Fig. 8.4(c)) monitors a small peak at 286 eV which is related to the C-S-C bond, and one pronounced peak at 284.4 eV, related to C-C (C=C) bonds. Both the peak shape of the second peak as well as the ratio between these two peaks show that all carbon atoms are detected within the pronounced peak. Especially the components related to the benzene ring (284.4 eV) are assigned. Furthermore, the XPS spectrum of the O 1s region (Fig. 8.4(d)) shows both the hydroxyl groups (531.4 eV) and the carboxyl groups (532.5 eV) in the TMBA related ratio 2:1.

8.2.2 Low coverage phases

To pursue the structural identification of the TMBA monolayer various high resolution STM scans were taken on the different domain structures. This paragraph

focuses on the low coverage domains (noted with "B" in the survey scans) with a structure of ordered, flat-lying molecules whereas the next paragraph describes the molecular structures within the high coverage domains of standing-up molecules ("C").
High resolution STM topography scans of the striped pattern "B" monitor variations in the domain structures and Fig. 8.6(a) shows some of them. The bright spots which build narrow bright lines are conspicuous. Due to the fact that the molecules are chemically bounded to the Au(111) surface via the sulfur atoms, this main protrusions can be related to the thioether head groups. Three different domain orientations are present on the surface according to the directions of the stripes, each orientation differing by an angle of 60°. This 3-fold rotational symmetry is caused by the underlying gold pattern, as investigated in detail for the comparable alkanethiol/Au(111) system [20]. Fig. 8.6(a) shows a part of the surface with mainly one row direction but two lines in the center of the scan are rotated by 120°, displaying a second orientation. Beside these different domain orientations, various domain structures were found on the surface which consist of rows running into the same direction and separated by dark areas but the inter-row distance changes between the structures. Two different domain structures are easy to distinguish in the STM image of Fig. 8.6(a) and are denoted as structure "B1" and "B2".

Structure "B1" consists of alternating bright and slightly darker narrow rows separated by dark spaces. Height profiles, such as shown in Fig. 8.6(b), across the lines monitor this alternating character with a structure periodicity of $b = 2.0 \pm 0.20\,\mathrm{nm}$. An exact analysis of the "B1" domain yields a periodicity of $a = 0.49 \pm 0.05\,\mathrm{nm}$ inside the rows. This distance is equal to the NNN-distance of the Au(111) surface pattern which is calculated to $\sqrt{3}a_0 = 0.49\,\mathrm{nm}$, with the gold lattice constant a_0. Accordingly, the thioether head groups are bonded to adjacent gold adsorption sites, extending in the $[11\overline{2}]$-direction. Beside the different height appearance an inversely phased spot appearance is found for neighbored rows. Thus, the unit cell vectors are $a = 0.49 \pm 0.05\,\mathrm{nm}$ and $b = 2.00 \pm 0.20\,\mathrm{nm}$ with an angle of $90° \pm 1$, which is equal to a (p×$\sqrt{3}$) unit cell with $p = 7$. This unit cell type is well known because many investigated structures of flat-lying alkanethiols show these $(p \times \sqrt{3})$ structures. The values for p comply with molecular length and surface coverage [151]. Although the STM scans allow to propose the unit cell with a high accuracy it is not possible to propose a detailed model of the molecular footprint

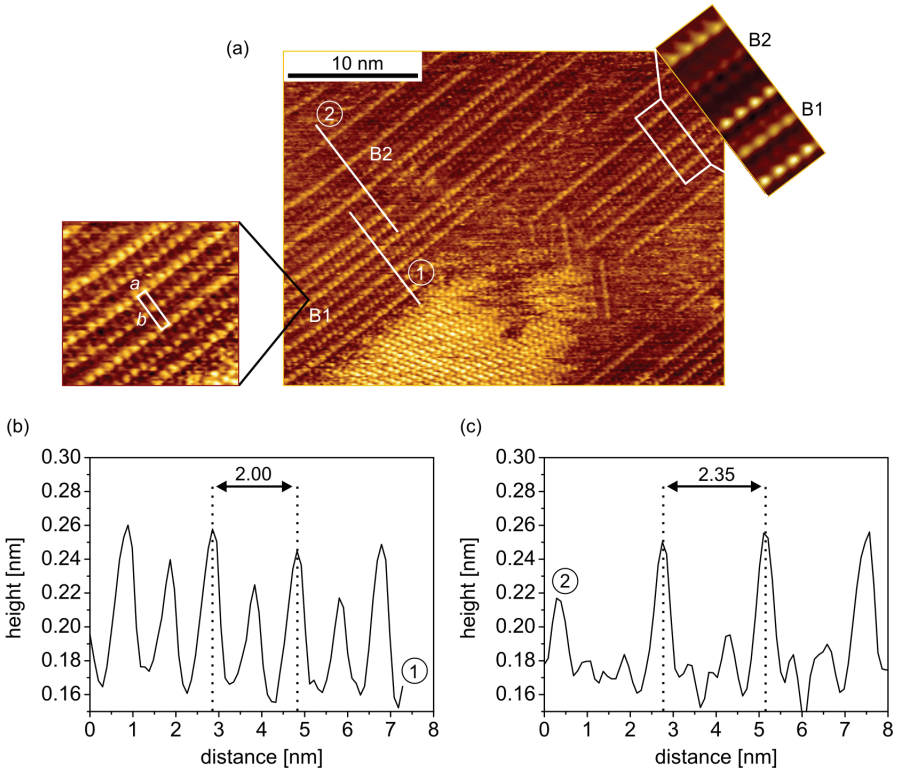

Figure 8.6: STM topography scan of different, low coverage domain structures of TMBA molecules on Au(111). The flat-lying molecules form various striped patterns on the gold surface. Two different periodic structures are visible and denoted with "B1" and "B2". The distance between two bright spots in one row is always $a = 0.49 \pm 0.05$ nm but the inter-row distance changes between the structures and also alternates inside one structure. The inset on the left hand side of (a) shows a zoom-in on structure "B1", highlighting the antiphase appearing of the spots in neighbored rows. Line scans are taken on the structures perpendicular to the bright rows for structure "B1" (b) and "B2" (c), monitoring the different inter-row distances. Additionally, the small inset of figure (a) shows a submolecular resolution image of a domain boundary between a row periodicity equal to that in structure "B1" and a second one equal to that in structure "B2". Note that in this special case the spots are all in-phase.

on the Au(111) surface. Only molecular moieties with intramolecular, intermolecular, or molecule/substrate interactions are detected by STM, giving hints to the real submolecular structure. In the case of structure "B1", collecting all measured data, the geometric length of a stretched TMBA molecule (~ 1.09 nm), and comparable structures reported in literature, points to a structure with two molecule

per unit cell ($\approx 0.49\,\mathrm{nm}^2$ per molecule). The sulfur head group atom is located at one corner of the unit cell and the molecule is oriented along the diagonal of the unit cell. The additional bright spot in the center of the unit cell monitors a high density of states at this point which can be caused by hydrogen bonds connecting the carboxylic end groups of two neighbored molecules. Such H-bonded carboxylate systems are known and reported in literature, e.g., for superstructures of BDCA molecules [158]. Furthermore, a slight overlap of the molecules at this point is possible and can not be excluded.

The second regular striped pattern ("B2") also consists of bright narrow lines with spots in a distance of $a = 0.49 \pm 0.05\,\mathrm{nm}$. These bright spots are related to the thioether head groups of the TMBA molecules, as described above. Neighbored rows are separated by wide dark spaces but in this pattern all rows have the same height. Additionally, the spots of neighbored rows are in-phase with a distance of $b = 2.35 \pm 0.24\,\mathrm{nm}$. One corresponding height profile rectangular to the rows is plotted in Fig. 8.6(c). The structure can be described through a rectangular $(p \times \sqrt{3})$ unit cell with $p = 8$ and a possible molecular packing configuration is a head to head configuration of molecules oriented along the large unit cell vector b. With a packing density of around $0.58\,\mathrm{nm}^2$ per molecule the "B2" structure is comparable to values reported for relaxed alkanethiols of similar molecular length [79]. The inset of Fig. 8.6 shows some further details of the molecular structure within the unit cell. Only small perturbations are visible in the wide dark spaces between the bright rows which shows that no hydrogen bonds exist between faces molecules. The perturbations can be related to the top carboxylate groups of the molecules or to interactions between the flat-lying π-system and the underlying gold substrate, dependent on the molecular tilt. Furthermore, slight variations in the peak appearance between faced molecules are visible, also recorded in the height profile of Fig.8.6(c), pointing to a slightly shifted molecular backbone structure. This shift can be caused by intramolecular hydrogen bonds or by intermolecular interactions between neighbored molecules.

A third molecular structure, denoted as "B3" in the following, with a striped pattern was found in the immediate vicinity of structure "B1" and "B2". Figure 8.7(a) shows a STM scan of the TMBA covered Au(111) surface with a large "B3" domain. Line scans along the NN- and NNN- directions are plotted in Fig. 8.7(b,c) showing a regular peak appearance inside the bright rows (b) but a more complex periodicity in between the rows (c). Bright rows, denoted as "H", alternate with

slightly darker appearing rows ("L") and the height difference can be measured to around 0.06 nm. Succeeding rows with the same intensity have an antiphase spot appearances (i.e., HH′HH′...), leading to slightly different peak distances (b', b'') in the line scans and the periodicity between equal rows gets $b = b' + b'' = 3.75 \pm 0.38$ nm. The distance of two spots in one row is measured to $a = 0.49 \pm 0.05$ nm and the "B3" structure can thus be described as c$(p \times \sqrt{3})$ structure with $p = 13$.

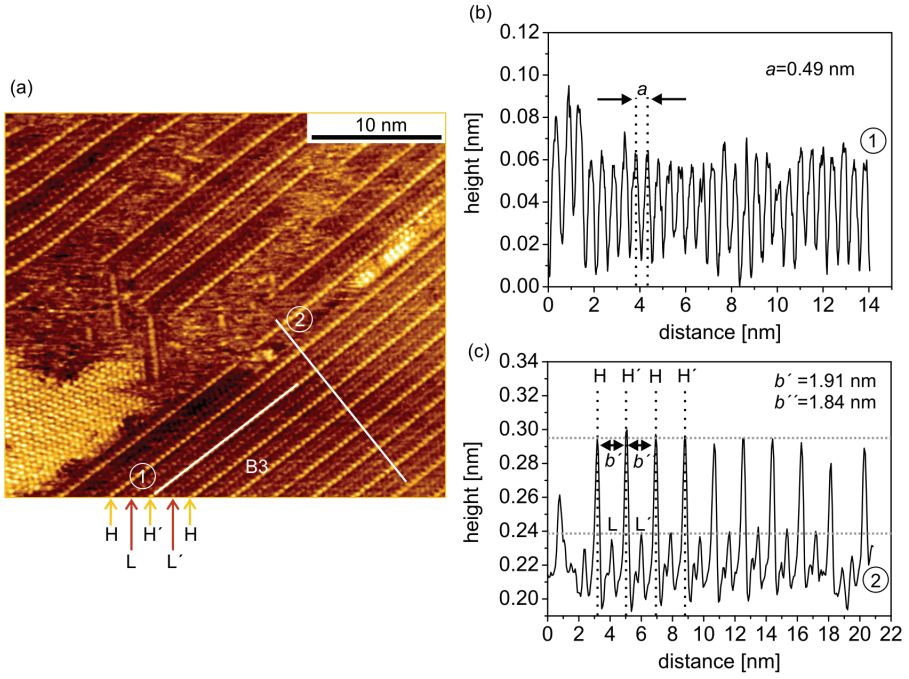

Figure 8.7: (a) STM topography scan of a third low coverage phase of TMBA on Au(111). The TMBA molecules build large defect poor structures and the spot distance in one row can be measured from line scans (b) to $a = 0.49$ nm. Neighbored rows have an alternating row sequence (HH′HH′) displayed in a line scan across the rows (c).

Taking these values and high resolution scans of the domain structure, like in Fig. 8.8(a) where additional molecular features are visible, allows to propose a detailed model of the molecular orientation on the Au(111) surface. The high resolution scan resolves the dark areas in between the bright rows in more detail and various small perturbations become visible. The pattern of every second area looks the same which leads to the suggestion of four molecules within the length of one

unit cell vector b. The molecules bind with their sulfur head groups to the gold surface and thus the bonded sulfur atoms are again related to the bright spots, building rows along the $[11\bar{2}]$-direction of the underlying gold substrate, whereas now two sulfur atoms build one bright spot. Assuming one of these sulfur atoms as situated on a triple hollow site the second one has to bind on a bridge site [159]. The peaks in every second bright row are shifted by half of the unit cell vector a. This shift corresponds to a change in the adsorption place for the sulfur atom from, e.g., hcp to fcc or vice versa. Positioning flat-lying molecules into the unit cell and assuming a slightly tilted molecule leads to a face to face configuration for the carboxylic end groups, as depicted in Fig. 8.8(b). Thus, H-bonds are probable yielding the slightly darker appearing rows. In principle, two molecular units, the nitrogen atom and the phenol ring, can cause a higher local electron conductance but due to the tilt inside the molecule only one additional spot per bounded molecule is likely. Accordingly, different rotated molecules cause the two pattern in the dark appearing areas.

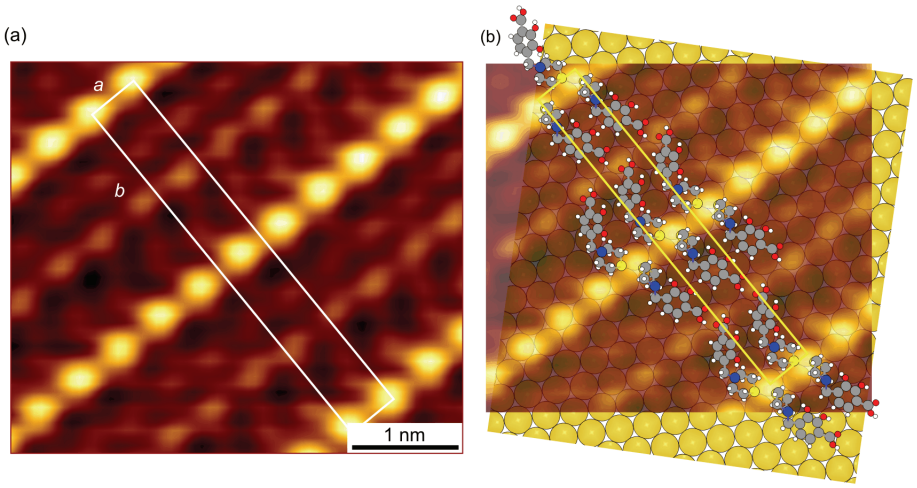

Figure 8.8: (a) High resolution image of the c($13 \times \sqrt{3}$) structure of TMBA on Au(111) with features of the molecular structure. Marked is the rectangular unit cell aligned at the bright thioether head group related features. (b) Three-layer model of the molecular orientation inside the structure with respect to the underlying gold substrate. The molecules are flat-lying on the surface in a slightly tilted configuration such that either the aromatic ring system is oriented flat on the underlying substrate or the nitrogen atom points up. The middle layer is added to the model to highlight the parts of the TMBA molecules which are visible in STM.

The resulting picture of the molecular orientation with respect to the underlying Au(111) surface is illustrated in Fig. 8.8(b). Beside the molecules and the gold lattice, spots highlight the molecular parts detected by STM. The mapping of the molecular features is surely not unambiguous but X-ray diffraction analysis on the crystal structure of the TMBA related carboxylate ester show exactly this tilted molecule symmetry. However, the molecular structure looks like there are four molecules per unit cell corresponding to a molecular footprint of $0.46\,\mathrm{nm}^2$ per molecule.

8.2.3 High coverage phases

Standing TMBA molecules, as observed in domain type "C" of Fig. 8.3, form highly ordered long range domains with a hexagonal unit cell. Additionally, domains with areas of $> 100\,\mathrm{nm}^2$ show distinct striped pattern related to superstructures. Two different superlattice structures can be identified for the TMBA molecules on Au(111) and will be described in detail in the following.

Figure 8.9(a) shows one gold terrace covered with TMBA molecules. The molecules are close-packed upright standing and ordered in domains. Different domains are separated by boundaries appearing as dark lines and rotational boundaries as well as antiphase boundaries can be identified. Two domain boundaries are marked in the STM image with black arrows, one has a very thin boundary region and one consists of a relatively large, smooth transition. These domain boundaries connect domains with different stripped patterns and different unit cell alignments which are highlighted in the image with red rectangles. Additionally, three different orientations of the domains are visible according to the directions of the stripes, each orientation differing by an angle of 60°. The domains in the lower part of the STM image have these three different orientations (marked with black lines) and the orientation in the fourth domain (upper part) is then equal to one of those. Figure 8.9(b) shows a high resolution scan of one domain and single molecules can be seen as protrusions. Cross sections along the NN- and NNN-directions yield a hexagonal unit cell with a vector of $a = 0.48 \pm 0.05\,\mathrm{nm}$. This lattice constant agrees with a $(\sqrt{3} \times \sqrt{3})\mathrm{R}30°$ unit cell with respect to the underlying gold surface structure. This structure is the basis of many superstructures for alkanethiol SAMs on Au(111) (compare section 5.4.1) and due to the fact that TMBA molecules adsorb also with a sulfur head group on the Au(111) surface

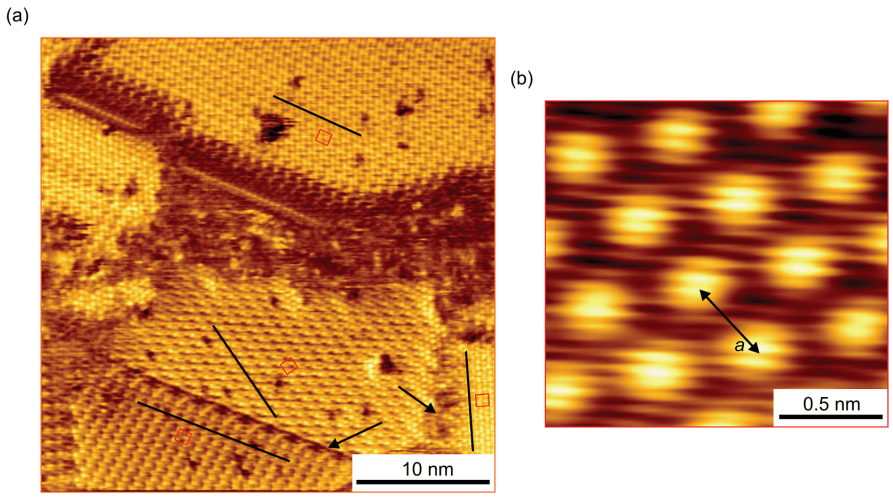

Figure 8.9: (a) STM Topography scan of a domain structure of standing TMBA molecules on Au(111). A typical domain structure with different unit cell orientations (red rectangles) is visible. The domains show a striped, superstructure related, pattern and are separated by domain boundaries which appear as dark lines or areas in STM (arrows). All three rotational symmetries are visible with the typical, gold lattice related, 120° angle in the lower part of the image (marked with black lines). The fourth domain in the upper part of the scan has consequently the same orientation as one of these three. (b) High resolution STM scan of the hexagonal unit cell of small domains without observable superlattice. The lattice vector $a = 0.48 \pm 0.05$ nm correspondents to the NNN-distance of the underlying gold substrate.

the present structure is denoted as α-phase [160]. The footprint of the TMBA molecules can be deduced to $0.216\,\mathrm{nm}^2$, the value as in the case of alkanethiols, dialkyl disulfides or cyclic dialkyl sulfides [154]. This points to a very dense packing of the standing TMBA molecules, however, it is in accordance with the space required for one molecule threaded in the lines of the striped phases.

With larger domain sizes superstructures with inequivalent molecules per unit cell become visible. Figure 8.10(a) shows a detail scan of a domain of around $500\,\mathrm{nm}^2$ size where the molecules can be seen in a striped pattern formed by the molecule protrusions of different heights. In high resolution scans (Figure 8.10(b)), the unit cell of the superstructure can be resolved and the unit cell parameters can be measured to $a = 0.77 \pm 0.08$ nm and $b = 0.97 \pm 0.10$ nm with an angle of $88.6 \pm 2°$. Three different heights are detectable in the height profile of Fig. 8.10(c). Fitting this structure to the underlying gold lattice shows that this unit cell is comparable

to a $(3 \times 2\sqrt{3})$ structure or, in analogy to alkanethiols, corresponds to the ϵ-phase of the c(4×2) structure [161, 162]. The variation of the unit cell compared to the theoretical values of $a = 0.865\,\text{nm}$ and $b = 0.999\,\text{nm}$ can be explained by the different twist angles of the TMBA molecules in close-packed arrays.

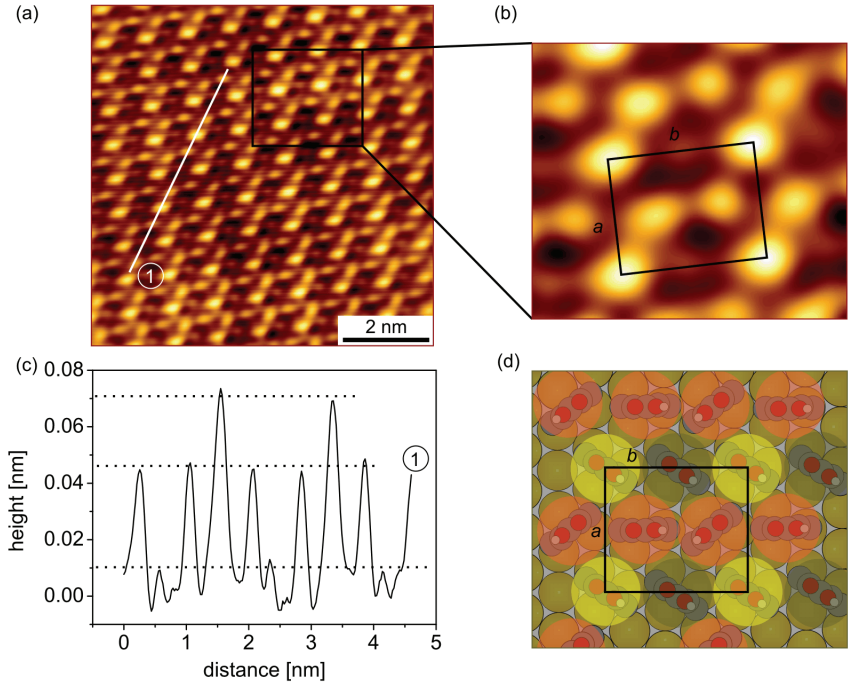

Figure 8.10: (a) STM scan of a large, defect free domain of standing TMBA molecules on Au(111). A stripped, superstructure related, pattern is visible and the unit cell (b) can be described with a $(3 \times 2\sqrt{3})$ structure. This structure is consistent with a c(4×2) supercell which is the common structure for close-packed alkanethiols. The height profile (c) across the pattern shows three different heights and a schematic drawing (d) of the structure with respect to distances and heights shows that the structure is consisted with the ϵ-phase, reported for alkanethiols.

Due to the special character of the molecules with hydroxyl groups at only one side of the aromatic ring system the molecules form hydrogen bonds between each other and thus preferentially form pairs. Furthermore, slight variations in the bonding sites of the sulfur head group to the gold lattice could cause such pairing, like reported for, e.g., biphenyl molecules [163]. Since STM provides only an image of the top of the SAM, these two explanations cannot be distinguished. The same

applies to the origin of the different heights detected by STM for one unit cell and it can be referred to investigations on alkanethiols which try to explain these height differences (compare section 5.4.1). Summarizing, the spatial arrangement of the TMBA molecules on the Au(111) surface is depicted in Fig. 8.10(d). Additionally, molecules with the same height appearance in STM are colored equally.

A second superstructure was found for TMBA on the same sample. Domain sizes with an area of above 650 nm^2 can be scanned by STM and Fig. 8.11(a) shows a $10 \times 10\,nm^2$ large zoom-in.

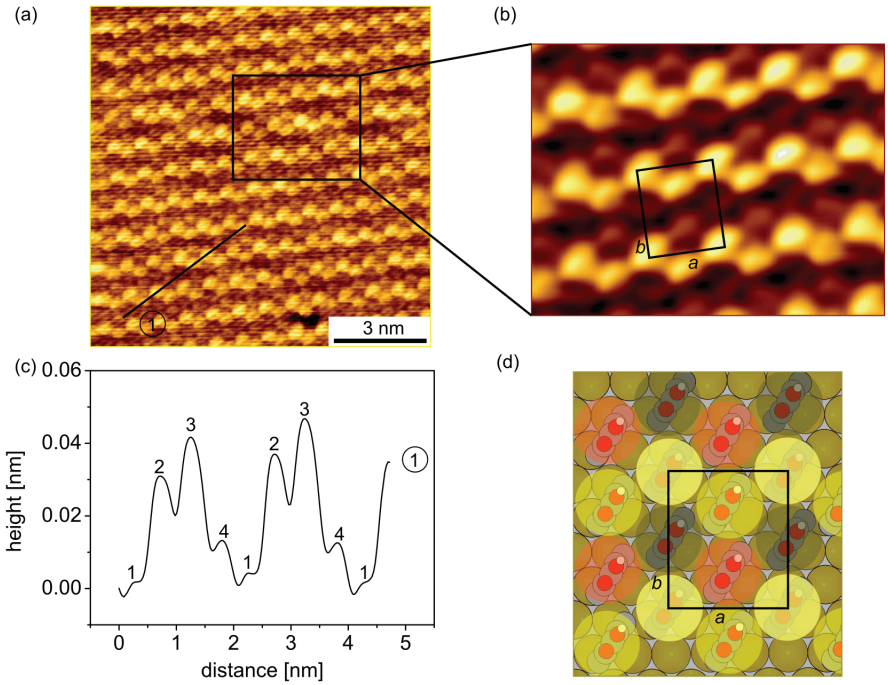

Figure 8.11: (a) STM scan of a large, defect free domain of standing TMBA molecules on Au(111) with a superstructure unequal to that of Fig. 8.10. Certainly the domain shows a stripped pattern and a unit cell (b) related to a c(4 × 2) structure but the height profile (c) across the pattern shows four different heights. A schematic drawing (d) of the structure with respect to distances and heights shows that the structure is consisted with the ζ-phase, reported for alkanethiols.

It gets visible that the striped pattern is caused by TMBA molecules which are ordered in a rectangular unit cell and appear in STM with different heights. With the help of line scans and unit cell detection tools of the STM software the unit cell

parameters can be measured precisely to $a = 0.88 \pm 0.09$ nm and $b = 0.98 \pm 0.10$ nm with an angle of $87.3 \pm 2°$. This unit cell is marked in the STM image of Fig. 8.11(b) where four different molecular spots can be detected within one unit cell. Line scans across the structure confirm these four different heights, marked in Fig. 8.11(c) with "1-4". Fitting this structure to the underlying gold lattice shows that also this unit cell is comparable to a $(3 \times 2\sqrt{3})$ structure and the spatial arrangement of the TMBA molecules on the Au(111) surface is depicted in Fig. 8.10(d). Molecules with the same height appearance in STM are colored equally here. Because of the four heights per unit cell it is equal to the ζ-phase of the c(4×2) structure of alkanethiols [75]. Note, that the superstructure here is found in SAMs prepared out of solution whereas for alkanethiols it is found, up to now, only for vapor deposited SAMs.

Comparing all topographic investigations on the TMBA molecules leads to the conclusion that these molecules have a high tendency to self-assemble in ordered arrays with various domain structures but large domain sizes and few vacancy islands. With XPS analysis it was proven that the molecules bind chemically on the surface with an intact molecular backbone. Although TMBA molecules have a much more complex molecular structure than alkanethiols they order in comparable structures, both for low coverage, lying-down type and for high coverage, standing-up type structures. This is in accordance with a study done by Noh et al. where they report on the self-assembly of small non-aromatic cyclic alkyl sulfides under chemisorption and formation of $(3 \times 2\sqrt{3})$ superstructures [154]. Summarizing, table 8.1 lists the six different structure described within this chapter with there orientation, unit cell and packing density per molecule.

notation	molecular orientation	unit cell	packing density [nm^2/molecule]
B1	flat-lying	$(7 \times \sqrt{3})$	0.49
B2	flat-lying	$(8 \times \sqrt{3})$	0.58
B3	flat-lying	c$(13 \times \sqrt{3})$	0.46
α-phase	upright standing	$(\sqrt{3} \times \sqrt{3})$R30°	0.21
ϵ-phase	upright standing	c(4×2)	0.21
ζ-phase	upright standing	c(4×2)	0.21

Table 8.1: Different structures of TMBA molecules reported within this work.

8.3 Electronic characterization of TMBA monolayers

Beside topography measurements, to analyze the self-assembly behavior of TMBA molecules on the Au(111) surface, distance dependent current-voltage spectroscopy was performed to gain first insights in the electronic structure of the TMBA molecules adsorbed on the surface. Current-voltage spectroscopy was measured by STM within the CITS mode (described in section 3.3.2) because multiple I-V measurements with an exact spatial position are taken simultaneously with the topographic signal during one scan in this mode. With this it is possible to detect differences in the electronic structure of neighbored molecules or to collect I-V data of flat-lying molecules. Unfortunately CITS is limited in resolution, since the spectra need to be acquired at a relatively high speed and the tunneling distance has to be set to large values to avoid a contact between tip and surface during scanning. CITS topography scans are not possible in high resolution but the molecule related features are visible even when they are unequal in height and the large number of I-V curves yields a precise image of the electronic structure. Spectroscopy curves were taken on domains of flat-lying molecules as well as on close-packed standing molecules and exemplary data are reported in the following.

In a first step, CITS data were collected for lying-down type molecules. Areas of around $3 \times 3\,\mathrm{nm}^2$ were scanned in CITS mode and analyzed separately. Successive enlarged parts of the scanned area were averaged and compared, starting with the submolecular features related to one molecule. Comparing the averaged I-V data or, more meaningful, their numerically calculated differential dI/dV characteristics, shows no differences in the LDOS within one molecule. This points to no fundamental transport barriers in the TMBA molecules. Thus, the dI/dV curves of one molecule were averaged and next compared to the dI/dV curves of the neighbored molecules. Also these curves show identical local density of states spectra which monitors a similar transport process for all molecules within one structure. Exemplary, Fig. 8.12(a) shows the averaged localized dI/dV curves for lying TMBA molecules within the same structure. Plotted are the conductivity curves for set point current between $I_{Set} = 0.1$ and $0.5\,\mathrm{nA}$ and a constant set point voltage of $V_{Set} = -1.7\,\mathrm{V}$. These distance dependent curves display the LDOS of the molecules and show that with decreasing tip-sample distances several molec-

ular orbitals are probed. Three peaks are detectable within a voltage window of ±2.0 V. One peak is detected at a negative bias voltage of around −0.9 V and is related to an occupied molecular orbital. Two further peaks are detected at 0.8 V and at 1.8 V which are related to unoccupied molecular orbital energies. Beside these pronounced peaks a small feature is detected at ≈ 0.2 V. Due to the energetic position of this feature close above the Fermi energy it can be related to a mixed molecule/surface state, similar to the contributions reported for the carboxylate/Cu(110) system in chapter 7.

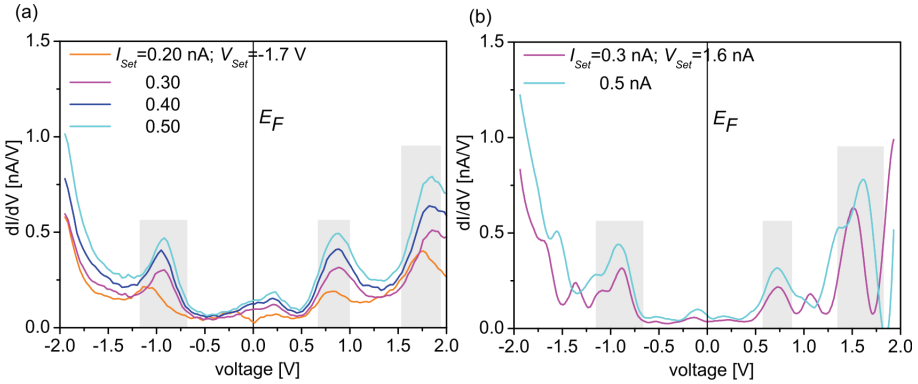

Figure 8.12: dI/dV characteristics of TMBA molecules chemically bonded to the Au(111) surface calculated from the measured I-V data on flat-lying molecules. The curves were taken on flat-lying molecules within the same characteristic striped pattern. Whereas the scans on the first domain (a) were taken at a constant set point voltage of $V_{Set} = -1.7$ V the second series (b) was taken at $V_{Set} = 1.6$ V. Highlighted are the detectable peaks corresponding to occupied and unoccupied molecular orbital energies. Characteristic for the LDOS plots of lying-down TMBA molecules is the detection of the mixed molecule/surface states located around the Fermi energy.

Due to the fact that no density of states studies, experimental or DFT based calculations, on a comparable bound system exist, it is not possible to make a statement on the origin of these peaks here. Only comparable studies on the LDOS of different structures of lying-down type molecules or LDOS plots of close-packed standing molecules can yield further information. Figure 8.12(b) shows the averaged localized dI/dV curves for a second domain with stripped pattern of lying-down type molecules now collected with positive set point voltages of $V_{Set} = 1.6$ V. A slightly different spectrum is visible pointing to a bias dependency of the spots, a change of the LDOS in the presence of the electric field, or simply to an influence of small variations in the tip-sample distance due to the small tip bias voltage

value difference of 0.1 and the different polarity. To analyze this in detail complex and time-consuming statistic investigations on all striped phase have to be done. Nevertheless, some conclusions can be drawn out of the scans recorded up to now. The first occupied peak appears for all investigated TMBA molecules with a flat-lying structure at $-0.9\,\mathrm{V}$. This points to a molecular orbital which does not shift in the electric field between tip and sample and due to its low energy a mapping to a sulfur related orbital is obvious [164]. Further, two unoccupied molecular orbitals are situated in energy below $2.0\,e\mathrm{V}$, the first one is monitored at an applied bias voltage range between $0.75\,\mathrm{V}$ and $1.0\,\mathrm{V}$ and the second one between $1.5\,\mathrm{V}$ and $2.0\,\mathrm{V}$. Finally, the small feature detected at $\approx 0.2\,\mathrm{V}$ has a complementary feature at negative values close below the Fermi level and thus they can be related to a bonding antibonding combination of the mixed molecule/surface states.

In a second step, CITS data were collected on standing-up type molecules. Measurements were done on small areas with $(\sqrt{3}\times\sqrt{3})\mathrm{R}30^\circ$ structure (α-phase) and on c(4×2) superstructures (ϵ-phase). No difference was detectable for molecules of the same domain even when they are ordered in a superlattice structure with different detectable heights and fundamental differences between these molecules can be ruled out. However, differences can be found between the conductivity curve of different phases and Fig. 8.13 shows exemplary the LDOS plots for TMBA molecules ordered in an ϵ-phase (a) and in an α-phase (b). All measured dI/dV on the superstructure show identical curve shapes even if they show different height distributions in the STM topography scans. This points to an equal electric conductance mechanism through all molecules within the structure. The LDOS plot for the TMBA molecules ordered in a superstructure assembly shows two peaks in the accessible voltage window of $\pm 2\,\mathrm{V}$. One peak at $-1.0\,\mathrm{V}$, related to the response of an occupied molecular orbital, and a second one at $1.5\,\mathrm{V}$, related to an unoccupied molecular orbital, are measurable. Thus, the peak energy for the first appearing peak at negative bias voltages is equal for flat-lying and standing-up molecules. Provided that this peak is related to the sulfur based orbital, the same peak energy for flat-lying and standing molecules points to a similar transport process and reconfirms the equal bonding mechanism. Furthermore, the flat region between the two peaks around the Fermi level attracts attention. No molecular states are detected around the Fermi level whereas peaks are visible in the LDOS of lying TMBA molecules. A simple explanation for this different curve shape can be given by the geometrical alignment of the molecules. In the

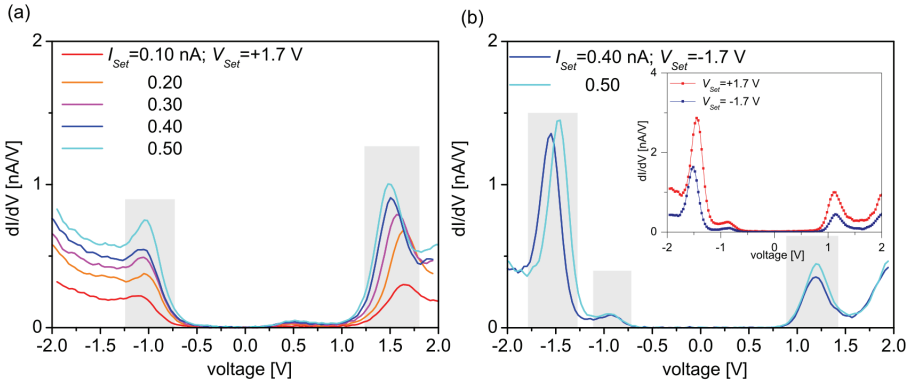

Figure 8.13: dI/dV characteristics of TMBA molecules chemically bonded to the Au(111) surface calculated from the measured I-V data on standing-up molecules. Displayed are the LDOS plots for molecules ordered in a c(4×2) superstructure with ϵ-phase (a) and in a $(\sqrt{3} \times \sqrt{3})$R30° structure (b). All displayed curves were taken at a constant set point voltage of $V_{Set} = -1.7\,\mathrm{V}$ respectively $V_{Set} = +1.7\,\mathrm{V}$ and show no bias polarity dependence, as visible in the inset of part(b). The detected differences in the curve shapes at positive voltages as well as for negative applied bias voltages smaller -1.25V can have various reasons. One possible reason is that molecules inside small domains without superstructure have different adsorption sites than the molecules inside a superstructure.

case of flat-lying molecules the whole molecular backbone is detectable with the STM whereas for close-packed standing molecules as a start only the molecular orbitals are detectable which point to the vacuum side or are highly delocalized. Mixed molecule/surface states are known to be localized directly above the substrate surface and thus the tip has to be immersed into the molecular layer before detecting these orbitals. However, this small tip sample distances yet destroy the molecular layer irreversibly. Comparing structures with (Fig. 8.13(a)) and without superlattice (Fig. 8.13(b)) shows slightly different peak positions and due to the independence of the applied bias polarity (inset in part (b)) different adsorption position on the gold lattice, different molecular twist angles or a change in the molecular conformation are possible explanations. First DFT calculations of close-packed TMBA molecules show, e.g., differences in the LDOS due to different adsorption places on the underlying gold lattice but a mapping of peaks to special molecular orbitals is possible only with further detailed calculations.

Finally, assuming that the peak at $\approx -1.0\,\mathrm{V}$ is a sulfur-gold bond mediated state which is located at the bonding unit and as thus fixed in energy for comparable molecules with the same bonding unit, the HOMO-LUMO gap of the TMBA/Au(111) system can roughly estimated to $\Delta E_{STM} = 2.5 - 3.0\,e\mathrm{V}$. This is a realistic value because additionally performed UV-VIS adsorption spectra on the TMBA molecule dissolved in DMF show an optical gap of $\Delta E_{STM} = 3.15\,e\mathrm{V}$ (compare Fig.8.14).

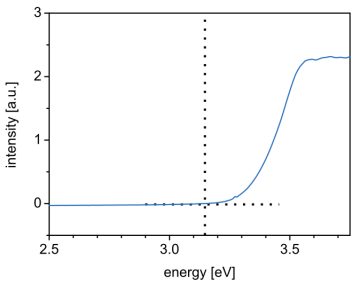

Figure 8.14: Optical absorption spectrum of TMBA dissolved in DMF. The horizontal and vertical dashed lines serve as guide to the eye to help determine the adsorption edge. The onset position of the energetically lowest adsorption band leads to an optical gap of $\Delta E_{opt} \sim 3.15\,e\mathrm{V}$ in the liquid phase.

8.4 Mixed Monolayers

TMBA molecules could work either as active molecules or layers themselves or as inert matrix system for the insertion of functional molecules, e.g., redox-active molecules. To analyze the insertion behavior of TMBA molecules into an insulating molecular matrix system the molecules were inserted into a dense monolayer of octanethiol molecules. Additionally to the topography investigations current-distance spectroscopy measurements were performed on the inserted molecules. The advantages of measuring the electronic transport through the TMBA molecule in a matrix environment are the reduced configurational degrees of freedom for the chemisorbed molecules in the alkanethiol matrix system and accordingly a well know reference system for the measurements is directly present.

8.4.1 Embedding TMBA molecules into a C8 SAM

Before mixed SAMs of alkanethiols and TMBA were examined, the structure of the pure alkanethiol monolayer was controlled. All samples show a monolayer of close-packed standing molecules ordered in large domains with c(4×2) structures.
Fig. 8.15 shows a SAM of octanethiol with embedded TMBA molecules. The TMBA molecules were embedded by immersing the preassembled and controlled C8 monolayer into a one millimolar solution of TMBA molecules for 16 hours. The SAM still shows the characteristic alkanethiol surface with c(4×2) structures, different superstructures, rotational and translational domain boundaries as well as etch pits (compare 8.15(a)). In addition to these features several new ones are visible. Whereas domain boundaries in C8 layers commonly appear darker in STM topography now domain boundary regions appear bright and blurry (Fig. 8.15(c)). Especially the regions around etch pits appear brighter and high resolutions scans of these areas (d) show bright large molecule spots. These spots are absent in the pure C8 layer and are, therefore, interpreted as embedded TMBA molecules. Thus, insertion preferentially takes place at defect sites such as domain boundaries or etch pits.
Rarely, small bunches of ordered molecules with larger feature sizes are displayed, like in the upper left corner of Fig. 8.15(a) (marked with a black circle). Line scans along the directions of the red and the black arrow show the regular appearance and the height difference to the surrounding octanethiol molecules (compare Fig. 8.15(b)). The next nearest neighbor distance between the TMBA molecules can be measured to $a = 0.81 \pm 0.04\,\mathrm{nm}$ and $b = 1.05 \pm 0.05\,\mathrm{nm}$. This distance matches with the c(4×2) unit cell, found for pure TMBA layers, but no molecules can be detected inside the cell. So it can be deduced that the adsorption of TMBA molecules is influenced by the gold surface lattice but not directly by the C8 layer. Furthermore, first DFT calculations on the adsorption energies of the close-packed structures of TMBA molecules show that for the molecules an adsorption on bridge sites is advantageous, whereas it is commonly assumed that alkanethiols adsorb on triple hollow sites of the gold lattice [58, 165]. That explains that small bunches of ordered molecules are found only surrounded by disordered areas. These disordered areas act as a kind of domain boundary. Further, the different adsorptions sides explain that only a few TMBA molecules are inserted as single molecules into a C8 domain.

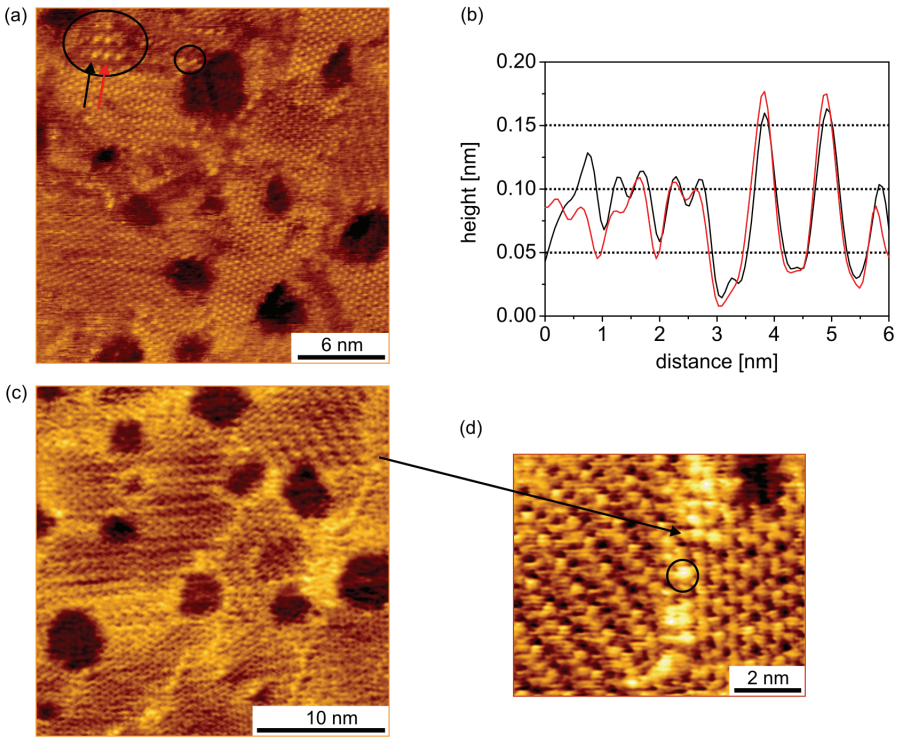

Figure 8.15: (a) $24 \times 24\,\mathrm{nm}^2$ large STM scan of a C8 SAM with embedded TMBA. The TMBA molecules are displayed as bright protrusions (see, e.g., in the small black circle). A small bunch of ordered molecules with a rectangular unit cell is additionally visible and marked with a larger circle. Line scans (b) along the directions of the two arrows monitor a conformation of standing-up type molecules for this domain. The STM scan of part (c) highlights the brightly appearance of the domain boundaries between the C8 domains and the inset of (d) shows large bright spots related to inserted TMBA molecules.

With longer immersing times of the C8 covered gold samples into the TMBA solution the resulting monolayer structure changes. Surprisingly, no more molecules are inserted into the C8 layer as it would be expected but a reorientation of the whole monolayer takes place. For storage times of more than 20 h the resulting monolayer structure shows a striped pattern with various different orientations. Figure 8.16(a) shows that this striped pattern coverages the whole gold terraces. Comparing height profiles taken on these structures with height profiles taken on upright standing and flat-lying structures of pure C8 as well as of pure TMBA molecules (section 8.2) shows that the displayed molecules are flat-lying on the sur-

face. The structure in the ordered domains can be described by a slightly distorted rectangular unit cell with the vectors $a = 0.47 \pm 0.05$ nm and $b = 2.60 \pm 0.20$ nm at an angle of $91.8 \pm 2°$. In terms of the underlying gold surface pattern this is equal to a $(p \times \sqrt{3})$ structure with the periodicity $p = 9$. High resolution STM scans, as plotted in Fig. 8.16(b), show that this structure consists of five different areas. Height profiles across the different areas monitor four peaks within one unit cell (see Fig. 8.16(c)).

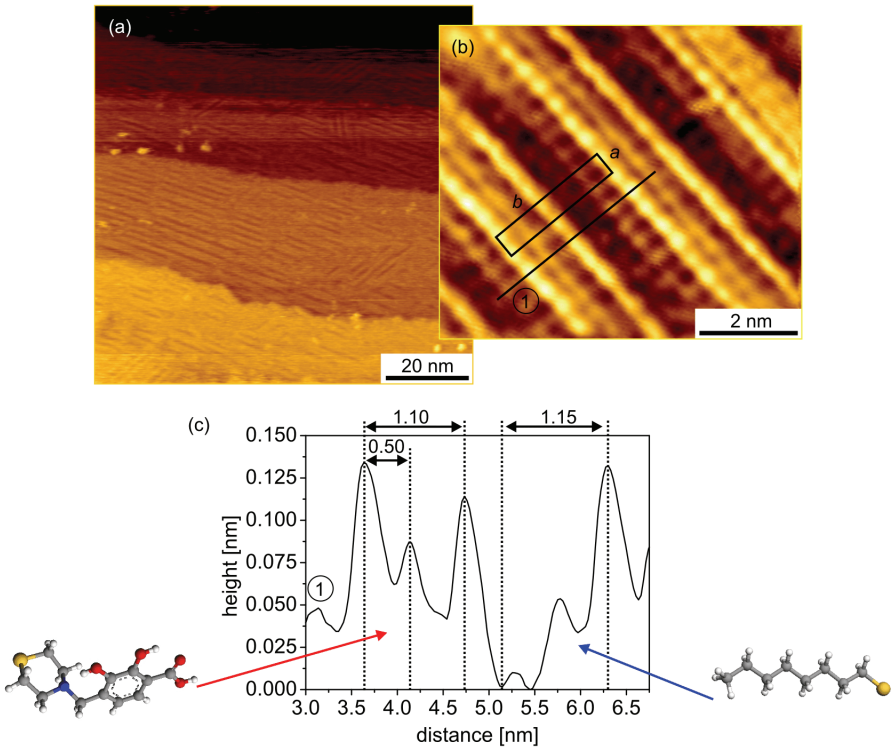

Figure 8.16: (a) $24 \times 24\,\text{nm}^2$ large survey scan of the mixed C8/TMBA monolayer after a TMBA exposure time of around 24h. The gold terraces are homogeneously covered by a striped molecular pattern. (b) High resolution topography scan on the striped pattern. The unit cell and the position of the line scan across the pattern are marked. The related line scan is plotted in (c). Comparable line scans on the striped pattern of pure C8 and pure TMBA molecules lead to the assumption of a mixed molecular structure. Whereas the left side on the scan correlates with a TMBA molecule the features on the right side are C8 molecule related.

To explain the molecular assembly in the striped pattern with the five different row heights the structure was compared with striped C8 pattern and striped

TMBA pattern. All striped C8 pattern, independent of the periodicity p show a large peak in the height profile, related to the sulfur head group which interacts with the gold surface, and a second peak around 0.08 nm lower in height which is related to the alkane chain. Assuming a periodicity of $p = 8 \pm 0.5$ for a layer of C8, as reported by M. Sharma et al. [166] (i.e., a length of 1.15 nm per molecule), this is exactly what is visible in the right part of the line scan in Fig. 8.16(c). The other part of the here reported structure has a different line profile with an additional peak and other distances. The easiest conclusion is that this part monitors a TMBA molecule. This is proven by comparing the peak ratios with that measured in the height profile of the pure TMBA layer (compare Fig. 8.7). The peak shape is identical with one main peak followed by a small one and at last the medium one. The main peak is related to the sulfur head group and the distance to the next peak fits exactly whereas the next distance is smaller for the case of the pure layer. But this small mismatch is a admissible tolerance due to a likely different tilt angle of the molecular backbone caused by different intermolecular interactions in the mixed layer.

8.4.2 Current decay parameters for TMBA molecules

The electronic properties of the TMBA molecule chemically bonded to the Au(111) surface were additionally studied by current-distance (I-z) spectroscopy, as described in section 3.3.2. Measurements were performed on single TMBA molecules inserted into the C8 matrix layer and additionally as reference on C8 molecules inside the domains. I-z measurements on the C8 molecular domains show the typical curve shape for C8, as reported, e.g., in [38]. The curves start with a low current below the noise level of the preamplifier until the tip-sample distance is small enough to get a stable tunneling contact. Above this point the current increases and the slope of the curve can be described by the vacuum decay constant, measured to $\beta_{Vac} = 21.6\,\mathrm{nm}^{-1}$. At the point of contact between tip and molecule a kink appears in the I-z curves and the slope is reduced. From the point of contact the tip starts to penetrate the octanethiol monolayer and the current slope resembles the tunneling decay constant of the octanethiol molecule. A value of $\beta_{C8} = 8.1\,\mathrm{nm}^{-1}$ is measured and is in accordance with the literature data which refer values of $\beta_{C8} = 8.8\,\mathrm{nm}^{-1}$ [167], or $\beta_{C8} = 7.0\,\mathrm{nm}^{-1}$ [168]. With these measurements it is supplementary proven that the superstructure domains

described above are C8 domains.
I-z curves recorded on the larger and brighter appearing molecular spots show a different characteristic and an exemplary curve, plotted on a semi logarithmic scale, is shown in Fig. 8.17. This I-z curve was taken on the molecule marked with a black circle in Fig. 8.15(d). The reported curve was taken by first retracting the tip and then approaching it towards the sample surface while simultaneously measuring the current. The origin of the x-axis denotes the position of the tip at the tunneling set point parameters ($I_{Set} = 0.443\,\mathrm{nA}$ and $V_{Set} = 1.28\,\mathrm{V}$). Negative displacements represent an increase in tunneling distance (i.e., the tip is retracted) and positive displacements represent a decrease in tunneling distance (i.e., the tip is moved towards the sample).

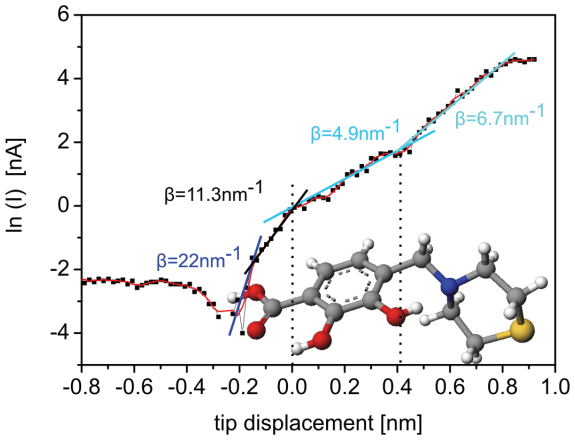

Figure 8.17: Current-distance spectroscopy of TMBA molecules chemically bonded on an Au(111) surface. The origin of the x-axis corresponds to the tunneling set point parameters ($I_{Set} = 0.443\,\mathrm{nA}$ and $V_{Set} = 1.794\,\mathrm{V}$). The slopes of the current in the semi logarithmic plot reflect the current-decay parameters (β) and are material dependent. The length of the different parts with a constant slope corresponds to the geometric length of the molecular moieties. New β values were found for the carboxylate unit, and the thiomorpholinomethyl group. The measured decay constant of the phenol ring fits to the literature values of the comparable biphenyl unit.

Starting at large tip-sample distances, i.e., on the left side of Fig. 8.17, first a low current region was detected where the current is determined by the noise level of the preamplifier. At a tip displacement of $-0.2\,\mathrm{nm}$ a jump in current was detected equal to a tunneling contact between tip and sample through the

vacuum gap. A tunneling decay constant of $\beta_{Vac} = 21.6\,\mathrm{nm}^{-1}$ can be evaluated by linear fitting this part of the curve. At a tip displacement of $-0.13\,\mathrm{nm}$ the contact point is reached and now the curve slopes monitor the contributions of the different molecular units. A first small region, related to the carboxylic top group of the molecule, can be identified with a relatively large slope of $\beta_{COOH} = 11.3\,\mathrm{nm}^{-1}$. No values for the tunneling decay constant of a carboxylate group are reported up to now but all successfully recorded I-z curves on embedded TMBA molecules show this region and similar values are recorded for the carboxylate unit of pyridinecarboxylic acids in paragraph 7.5.2. With a tip displacement of around zero nanometer the curve shape flattens due to the phenol ring group. A value of $\beta_{Ph} = 4.9\,\mathrm{nm}^{-1}$ is found which is comparable to the decay constant values of other π-conjugated ring systems, e.g., for the phenyl moiety with $\sim 4.2\,\mathrm{nm}^{-1}$ [141], and as expected higher as that of the pyridine moiety with $\sim 3.9\,\mathrm{nm}^{-1}$ (see paragraph 7.5.2). Further decreasing the tip-sample distance results again in an increase of the slope. This part of the I-z characteristic monitors the tunneling properties of the thiomorpholinomethyl group which builds the transition region to the gold surface. A tunneling decay constant of $\beta_{TMM} = 6.7\,\mathrm{nm}^{-1}$ describes this region.
The conductance of the thiomorpholinomethyl group can be roughly described by an equivalent circuit diagram of a conductance describing the methyl group connected in series with two conductances in parallel, one for each branch of the thiomorpholino group. All three conductances can approximately be described by

$$G_n = G_{n,0} e^{-\beta_{CH_2} d_n}, \tag{8.1}$$

where β_{CH_2} is the decay constant of a methyl group and d_n is the length of the unit n. With a value of $\beta_{CH_2} = 8.1\,\mathrm{nm}^{-1}$, as taken from the measurements of C8 molecules on the same sample, a conductance of the thiomorpholinomethyl group can be calculated to $\beta_{TMM} = 6.7\,\mathrm{nm}^{-1}$ which is in good agreement with the measured data.

An additional parameter which is available from the I-z spectroscopy data and which describes the molecular transport properties within the junction geometry is the conductance G [169]. The conductance can be calculated from the measured current at the contact point of tip and molecule using the relation

$$G = \frac{I_{contact}}{V_{Set}}. \tag{8.2}$$

Due to the mixed monolayer, it is possible to measure this value in a first step for a known reference system (C8), compare it to literature data, and then measure the new TMBA molecular system within the same experimental environment. A value of $G(\mathrm{C8}) = 0.057\,\mathrm{nS}$ is calculated from the contact current value of the C8 molecules which is in accordance with the values reported by Akkerman et al. [169]. For the TMBA molecules a conductance of $G_0(\mathrm{TMBA}) = 0.10\,\mathrm{nS}$ is found which is twice the conductance of an alkanethiol but significantly lower than that of small carboxylic acid molecules like pyridinecarboxylic acid (0.37 nS, calculated from the I-z spectroscopy data plotted in Fig. 7.23 of chapter 7) on Cu(110) surfaces.

8.5 Conclusion

TMBA self-assembled monolayers were grown from solution and characterized by STM and XPS. It could be proven by XPS that the TMBA molecules chemisorb as complete molecule and without C-S-C bond cleavage on the Au(110) surface. STM scans reveal that the molecules assemble in highly ordered structures and that large domains are built. Flat-lying as well as standing-up molecular domains are present on the surface and various structures are formed. The domains are separated by domain boundaries and rotational as well as translational transitions were found. Three orientations were recorded which are related to the three fold rotational symmetry of the underlying gold substrate. Flat-lying molecular structures have a characteristic striped pattern and can be described with respect to the underlying gold surface pattern as $(p \times \sqrt{3})$ structures. Standing-up type molecules form $(\sqrt{3} \times \sqrt{3})\mathrm{R30}^\circ$ structures and larger domains show a distinct $\mathrm{c}(4 \times 2)$ superstructure pattern. Two different superstructures were obtained on the measured samples equal to the ϵ- and ζ-phase of alkanethiols.
Electronic investigations of the TMBA molecules monitor a molecule mediated tunneling process within the accessible voltage window of $\pm 2.0\,\mathrm{V}$. The measured LDOS characteristics are dependent on the molecular adsorption geometry. Mixed molecule/surface states for example were only probed in spectroscopy for flat-lying molecules because for standing-up molecules the tip has to penetrate the molecular film before probing these localized molecular orbitals which causes a destruction of the layer. However, a HOMO-LUMO gap smaller than $3.0\,e\mathrm{V}$ could be measured by current-voltage spectroscopy.

Insertion experiments in a C8 monolayer matrix show that TMBA molecules preferentially adsorb at defect sides or at domain boundaries, pointing to different adsorption places for C8 and TMBA molecules. For small TMBA exposure times only a few bunches of ordered structures were found and C8 and TMBA domains are separated. With long storage times for the C8 monolayers in a TMBA based solution, structures of flat-lying molecules were found. C8 and TMBA molecules build these structures in equal parts.
I-z spectroscopy measurements on inserted TMBA molecules reveal the in section 7.5.2 measured tunneling decay constant of the carboxylic (carboxylate) group. A decay constant for a phenol group of $\beta_{Ph} = 4.9\,\mathrm{nm}^{-1}$ was measured, which is comparable to literature data, and additionally a decay constant for the thiomorpholinomethyl group was measured for the first time.

9 Molecules on Pt nanowires on Ge(001) - Triphenylphosphane

The Pt/Ge(001) surface is a particularly attractive candidate to be used as a template in molecular electronics since it predominately consists of arrays of dimerized, perfectly straight, and virtually defect free monoatomic Pt chains [92,119,170]. It can be used as structured template for molecular self-assembly or the Pt chains can be used as interconnects between nanoscale devices. Within the scope of this thesis the self-assembly behavior of different molecules onto the Pt/Ge(001) surface is investigated, with the focus on candidates which preferentially assemble on Pt chains.

Due to the fact that CO molecules adsorb on Pt chains as reported by N. Oncel [171] first experiments were done with pentane-2,4-dione (acetylacetone, $C_5H_8O_2$) and with 2,3-dihydroxybutanedioic acid (tataric acid, $C_4H_6O_6$) which have oxygen atoms that can in principle bind to Pt chains. The substances are also known to build complexes with platinum. STM topography investigations of the vapor deposited molecules on the Pt/Ge(001) substrates show in both cases a uniform molecular coverage of the whole surface with no difference between Pt chains and Ge surface. Another molecule which is well known from catalytic chemistry is triphenylphosphane ($C_{18}H_{15}P$, PPh_3). It is a common organophosphorus compound which is widely used as a catalyst for organic synthesis and as an intermediate for phase-transfer catalysts and Wittig reactions. As a ligand for many metals to form coordination compounds, it is often used to bind with transition metals, such as Pd, Pt, Ru, Ni, and Os [172]. Application oriented paper in other research fields explicitly show PPh_3 in combination with platinum, e.g., for catalytic reactions in direct methanol fuel cells [173]. PPh_3 binds via the phosphor atom to platinum and the three phenyl rings can be used as molecular backbone for the substitution of further functional groups. In the following chapter first STM investigations on the Pt/Ge(001)/PPh_3 system will be shown.

9.1 Experimental details

Clean Ge(001) substrates with Pt nanowires were prepared as described in section 6.3. After reformation of the Pt chains, the surface cleanness was checked by STM (as reported in section 6.3) and the samples were transferred into the preparation chamber of the UHV-STM system. Triphenylphosphane was used as purchased by Sigma-Aldrich with a purity of $> 99\,\%$. PPh_3 is in solid phase at room pressure and was used for deposition after several freezing thawing cycles in vacuum. It was deposited from vapor phase in-situ using a demountable and separately pumped home-built, knudsen-type thermal evaporator, as described in paragraph 3.3.1. PPh_3 molecules were sublimated at a background pressure of $2 \cdot 10^{-5}\,\mathrm{mbar}$ and a temperature of 350 K while the substrate was kept at room temperature. All results shown in this thesis were acquired on samples exposed to PPh_3 for 30 s. To increase the molecular order on the substrate the samples were heated after deposition in an environmental pressure of $10^{-9}\,\mathrm{mbar}$ to temperatures of around 323 K for 30 min. The resulting films were investigated by imaging in constant current mode with UHV-STM. Homemade electrochemically etched tungsten tips were used as STM-tips.

9.2 Structural investigations

First investigations on the Pt/Ge(001) samples exposed to triphenylphosphine show that only a small amount of molecules covers the surface. The characteristic surface structure of the Pt/Ge(001) system is visible with flat germanium terraces and bright appearing platinum chains. In Fig. 9.1(a) an overview STM image ($90 \times 90\,\mathrm{nm}^2$) of a Pt modified Ge(001) surface after exposure to PPh_3 is shown. The surface was scanned at room temperature with a tunneling set point current of $I_{Set} = 0.917\,\mathrm{nA}$ and a bias voltage of $V_{Set} = -1.692\,\mathrm{V}$. Clearly visible are the germanium terraces oriented in (001)-direction and covered with a number of platinum chains. They appear as bright lines with a width of exactly one Pt atom and the distance of neighboring chains is 1.6 nm. Additionally visible in the image are circular spots located on top of the Pt chains and sometimes also on the clean germanium areas, preferentially at step edges. These circular spots were not present before the exposure to PPh_3. Moreover, an increase of the exposure of PPh_3 leads to an increase in the density of these white circular spots up to

a coverage where the Pt chains are no longer visible. Therefore, these spots are attributed to PPh_3 molecules adsorbed on the Pt chains.

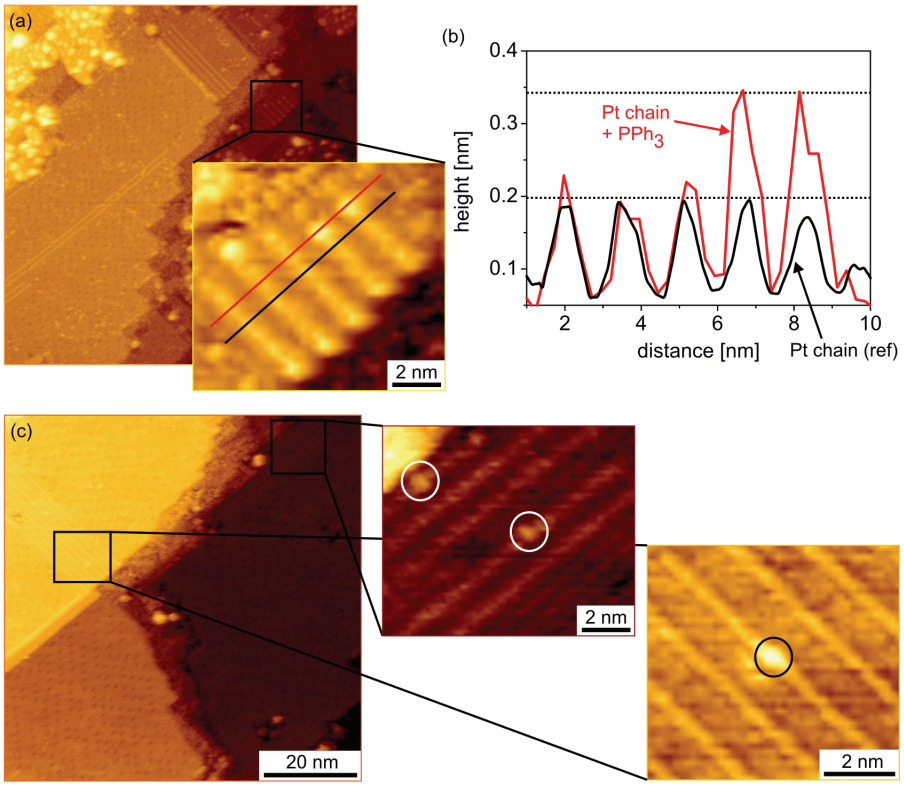

Figure 9.1: (a) STM survey scan ($90 \times 90\,nm^2$) of a Pt modified Ge(001) surface after exposure to triphenylphosphane. The surface shows the typical character of flat germanium terraces with straight bright lines consisting of Pt atoms. Single triphenylphosphine molecules (brighter spots) are found preferentially adsorbed on the Pt atomic chains (inset). (b) Height profiles across the Pt chains covered with molecules (red) and without molecules (black) show that the molecular center is on top of a Pt dimer. Furthermore, the molecules are adsorbed in a flat geometry on the Pt atoms, they have a height of around 0.15 nm in the scan. (c) STM survey scan of a Pt modified Ge(001) surface after exposure to triphenylphosphine and heating to around 323 K. The germanium surface appears with less molecular features whereas the Pt chains are still decorated with single PPh_3 related features (insets).

Higher resolution scans, like plotted in the inset of Fig. 9.1(a), show that the circular spots are located preferentially on top of the Pt dimer rows and the apparent size of the circular features is consistent with the diameter of the triphenylphos-

phine molecule of around 1.0 nm. This is shown more clearly in the height profile of Fig. 9.1(b). The profile in this figure is taken across the Pt chains as indicated by the red line drawn in the inset of Fig. 9.1(a). As a reference profile, the height profile of the clean Pt chain is also plotted, as indicated by the black line in the inset of Fig. 9.1(a). The molecule related features appear in the middle of the Pt chain and with twice the height compared to the Pt atoms. The topographic center of the molecule is positioned on top of the Pt atoms and due to the molecular diameter it can be concluded that one triphenylphosphine molecule covers one Pt dimer.

Heating the samples to moderate temperatures of around 323 K and scanning the surfaces again after cooling down shows that the germanium surface gets cleaner and no molecular features can be detected on chain free areas. Figure 9.1(c) shows a STM overview scan ($76 \times 76\,\mathrm{nm}^2$) with a noticeably cleaner surface. The image is taken again with a negative sample bias voltage ($V_{Set} = -0.973\,\mathrm{V}$) and a set point current of $I_{Set} = 0.917\,\mathrm{nA}$. The two insets show that molecular features are still present on top of the Pt chains. This points to triphenylphosphine molecules connected only loosely to the germanium surface which can move or desorb easily from the surface while the bond between triphenylphosphine molecules and platinum atoms is stronger. Summarizing, these first investigations show that triphenylphosphane is a promising candidate for molecular self-assembly on Pt nanowires. Single molecular features could be identified on top of the Pt chains but further investigations should follow which successively investigate the influence of temperature on the self-assembly process, e.g., by heating the substrate to moderate temperatures during the PPh_3 exposure.

10 Conclusion

This thesis explored the structure and electronic properties of building blocks for molecular electronics. Particularly, with view to a possible integration of molecular devices in hybrid semiconductor/molecular (CMOL) integrated circuits, the carboxylate/Cu(110) system was in the focus of experiments.

Carboxylates on Cu(110) surfaces

With the combination of the metallic Cu(110) surface and carboxylic acid molecules a new promising material system has been introduced for molecular electronics. The Cu(110) surface, used as nanotemplate, in combination with the carboxylic anchor group forms a stable interface which differs from the well known gold/thiol interface. Due to the patterned surface a directed molecular bonding is forced which leads to a stronger bond. A large dipole moment and a stable density of states distribution at the interface region protect the bond against influences of the molecular backbone, permitting the use of a large variety of functional molecules at uniform bonding conditions. To illustrate the relations between molecular moieties and electron transport properties this study includes a stepwise increase in complexity of molecules. An extension and functionalization of the molecular system up to hierarchical structures was performed and possible transitions to three terminal devices were shown in the following. Structural and electronic transport properties were investigated for a series of carboxylates with systematically substituted atoms or added functional groups. Attention was paid to the fact that only one part of the molecule was substituted per investigation step and that the adsorption configuration on the Cu(110) surface stays the same.

Investigations were started on clean copper substrates and the Cu(110) structure was described in detail due to its new application as direct nanotemplate in molecular electronics. It had been taken into account that copper oxidizes upon

contact with atmosphere and that oxygen can inhibit the self-assembly process of molecules. Hence copper surfaces were cleaned under vacuum conditions before molecule deposition. This preparation process was adapted to the existing equipment and optimized to achieve surface cleanliness and substrate roughness in atomic dimensions. Beside STM, AES, and LEED images were employed to characterize the copper surface. Single crystals were used in all investigations. For continuing studies the state of the art in copper thin film fabrication was reported and own deposition results were added. They were performed within the the framework of a project which deals with the direct combinations of current CMOS technology and molecular electronics (CMOL).

Four different molecules are presented within this work, including benzenecarboxylic acid, which is the smallest molecule that can be linked precisely to the Cu(110) surface and additionally has an intermolecular acting unit. Its SAM structures are well known and thus it is used as reference system for investigations. Its structural and electron transport properties were investigated first and described in great detail. Close-packed SAMs of upright standing molecules have been fabricated for all carboxylates under investigation which is the prerequisite for comparable electronic investigations. Successfully performed electronic transport investigations on the carboxylate/Cu(110) system are reported here for the first time.

The focus of studies was set on how the substitution pattern of the various carboxylates chemisorbed on the Cu(110) surfaces influences the HOMO-LUMO gap. For this purpose also DFT calculations were performed which model the LDOS of the combined carboxylate/Cu(110) systems and were compared to experimentally achieved results. The DFT calculations were done by V. Caciuc and N. Atodiresei at the Forschungszentrum Jülich. An understanding of control parameters to tune the HOMO-LUMO gap of the carboxylates was developed, i.e., it is possible to predict the HOMO-LUMO gaps theoretically and verify them experimentally. On one side, it could be demonstrated that the chemical bond formed between the respective carboxylate and the copper surface is not influenced by the HOMO-LUMO gap of the molecule. That means only the anchor group located at the molecule and the surface states of the metal determine the interface properties. The related occupied MO σ_1 stays at a constant energy for all molecules under investigation. On the other side, modifications of the aromatic ring system and of the functional groups influence the HOMO-LUMO gap. It was found that carboxylic groups as well as nitrogen substituents in the aromatic ring system

lead to a reduction of the HOMO-LUMO gap. Combining both experimental series a reduction of the gap in the order $\Delta E_{BCA} > \Delta E_{BDCA} > \Delta E_{PCA} > \Delta E_{PDCA}$ was observed. A detailed analysis of all experimentally probed molecular orbitals has shown that the calculated LDOS represents a characteristic fingerprint corresponding to the substitution pattern of the carboxylates bonded to Cu(110). With a detailed knowledge of the system parameters it is now possible to make precise theoretical predictions on the transport properties of other carboxylate species. For example, molecules like pyrazinedicarboxylic acid ($C_4H_2N_2(COOH)_2$) with two nitrogen atoms in the ring system will even show up with a smaller HOMO-LUMO gap than the carboxylates investigated experimentally so far. Thus, a first toolbox is composed which allows to combine molecular moieties to build up a molecule linked to a metallic electrode with a designed functionality. This knowledge is an important step forward to molecular electronics, because now the HOMO-LUMO gap and with this the energy difference between LUMO and Fermi level can be tuned, which determines electron injection barriers in devices build up of molecules.
Highlights of these combined investigations are not only that both, experiments and calculations, fit excellently together and that the LDOS of a combined molecule/metal system can be displayed in great detail but also that the spatial distribution of different orbitals has been mapped by STS. Distance dependent current-voltage spectroscopy measurements confirmed that ring related π-orbitals are probed in a wide current set point range due to their theoretically proposed delocalized character. In contrast, the σ-type orbitals are located directly at their related atoms and thus are detected only in between a small distance window. Furthermore, a detailed experimental study in combination with energy calculations for pyridine-2,5-dicarboxylic acid has shown that it is possible to identify different adsorption configurations and conformations of one molecule under different experimental conditions. A conformational change of the detected molecules caused by the applied electric field between tip and Cu substrate was monitored. Hence combining DFT calculations and STS enables a detailed electronic mapping of molecules connected to a metallic surface. Thus, a monitoring and manipulation of molecular properties in a controlled and defined way with atomic precision is permitted.

Additionally, system parameters like the tunneling junction symmetry or the local tunneling barrier height were extracted from I-V characteristics. Within the

approximations of a coherent molecular transport model, an estimation of the absolute value of the vacuum gap size was made for different set point currents. Typical values were found to be between 0.4 and 0.1 nm.
The tunneling process was further studied by transition voltage spectroscopy and for all investigated molecule species a transition between direct tunneling at large tip-sample distances and molecule orbital mediated tunneling for smaller distances was found. The onset of this molecule orbital mediated tunneling is molecule specific and follows the LDOS distribution precisely.
Current-distance dependent measurements were performed on selected carboxylates and the tunneling decay constant for the pyridine ($\beta_{Pyridine} = 3.9\,\mathrm{nm}^{-1}$) as well as for the carboxylic moiety ($\beta_{COOH} = 11.4\,\mathrm{nm}^{-1}$) was assigned for the first time.

In order to characterize π-π intermolecular interactions between neighbored molecules a small amount of carboxylic acids was embedded into a matrix of a self-assembled monolayer of suitable host molecules. First investigations of the fabrication of a mixed carboxylate monolayer on Cu(110) surface showed a successful embedding of pyridine-2-carboxylic acid into a benzenecarboxylic acid layer. Both molecules have a nearly identical length but pyridine-2-carboxylic acid appeared higher (brighter) in the STM topography images of the mixed layer, confirming the smaller decay constant of the pyridine unit compared to the decay constant of the phenyl unit. These further investigation steps point out that the carboxylate/copper system is suitable for more complex structures like mixed systems of electronically active and inactive molecules or hierarchical structures where different electron transport paths exist within the molecular layer.

Carboxylates with a second anchoring group on Au(111) surfaces

Testing carboxylic acid molecules for applications in devices, the carboxylate based molecule TMBA was studied on a different metal substrate (here gold), which could act as top electrode contact. The TMBA molecule has a diode functionality because it includes a carboxylic anchor group as well as a thiol anchor group and thus can chemically bind to two different electrode materials. It presents a more complex molecule within the toolbox of carboxylates.

Due to the fact, that Au(111) thin films deposited on mica templates became a kind of standard in molecular electronic research in the last years the system is only roughly described in its characteristics here.
TMBA is a new, in the group of Prof. Albrecht at the RWTH Aachen University, synthesized molecule, and its self-assembly behavior was tested first. Self-assembled monolayers were grown from solution and characterized by STM and XPS. It could be proven by XPS that the TMBA molecules chemisorb as complete molecule and without C-S-C bond cleavage on the Au(111). STM scans revealed that the molecules assemble in highly ordered structures and that large domains are built. A number of structures was discovered and a detailed understanding of the formation of monolayers was achieved.
Insertion experiments in a C8 monolayer matrix have shown that TMBA molecules preferentially adsorb at defect sites or at domain boundaries. Long term studies revealed a flat-lying molecule geometry with a uniform structure built by TMBA and C8 molecules.

Electronic investigations of the TMBA molecules monitored a molecular orbital mediated tunneling process within the accessible voltage window. The measured LDOS characteristics are dependent on the molecular adsorption geometry. Mixed molecule/surface states for example were only probed for flat-lying molecules. For standing-up molecules the tip would have to penetrate the molecular film before probing these localized molecular orbitals which would causes a destruction of the layer. However, a HOMO-LUMO gap smaller than 3.0 eV could be measured by current-voltage spectroscopy.

Current-distance spectroscopy measurements confirmed the decay constant of the carboxylic moiety obtained on the PCA/Cu(110) system. Thus, the decay constant seems to be independent on the molecular environment because measurements on the neutral and on the chemisorbed moiety show comparable values. The obtained decay constant for the phenol moiety is comparable to values reported for biphenyl or phenyl units revealing that the decay constant for phenyl rings is independent on the number of rings and of the hydroxyl side groups. Additionally, I-z spectroscopy was performed on a thiomorpholinomethy unit for the first time and the value of $\beta_{TMM} = 6.7\,\mathrm{nm}^{-1}$ could be interpreted using an equivalent circuit diagram.

Semiconductor surfaces with metal nanowires form a template for molecular self-assembly

Further, a short excursion presented a different approach to combine molecular electronics with common CMOS technology. Combining the semiconductor surface Ge(001) with self-assembled Pt nanowires leads to a nanotemplate for molecular assembly. In a cooperation with Prof. Zandvliet and his research group at the University of Twente, which have great experience in investigating these nanotemplates, studies were performed to combine Ge(001) surfaces modified with Pt nanowires and organic molecules. A great challenge was the handling and transport of the nanotemplates without a vacuum environment. A process was established to cover the Ge(001)/Pt surface with an oxygen protection layer under UHV in Twente, to transport the samples in the "trouser pocket" to Jülich, and to carefully remove the oxygen layer under ultra high vacuum condition. Thus, the focus of these studies was how to remove this capping layer, to reactivate the striped surface pattern, and to characterize the topographical structures before bringing molecules onto the surface. First results were presented for triphenylphosphane molecules which preferentially adsorb on the nanowires.

Outlook

This thesis provides systematic insights into the electron transport properties of carboxylates in combination with the copper surface and additionally with the gold surface. It is shown that the carboxylate/copper system fulfills the requirements to be used in molecular electronics and that it is possible to build hierarchical structures by the matrix isolation method. Thus, further investigation steps should now combine various carboxylic acids and investigate the interactions within the resulting monolayers. DFT calculations point out that there will be only very weak π-π interactions between neighbored molecules. This can be experimentally verified in a next investigation step by using the mixed molecular layers shown in this work, performing current-voltage spectroscopy on both molecular species of the layer and comparing these results with that of the pure layers. "Neighbor-effects" will be monitored as a shift of molecular orbital energies in the LDOS plots. If there is indeed only a small, or even no detectable influence, in a next

step molecules with hydrogen-bonds or charge transfer interactions can be studied using the matrix isolation method. The peaks obtained from the differential conductance curves can be compared to the results of DFT calculations. These investigations will show how to tune the electronic transport through the carboxylate/Cu(110) system by an external field created by neighboring molecules.
Additionally, molecules with electronically active centers like the TMBA based complexes shown in Fig. 8.1 of chapter 8 should be inserted into monolayers of TMBA or into electronically more inactive carboxylates like, e.g., benzenecarboxylic acid. Studies should focus on the influence upon the electron transport through the active molecule using an external field which is either directly applied or created by neighboring molecules. Exploiting the electron transport properties along different transport paths could be used to build up a molecular device.
Finally, it should be noticed that a further tuning of the experimental set up in terms of lower pressures in the deposition chamber and a detailed preliminary investigation of the sublimation point of the molecules as a function of pressure will lead to well defined mixed structures with only single embedded functional molecules.
Semiconductor surfaces in combination with metal wires used as nanotemplate for molecular self-assembly build an interesting and promising alternative to metal/molecule systems and surely will be investigated in detail in the next years. Concerning the triphenylphosphane molecules on the Pt nanowire modified Ge(001) surface a clear tendency of the adsorption behavior is visible but a detailed analysis is required to give a clear statement.

Bibliography

[1] N.J. Tao, Electron transport in molecular junctions. *Nature Nanotechnology* **1**, 173–181 (2006).

[2] C. Joachim, J.K. Gimzewski, A. Aviram, Electronics using hybrid-molecular and mono-molecular devices. *Nature* **408**, 541–548 (2000).

[3] R. Stadler, Editors P. Grütter, W. Hofer, F. Rosei, *Properties of Single Organic Molecules on Crystal Surfaces*. Imperial College Press, London, 2006.

[4] J.D. Swalen, D.L. Allara, J.D. Andrade, E.A. Chandross, S. Garoff, J. Israelachvili, T.J. McCarthy, R. Murray, R.F. Pease, J.F. Rabolt, K.J. Wynne, H. Yu, Molecular Monolayers and Films. *Langmuir* **3**, 932–950 (1987).

[5] J.V. Barth, G. Constantini, K. Kern, Engineering atomic and molecular nanostructures at surfaces. *Nature* **437**, 671–679 (2005).

[6] J.M. Lehn, *Supramolecular Chemistry*. Wiley-VCH, Weinheim, 1995.

[7] M. Ruben, J. Rojo, F.J. Romero-Salguero, L.H. Uppadine, J.-M. Lehn, Grid-Type Metal Ion Architectures: Functional Metallosupramolecular Arrays. *Angewandte Chemie International Edition* **43**, 3644–3662 (2004).

[8] N. Kang, A. Erbe, E. Scheer, Observation of negative differential resistance in DNA molecular junctions. *Applied Physics Letters* **96**, 23701/1–3 (2010).

[9] U. Sivan, Editor R. Waser, *Nanotechnology: Volume 3: Information Technology I*. Wiley-Vch, Weinheim, 2008.

[10] J. Elbaz, Z.G. Wang, R. Orbach, I. Willner, pH-Stimulated Concurrent Mechanical Activation of Two DNA "Tweezers". A "SET-RESET" Logic Gate System. *Nano Letters* **9**, 4510–4514 (2009).

[11] K. Keren, R.S. Berman, E. Buchstab, U. Sivan, E. Braun, DNA-Templated Carbon Nanotube Field-Effect Transistor. *Science* **302**, 1380–1382 (2003).

[12] A. Aviram, M.A. Ratner, Molecular Rectifiers. *Chemical Physics Letters* **29**, 277–283 (1974).

[13] R.M. Metzger, Unimolecular Electrical Rectifiers. *Chemical Reviews* **103**, 3803–3834 (2003).

[14] M. Di Ventra, S.T. Pantelides, N.D. Lang, The benzene molecule as a molecular resonant-tunneling transistor. *Applied Physics Letters* **76**, 3448–3450 (2000).

[15] J.Y. Ouyang, C.W. Chu, D. Sieves, Y. Yang, Electric-field-induced charge transfer between gold nanoparticle and capping 2-naphthalenethiol and organic memory cells. *Applied Physics Letters* **86**, 123507/1–3 (2005).

[16] H.S. Cho, N.W. Song, Y.H. Kim, S.C. Jeoung, S. Hahn, D. Kim, S.K. Kim, N. Yoshida, A. Osuka, Ultrafast Energy Relaxation Dynamics of Directly Linked Porphyrin Arrays. *Journal of Physical Chemistry A* **104**, 3287–3298 (2000).

[17] J. Park, A.N. Pasupathy, J.I. Goldsmith, C. Chang, Y. Yaish, J.R. Petta, M. Rinkoski, J.P. Sethna, H.c.D. Abruna, P.L. McEuen, D.C. Ralph, Coulomb blockade and the Kondo effect in single-atom transistors. *Nature* **417**, 722–725 (2002).

[18] J. Chen, M.A. Reed, A.M. Rawlett, J.M. Tour, Large On-Off Ratios and Negative Differential Resistance in a Molecular Electronic Device. *Science* **286**, 1550–1552 (1999).

[19] K.K. Likharev, Hybrid CMOS/Nanoelectronic Circuits: Opportunities and Challenges. *Journal of Nanoelectronic and Optoelectronic* **3**, 203–230 (2008).

[20] G.E. Poirier, Characterization of Organosulfur Molecular Monolayers on Au(111) using Scanning Tunneling Microscopy. *Chemical Reviews* **97**, 1117–1127 (1997).

[21] M.C. Lennartz, N. Atodiresei, L. Müller-Meskamp, S. Karthäuser, R. Waser, S. Blügel, Cu-Adatom-Mediated Bonding in Close-Packed Benzoate/ Cu(110)-Systems. *Langmuir* **25**, 856–864 (2009).

[22] F. Chen, J. Hihath, Z.F. Huang, X.L. Li, N.J. Tao, Measurement of single-molecule conductance. *Annual Review of Physical Chemistry* **58**, 535–564 (2007).

[23] M.C. Desjoqueres, D. Spanjaard, *Concepts in Surface Physics*. Springer, Berlin, 1996.

[24] R.G. Parr, W. Yang, *Density Functional Theory of Atoms and Molecules*. Oxford University Press, 1989.

[25] Nicolae Atodiresei, *First Principles Theory of Organic Molecules on Metal Surfaces: Formate, 3-Thiophene-carboxylate and Glycinate on Cu(110)*. Ph.D. thesis, RWTH Aachen, 2005.

[26] F. Zahid, M. Paulsson, S. Datta, Editor H. Morkoc, *Advanced Semiconductors and Organic Nano-Techniques*. Academic Press, 2003.

[27] S. Datta, W. Tian, S. Hong, R. Reifenberger, J.I. Henderson, C.P. Kubiak, Current-voltage characteristics of self-assembled monolayers by scanning tunneling microscopy. *Physical Review Letters* **79**, 2530–2533 (1997).

[28] S.M. Sze, *Physics of Semiconductor Devices*. Wiley, New York, 2003.

[29] J.G. Simmons, Generalized Formula for the Electric Tunnel Effect between Similar Electrodes Separated by a Thin Insulating Film. *Journal of Applied Physics* **34**, 1793–1803 (1963).

[30] W. Wang, T. Lee, M.A. Reed, Mechanism of Electron Conduction in Self-Assembled Alkanethiol Monolayer Devices. *Physical Review B* **68**, 035416/1–7 (2003).

[31] G. Binning, H. Rohrer, Scanning Tunneling Microscopy - from Birth to Adolescence. *Reviews of Modern Physics* **59**, 615–625 (1987).

[32] J. Bardeen, Tunneling from a Many-Particle Point of View. *Physical Review Letters* **6**, 57–59 (1961).

[33] J. Tersoff, D.R. Hamann, Theory and Application for Scanning Tunneling Microscope. *Physical Review Letters* **50**, 1998–2001 (1983).

[34] J. Tersoff, D.R. Hamann, Theory of the scanning tunneling microscope. *Physical Review B* **31**, 805–813 (1985).

[35] N.D. Lang, Spectroscopy of single atoms in the scanning tunneling microscope. *Physical Review B* **34**, 5947–5950 (1986).

[36] L.A. Bumm, J.J. Arnold, T.D. Dunbar, D.L. Allara, P.S. Weiss, Electron Transfer through Organic Molecules. *Journal of Physical Chemistry B* **103**, 8122–8127 (1999).

[37] A. Salomon, C. Cahen, S. Lindsay, J. Tomfohr, V.B. Engelkes, C.D. Frisbie, Comparison of Electronic Transport Measurements on Organic Molecules. *Advanced Materials* **15**, 1881–1890 (2003).

[38] L. Müller-Meskamp, S. Karthäuser, H.J.W. Zandvliet, M. Homberger, U. Simon, R. Waser, Field-Emission Resonances at Tip/α,ω-Mercaptoalkyl Ferrocene/Au Interfaces Studied by STM. *Small* **5**, 496–502 (2009).

[39] S. Hüfner, *Photoelectron Spectroscopy: Principles and Applications*. Springer, Berlin, 2003.

[40] D.A. Shirley, High-Resolution X-Ray Photoemission Spectrum of Valance Bands of Gold. *Physical Review B* **5**, 4709–4714 (1972).

[41] P. Hohenberg, W. Kohn, Inhomogeneous Electron Gas. *Physical Review* **136**, B864–B870 (1964).

[42] R.P. Feynman, Forces in Molecules. *Physical Review* **56**, 340–343 (1939).

[43] H. Hellmann, *Einführung in die Quantenchemie*. Deuticke, Leipzig, 1937.

[44] W. Kohn, L.J. Sham, Self-Consistent Equations Including Exchange and Correlation Effects. *Physical Review* **140**, A1133 (1965).

[45] J.P. Perdew et al., Generalized Gradient Approximation Made Simple. *Physical Review Letters* **77**, 3865–3868 (1996).

[46] M.C. Payne, M.P. Teter, D.C. Allan, T.A. Arias, J.D. Joannopoulos, Iterative minimization techniques for ab initio total-energy calculations: molecular dynamics and conjugate gradients. *Reviews of Modern Physics* **64**, 1045–1097 (1992).

[47] G. Kresse, J. Hafner, Ab initio molecular dynamics for liquid metals. *Physical Review B* **47**, 558–561 (1993).

[48] G. Kresse, J. Furthmüller, Efficient iterative schemes for *ab initio* total-energy calculations using a plane-wave basis set. *Physical Review B* **54**, 11169–11186 (1996).

[49] P.E. Blöchl, Projector augmented-wave method. *Physical Review B* **50**, 17953–17979 (1994).

[50] K.L. Prime, G.M. Whitesides, Self-Assembled Organic Monolayers: Model Systems for Studying Adsorption of Proteins at Sufaces. *Science* **252**, 1164–1167 (1991).

[51] S.M. Barlow, R. Ravel, Complex Organic Molecules at Metal Surfaces: Bonding, Organisation and Chirality. *Surface Science Reports* **50**, 201–341 (2003).

[52] J. Rickert, T. Weiss, W. Göpel, Self-assembled Monolayers for Chemical Sensors: Molecular Recognition by Immobilized Supramolecular Structures. *Sensors and Actuators B-Chemical* **31**, 45–50 (1996).

[53] S.V. Atre, B. Liedberg, D.L. Allara, Chain Length Dependence of the Structure and Wetting Properties in Binary Composition Monolayers of OH- and CH3-Terminated Alkanethiolates on Gold. *Langmuir* **11**, 3882–3893 (1995).

[54] J. Scherer, M.R. Vogt, O.M. Magnussen, R.J. Behm, Corrosion of Alkanethiol-Covered Cu(100) Surfaces in Hydrochloric Acid Solution Studied by in-Situ Scanning Tunneling Microscopy. *Langmuir* **13**, 7045–7051 (1997).

[55] Z.J. Donhauser, B.A. Mantooth, K.F. Kelly, L.A. Bumm, J.D. Monnell, J.J. Stapleton, D.W. Price, A.M. Rawlett, D.L. Allara, J.M. Tour, P.S. Weiss, Conductance Switching in Single Molecules Through Conformational Changes. *Science* **292**, 2303–2307 (2001).

[56] A. Gölzhäuser, W. Geyer, V. Stadler, W. Eck, M. Grunze, K. Edinger, T. Weimann, P. Hinze, Nanoscale patterning of self-assembled monolayers with electrons. *Journal of Vacuum Science & Technology B* **18**, 3414–3418 (2000).

[57] S. De Feyter, F.C. De Schryver, Self-assembly at the Liquid/Solid Interface: STM Reveals. *Journal of Physical Chemistry B* **109**, 4290–4302 (2005).

[58] F. Schreiber, Structure and Growth of Self-assembling Monolayers. *Progress in Surface Science* **65**, 151–256 (2000).

[59] F. Schreiber, Self-assembled monolayers: from 'simple' model systems to biofunctionalized interfaces. *Journal of Physics: Condensed Matter* **16**, R881–R900 (2004).

[60] K. Heister, M. Zharnikov, M. Grunze, L.S.O. Johansson, Adsorption of Alkanethiols and Biphenylthiols on Au and Ag Substrates: A High-Resolution X-ray Photoelectron Spectroscopy Study. *Journal of Physical Chemistry B* **105**, 4058–4061 (2001).

[61] J.C. Love, D.B. Wolfe, R. Haasch, Formation and Structure of Self-Assembled Monolayers of Alkanethioles on Palladium. *Journal of the American Chemical Society* **125**, 2597–2609 (2003).

[62] K. Slowinski, H.K.Y. Fong, M. Majda, Mercury-Mercury Tunneling Junctions. 1. Electron Tunneling Across Symmetric and Asymmetric Alkanethiolate Bilayers. *Journal of the American Chemical Society* **121**, 7257–7261 (1999).

[63] A.F. Carley, P.R. Davies, R.V. Jones, K.R. Harikumar, M.W. Roberts, An STM and XPS study of the chemisorbtion of methyl mercaptan at a Cu(110) surface. *Surface Science* **490**, L585–L591 (2001).

[64] D. Kockmann, B. Poelsema, H.J.W. Zandvliet, Transport through a Single Octanethiol Molecule. *Nano Letters* 1147–1151 (2009).

[65] I. Platzman, C. Saguy, R. Brener, R. Tannenbaum, H. Haick, Formation of Ultrasmooth and Highly Stable Copper Surfaces through Annealing and Self-Assembly of Organic Monolayers. *Langmuir* **26**, 191–201 (2010).

[66] B. Lüssem, S. Karthäuser, H. Haselier, R. Waser, The origin of faceting of ultraflat gold films epitaxially grown on mica. *Applied Surface Science* **249**, 197–202 (2005).

[67] L. Müller-Meskamp, B. Lüssem, S. Karthäuser, R. Waser, Rectangular $(3 \times 2\sqrt{3})$ Superlattice of a Dodecanethiol Self-Assembled Monolayer on Au(111) Observed by Ultra-High-Vacuum Scanning Tunneling Microscopy. *Journal of Physical Chemistry B* **109**, 11424–11426 (2005).

[68] B.G. Frederick, F.M. Leibsle, S. Haq, N.V. Richardson, Evolution of Lateral Order and Molecular Reorientation in the Benzoate/Cu(110) System. *Surface Review and Letters* **3**, 1523–1546 (1996).

[69] C.D. Bain, G.M. Whitesides, Formation of Monolayers by the Coadsorption of Thiols on Gold: Variation in the Length of the Alkyl Chain. *Journal of the American Chemical Society* **111**, 7164–7175 (1989).

[70] P. Fenter, A. Eberhardt, K.S. Liang, P. Eisenberger, Epitaxy and chain-length dependent strain in self-assembled monolayers. *Journal of Chemical Physics* **106**, 1600–1608 (1997).

[71] E. Delamarche, B. Michel, Ch. Gerber, D. Anselmetti, H.-J. Guentherodt, H. Wolf, H. Ringsdorf, Real-Space Observation of Nanoscale Molecular Domains in Self-Assembled Monolayers. *Langmuir* **10**, 2869–2871 (1994).

[72] C. Vericat, M.E. Vela, G.A. Benitez, J.A. Martin Gago, X. Torrelles, R.C. Salvarezza, Surface characterization of sulfur and alkanethiol self-assembled monolayers on Au(111). *Journal of Physics: Condensed Matter* **18**, R867–R900 (2006).

[73] E. Delamarche, B. Michel, H.A. Biebuyck, C. Gerber, Golden Interfaces: The Surface of Self-Assembled Monolayers. *Advanced Materials* **8**, 719–729 (1996).

[74] J. Noh, M. Hara, Molecular-Scale Growth Processes of Alkanethiol Self-Assembled Monolayers on Au(111). *RIKEN Review* **38**, 49–51 (2001).

[75] B. Lüssem, L. Müller-Meskamp, S. Karthäuser, R. Waser, A New Phase of the c(4× 2) Superstructure of Alkanethiols Grown by Vapor Phase Deposition on Gold. *Langmuir* **21**, 5256–5258 (2005).

[76] A. Riposan, G.-Y. Liu, Significance of Local Density of States in the Scanning Tunneling Microscopy Imaging of Alkanethiol Self-Assembled Monolayers. *Journal of Physical Chemistry B* **110**, 23926–23937 (2006).

[77] G.E. Poirier, Mechanism of Formation of Au Vacancy Islands in Alkanethiol Monolayers on Au(111). *Langmuir* **13**, 2019–2026 (1997).

[78] C. Schönenberger, J.A.M. Sondag-Huethorst, J. Jorritsma, L.G.J. Fokkink, What are the "Holes" in Self-Assembled Monolayers of Alkanethiols on Gold? *Langmuir* **10**, 611–614 (1994).

[79] G.E. Poirier, Coverage-Dependent Phases and Phase Stability of Decanethiol on Au(111). *Langmuir* **15**, 1167–1175 (1999).

[80] N. Camillone III, T.Y.B. Leung, P. Schwartz, P. Eisenberger, G. Scoles, Chain Length Dependence of the Striped Phases of Alkanethiol Monolayers Self-Assembled on Au(111): An Atomic Beam Diffraction Study. *Langmuir* **12**, 2737–2746 (1996).

[81] C. Munuera, E. Barrena, C. Ocal, Chain-Length Dependence of Metastable Striped Structures of Alkanethiols on Au(111). *Langmuir* **21**, 8270–8277 (2005).

[82] H.A. Biebuyck, G.M. Whitesides, Interchange between Monolayers on Gold Formed from Unsymmetrical Disulfides and Solutions of Thiols - Evidence for Sulfur-Sulfur Bond Cleavage by Gold Metal. *Langmuir* **9**, 1766–1770 (1993).

[83] J. Noh, T. Murase, K. Nakajima, H. Lee, M. Hara, Nanoscopic Investigation of the Self-assembly Processes of Dialkyl Disulfides and Dialkyl Sulfides on Au(111). *Journal of Physical Chemistry B* **104**, 7411–7416 (2000).

[84] C.J. Zhong, M.D. Porter, Evidence for Carbon-Sulfur Bond Cleavage in Spontaneously Adsorbed Organosulfide-Based Monolayers at Gold. *Journal of the American Chemical Society* **116**, 11616–11617 (1994).

[85] J. Noh, H.S. Kato, M. Kawai, M. Hara, Surface and Adsorption Structures of Dialkyl Sulfide Self-Assembled Monolayers on Au(111). *Journal of Physical Chemistry B* **106**, 13268–13272 (2002).

[86] M.W.J. Beulen, B.-H. Huisman, P.A. van der Heijden, F.C.J.M. van Veggel, M.G. Simons, E.M.E.F. Biemond, P.J. de Lange, D.N. Reinhoudt, Evidence for Nondestructive Adsorption of Dialkyl Sulfides on Gold. *Langmuir* **12**, 6170–1672 (1996).

[87] F.P. Netzer, M.G. Ramsey, Structure and Orientation of Organic-Molecules on Metal-Surfaces. *Critical Reviews in Solid State and Materials Sciences* **17**, 397–475 (1992).

[88] Q. Chen, C.C. Perry, B.G. Frederick, N.V. Richardson, Structural aspects of the low-temperature deprotonation of benzoic acid on Cu(110) surfaces. *Surface Science* **446**, 63–76 (2000).

[89] J.T. Yates Jr. D.B. Dougherty, P. Maksymovych, Direct STM Evidence for Cu-benzoate Surface Complexes on Cu(110). *Science* **600**, 4484–4491 (2006).

[90] B.G. Frederick, Q. Chen, F.M. Leibsle, M.B. Lee, K.J. Kitching, N.V. Richardson, Long-range periodicity in c(8x2) benzoate/Cu(110): a combined STM, LEED, HREELS study. *Surface Science* **394**, 1–25 (1997).

[91] J.A. Theobald, N.S. Oxtoby, M.A. Phillips, N.R. Champness, P.H. Beton, Controlling molecular deposition and layer structure with supramolecular surface assemblies. *Nature* **424**, 1029–1031 (2003).

[92] O. Gurlu, O.A.O. Adam, H.J.W. Zandvliet, B. Poelsema, Self-organized, one-dimensional Pt nanowires on Ge(001). *Applied Physics Letters* **83**, 4610–4612 (2003).

[93] A. Cossaro, R. Mazzarello, R. Rousseau, L. Casalis, A. Verdini, A. Kohlmeyer, L. Floreano, S. Scandolo, A. Morgante, M.L. Klein, G. Scoles, X-ray Diffraction and Computation Yield the Structure of Alkanethiols on Gold(111). *Science* **321**, 943–946 (2008).

[94] C.C. Perry, S. Haq, B.G. Frederick, N.V. Richardson, Face specificity and the role of metal adatoms in molecular reorientation at surfaces. *Surface Science* **409**, 512–520 (1998).

[95] Arie van Houselt, *Structurel and Electronic Properties of Pt/Ge(001) and Au/Ge(001).* Ph.D. thesis, University Twente, 2008.

[96] C. Chidsey, D. Loiacono, T. Selator, S. Nakahara, STM Study of the Surface Morphology of Gold on Mica. *Surface Science* **200**, 45–66 (1988).

[97] C.E.D. Chidsey, D.N. Loiacono, Chemical Functionality in Self-assembled Monolayers: Structural and Electrochemical Properties. *Langmuir* **6**, 682–691 (1990).

[98] H.O. Finklea, S. Avery, M. Lynch, Blocking Oriented Monolayers of Alkyl Mercaptans on Gold Electrodes. *Langmuir* **3**, 409–413 (1987).

[99] U. Hoepfner, H. Hehl, L. Brehmer, Preparation of ordered thin gold films. *Applied Surface Science* **152**, 259–265 (1999).

[100] Björn Lüssem, *Molecular Electronic Building Blocks Based on Self-assembled Monolayers*. Ph.D. thesis, RWTH Aachen, 2006.

[101] Lars Müller-Meskamp, *Ferrocens as Potential Building Blocks for Molecular Electronics Self-assembly and Tunneling Spectroscopy*. Ph.D. thesis, RWTH Aachen, 2007.

[102] J. Perdereau, J.P. Biberian, G.E. Rhead, Adsorption and surface alloying of lead monolayers on (111) and (110) faces of gold. *Journal of Physics F: Metal Physics* **4**, 798–806 (1974).

[103] M.P. Everson, L.C. Davis, R.C. Jaklevic, W. Shen, Effects of surface states features upon the Au(111) surface state local density of states studied with scanning tunneling spectroscopy. *Journal of Vacuum Science & Technology B* **9**, 891–896 (1991).

[104] W. Chen, V. Madhavan, T. Jamneala, M.F. Crommie, Scanning Tunneling Microscopy Observation of an Electronic Superlattice at the Surface of Clean Gold. *Physical Review Letters* **80**, 1469–1472 (1998).

[105] S. Hüfner, *Photoelectron Spectroscopy: Principles and Applications*. Springer, Berlin, 2003.

[106] B.V. Crist, *Handbooks of Monochromatic XPS Spectra - Vol. 1 - The Elements and Native Oxides*. XPS International, Inc., Japan, 1999.

[107] Maria Christina Lennartz, Selbstorganisation von Alkanthiolen und Carboxylaten auf Au(111)- und Cu(110)-Oberflächen. diploma thesis, RWTH Aachen, 2007.

[108] K. Oura, V.G. Lifshitz, *Surface Science: An Introduction*. Springer, Berlin, 2003.

[109] L.D. Sun, M. Hohage, P. Zeppenfeld, Oxygen-induced reconstructions of Cu(110) studied by reflectance difference spectroscopy. *Physical Review B* **69**, 45407/1–6 (2004).

[110] D.S. Martin, R.J. Cole, P. Weightman, Effects of ion bombardment on the optical and electronic properties of Cu(110). *Physical Review B* **72**, 35408/1–8 (2005).

[111] D.S. Martin, A. Maunder, P. Weightman, Thermal Behavior of the Cu(110) Surface Studied by Reflection Anisotropy Spectroscopy and Scanning Tunneling Microscopy. *Physical Review B* **63**, 155403/1–8 (2001).

[112] W.M. Kuschke, A. Kretschmann, R.M. Keller, R.P. Vinci, C. Kaufmann, E. Arzt, Textures of Thin Copper Films. *Journal of Materials Research* **13**, 2962–2968 (1998).

[113] B. Okolo, P. Lamparter, U. Welzel, T. Wagner, E.J. Mittemeijer, The effect of deposition parameters and substrate surface condition on texture, morphology and stress in magnetron-sputter-deposited Cu thin films. *Thin Solid Films* **474**, 50–63 (2005).

[114] V. Venugopal, B.J. Thijsse, Defects of ultrathin Cu films on Mo(110) studied by thermal helium desorption spectrometry. *Journal of Physics D: Applied Physics* **42**, 165412/1–7 (2009).

[115] H.J.W. Zandvliet, The Ge(001) surface. *Physics Reports-Review Section of Physics Letters* **388**, 1–40 (2003).

[116] T. Sato, M. Iwatsuki, H. Tachihara, Detection of the flip-flop motion of buckled dimers on a Ge(001) surface by STM. *Journal of Electron Microscopy* **48**, 1–7 (1999).

[117] A. van Houselt, R. van Gastel, B. Poelsema, H.J.W. Zandvliet, Dynamics and Energetics of Ge(001) Dimers. *Physical Review Letters* **97**, 266104/1–4 (2006).

[118] O. Gurlu, H.J.W. Zandvliet, B. Polsema, S. Dag, S. Ciraci, Initial stages of Pt growth on Ge(001) studied by scanning tunneling microscopy and density functional theory. *Physical Review B* **70**, 085312/1–10 (2004).

[119] M. Fischer, A. van Houselt, D. Kockmann, B. Poelsema, H.J.W. Zandvliet, Formation of atomic Pt chains on Ge(001) studied by scanning tunneling microscopy. *Physical Review B* **76**, 245429/1–5 (2007).

[120] B.G. Frederick, Q. Chen, F.M. Leibsle, S.S. Dhesi, N.V. Richardson, Electron-stimulated disordering in c(8× 2) benzoate/Cu(110): a combined STM, LEED and HREELS study. *Surface Science* **394**, 26–46 (1997).

[121] N.D. Lang, Resistance of a one-atom contact in the scanning tunneling microscope. *Physical Review B* **36**, 8173–8176 (1987).

[122] H. Ishii, K. Sugiyama, E. Ito, K. Seki, Energy Level Alignment and Interfacial Electronic Structures at Organic/Metal and Organic/Organic Interfaces. *Advanced Materials* **11**, 605–625 (1999).

[123] S. Braun, W.R. Salaneck, M. Fahlman, Energy-Level Alignment at Organic/Metal and Organic/Organic Interfaces. *Advanced Materials* **21**, 1450–1472 (2009).

[124] L. Vitali, G. Levita, R. Ohmann, A. Comisso, A. De Vita, K. Kern, Portrait of the potential barrier at metal-organic nanocontacts. *Nature Materials* **9**, 320–323 (2010).

[125] M. Pascal, C.L.A. Lamont, M. Kittel, J.T. Hoeft, R. Terborg, M. Polcik, J.H. Kang, R. Toomes, D.P. Woodruff, Quantitative structural determination of the high coverage phase of the benzoate species on Cu(110). *Surface Science* **492**, 285–93 (2001).

[126] J. Lee, I.A. Balabin, D.N. Beratan, J.G. Lee, J.T. Yates, Charge transfer through chemisorbed organic molecules - Neutralization of ionization processes at local sites in the molecule. *Chemical Physics Letters* **412**, 171–175 (2005).

[127] J.M. Beebe, B. Kim, J.W. Gadzuk, C.D. Frisbie, J.G. Kushmerick, Transition from Direct Tunneling to Field Emission in Metal-Molecule-Metal Junctions. *Physical Review Letters* **97**, 26801/1–4 (2006).

[128] J.M. Beebe, B. Kim, C.D. Frisbie, J.G. Kushmerick, Measuring Relative Barrier Heights in Molecular Electronic Junctions with Transition Voltage Spectroscopy. *ACS Nano* **2**, 827–832 (2008).

[129] S.H. Choi, B. Kim, C.D. Frisbie, Electrical Resistance of Long Conjugated Molecular Wires. *Science* **320**, 1482–1486 (2008).

[130] G. Wang, T.W. Kim, G. Jo, T. Lee, Enhancement of Field Emission Transport by Molecular Tilt Configuration in Metal-Molecule-Metal Junctions. *Journal of the American Chemical Society* **131**, 5980–5985 (2009).

[131] S.A. DiBenedetto, A. Facchetti, M.A. Ratner, T.J. Marks, Charge Conduction and Breakdown Mechanisms in Self-Assembled Nanodielectrics. *Journal of the American Chemical Society* **131**, 7158–7168 (2009).

[132] E.H. Huisman, C.M. Guédon, B.J. van Wees, S.J. van der Molen, Interpretation of Transition Voltage Spectroscopy. *Nano Letters* **9**, 3909–3913 (2009).

[133] H. Proehl, M. Toerker, F. Sellam, T. Fritz, K. Leo, C. Simpson, K. Müllen, Comparison of ultraviolet photoelectron spectroscopy and scanning tunneling spectroscopy measurements on highly ordered ultrathin films of hexaperi-hexabenzocoronene on Au(111). *Physical Review B* **63**, 205409/1–6 (2001).

[134] D. Cahen, A. Kahn, E. Umbach, Energetics of molecular interfaces. *Materials Today* **8**, 32 – 41 (2005).

[135] D.S. Martin, R.J. Cole, S. Haq, Creating a functionalized surface: The adsorption of terephthalic acid onto Cu(110). *Physical Review B* **66**, 155427/1–8 (2002).

[136] F.M. Chua, Y. Kuk, P.J. Silverman, Oxygen-Chemisorption on Cu(110): An Atomic View by Scanning Tunneling Microscopy. *Physical Review Letters* **63**, 386–389 (1989).

[137] Y. Li, J. Zhao, X. Yin, G. Yin, Ab Initio Investigations of the Electric Field Dependence of the Geometric and Electronic Structures of Molecular Wires. *Journal of Physical Chemistry A* **110**, 11130–11135 (2006).

[138] J. Schnadt, J. Schiessling, J.N. O'Shea, S.M. Gray, L. Patthey, M.K.J. Johansson, M. Shi, J. Krempaskỳ, J. Åhlund, P.G. Karlsson, P. Persson, N. Mårtensson, P.A. Brühwiler, Structural study of adsorption of isonicotinic acid and related molecules on rutile TiO_2(110) I: XAS and STM. *Surface Science* **540**, 39–54 (2003).

[139] J. Schnadt, J.N. O'Shea, L. Patthey, J. Schiessling, J. Krempaskỳ, M. Shi, N. Mårtensson, P.A. Brühwiler, Structural study of adsorption of isonicotinic acid and related molecules on rutile TiO_2(110) II: XPS. *Surface Science* **544**, 74–86 (2003).

[140] L. Limot, J. Kröger, R. Berndt, A. Garcia-Lekue, W.A. Hofer, Atom Transfer and Single-Adatom Contacts. *Physical Review Letters* **94**, 126102/1–4 (2005).

[141] D.J. Wold, R. Haag, M.A. Rampi, C.D. Frisbie, Distance Dependence of Electron Tunneling through Self-Assembled Monolayers Measured by Conducting Probe Atomic Force Microscopy: Unsaturated versus Saturated Molecular Junctions. *Journal of Physical Chemistry B* **106**, 2813–2816 (2002).

[142] N. Atodiresei, K. Schroeder, S. Blügel, Density-functional theory study on the arrangement of adsorbed formate molecules on Cu(110). *Physical Review B* **75**, 115407/1–14 (2007).

[143] N. Atodiresei, V. Caciuc, K. Schroeder, S. Blügel, First-principles investigation of terephthalic acid on Cu(110). *Physical Review B* **76**, 115433/1–8 (2007).

[144] J. Repp, G. Meyer, S. Paavilainen, F.E. Olsson, M. Persson, Imaging Bond Formation Between a Gold Atom and Pentacene on an Insulating Surface. *Science* **312**, 1196–1199 (2006).

[145] V. Simic-Milosevic, J. Meyer, K. Morgenstern, Chirality Change of Chloronitrobenzene on Au(111) Induced by Inelastic Electron Tunneling. *Angewandte Chemie International Edition* **48**, 4061–4064 (2009).

[146] H.L. Tierney, A.E. Baber, E.C.H. Sykes, A. Akimov, A.B. Kolomeisky, Dynamics of Thioether Molecular Rotors: Effects of Surface Interactions and Chain Flexibility. *Journal of Physical Chemistry C* **113**, 10913–10920 (2009).

[147] M.A. Lingenfelder, H. Spillmann, A. Dmitriev, S. Stepanow, N. Lin, J.V. Barth, K. Kern, Towards surface-supported supramolecular architectures: tailored coordination assembly of 1,4-benzenedicarboxylate and Fe on Cu(100). *Chemistry-A European Journal* **10**, 1913–1919 (2004).

[148] B. Lüssem, L. Müller-Meskamp, S. Karthäuser, R. Waser, M. Homberger, U. Simon, STM Study of Mixed Alkanethiol/Biphenylthiol Self-Assembled Monolayers on Au(111). *Langmuir* **22**, 3021–3027 (2006).

[149] M. Albrecht, M. Fiege, M. Baumert, M. de Groot, R. Frohlich, L. Russo, K. Rissanen, Hierarchical lithium-templated assembly of helicate-type complexes: How versatile is this reaction? *European Journal of Inorganic Chemistry* 609–616 (2007).

[150] Miriam Baumert, *Funktionalisierte hierarchisch gebildete Helicate*. Ph.D. thesis, RWTH Aachen, 2009.

[151] C. Vericat, M.E. Vela, R.C. Salvarezza, Self-assembled monolayers of alkanethiols on Au(111): surface structures, defects and dynamics. *Physical Chemistry Chemical Physics* **7**, 3258–3268 (2005).

[152] F. von Wrochem, F. Scholz, A. Schreiber, H.-G. Nothofer, W.E. Ford, P. Morf, T. Jung, A. Yasuda, J.M. Wessels, Structure and Conductance of Aromatic and Aliphatic Dithioacetamide Monolayers on Au(111). *Langmuir* **24**, 6910–6917 (2008).

[153] T. Ishida, N. Choi, W. Mizutani, H. Tokumoto, I. Kojima, H. Azehara, H. Hokari, U. Akiba, M. Fujihira, High-resolution X-ray photoelectron spectra of organosulfur monolayers on Au(111): S(2p) spectral dependence on molecular species. *Langmuir* **15**, 6799–6806 (1999).

[154] J. Noh, Y. Jeong, E. Ito, M. Hara, Formation and Domain Structure of Self-Assembled Monolayers by Adsorption of Tetrahydrothiophene on Au(111). *Journal of Physical Chemistry C* **111**, 2691–2695 (2007).

[155] D.L. Pugmire, M.J. Tarlov, R.D. van Zee, Structure of 1,4-Benzenedimethanethiol Self-Assembled Monolayers on Gold Grown by Solution and Vapor Techniques. *Langmuir* **19**, 3720–3726 (2003).

[156] T. Ishida, M. Hara, I. Kojima, S. Tsuneda, N. Nishida, H. Sasabe, W. Knoll, High Resolution X-ray Photoelectron Spectroscopy Measurements of Octadecanethiol Self-Assembled Monolayers on Au(111). *Langmuir* **14**, 2092–2096 (1998).

[157] A.J. Leavitt, Jr. T.P. Beebe, Chemical reactivity studies of hydrogen sulfide on Au(111). *Surface Science* **314**, 23–33 (1994).

[158] S. Clair, S. Pons, A.P. Seitsonen, H. Brune, K. Kern, J.V. Barth, STM Study of Terephthalic Acid Self-Assembly on Au(111): Hydrogen-Bonded Sheets on an Inhomogeneous Substrate. *Journal of Physical Chemistry B* **108**, 14585–14590 (2004).

[159] S.B. Darling, A.W. Rosenbaum, Y. Wang, S.J. Sibener, Coexistence of the $(23 \times \sqrt{3})$ Au(111) Reconstruction and a Striped Phase Self-Assembled Monolayer. *Langmuir* **18**, 7462–7468 (2002).

[160] C.A. Widrig, C.A. Alves, M.D. Porter, Scanning Tunneling Microscopy of Ethanethiolate and n-Octadecanthiolate Monolayers Spontaneously Adsorbed at Gold Surfaces. *Journal of the American Chemical Society* **113**, 2805–2810 (1991).

[161] K. Kobayashi, H. Yamada, T. Horiuchi, K. Matsushige, The Molecular Arrangements of Alkanethiol Self-Assembled Monolayers on Au(111) Studied by Scanning Tunneling Microscopy. *Japanese Journal of Applied Physics* **37**, 6183–6185 (1998).

[162] T. Fukuma, T. Ichii, K. Kobayashi, H. Yamada, K. Matsushige, Molecular-scale noncontact atomic force microscopy contrasts in topography and energy dissipation on c(4x2) superlattice structures of alkanethiol self-assembled monolayers. *Journal of Applied Physics* **95**, 1222–1226 (2004).

[163] B. Lüssem, L. Müller-Meskamp, S. Karthäuser, M. Homberger, U. Simon, R. Waser, Electrical and structural characterization of biphenylethanethiol SAMs. *Journal of Physical Chemistry C* **111**, 6392–6397 (2007).

[164] J. Tomfohr, O.F. Sankey, Theoretical analysis of electron transport through organic molecules. *Journal of Chemical Physics* **120**, 1542–1554 (2004).

[165] A. Ulman, Formation and Structure of Self-Assembled Monolayers. *Chemical Reviews* **96**, 1533–1554 (1996).

[166] M. Sharma, M. Komiyama, J.R. Engstrom, Observation from Scanning Tunneling Microscopy of a Striped Phase for Octanethiol Adsorbed on Au(111) from Solution. *Langmuir* **24**, 9937–9940 (2008).

[167] V.B. Engelkes, J.M. Beebe, C.D. Frisbie, Length-Dependent Transport in Molecular Junctions Based on SAMs of Alkanethiols and Alkanedithiols: Effect of Metal Work Function and Applied Bias on Tunneling Efficiency and Contact Resistance. *Journal of the American Chemical Society* **126**, 14287–14296 (2004).

[168] E. Wierzbinski, K. Slowinski, In Situ Wiring of Single Molecules into an Electrical Circuit via Electrochemical Distance Tunneling Spectroscopy. *Langmuir* **22**, 5205–5208 (2006).

[169] H.B. Akkerman, B. de Boer, Electrical conduction through single molecules and self-assembled monolayers. *Journal of Physics: Condensed Matter* **20**, 013001/1–20 (2008).

[170] N. Oncel, A. van Houselt, J. Huijben, A.S. Hallbäck, O. Gurlu, H.J.W. Zandvliet, B. Poelsema, Quantum Confinement between Self-Organized Pt Nanowires on Ge(001). *Physical Review Letters* **95**, 116801/1–4 (2005).

[171] N. Oncel, W.J. van Beek, J. Huijben, B. Poelsema, H.J.W. Zandvliet, Diffusion and binding of CO on Pt nanowires. *Surface Science* **600**, 4690–4693 (2006).

[172] J. Gao, Z.W. Wang, D.M. Xu, R.K. Zhang, Solubilities of Triphenylphosphine in Ethanol, 2-Propanol, Acetone, Benzene, and Toluene. *Journal of Chemical and Engineering Data* **52**, 189–191 (2007).

[173] Y.Y. Mu, H.P. Liang, J.S. Hu, L. Jiang, L.J. Wan, Controllable Pt Nanoparticle Deposition on Carbon Nanotubes as an Anode Catalyst for Direct Methanol Fuel Cells. *Journal of Physical Chemistry B* **109**, 22212–22216 (2005).

1. **Ferrocenes as Potential Building Blocks for Molecular Electronics**
   Self-Assembly and Tunneling Spectroscopy
   by L. Müller-Meskamp (2008), 153 pages
   ISBN: 978-3-89336-509-8

2. **Magnetic Proximity Effects in Highly-ordered Transition Metal Oxide Heterosystems studied by Soft x-Ray Photoemission Electron Microscopy**
   by I. P. Krug (2008), XX, 180 pages
   ISBN: 978-3-89336-521-0

3. **Seltenerd-basierte ternäre Oxide als alternative Gatedielektrika**
   von J. M. Roeckerath (2008), 148 Seiten
   ISBN: 978-3-89336-543-2

4. **Strominduzierte Magnetisierungsdynamik in einkristallinen Nanosäulen**
   von R. Lehndorff (2009), I, 86 Seiten
   ISBN: 978-3-89336-564-7

5. **Magnetization Dynamics in Magnetically Coupled Heterostructures**
   von A. Kaiser (2009), X, 121 pages
   ISBN: 978-3-89336-577-7

6. **Resistive switching in Pt/TiO_2/PT**
   by D. S. Jeong (2009), vii, 133 pages
   ISBN: 978-3-89336-579-1

7. **Electromechanical Force Microscopy and Tip-Enhanced Raman Spectroscopy for Polar Oxide Nanoparticles**
   by S. Röhrig (2009), vi, 114 pages
   ISBN: 978-3-89336-600-2

8. **Investigation of resistive switching in barium strontium titanate thin films for memory applications**
   by W. Shen (2010), 114 pages
   ISBN: 978-3-89336-608-8

9. **Nanostrukturierte Metallelektroden zur funktionalen Kopplung an neuronale Zellen**
   von D. Brüggemann (2010), vii, 160 Seiten
   ISBN: 978-3-89336-627-9

10. **Integration of resistive switching devices in crossbar structures**
    by Chr. Nauenheim (2010), XII, 142 pages
    ISBN: 978-3-89336-636-1

11. **Correlation between Raman spectroscopy and electron microscopy on individual carbon nanotubes and peapods**
by C. Spudat (2010). xiv, 125 pages
ISBN: 978-3-89336-648-4

12. **DC and RF Characterization of NiSi Schottky Barrier MOSFETs with Dopant Segregation**
by C. J. Urban (2010), iv, 151 pages
ISBN: 978-3-89336-644-6

13. **Alternative Systems for Molecular Electronics: Functionalized Carboxylic Acids on Structured Surfaces**
by M. C. Lennartz (2010), 183 pages
ISBN: 978-3-89336-667-5

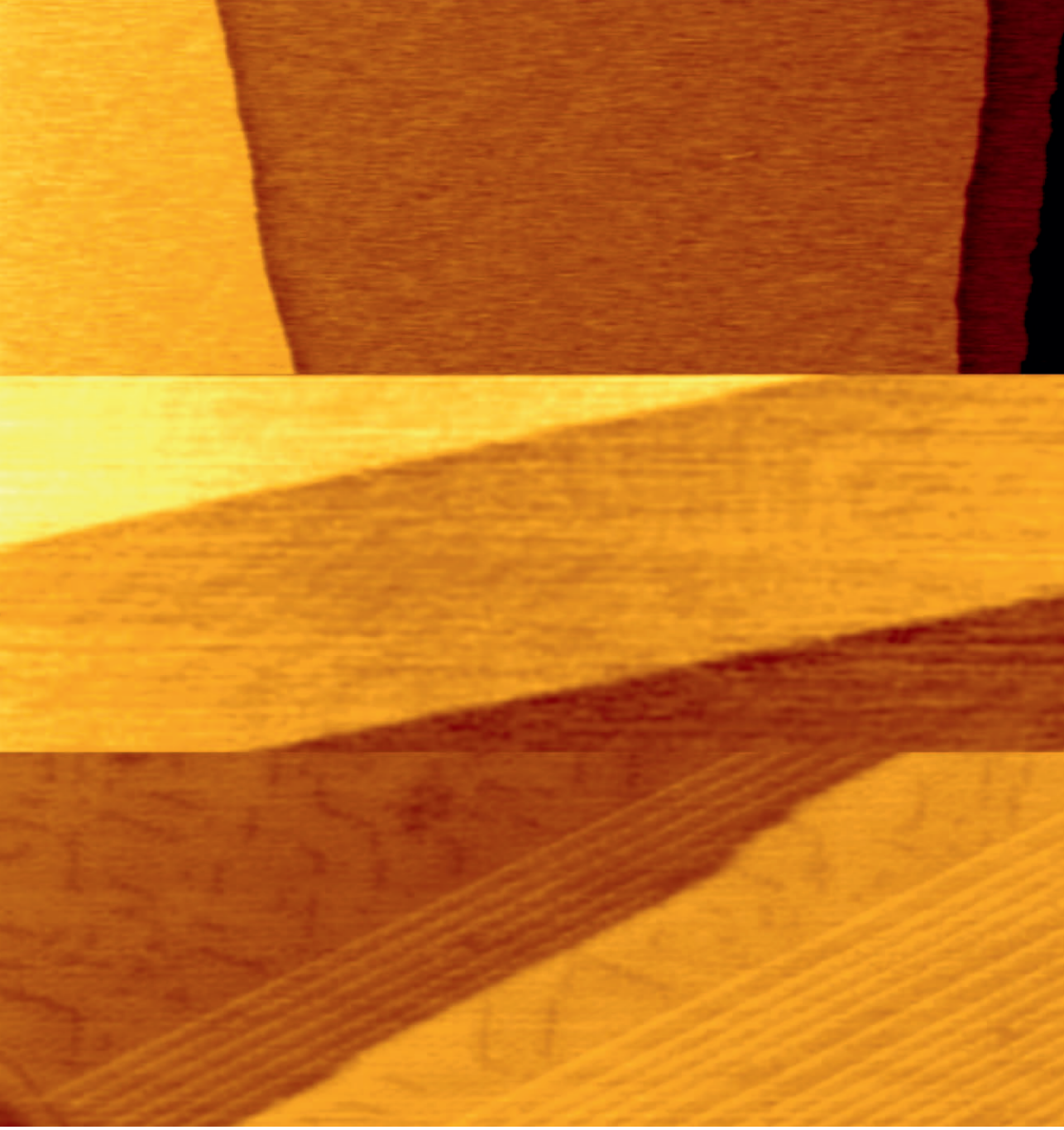

Information / Information
Band / Volume 13
ISBN 978-3-89336-667-5

JÜLICH
FORSCHUNGSZENTRUM